

Twisted Rylene Bisimides for Organic Solar Cells and Strong Chiroptical Response in the Near Infrared



Dissertation zur Erlangung des
naturwissenschaftlichen Doktorgrades
der Julius-Maximilians-Universität Würzburg

vorgelegt von

Bernhard Mahlmeister

aus Aschaffenburg

Würzburg 2023



Eingereicht bei der Fakultät für Chemie und Pharmazie am:

25. Oktober 2023

Gutachter der schriftlichen Arbeit:

1. Gutachter: Prof. Dr. Frank Würthner
2. Gutachter: Dr. Princekumar Ravat

Prüfer des öffentlichen Promotionskolloquiums:

1. Prüfer: Prof. Dr. Frank Würthner
2. Prüfer: Dr. Princekumar Ravat
3. Prüfer: Jun.-Prof. Dr. Agnieszka Nowak-Król

Datum des öffentlichen Promotionskolloquiums:

07. Dezember 2023

Doktorurkunde ausgehändigt am:

List of Abbreviations

A	–	acceptor
a.u.	–	arbitrary units
ADF	–	Amsterdam density functional
AFM	–	atomic force microscopy
APCI	–	atmospheric pressure chemical ionization
BCP	–	bathocuproine
BHJ	–	bulk heterojunction
CB	–	chlorobenzene
CB	–	circular birefringence
CD	–	circular dichroism
CPL	–	circularly polarized luminescence
CT	–	charge transfer
CV	–	cyclic voltammetry
D	–	donor
DCM	–	dichloromethane
DCTB	–	<i>trans</i> -2-[3-(4- <i>tert</i> -butylphenyl)-2-methyl-2-propenylidene]malono-nitrile
DFT	–	density functional theory
Dipp	–	2,6-diisopropylphenyl
DMF	–	dimethylformamide
DMSO	–	dimethylsulfoxide
DNA	–	deoxyribonucleic acid
DPV	–	differential pulse voltammetry
e.g.	–	<i>exempli gratia</i>
<i>ee</i>	–	enantiomeric excess
EM	–	electromagnetic
equiv	–	equivalents
ESI	–	electron spray ionization

FMO	–	frontier molecular orbital
fwhm	–	full width at half maximum
GPC	–	gel permeation chromatography
HOMO	–	highest occupied molecular orbital
HONTO	–	highest occupied natural transition orbital
HOPG	–	highly oriented pyrolytic graphite
HPLC	–	high-performance liquid chromatography
HRMS	–	high-resolution mass spectrometry
i.e.	–	<i>id est</i>
ITO	–	indium tin oxide
LB	–	linear birefringence
LD	–	linear dichroism
LUMO	–	lowest unoccupied molecular orbital
LUNTO	–	lowest unoccupied natural transition orbital
m.p.	–	melting point
MALDI	–	matrix-assisted laser desorption ionization
MeCN	–	acetonitrile
MTDM	–	magnetic transition dipole moment
NDI	–	naphthalene diimide
NFA	–	non-fullerene acceptor
NHE	–	normal hydrogen electrode
NIR	–	near infrared
NMR	–	nuclear magnetic resonance
NTO	–	natural transition orbital
OLED	–	organic light-emitting diode
OPV	–	organic photovoltaic
OSC	–	organic solar cell
OTFT	–	organic thin-film transistor
PAH	–	polycyclic aromatic hydrocarbon

PBI	–	perylene bisimide
PCE-10	–	Poly[4,8-bis(5-(2-ethylhexyl)thiophen-2-yl)benzo[1,2-b;4,5b']dithiophene-2,6-diyl-alt-(4-(2-ethylhexyl)3-fluorothieno[3,4-b]thiophene-)-2-carboxylate-2-6-diyl]
PEDOT:PSS	–	poly(3,4-ethylenedioxythiophene)-poly(styrenesulfonate)
PMMA	–	poly(methyl methacrylate)
POM	–	polarization optical microscope
ppm	–	parts per million
PTE	–	perylene tetraester
QBI	–	quaterrylene bisimide
SCE	–	standard calomel electrode
SCLC	–	space-charge limited current
TBAHFP	–	tetrabutylammonium hexafluorophosphate
TCE	–	1,1,2,2,-tetrachloroethane
TD-DFT	–	time-dependent density functional theory
TOF	–	time of flight
UV–vis–NIR	–	ultraviolet–visible–near-infrared

Physical Quantities, Constants and Units

α_{agg}	–	degree of aggregation
B_{CPL}	–	circularly polarized luminescence brightness
c	–	concentration
d	–	thickness
δ	–	chemical shift
E	–	energy
$E_{\text{red/Ox}}$	–	reduction/oxidation potential
ε	–	molar extinction coefficient
ε_{L}	–	molar extinction coefficient for left circularly polarized light

ε_R	–	molar extinction coefficient for right circularly polarized light
$\Delta\varepsilon$	–	circular dichroism
EQE	–	external quantum efficiency
FF	–	fill factor
g_{abs}	–	absorption dissymmetry factor
g_{lum}	–	emission dissymmetry factor
ΔG	–	Gibbs free energy
ΔG^\ddagger	–	Gibbs free energy of activation
ΔH	–	molar enthalpy
I	–	intensity
I_L	–	emission intensity of left circularly polarized light
I_R	–	emission intensity of right circularly polarized light
ΔI	–	difference of emission intensity for left and right circularly polarized light
J	–	interchromophoric coupling energy
J_{sc}	–	short-circuit current density
k	–	rate constant
k_B	–	Boltzmann constant
λ	–	wavelength
M	–	molecular weight
\mathbf{m}	–	magnetic transition dipole moment
$\boldsymbol{\mu}$	–	electric transition dipole moment
μ	–	charge carrier mobility
mdeg	–	millidegree
n	–	amount of substance
OD	–	optical density
$\Delta\tilde{\nu}_{\text{Stokes}}$	–	Stokes shift
PCE	–	power conversion efficiency
Φ_{Fl}	–	fluorescence quantum yield
Φ_{PL}	–	photoluminescence quantum yield

p	–	pressure
ρ	–	density
R	–	rotatory strength
R_q	–	root-mean square roughness
\mathbf{r}	–	interchromophoric distance vector
rpm	–	rounds per minute
S_n	–	n^{th} electronic singlet state
s	–	second
T	–	temperature
t	–	time
$t_{+/-}$	–	transfer integral for holes and electrons
τ_{rac}	–	racemization half-life times
ϑ	–	angle between electric and magnetic transition dipole moments
V	–	interchromophoric coupling energy
V_{OC}	–	open-circuit voltage
v:v	–	volumetric ratio

Table of Contents

<u>CHAPTER 1</u>	<u>1</u>
<u>Introduction and Aim of the Thesis</u>	<u>1</u>
<u>CHAPTER 2</u>	<u>6</u>
<u>State of Knowledge</u>	<u>6</u>
2.1 Theoretical Description of Circular Dichroism	6
2.1.1 Inherent Chirality and Molecular Chirality	8
2.1.2 Excitonic Chirality and Supramolecular Chirality	11
2.2 Chiral Rylene Bisimide Dyes	17
2.2.1 Inherently Chiral Twisted Monomeric Dyes	17
2.2.2 Exciton-coupled Dyes	21
2.2.3 <i>Bay</i> -annulated Rylene Dyes	31
<u>CHAPTER 3</u>	<u>40</u>
<u>Axially Chiral <i>Bay</i>-tetraarylated Perylene Bisimide Dyes as Non-fullerene Acceptors in Organic Solar Cells</u>	<u>40</u>
3.1 Introduction	41
3.2 Twisted PBIs Designed as Non-fullerene Acceptors	44
3.3 Molecular Packing	47
3.4 Impact of Enantiopurity on Organic Solar Cell Performance	50
3.5 Chiral Packing in Single Crystals and Thin Films	53
3.6 Conclusion	57
<u>CHAPTER 4</u>	<u>58</u>
<u>Helically Twisted Nanoribbons Based on Emissive Near-Infrared Responsive Quaterrylene Bisimides</u>	<u>58</u>
4.1 Introduction	59
4.2 Synthesis	61
4.3 Structural Properties	63
4.4 Absorption Properties	65
4.5 Fluorescence Properties	66
4.6 Chiroptical Properties	67
4.7 Conclusion	69
<u>CHAPTER 5</u>	<u>70</u>
<u>Enantiopure J-Aggregate of Quaterrylene Bisimides for Strong Chiroptical NIR-Response</u>	<u>70</u>
5.1 Introduction	71
5.2 Synthesis	74
5.3 Optical Properties and Aggregation	75
5.4 Chiroptical Properties	78
5.5 Structural Properties	79
5.6 Theoretical Calculations of Chiroptical Response	82
5.7 Conclusion	86
<u>CHAPTER 6</u>	<u>87</u>
<u>Summary and Conclusion</u>	<u>87</u>

<u>CHAPTER 7</u>	<u>92</u>
<u>Zusammenfassung und Fazit</u>	<u>92</u>
<u>CHAPTER 8</u>	<u>98</u>
<u>Appendix</u>	<u>98</u>
8.1 Supporting Information for <i>Chapter 3</i>	98
8.2 Supporting Information for <i>Chapter 4</i>	117
8.3 Supporting Information for <i>Chapter 5</i>	154
<u>Bibliography</u>	<u>177</u>
<u>Danksagung</u>	<u>191</u>
<u>List of Publications</u>	<u>193</u>

CHAPTER 1

—

Introduction and Aim of the Thesis

Chirality is the inherent geometric property of an object and its mirrored counterpart to be non-superimposable by any translation or rotation.^[1] Chirality pervades the entire universe and chiral objects can be as massive as a spiral galaxy^[2] or as small as a nanoparticle^[3] or a molecule. Remarkably, even light itself can be chiral, then characterized by its discrimination into left and right circular polarization. In our world, electromagnetic (EM) radiation, and visible light in particular, serves as the most widely employed medium of transmitting information. Organic dyes such as polycyclic aromatic hydrocarbons (PAHs) with extended π -scaffolds are highly light absorbing, which means they show a strong resonance to the incident EM light. Accordingly, the driving electric field of the EM radiation can induce an electric dipole into the absorbing molecule. Beyond that, chiral molecules exhibit the unique property of an interplay with the magnetic component of this incident light. This means, an oscillating electric dipole is not only generated by the electric but also the magnetic field of the incident radiation.^[4] Thus, chiral molecules can handle an additional information content compared to achiral ones, which also recently motivated for the realization of chiral spintronic devices.^[5] The ‘chiroptical response’ offers versatile spectroscopic utility but of course, only comes into play if there is an imbalance of the addressed chiral molecules in terms of left- and right-handed counterparts called ‘enantiomers’. Luckily, this imbalance is actually a fundamental condition in nature. Of most natural building blocks, such as amino acids or sugars, only one enantiomer prevails naturally. The molecular homochirality of these building blocks translates into the supramolecular chirality of proteins, biopolymers or DNA helices. Thus, life itself is essentially homochiral,^[6] and chiroptical spectroscopy can probe the structural properties of its various shapes.^[7]

The most utilized chiroptical property is the circular dichroism (CD, see Figure 1), which describes the molecules’ interaction with circularly polarized light regarding absorption or emission. When illuminated with circularly polarized light, an enantiomer or a homochiral supramolecular structure appears in a different color compared to its mirror object. If molecules come into excitonic coupling, the chiroptical response changes drastically and can increase by orders of magnitudes.^[8-9]

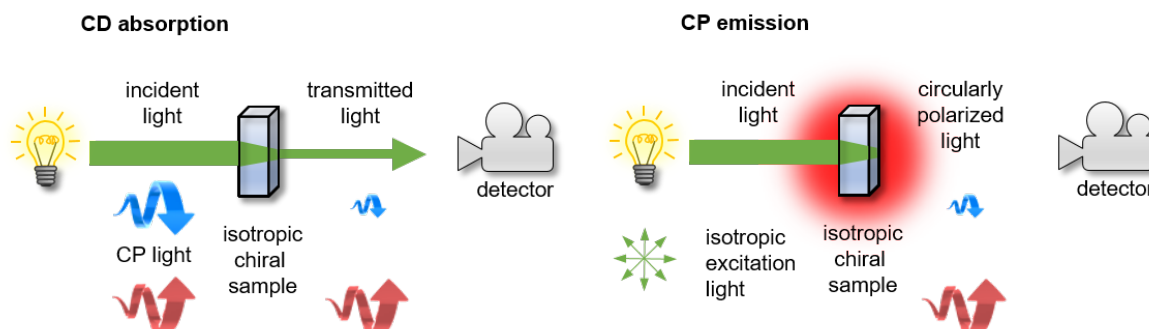


Figure 1. Schematic overview of an isotropic sample's CD absorption (left) and CP emission (right) spectroscopy. Left and right circularly polarized light is depicted as red and blue spiral arrows, respectively.

There are currently two major concepts for utilizing this phenomenon. In the first, CD spectroscopy serves as an analytical tool. This spectral information and the difference in signal magnitude provide powerful information about the object's structure, such as DNA's secondary or tertiary structures,^[10] or protein interactions in solution,^[11] or even *in vivo*.^[12-13] In addition to directly probing natural chiral structures, chemically tailored chiral chromophores, which can exhibit a much stronger chiroptical response, can be designed to establish precise interactions with these biological structures. This enables them to function as probes with exceptional structural sensitivity.^[14] For biomedical applications, it is now highly desirable to shift the chiroptical response of these probes into the near-infrared spectral window to ease *in vitro* or *in vivo* analysis.^[15] The second concept of CD utilization aims for the emission of mainly single-handed circularly polarized (CP) light (see Figure 1). For this, today's most demanded application is the use of a CP emitter in an organic light-emitting diode (OLED) for display technology. Due to the unique polarization properties of such CP light, it can out-couple way more efficiently from displays equipped with necessary polarization filters than non CP-OLEDs.^[16] Both mentioned applications utilizing CD absorption or CPL emission, necessitate organic chromophores with a stable chiral conformation, strong chiroptical response, excellent chemical and photostability, as well as significant tinctorial and emission strength. Additionally, when implemented into an electronic solid-state device, the chromophores must also show proper morphology and charge transport properties. The search for molecular or supramolecular chromophore systems with these combined properties is a steadily growing field of research.^[8, 17-18]

The perylene bisimide (PBI) chromophore is a well-established building block both for spectroscopic probes in biomedical applications as well as for (supra-) molecular materials.^[19] However, the PBI-based design of chiral materials is underdeveloped. To render a PBI inherently chiral, its π -scaffold has to be chirally twisted e.g. by a fourfold *bay*-substitution

forming separable *P*- and *M*-enantiomers (see Figure 2). To substantially increase its chiroptical response by excitonic coupling of multiple chromophores, PBIs have to come into close vicinity. Integrating both aspects is a non-trivial challenge, as achieving the necessary twist usually involves introducing steric congestion from attached substituents, potentially compromising the molecule's propensity for π - π interactions. The same trade-off is faced regarding the incorporation into a solution-processed organic thin-film device. Hence, the PBI's core twist itself substantially improves the solubility for device processability but it also lowers the resulting device's charge-transport properties due to the lack of tight intermolecular interactions.

The most straightforward approach to a PBI with a chirally stable core-twist was achieved in 2006 by introducing phenyl substituents into the four PBI *bay*-positions.^[20] This molecule was further investigated and successfully used as non-fullerene acceptor in an organic solar cell (OSC) in 2015.^[21] However, the inherent chirality of its twisted perylene building block has never been appreciated in the solid state, and only racemic mixtures have been utilized in devices so far. Furthermore, there have been no endeavors to enhance the chiroptical response of the resulting chirally twisted PBI-based chromophores through intermolecular interactions despite PBIs being archetypal for electronically coupled supramolecular architectures in general.^[19] The hitherto reported use of racemic mixtures as non-fullerene acceptors (NFAs) in OSCs is apparently reasonable, considering the isotropic radiation of the sun. Here, no chiroptical properties are exploited as they were in chiral sensing devices such as chiral phototransistors or chiral photodiodes. However, the implementation of an organic material into an OSC is a valid approach to evaluate the general suitability of a chiral molecular design for organic thin-film devices in general regarding fundamental device properties such as morphology forming and charge-transport properties.

The present thesis explores the chirality of the twisted *bay*-arylated perylene motif within the context of an organic thin-film device. For this, the robust device modality of an OSC is chosen. Further on, it aims to increase its chiroptical properties, both at the molecular and at the supramolecular levels (see Figure 2). This is accomplished by expanding the π -scaffold from a PBI to a quaterylene bisimide (QBI) and thus shifting its chiroptical response towards the NIR spectral region.

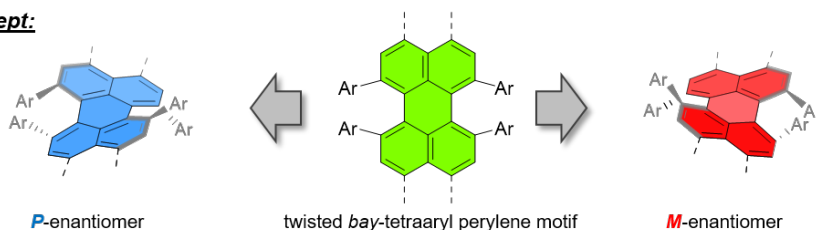
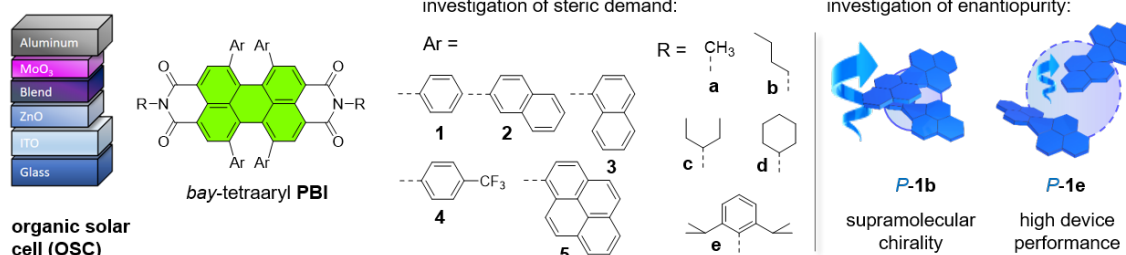
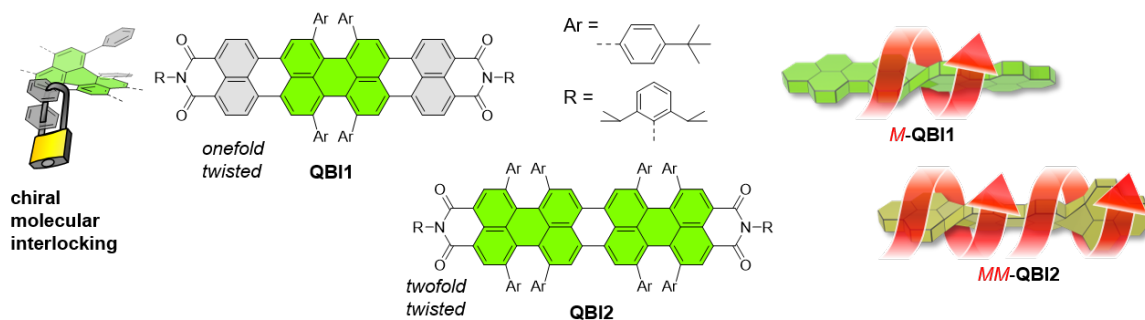
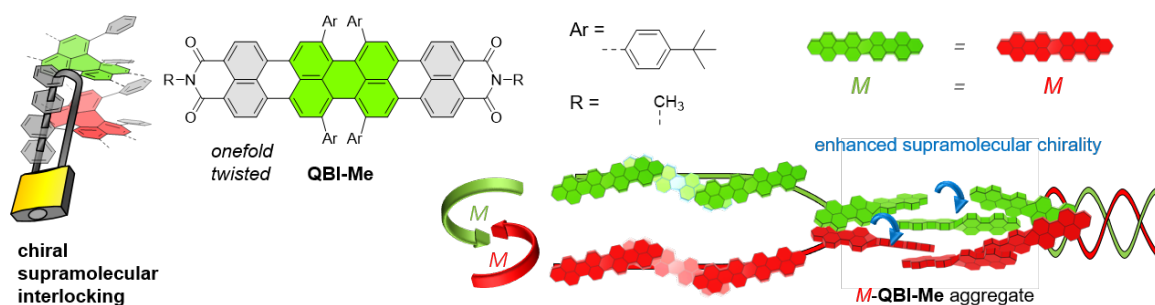
General Concept:**Chapter 3:** Axially Chiral Bay-tetraarylated Perylene Bisimide Dyes as Non-fullerene Acceptors in Organic Solar Cells**Chapter 4:** Helically Twisted Nanoribbons Based on Emissive Near-Infrared Responsive Quaterrylene Bisimides**Chapter 5:** Enantiopure J-Aggregate of Quaterrylene Bisimides for Strong Chiroptical NIR-Response

Figure 2. Outline of the present thesis along the chemical structures and the schematic representations of the investigated molecules.

Chapter 2 is divided into two parts. The first part will introduce the basic concepts of the theoretical calculations of electric circular dichroism (ECD). Along with literature examples, these concepts are applied to increase the chiroptical response of molecular and supramolecular systems. The second part will give a broad literature overview on chiral perylene bisimides concerning their historical developments in molecular and supramolecular chirality, aiming for strong chiroptical properties.

Chapter 3 describes the investigation of the molecular library of previously reported^[22] *bay*-tetraarylated PBIs **1–5** as NFAs in solution-processed polymer-based OSCs. The study highlights the impact of the steric demand of various *bay*- and imide-substituents on the OSC performance. The effect of enantiopurity in comparison to a racemic mixture on the device performance is investigated for two derivatives in detail. The discussion is based on thin-film device characterization, single-crystal X-ray analysis, and chiroptical spectroscopy.

Chapter 4 extends the twisted perylene scaffold formally by two naphthalene units to the first two members of the new molecule class of configurational stable chiral quaterrylene bisimides (QBIs). The synthesis and characterization of the tetraarylated onefold twisted **QBI1** and the octaarylated twofold twisted **QBI2** is reported. Special attention is paid to the near-infrared (NIR) emission facilitated by the rigid and interlocked geometry of the chiral π -scaffold. The chiroptical properties of monomers of the *P*- and *M*-enantiomer of **QBI1**, as well as the *PP*- and *MM*-enantiomers of **QBI2**, are investigated in solution. The molecular geometry is deduced from single-crystal X-ray analysis.

In *Chapter 5*, the onefold twisted QBI is modified towards small methyl imide-substituents allowing for a slip-stacked arrangement in a supramolecular assembly governed by van-der-Waals interactions. The resulting solid-state J-aggregate of **QBI-Me** is investigated by chiroptical spectroscopy and microscopy. Based on the supramolecular arrangement found in the racemic single-crystal X-ray structure and the morphology of the enantiopure aggregate as deduced by AFM, a structural model of the enantiopure aggregate is provided and substantiated by theoretical calculation of its circular dichroism spectrum.

Chapter 6 and *Chapter 7* summarize and conclude the results of the present thesis in English and German, respectively.

Chapter 8 provides additional experimental and theoretical data for *Chapter 3*, *Chapter 4*, and *Chapter 5*. This information includes the methods and materials as well as all synthesis along with spectroscopic and crystallographic data.

CHAPTER 2

—

State of Knowledge

The present chapter is divided into two subchapters. The first subchapter will briefly define circular dichroism and will introduce its theoretical description to maximize this phenomenon for molecular and supramolecular systems. The discussion is guided along the fundamental Rosenfeld equation. The first part will start on a molecular level, presenting various geometries of chiral dyes. In the second part, the Rosenfeld equation is adapted and expanded in an excitonic model that describes bis-chromophores and supramolecular entities in H- and J-type excitonic systems.

The second subchapter provides a literature overview on chiral rylene bisimides and their chiroptical response along molecular structures with increasing complexity and is discussed within three parts. The discussion starts with inherently chiral single-core PBIs in the first part. The second part presents PBI entities with excitonic chirality, starting with archetypal (a-)chiral geometries of bis-chromophores followed by PBI H- and J-aggregates. This part highlights the challenges in the supramolecular design to obtain a strong chiroptical response. It will close with an example of a solid-state thin-film application. The third part presents *bay*-annulated PBIs and thus connects all previous chapters concerning structural motifs and excitonic chirality.

2.1 Theoretical Description of Circular Dichroism

Chiral materials or solutions of chiral molecules show ‘optical activity’, a historic term associated with specific optical properties in response to linear or circularly polarized light, respectively, in terms of absorption and refraction. These inherent properties are labeled circular birefringence (CB), circular dichroism (CD), linear birefringence (LB), and linear dichroism (LD). Thereby, birefringence is associated with refraction and dichroism with absorption. Absorption and refraction are Kramers-Kronigs transforms to each other, which allows to deduce the spectral progression of the refractive index when the absorption spectrum is known and vice versa.^[23] Accordingly, CB and CD, as well as LB and LD, are Kramers-Kronigs transforms to each other, too. CB was the first phenomenon of ‘optical activity’, which explains

the optical rotation of linearly polarized light passing through an isotropic sample. This was first summarized by Van't Hoff and Le Bel in 1874.^[24] The synonyms of CB, such as ‘optical rotation’, ‘optical rotation dispersion’ (ORD), and ‘circular double refraction’, are derived from the corresponding analytical technique to evaluate the specific rotation of chiral liquids and solutions.^[23]

CD describes the difference between left- and right circularly polarized light being absorbed or emitted by a material or isotropic liquid. However, the term ‘CD’ is typically only associated with the CD absorption, whereas the CD emission is usually termed ‘circularly polarized luminescence’ (CPL). This terminology will also be used in this thesis.^[23]

The connection between quantum mechanical states and ‘optical activity’ was established by Léon Rosenfeld in 1929.^[25] The circular dichroism $\Delta\varepsilon$ for the electric transition from one state to another is proportional to the so-called rotatory strength R . This is the chiroptical equivalent to the dipole strength in absorption spectroscopy. R is defined as the imaginary part of the scalar product of the electric ($\boldsymbol{\mu}$) and magnetic (\mathbf{m}) transition dipole moment:

$$R = \text{Im}(\boldsymbol{\mu} \cdot \mathbf{m}) = |\boldsymbol{\mu}||\mathbf{m}|\cos \vartheta. \quad (1)$$

Both vectors form the angle ϑ , which must be non-orthogonal to obtain an R of non-zero. R is then usually folded with a Gaussian or Lorentzian function of a specific bandwidth to derive an actual circular dichroism spectrum from this.

The dissymmetry factor g for CD absorption is defined as the quotient of $\Delta\varepsilon$ and the molar extinction coefficient ε . ε_L and ε_R describe the molar extinction coefficient of left and right circularly polarized (CP) light, respectively:

$$g_{\text{abs}} = \frac{\Delta\varepsilon}{\varepsilon} = \frac{\varepsilon_L - \varepsilon_R}{\frac{1}{2}(\varepsilon_L + \varepsilon_R)}. \quad (2)$$

This can approximately^[26-27] be expressed as

$$g_{\text{abs}} \approx \frac{4R}{\boldsymbol{\mu}^2} \approx \frac{4|\mathbf{m}|\cos \vartheta}{\boldsymbol{\mu}}. \quad (3)$$

The emission dissymmetry g_{lum} is defined analogously to Eq. (2), including the difference in emission intensity ΔI of left CP light (I_L) versus right CP light (I_R):

$$g_{\text{lum}} = \frac{\Delta I}{\frac{1}{2}\Delta I} = \frac{I_L - I_R}{\frac{1}{2}(I_L + I_R)}. \quad (4)$$

For the emission of CP light, a characteristic value for the brightness (B_{CPL}) has been introduced in 2021:

$$B_{\text{CPL}} \approx \varepsilon \cdot \Phi \cdot \frac{|g_{\text{lum}}|}{2}. \quad (5)$$

This quantity combines the photoluminescence quantum yield Φ_{PL} with the measure of molar absorption ε and the emission dissymmetry g_{lum} . This allows a quantitative comparison between molecules with high CPL dissymmetries but low quantum yields and vice versa.

In principle, the fundamental equations (1)–(3) are sufficient for calculating the chiroptical response of any chiral molecule or aggregate. However, computing the required quantities remains challenging due to the limited availability of suitable molecular wavefunctions. Historically, the efforts for theoretical calculations of chiroptical spectra resulted in two approaches. This division is still present today and will be discussed in the following two chapters. The first approach will be discussed in *Chapter 2.1.1*. It is the use of ab initio calculations for solving the electronic Schrödinger equation providing the necessary parameters $\boldsymbol{\mu}$ and \mathbf{m} . The second approach is described in *Chapter 2.1.2*. Here, the use of an exciton model is introduced. Accordingly, systems, either molecular or supramolecular, are subdivided into groups. The interactions between these entities are then mainly considered electrostatic.^[23] This differentiation can be alternatively recalled as (i) the mixing of transitions within a single chromophore and (ii) the coupling of transitions between individual chromophores.^[28]

2.1.1 Inherent Chirality and Molecular Chirality

Condon, Altar, and Eyring were the first to implement the contribution of intrinsic magnetic dipole moments to the calculations of optical rotation within their one-electron theory, which later expanded to a many-electron picture.^[29-31] State-of-the-art time-dependent density functional theory (TD-DFT) methods, which are implemented in commercial computer programs, provide R following the Rosenfeld equation using two different formulas. These are the ‘dipole length’ formalism and the ‘dipole velocity’ formalism. These are equivalent for exact wavefunctions but no longer for approximate calculations such as the utilized TD-DFT methods. The lengths formalism has proven to be robust and less sensitive to the quality of the wave function compared to the velocity formalism. However, the magnetic transition dipole moment \mathbf{m} obtained from the lengths formalism is dependent on the choice of the specific coordinate system of the computed molecule or supramolecular entity. It is therefore common to compare the results of both calculations, especially for large systems, and check if the choice of the specific coordinate system in the length formalism does cause a significant deviation in

obtained values.^[23, 32-33] The prediction of CD spectra by ab initio calculations has recently grown substantial importance in the research field of chiral PAHs, particularly carbohelicenes, to maximize the molecular dissymmetry. Implementing helical architectures into the scaffolds of polycyclic aromatic hydrocarbons (PAHs) or the fusion of helicenes defines the molecular chiroptical response. The Rosenfeld equation (Eq. 1) contains the magnitudes of μ and m and their respective angle ϑ . These can be assessed by ab initio calculations to increase R . To increase the dissymmetry g , it could also be useful to reduce μ according to Eq. 2. The discussion on a systematic approach to improving the molecular design for maximizing the chiroptical response can be partly guided along these individual parameters, which will be briefly discussed in the following section.^[34]

The discussion will start with μ , which is for small organic molecules commonly by two orders of magnitude higher than m within their respective cgs units. According to Eq. 2, reducing μ could be a valid design strategy to increase the molecular dissymmetry. However, this approach is not notably mentioned in recent literature as it is connected to unfavorable changes in related characteristics, such as the reduction of molecular extinction or radiative rates.^[35] Therefore, the first discussed parameter is the angle ϑ . It has been shown by Mori in recent years how these parameters behave and change for different molecular symmetries of carbohelicenes 5–7 (Figure 3).^[27, 36]

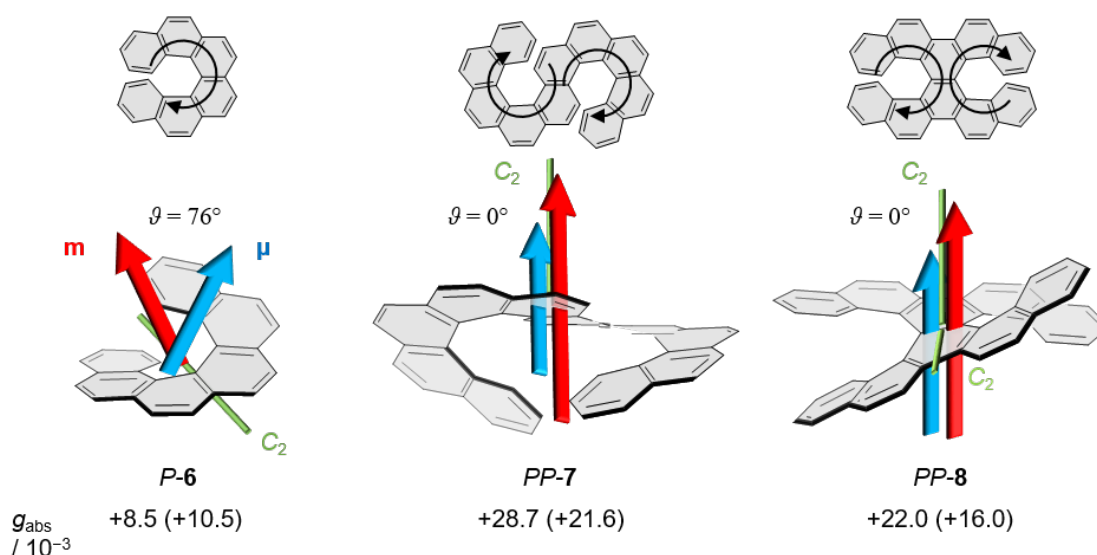


Figure 3. Chemical structures of the *P*-enantiomers of single helicene *P-6* in C_2 symmetry as well as of the fused double carbo[5]helicenes *P-7* and *PP-8* in C_2 and D_2 symmetry, respectively. For the ground state of their respective 1B_b band, the respective μ (blue arrows) and m (red arrows) are visualized. The scaling of the vectors is given relative to the vectors in *P-6*. The angle ϑ between μ and m , the symmetry axes (green), and the calculated g_{abs} values are also indicated. The experimental g_{abs} values are given in brackets.^[27]

For all systems, calculations have been conducted for the ground state of the 1B_b band (see Figure 3) as well as for the ground and excited state of the 1L_b band (not shown here). These bands correspond to the main CD band as well as for the CPL active transition, respectively. It could be demonstrated that $\boldsymbol{\mu}$ and \boldsymbol{m} of the 1B_b band of single helicene **5** include a ϑ of 76° . This becomes favorably parallelized upon helicene fusing to obtain the double helicenes **6** and **7** in the ‘S’ or ‘X’-shape, respectively. The calculations retrace the experimental key-values g_{abs} (see Figure 3) and g_{lum} (not shown here), highlighting the possibility of a symmetry-based rational design. However, the role of each parameter $\boldsymbol{\mu}$, \boldsymbol{m} , and ϑ cannot be assessed entirely individual. It is observed that these characteristics can partly outweigh each other in this symmetry-based approach.

Sato, Isobe, and co-workers reported two chiral nanobelts in 2019 (*P*)-**9** and (*P*)-(*P*)-**10** (Figure 4a). This is a unique example where the special molecular geometry accounts for two characteristics: first, for a dominant magnitude of \boldsymbol{m} and, second, for a favorable ϑ .

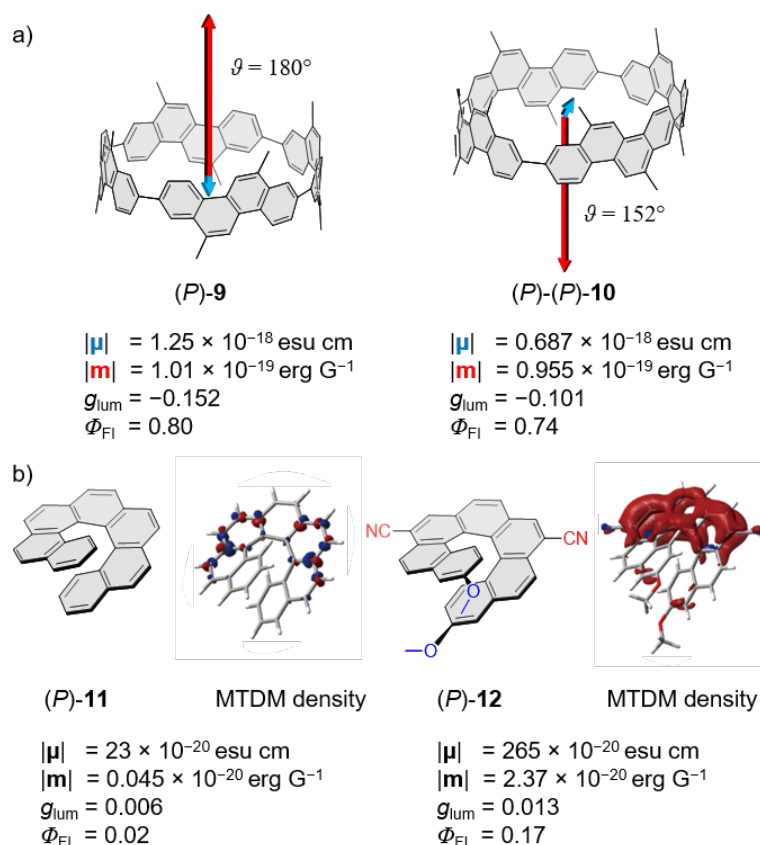


Figure 4. (a) Chemical structures of unique chiral nanobelt geometries of (*P*)-**9**^[37] and (*P*)-(*P*)-**10**^[37] along their $\boldsymbol{\mu}$ and \boldsymbol{m} depicted as blue and red arrows, respectively. (b) Chemical structures of carbo[7]helicenes (*P*)-**11**^[35] and (*P*)-**12**^[35] along with the spatial distribution of their respective electric and magnetic transition dipole moment (MTDM) densities for the CPL active S_1 - S_0 transition. The values of $\boldsymbol{\mu}$, \boldsymbol{m} , g_{lum} and Φ_{FI} are provided as well. Adapted with permission from ref. [35]. Copyright 2021, American Chemical Society.

Accordingly, (*P*)-**9** shows an \mathbf{m} value of 1.01×10^{-19} erg G⁻¹, which is an order of magnitude higher than for the main transition of most carbohelicenes,^[27] and $\vartheta = 180^\circ$ is favorably parallelized. Hence, g_{lum} raised up to -0.152 , which is the highest g -value of a purely organic molecule, while also reaching an impressive fluorescence quantum yield Φ_{FI} of 80% of the strong emission band at 443 nm.^[37]

The increase of \mathbf{m} by a pure chemical approach was achieved by Matsuda and co-workers presented in 2021 for carbo[7]helicenes. They decorated the pristine **11** with both electron withdrawing and electron donating groups to obtain **12** (Figure 4b). This led to an increase of \mathbf{m} by a factor of ~ 10 and rendered the CPL emission of the S₁–S₀ transition magnetically allowed. Thus, also Φ_{FI} increased from 2% to 17% and the g_{lum} accordingly from 0.006 to 0.013. To understand this design strategy, the depiction of $\boldsymbol{\mu}$ and \mathbf{m} as vectors was no longer sufficient. Instead, the transition dipole moment densities had been analyzed whose spatial integrals correspond to the vectors $\boldsymbol{\mu}$ and \mathbf{m} . Hence, a characteristic spatial distribution of the frontier molecular orbitals (FMOs) has been observed, which can become a tool for future studies. This is depicted in Figure 4b for the magnetic transition dipole moment (MTDM) density. However, no common design rules for chemical modifications of a carbohelicene could be deduced from this so far.

Besides these approaches on molecular geometry and symmetry, the control of \mathbf{m} can be controlled by implementing a heavy metal atom complexed by a chiral molecular environment by exploiting the heavy atom's spin-orbit coupling. The conceptual understanding of chiral lanthanide complexes dates back to the work of Richardson in 1980.^[38] It has been recently recalled in a review^[39] article and will not be further discussed in the present thesis.

2.1.2 Excitonic Chirality and Supramolecular Chirality

Apart from intrinsically asymmetric chromophores such as carbohelicenes, which have been discussed in the previous chapter, the optical activity of the vast majority of molecules has no inherent source within their respective scaffold themselves. Instead, it originates from relative mutual orientations between subunits. Before the advent of available ab initio calculations, the chiroptical response of such a molecular system could be readily derived from theoretical approaches that rely on the separation of chemical groups and the analysis of their mutual orientation as well as their individual transition dipole moments or polarizabilities.^[23]

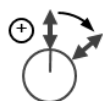
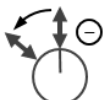
Kirkwood and Kuhn were the first to derive a so-called polarizability model by exploiting electric and magnetic transition dipole moments in 1937.^[40] This approach was adapted by Moffitt, resulting in an excitonic modification in 1956 to account for degenerate optical

transitions in chiral polymers.^[41] Subsequently, comprehensive symmetry rules for the chiroptical spectroscopy could be derived by Schellman in 1968.^[30] In this decade, significant progress in developing molecular exciton models was achieved. Kasha presented in 1965 his entirely non-empiric approach to understanding the optical signature of molecular systems as well as supramolecular aggregates in terms of H- and J-type coupling within the dipole approximation.^[42-43] Simultaneously, Davydov and Sheka provided a corresponding exciton model for organic molecules in the condensed phase.^[44] All of these mentioned developments led to the expression of the ‘exciton chirality method’, which allows the assignment of the absolute configuration of chiral multi-chromophore systems or natural products by circular dichroism (CD) spectroscopy if the type of excitonic coupling is known. Among others, this was comprehensively studied by Bayley^[28] or Harada and Nakanishi^[45-46] in the early 1970s. Hence, a quantitative definition of exciton chirality for two identical chemical moieties, e.g., chromophores A and B, contains the term:

$$\Delta\varepsilon \sim \mathbf{r}_{AB} \cdot (\boldsymbol{\mu}_A \times \boldsymbol{\mu}_B) V_{AB} \quad (6)$$

with the interchromophoric distance vector \mathbf{r} , the electric transition dipole moments $\boldsymbol{\mu}$ of the individual chromophores, and the transition dipole interaction energy V . The latter is considered as electrostatic Coulomb interaction within the point dipole approximation with a distance dependency of $\sim r^{-3}$. This was demonstrated for bis-*para*-substituted benzoates, leading to the formulation of ‘positive’ chirality along a CD couplet with a positive first and a negative second Cotton effect as well as the ‘negative’ chirality vice versa (see Table 1), with an energy splitting of $2V$.

Table 1. Definition of the exciton chirality rule by Harada and Nakanishi.^[46]

	Qualitative definition	Quantitative definition	Cotton effect
positive chirality		$\mathbf{r}_{AB} \cdot (\boldsymbol{\mu}_{A\alpha} \times \boldsymbol{\mu}_{B\alpha}) V_{ij} > 0$	Positive 1 st and negative 2 nd Cotton effects
negative chirality		$\mathbf{r}_{AB} \cdot (\boldsymbol{\mu}_{A\alpha} \times \boldsymbol{\mu}_{B\alpha}) V_{ij} < 0$	Negative 1 st and positive 2 nd Cotton effects

The two chemical moieties are denoted as A (front) and B (back). α denotes an optical transition.

For the classes of molecules discussed by Harada and Nakanishi, the calculated V was always positive, denoted as H-type coupling. Even though the authors emphasized its distinct

calculation for unknown chromophore geometries,^[46] negative values of V along J-type coupling are underrepresented in the literature. The according alleged inversion of this excitonic chirality is significantly less known. Within the growing field of supramolecular chemistry, the exciton chirality method has gained importance as this model is readily available for assigning the helicity of large aggregates by CD spectroscopy.

The proper use of the exciton chirality method has recently been recaptured by a series of articles by Painelli, Sissa and Thomas, and co-workers.^[4, 47-48] They displayed this rule from a geometric perspective of two chromophores along the discrimination into H- or J-type coupling, forming either a helix geometry or a ‘creeper’ geometry, respectively (see Figure 5). The model applies to the dimer case and also when the molecules translate into extended aggregates. The branches of the CD couplet are defined as R_+ and R_- . The sign of V defines both the splitting as well as the relative mutual spectral position of R_+ and R_- . Hence, for the right-handed H-type case, a positive couplet with redshifted R_- and blueshifted R_+ is present, and vice versa for the J-type (see Figure 5).

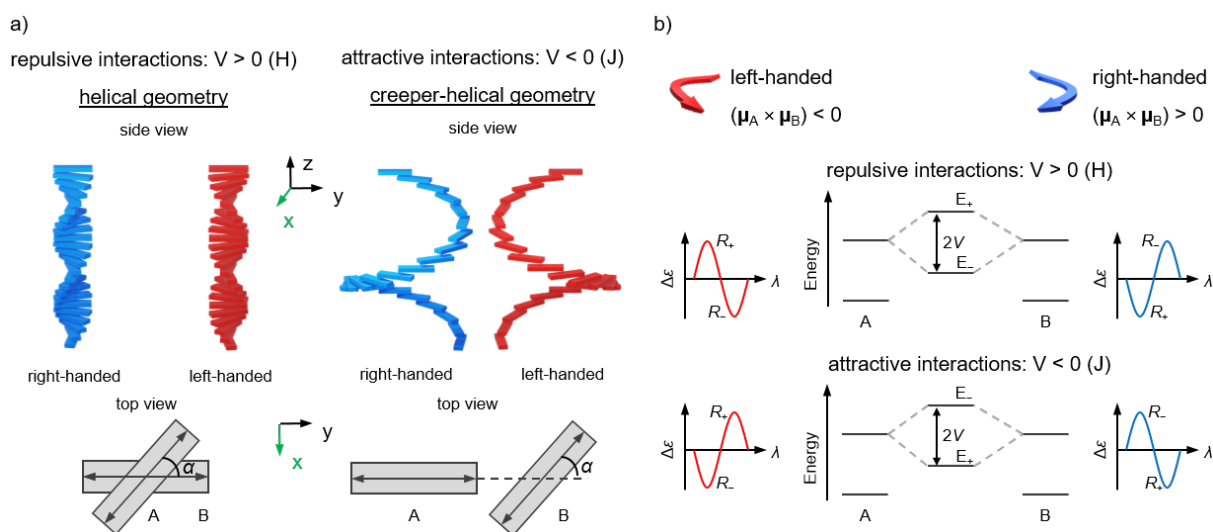


Figure 5. Schematic depiction of (a) the mutual chromophore arrangement in right- (blue) or left- (red) handed helix (left) or creeper-helix (right) geometry within an aggregate of 24 chromophores (top) or two chromophores (bottom) A and B, which include an angle $\alpha = 20^\circ$. (b) Schematic depiction of energy levels and spectral position of R_+ and R_- band of the CD couplet of the corresponding excitations.^[48]

Within their model, the authors also account for the opposing bands' equal energy integrals, termed conservative behavior. Thus, R_+ and R_- sum up to zero and are defined as:

$$R_+ = -\frac{1}{2} \frac{E_{E^+} - E_G}{2\hbar} (\sqrt{1-\rho} - \sqrt{\rho})^2 \mathbf{r}_{AB} \cdot (\boldsymbol{\mu}_A \times \boldsymbol{\mu}_B), \quad (7)$$

$$R_- = -\frac{1}{2} \frac{E_{E^-} - E_G}{2\hbar} (\sqrt{1-\rho} - \sqrt{\rho})^2 \mathbf{r}_{AB} \cdot (\boldsymbol{\mu}_A \times \boldsymbol{\mu}_B), \quad (8)$$

$$E_G = -V \frac{\sqrt{\rho}}{\sqrt{1-\rho}}, \quad (9)$$

$$\rho = \frac{1}{2} \left(1 - \frac{E_M}{\sqrt{V^2 + E_M^2}} \right). \quad (10)$$

The chromophoric center-to-center distance vector is given by \mathbf{r}_{AB} , E_M is the monomeric excitation energy, and V is the interchromophoric Coulomb coupling which defines the energetic difference between the exciton states $E_{E+} = E_M + V$ and $E_{E-} = E_M - V$.

The hitherto depicted excitonic models solely handle coupled chromophores as electric transition dipole moments within a framework of oscillating dipoles or polarizable objects. In this framework, magnetic transition dipole moments vanish, and the molecular transitions are only regarded as linear charge displacements.^[30] Therefore, this approach does not display the rotational strength (Eq. 1) in its entirety. Schellman first summarized this in 1968 for the picture of two coupled chromophores with two excited states within the excitonic picture.^[30] Accordingly, three mechanisms account for the rotatory power, all based on the Rosenfeld equation. The first is the one-electron mechanism (μ -m term), locating an electric and a magnetic transition on one chromophore and handling the second chromophore as a static environment. The calculations discussed in the previous chapter are rooted in this approach. The second mechanism considers two single electric transitions of each chromophore (μ - μ term) called the Kuhn-Kirkwood mechanism with the exciton modification of Moffitt. The third mechanism considers the electric transition of one chromophore and the magnetic transition of the other chromophore and vice versa. This mechanism was usually considered minor until Woody and Tinoco's early work^[49] and was later termed as μ -m term. The individual expressions of R by Schellman are presented in Table 2.^[30]

Table 2. Origins of optical activity for a simple model with two electronic transitions.^[30]

Mechanism		Group A contribution	Group B contribution	Rotatory Strength*
Dipole-dipole coupling	Nondegenerate	μ_A	μ_B	$R_A = \frac{-V}{\hbar c(\varepsilon_2^2 - \varepsilon_1^2)} \mathbf{r}_{AB} \cdot (\boldsymbol{\mu}_B \times \boldsymbol{\mu}_A)$
	Degenerate (Moffitt)	μ_A	μ_B	$R_A = \pm \frac{\pi}{2\lambda_1} \mathbf{r}_{21} \cdot (\boldsymbol{\mu}_B \times \boldsymbol{\mu}_A)$
One electron		μ_β	Static environment	$R_\alpha = -\frac{V_{\alpha\beta}}{\varepsilon_\beta - \varepsilon_\alpha} (\boldsymbol{\mu}_\beta \cdot \boldsymbol{\mu}_\alpha)$
μ_B - m_A		m_A	μ_B	$R_A = \frac{-V_{AB}}{(\varepsilon_B - \varepsilon_A)} (\boldsymbol{\mu}_B \cdot \mathbf{m}_A)$

* α and β denote two optical transitions, and ε is the molar extinction coefficient.

The μ -m term did not appear in the original expression of the exciton chirality rule (see Table 1). The problem of this issue has been pointed out so far most impressively in 2014 by

Bruhn, Pescitelli, Bringmann, and co-workers.^[50] They presented an axial chiral BODIPY derivative **13** (Figure 6) with a substantial magnetic component of the respective monomers rendering the μ -m coupling term dominant, which even exceeds the contribution of the μ - μ term with opposing sign. Thus, a positive exciton couplet was observed for the *M*-enantiomer which contradicts the common expression of the exciton chirality rule (see Figure 6).

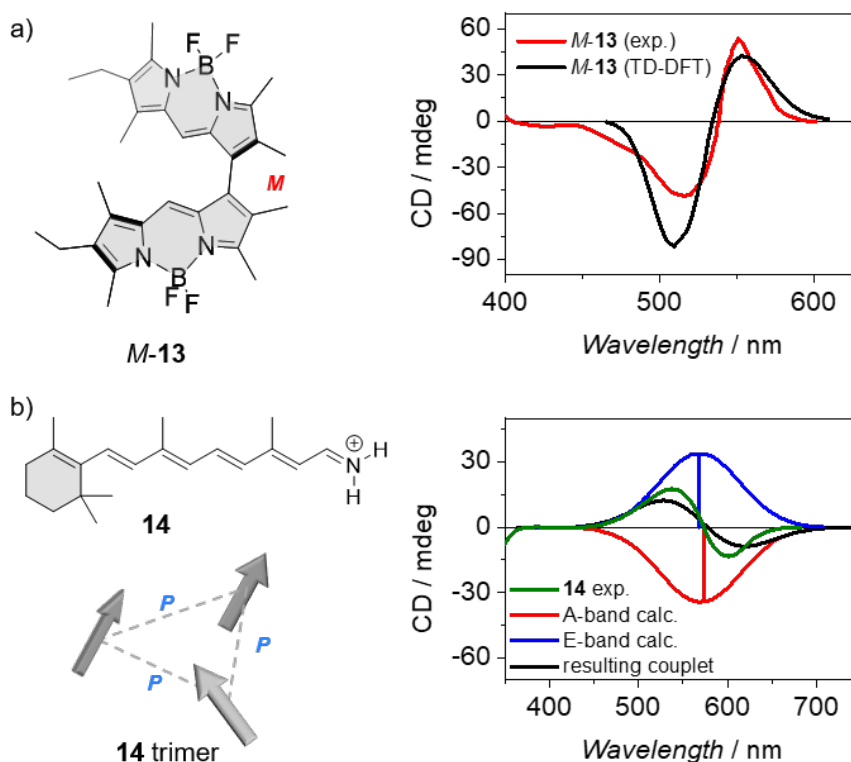


Figure 6. (a) Chemical structure of the *M*-enantiomer of **13**^[50] along its experimental (red) and TD-DFT simulated (black) CD spectra in solution. (b) Chemical structure of the **14**^[51] trimer complex along the experimental spectrum (green) as well as its simulated A- (red) and E-band (blue), and the resulting CD couplet (black) calculated from an exciton model, including various *intratrimeric* as well as *intertrimeric* contributions with dominant J-type coupling. The spectral data are adapted with permission (a) from ref. [50] copyright 2015, Wiley-VCH Verlag GmbH & Co. KGaA, Weinheim, as well as (b) from ref. [51]. Copyright 2012 American Chemical Society.

The authors provided an expression of the Rosenfeld equation for the two chromophores A and B by combining the μ - μ term and the μ -m term (see eq. 11). The total rotatory strength R for the branches α and β (corresponding to R_+ and R_- in eq. 7, 8) is given by:

$$R^{\alpha\beta} = \pm \frac{1}{2} \pi \sigma_0 \mathbf{r}_{AB} \cdot (\boldsymbol{\mu}_A \times \boldsymbol{\mu}_B) + \frac{1}{2} \text{Im}[(\boldsymbol{\mu}_A \mp \boldsymbol{\mu}_B) \cdot (\mathbf{m}_A \mp \mathbf{m}_B)]. \quad (11)$$

Herein, σ_0 is the excitation energy. Accordingly, the rotatory strength of the combined μ - μ - and μ -m terms are stored into each branch of the exciton couplet with opposing signs, respectively. The results were compared with TD-DFT calculations, including the chromophore distance as

critical parameter. Both the calculation of R utilizing Eq. 11 as well as the ab initio method led to the correct prediction of the sign of the couplet.

Eq. 11 depicts R as an additive quantity of the μ - μ -term and the μ - m term for the calculation of an H-coupled bis-chromophore system. The validity of this approach was comprehensively demonstrated even for calculating the CD couplet of the trimer complex of bacteriorhodopsin (**13**) in purple membrane in *PPP*-configuration (see Figure 6). The exciton-based calculations defined R_A and R_E (corresponding to R_+ and R_- in eq. 7, 8). Both μ - μ and μ - m terms of the *intratrimeric*, as well as several *intertrimeric* contributions had been evaluated. These contributions also included J- and H-type coupling that partly opposed each other. The J-type contributions dominate, leading to a negative CD couplet for the *P*-arranged chromophores. This work highlights the requirement for a thorough elucidation of the coupling parameter V . The investigation of the chiroptical response of the bacteriorhodopsin (**13**) complex has a long history. The work of Pescitelli and Woody points out the computational challenges as well as the flaws of multiple previous discussions on **13**. This includes the origin-dependence of the magnetic transition dipole moment, the impact of V , and the conservation of R_{total} to zero, thus providing a sound educational article.^[51]

A similar expression for the rotatory strength of a CD couplet for an excitonic bis-chromophore has just recently been reported, which even includes the inherent chirality of the monomeric units as R_{mon} μ - m term from the fundamental Rosenfeld Eq. 1 added up with Eq. 11 for the hitherto discussed $R_{\mu-\mu}$ and $R_{\mu-m}$ contributions, which then defines the two exciton bands R_+ and R_- with opposing signs as the sum $R_{\text{total}} = R_{\text{mon}} + R_{\mu-\mu} + R_{\mu-m}$.^[52-53]

Within the previous *Chapter 2.1.1* and the present *Chapter 2.1.2*, the approaches and mechanisms for the calculation of CD spectra have been sketched along the Rosenfeld equation (Eq. 1). Its utilization and derivation accounting for different coupling mechanisms have briefly been outlined for suitable literature examples. It has been shown that the exciton picture provides a decent rationalization of CD spectra if sufficient care is taken to evaluate the critical coupling parameter V and the μ - m term. However, the computational prediction of chromophore coupling, especially for long ranges, remains also problematic for ab initio calculations such as TD-DFT methods. Therefore, each (supra-) molecular system requires individual treatment and approximations. If excitonic models are applied, which are still needed as approximations for large systems, a mutual corroboration with ab initio calculations is commonly provided. The discussion of calculated CD spectra usually refers only to the main optical excitation, and the prediction of high-energy transition chirality remains challenging.

2.2 Chiral Rylene Bisimide Dyes

2.2.1 Inherently Chiral Twisted Monomeric Dyes

Inherent molecular chirality in perylene bisimide (PBI) dyes is obtained by mutually twisting the two naphthalene subplanes towards each other, resulting in a contorted π -backbone with torsion angles of up to $\pm 40^\circ$. If this twisted PBI geometry is kept conformationally stable, not only the solubility increases drastically, but two stereoisomers can be resolved. Unfortunately, the classification and nomenclature of this inherent chirality of PBIs are not fully consistent throughout the literature. Most frequently, it follows the first publications, stressing the picture of axial chirality of the outmost two naphthalene units even if these units are annulated and not connected by a (conformationally hindered) single-bond. Accordingly, the stereoisomers are denoted as *P*- and *M*-atropo-enantiomers as deduced from the Newman projection (see Figure 7a, right, top).^[54] Additionally, the chirality of twisted PBIs can also be interpreted as inherent chirality of a fused double-helicene (see Figure 7a, right, bottom). The latter picture is useful when comparing chiral PBIs with rather similar π -scaffolds discussed in the vastly emerging research community of carbo[n]helicenes.^[27] It is important to note that in these two cases, the nomenclature is fairly consistent with the topography of the π -backbone, which mainly defines the chiroptical response. In contrast, by applying rules of planar chirality, the descriptor might change upon chemical substitution, even though the molecules' helicity and thus its chiroptical properties remain constant (see the following *Chapter 2.2.2*).^[55]

The possibility of chirally twisted PBIs has already been recognized within studies on fourfold *bay*-substituted PBIs in the 1990s,^[56-58] but the first two experimental reports were only published in 2007^[59-60] presenting two concepts of preserving a stable chiral PBI backbone twist. The first concept is a 'macrocyclic' approach using the strain, which is introduced by either one (not shown here)^[61] or two^[59] bridging units that interconnect two the diagonal *bay*-positions 1,7- and 6,12- in **15** (see Figure 7b). The second concept was recently termed '*bay*-crowding'^[62] and approaches and utilizes the sterical congestion of four *bay*-substituents in **16** (see Figure 7b). These substituents interlock each other and ensure the chirally twisted core geometry dependent on their size and shape. The conformational stability can be assessed by thermally driven interconversion experiments of the conformers by CD spectroscopy or dynamic NMR.

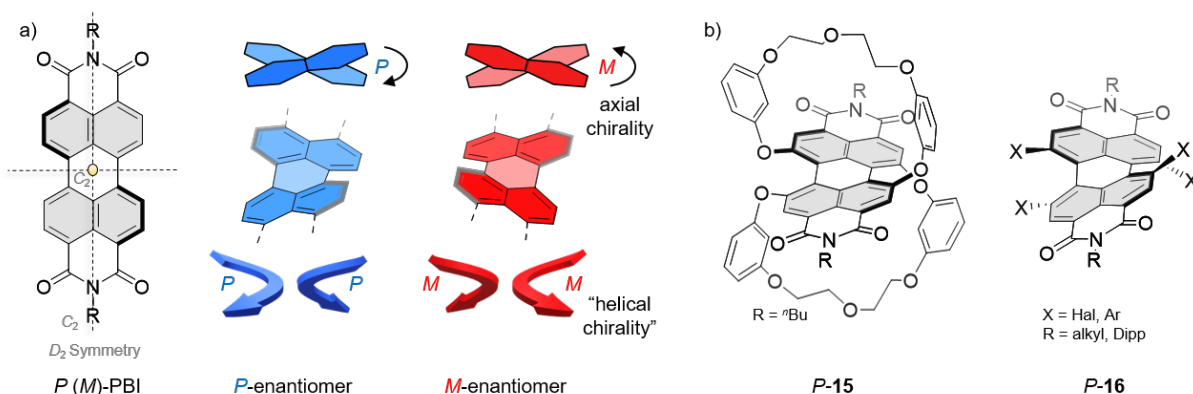


Figure 7. (a) Schematic structure of an inherent chiral PBI (left). The chirality-inducing core-twist is depicted as Newman projection (right, top) or shown as double-helicene (right, bottom). The perylene cores are colored in blue (P) and red (M), respectively. C_2 Symmetry axes of the PBI are shown as dotted gray line. (b) The P -enantiomers of **15**^[59] and **16**^[60] represent examples of the ‘macrocyclic’ or ‘bay-crowding’ approach, respectively. Dipp = 2,6-Diisopropylphenyl.

This provides a free enthalpy of activation ΔG^\ddagger , determined from the racemization rate constant k_{rac} . The racemization experiment can afford the half-lifetime τ_{rac} and the associated k_{rac} according to Eq. 13 at a given temperature T by applying the Arrhenius equation Eq. 14 and the Eyring equation eq. 15:^[60]

$$A = A_0 \exp[-k_{\text{rac}}t], \quad (13)$$

$$t_{1/2} = \frac{\ln(2)}{k_{\text{rac}}}, \quad (14)$$

$$\Delta G^\ddagger = -RT \ln \left(\frac{hk_{\text{rac}}}{\kappa k_{\text{b}}T} \right). \quad (15)$$

For such a system of two interconverting enantiomers, the transition parameter κ equals 0.5. Following the early definition of $\bar{O}ki$,^[54] atropisomers can be reasonably resolved with τ_{rac} of at least 1000 s at a temperature T corresponding to $\Delta G^\ddagger > 93 \text{ kJ mol}^{-1}$. For fourfold bay-substituted PBIs, this barrier had been rationalized by Osswald *et al.* in both theory and experiment with regard to the substituent size, which is required for room-temperature stable atropo-enantiomers.^[60] Equal ΔG^\ddagger values had been determined at various temperatures. Thus, stable chirality is obtained for the bay-tetrabromo PBI ($118 \pm 1 \text{ kJ mol}^{-1}$) but not for the corresponding chloro- ($98 \pm 1 \text{ kJ mol}^{-1}$) or fluoro- ($40 \pm 5 \text{ kJ mol}^{-1}$) derivatives. Also, the widely utilized bay-tetraphenoxy PBI ($60 \pm 3 \text{ kJ mol}^{-1}$) is not conformationally stable due to the flexibility of the oxygen linker.^[60] However, this issue could be overcome when connecting the adjacent phenoxy substituents in *ortho*-position by a sigma bond. Thus, a rather stable configuration is obtained for the 2,2-biphenol- in **17** (98.5 kJ mol^{-1}),^[63] and an extraordinary

stability is achieved for the corresponding 2,2-binaphthol-bridging unit (165 kJ mol⁻¹) in **18** (Figure 8).^[63]

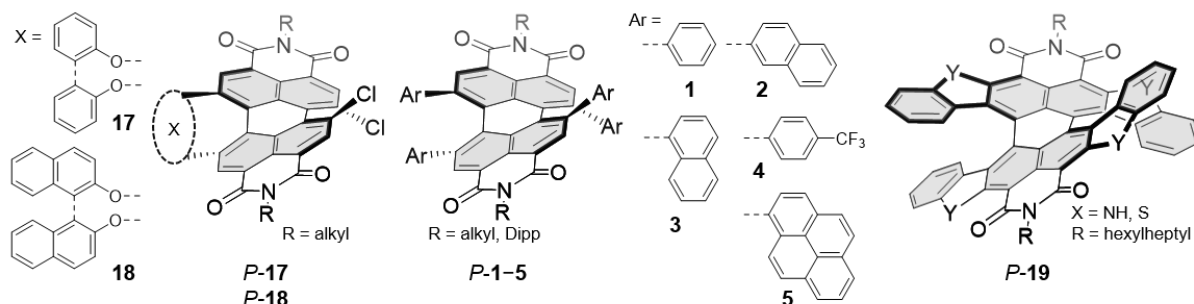


Figure 8. Chemical structures of the *P*-enantiomers of inherently chiral PBIs **17**,^[63] **18**,^[63] **1–5**,^[22] and **19**.^[64]

In contrast to the aryloxy-substituted PBIs, Osswald *et al.* estimated that the chirality is as stable as for the bromo-derivatives if the phenyl substituents are directly attached to the four PBI's *bay*-positions.^[60] The chronology of such *bay*-tetraarylated PBIs starts in 2006 with the first synthetic access to the tetraphenyl derivative by the Zhu group utilizing an Ag-mediated Suzuki coupling.^[20] The synthetic scope was extended by the Hoffmann group in 2010, applying pristine Suzuki-coupling conditions.^[65] This allowed for further synthetic variations in 2014, along with the first chiroptical investigation of *bay*-tetraphenyl PBIs.^[66] In 2021, Renner *et al.* presented an in-depth study of chiral and conformational properties of various *bay*-tetraaryl PBIs **1–5**. First, the high racemization barrier of *bay*-tetraphenyl PBIs, which Osswald had predicted, was eventually confirmed experimentally with values of $\Delta G^\ddagger = 119 \pm 2$ kJ mol⁻¹ measured at various temperatures.^[22] Second, this work gave the first crystallographic proof of a chiral tetraarylated PBI showing highly contorted π -cores with twist angles of up to 36.6° between the outmost naphthalene planes. Third, the study was further extended to an enlargement of *bay*-substituents from pristine phenyl and trifluoromethylphenyl to 1-naphthyl, 2-naphthyl, and 1-pyrene. These new congeners do not follow a simple interconversion of two chiral conformers but exhibit a rich conformational isomerism which dynamic ¹H NMR could statistically deduce.

Besides the investigation of the chirality of the twisted *bay*-arylated PBIs, a *bay*-phenyl^[21] and a *bay*-1-naphthyl^[67] derivative had been successfully applied as non-fullerene acceptors in organic solar cells in 2015 and 2016, respectively. In these works, the molecular design is focused on the high solubility of the PBIs, which is implied in the twisted backbone geometry, but the chirality itself was not investigated. High solubility is needed to form a proper thin-film morphology by spin-casting from the binary blend with a donor polymer.

The twisted backbone of the *bay*-tetraphenyl perylene is the fundamental molecular motif of the present thesis and will be discussed in brief. The chiroptical properties of the corresponding PBI **1e**^[22] are the most investigated ones within this family and do not only well represent all *bay*-substituted congeners but also the structurally related peropyrenes^[68] and double carbo[7]helicenes (**19**) to a certain extend.^[64, 69-70]

The *bay*-unsubstituted parent PBI **20** (Figure 9) shows strong and sharp absorption of its S₀–S₁ transition with pronounced vibronic progression at 535 nm and a very weak S₀–S₂ transition at around 350 nm. In contrast, the *bay*-tetraphenyl PBI **1e** shows a very broad overall absorption with only a small vibronic shoulder in the main transition band. Along the spectral broadening, the extinction of the S₀–S₁ band drops down drastically from 99000 (**20**) to 23000 M⁻¹ cm⁻¹, whereas the S₀–S₂ band gains in intensity from 2000 (**20**) to 18000 M⁻¹ cm⁻¹. Both transitions are strongly redshifted by 2250 cm⁻¹ and 5840 cm⁻¹ to 608 nm and 440 nm, respectively. These spectral changes had been attributed to both the twist-induced broadening of the density of states as well as the contributions of phenyl substituents in the main S₀–S₁ transition.^[66] The latter one could be deduced from TD-DFT calculations along the phenyl substituents' role to increase the S₀–S₂ intensity drastically.^[22, 66]

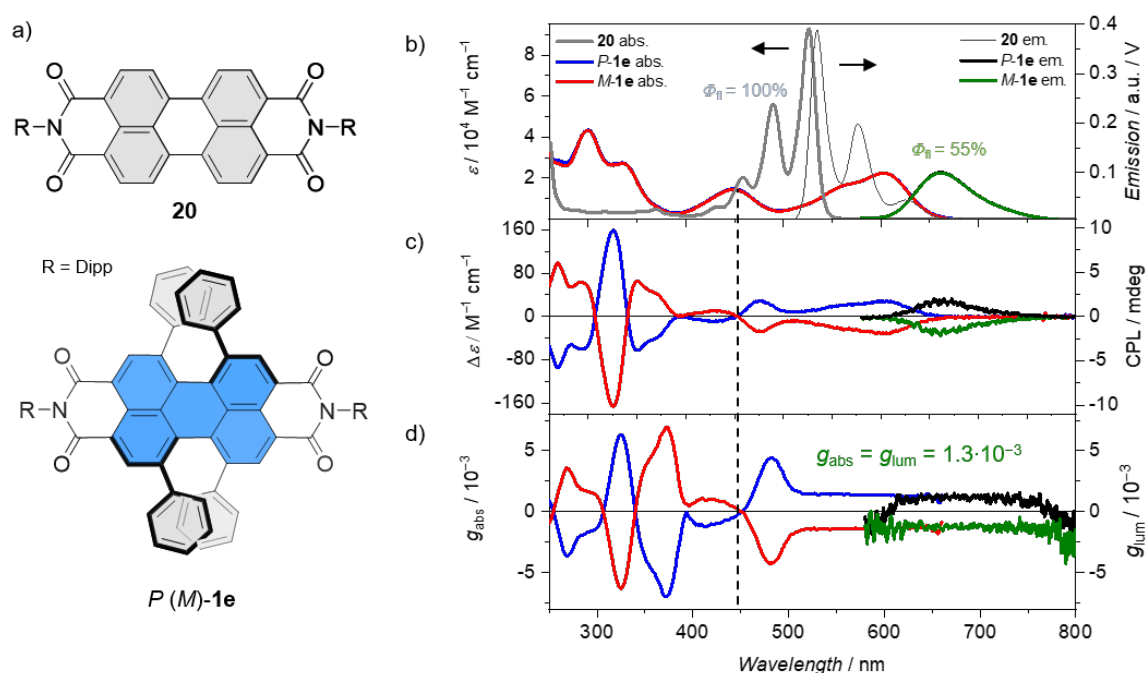


Figure 9. Chemical structures of *bay*-unsubstituted **20**^[71] (top) and chiral *bay*-phenyl **1e**^[22] along their spectral properties in DCM solution. (b) UV–vis–NIR absorption and emission, (c) CD absorption and CPL emission spectra, and (d) dissymmetry factors g_{abs} and g_{lum} . All absorption properties of *P/M*-**1e** are shown in blue/red, and the respective emission properties in black/green, respectively. The spectra of **20** are shown in gray. The units of total emission are given in a.u. (fluorescence measurement) and V (CPL measurement). The spectra of **20** are adapted from ref. [71] with permission from the Royal Society of Chemistry.

The chiroptical properties can be assessed by circular dichroism spectroscopy in both absorption (CD) as well as emission (CPL). The CD spectrum shows a monosignated band strictly following the spectral progression of the main S_0 – S_1 absorption band. The sign follows the ‘exciton chirality rule’^[45] and is positive for the *P*-enantiomer and negative for the *M*-enantiomer as deduced from TD-DFT calculations. This results in an overall constant absorption dissymmetry factor g_{abs} with a value of $\pm 1.3 \times 10^{-3}$ (see Figure 9). This value is relatively high due to the favorable D_2 symmetry of the molecule (see Figure 3)^[66] along with the favorable 180° geometry of the corresponding electric transition dipole moment $\boldsymbol{\mu}$ and the magnetic transition dipole moment \mathbf{m} , both oriented along the long molecular axis. The degree of contortion of the π -system is usually accompanied by an increase in \mathbf{m} , leading to an overall increased g_{abs} along the system’s $\boldsymbol{\mu}$ decrease (see Eq. 3).^[72] In contrast to the monosignated CD transition of the main band, the S_0 – S_2 transition involves multiple energetically degenerative transitions, which result for the *P*-enantiomer into a positive couplet in the CD spectrum crossing zero close to the absorption maximum at 440 nm and vice versa for the *M*-enantiomer. The high-energy transitions below 400 nm have not been assigned so far. **1e** shows a structureless, broad and redshifted emission band with large Stokes shift of $\Delta\tilde{\nu}_{\text{Stokes}} = 1740 \text{ cm}^{-1}$ typical for this class of molecules and thus contrasting the sharp and narrow emission ($\Delta\tilde{\nu}_{\text{Stokes}} = 200 \text{ cm}^{-1}$) of the parent PBI **20**. Also, the fluorescence quantum yield drops down from unity to 55%. Whether this is attributed to the molecular geometry or simply due to the energy-gap law^[73] has not been investigated so far. It is noteworthy that the emission properties are indeed dependent on the choice of aryl substituent. Besides the phenyl-substituted **1e**, the pyrene derivative **4a** (Figure 8) showed excimer-like emission with strong HOMO-LUMO separation. This is also congruent with the [7]carbohelicenes, whose analogy has been mentioned before, where the annulation of pyrene shows similar behavior.^[74] Analogously to the CD absorption of the S_0 – S_1 band of **1e**, a strong CPL signal (Figure 9) can be detected with an overall constant emission dissymmetry factor g_{lum} of $\pm 1.3 \times 10^{-3}$. These entirely equal g_{abs} and g_{lum} values are rather an exception than the rule for inherently chiral small organic molecules. A g_{lum} value as high as the corresponding g_{abs} value can be interpreted as a consequence of the rigid interlocked π -backbone with no conformational change upon electronic excitation.^[16, 22, 27]

2.2.2 Exciton-coupled Dyes

To obtain chiral excitonic coupling with perylene dyes, chromophores have to be oriented in a stable chiral mutual orientation, which requires an orientation of the chromophores’ electric transition dipole moments $\boldsymbol{\mu}$ different from 0° or 180° as well as a considerable inter-

chromophoric coupling strength. The simplest case for chiral excitonic coupling is a conformationally fixed dimer. For the case of a closed dimeric PBI entity, the two structurally similar cyclophanes **21**^[75] of Weh *et al.* and **22**^[55] of Penty *et al.* can serve as model compounds. The PBI cyclophane **21** follows the macrocyclic approach discussed in the previous chapter, which introduces stable inherent monomeric chirality (see Figure 10) and has been investigated as tool for chiral recognition and deracemization for carbo[4]helicenes. The two chiral *P*-chromophores are interconnected by the imide positions. Despite the remarkable π -distance of 7.2 Å as deduced from single-crystal X-ray structure, a significant H-type excitonic coupling could be determined. However, due to the almost collinear chromophore arrangement, no excitonic contribution to the chiroptical response could be detected. The CD absorption spectra only revealed a monosignated band of the main S_0 – S_1 UV–vis transition with a decent but monomolecular g_{abs} of $\pm 1.2 \times 10^{-3}$.^[75] As a side note, a similar cyclophane^[76] was built up not only from the aforementioned *bay*-aryloxy PBI but from the discussed *bay*-tetraarylated PBI (not shown here). This cyclophane showed a monomolecular chiroptical response owing elevated g_{abs} and g_{lum} values of up to $\pm 2.1 \times 10^{-3}$ due to the rigidified geometry even though (achiral) H-type coupling is entirely impeded.^[76]

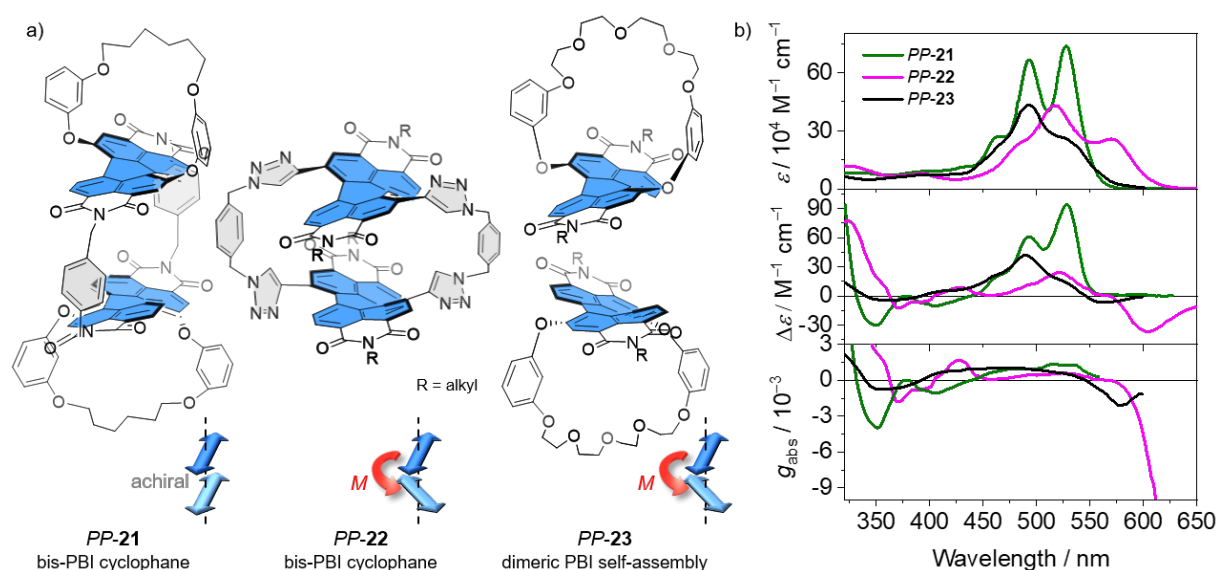


Figure 10. (a) Chemical structures of cyclophanes *PP-21*,^[75] and *PP-22*^[55] and the self-assembled dimer of *P-23*^[61] along their (b) chiroptical properties of *PP-21* (chloroform, green), *PP-22* (toluene, magenta) and of *PP-23* ($c = 1 \times 10^{-3}$ M in *n*-hexane, black). The structures of the twisted *P*-enantiomers are highlighted in blue. Their electric transition dipole moments within the cyclophane are schematically depicted as blue arrows along their mutual orientation.

In contrast, the PBI cyclophane **22** of Penty *et al.* is *bay*-linked via the PBI's 1,7-positions (see Figure 10).^[55] This structural motif that has been previously investigated for a chiral bis-PBI

macrocycle^[77] but was now optimized for homochiral π - π stacking at close distances of 3.7 Å to boost the chiroptical response. As a note, the authors assigned their inherent PBI chirality along the rules of planar chirality (see the previous *Chapter 2.2.1*), leading to the opposite descriptor. For comparability reasons within this thesis, their descriptor will be reassigned following the rules of axial chirality. By this means, the chiral PBI bis-macrocycle **22** is obtained in a clockwise (*P*) and anticlockwise (*M*) mutual PBI orientation (see Figure 10a), defining the bisignate CD absorption of the main S_0 - S_1 transition. The sign of this CD couplet is congruent with the exciton chirality rule for H-type coupled dyes (see Figure 10b). Interestingly, the monomeric subunits themselves are forced into the opposite molecular handedness as deduced from single-crystal X-ray analysis. Accordingly, the dimer of two *P*-PBIs shows an opposite mutual *M*-orientation and vice versa for the other enantiomer. Even though a decomposition analysis of the molecular and supramolecular contributions to the chiroptical properties has not been provided by the authors, opposing signal contributions might explain for the rather low g_{abs} of $\pm 5 \times 10^{-4}$ at the λ_+ branch at 522 nm and the very high g_{abs} of the λ_- branch of $\pm 9 \times 10^{-2}$ at 600 nm of the asymmetric CD couplet (see Figure 10). In contrast to the CD absorption, the excimer-like emission reaches high g_{lum} values of $\pm 10^{-2}$ within a monosignated CPL band corresponding to the sign of the lowest-energy branch in the CD absorption spectrum. It is among the highest reported values for such small bis-chromophoric entities. These examples of PBI cyclophanes **21** and **22** highlight the importance of the excitonic contribution to reach a high chiroptical response beyond the modest dissymmetry of most small organic molecules and indicate the challenge to avoid opposite signal contributions.

The dissymmetry can be maximized by self-assembly to exploit the excitonic coupling of a multitude of chromophores within extended aggregates. In principle, the chiral mutual orientation between chromophores within the assembly can be achieved by enantiopure chiral side chains attached to planar PBI scaffolds or by the π - π interactions of PBIs that are chirally twisted themselves. However, it has to be considered that the introduction of monomeric chirality by the rigid interlocking of PBI *bay*-substituents is at the expense of the capability for supramolecular self-assembly. The sterical shielding reduces the π - π interactions compared to undecorated planar PBIs. Therefore, there is so far only a single example of core-twisted PBIs, which undergo self-assembly into a supramolecular structure showing excitonic chirality for the main optical transition. Macrocycle **23**^[61] (see Figure 10) is only onefold diagonally *bay*-bridged (compare with **15**, Figure 9) and has therefore one PBI-side open for π -stacking.

The chiroptical response closely resembles that of the cyclophane **22**. The *P*-enantiomers show predominant H-type coupling and form *M*-helical dimers, resulting in a CD couplet of negative chirality. A decent g_{abs} of $\pm 1 \times 10^{-3}$ is reached at the maximum of the λ_+ branch at 490 nm and at the λ_- branch at 564 nm, respectively. However, closed, dimeric species cannot benefit from extended chromophore coupling, which could otherwise boost the chiroptical response.^[8-9, 78]

To obtain chiral aggregates, it is common to use twisted but flexible PBI cores whose chirality is defined within the self-assembly process. Here, the chromophore flexibility facilitates the process of PBI self-assembly. These twisted but flexible PBIs, such as *bay*-chlorinated or *bay*-aryloxy PBIs, are prone to self-assembly into effective co-facial H- and slip-stacked J-type aggregates (see **24** and **25** in Figure 11a).^[19, 79] The impact of core flexibility on the formation of aggregate has been comparatively studied for the twisted but flexible *bay*-chlorinated PBIs versus planar and rigid PBIs. Therefore, the supramolecular order increases by switching from a planar to a twisted geometry, even though its molecular order decreases.^[80]

Among the twisted fourfold *bay*-substituted PBIs, the family of *bay*-oxygen substituted PBIs such as aryloxy or acyloxy^[81] PBIs is by far the most explored one. The high degree of conformational flexibility ($\Delta G^\ddagger = 60 \pm 3 \text{ kJ mol}^{-1}$, see the previous chapter) even exceeds the flexibility of *bay*-tetrachloro PBIs ($\Delta G^\ddagger = 98 \pm 1 \text{ kJ mol}^{-1}$).^[60] Without further chiral induction, the handedness of the PBI core twist is defined during the self-assembly process and, hence trapped within the aggregated state.^[82, 85-86] A large number of PBIs has been investigated where a racemic system undergoes self-sorting into either heterochiral assemblies or homochiral aggregates of *P*- and *M*-entities (see **26–29** in Figure 11). The polymorphism of such a system has been the subject of many studies.^[81, 87] The structural proof of a racemic system with a slip-stacked arrangement of alternating *P*- and *M*-PBIs into single- or double-strands by single-crystal X-ray analysis was first obtained for **26** (Figure 11b). However, as the monomers do not possess stable inherent chirality, the resultant homochiral assemblies are always present in a 50:50 mixture without further chiral bias. This bias can be applied in two ways to design efficient H- or J-type coupled assemblies. First, with the attachment of enantiopure chiral side chains to the *bay*-aryloxy PBI and second, with chiral molecules that co-assemble with the achiral PBI core. For the first case, natural sources of chirality are readily available such as chiral terpene-derived alkyl residues. This allowed for the first report on pristine PBI J-aggregates of **27** or **28** with exclusively unidirectional helicity in 2007 (see Figure 11c). In **28**, the chromophores assemble due to π - π interactions guided by complementary H-bonds into a slip-stacked linear geometry. The branched chiral alkyl chains ensure the unidirectionality of

each helical aggregate, resulting in a net chirality of the ensemble. This unidirectionality is not obtained for **27**, resulting into a mix of *P*- and *M*-aggregates. In 2012, this motif was taken up for the J-aggregates of **29**, which for the first time possessed monomeric axial chirality of the PBI with no further need for chiral alkyl chains (see Figure 11d).

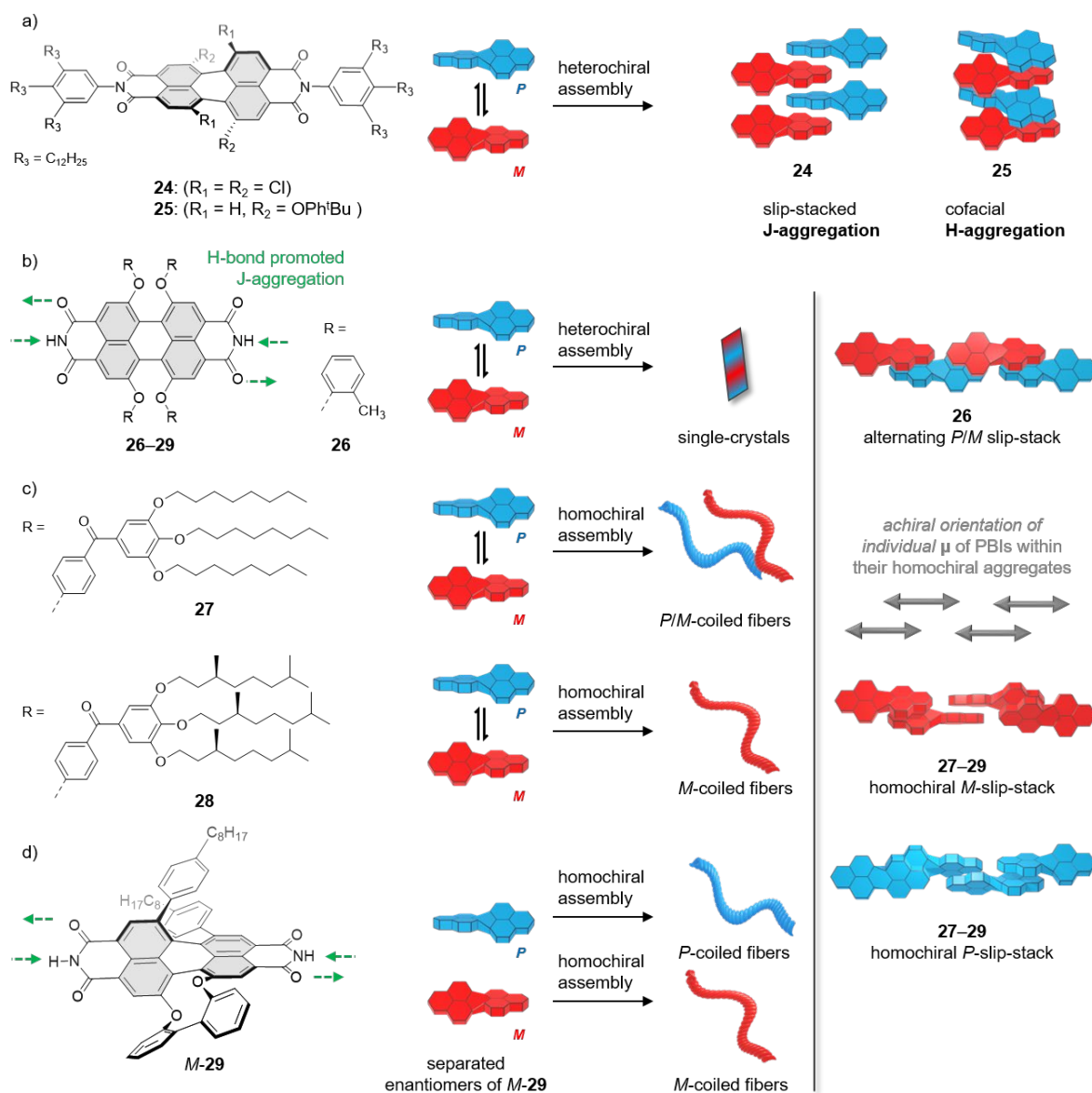


Figure 11. (a) Schematic representation of twisted fourfold bay-substituted PBI forming racemic H- (**24**) or J- (**25**) aggregates.^[79] (b) H-bond promoted J-type aggregation of twisted bay-aryloxy PBIs **26**,^[82] (c) **27**, **28**,^[83] and (d) **29**^[84] into either homochiral or heterochiral assemblies. The achiral orientation of the PBI's electric transition dipole moment (μ), as well as a scheme of the assemblies is presented on the right side. Note that in the study of **28**, heterochiral assembly has not been addressed.^[83]

However, in both cases of **28** and **29**, the collinear PBI arrangement in the respective aggregates prohibits excitonic chirality. Thus, the main optical S_0 – S_1 transitions in the CD absorption spectra remain monosignated (compare with Figure 10 and see Figure 11, right).

As the second natural source of chirality next to terpene derivatives, sugars have been widely investigated with the perspective of biomedical sensing applications. This envisions the combination of high binding affinities of cells to sugars with the high structural sensitivity of chiroptical spectroscopy. Various sugar-substituted PBI aggregates have been reported, such as the D-glucopyranoside-substituted **30** (Figure 12).

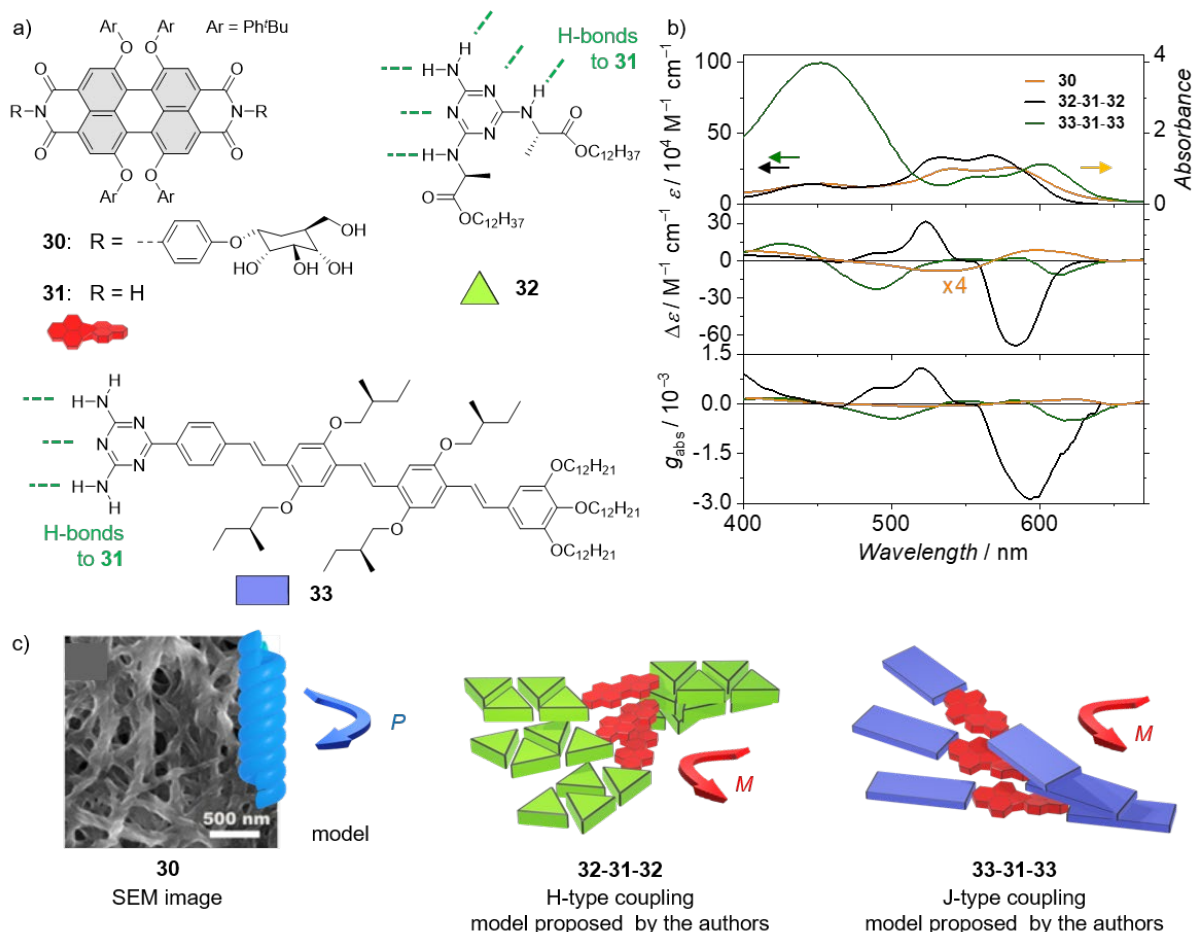


Figure 12. (a) Chemical structures of twisted fourfold bay-substituted PBIs forming H- or J-aggregates with chirality only promoted by a chiral sugar side chain (PBI **30**^[91]) or PBI **31** in co-assembly with a chiral melamine or chiral oligo(phenylene vinylene) derivative by hydrogen bonding into the dyads **32-31-32**,^[92] and **33-31-33**,^[93-94] respectively. (b) Chiroptical properties of the assemblies in THF/H₂O (1:9 v:v, **30**, orange) or MCH (**32-31-32** black, **33-31-33**, green). Note the 4x scaling of the CD spectrum of **30**. (c) Structural models, as proposed by the authors, including the SEM image of the aggregates of **30**. Note: The J-type slip-stacked model of **33-31-33** is possibly incorrect, and the helicity of its ‘creeper’ arrangement has to be changed from counterclockwise (*M*) to clockwise (*P*) to corroborate both chiroptic and microscopic measurements. Spectral and microscopic data of **30** and **33-31-33** are adapted with permission from ref. [91] and ref. [94]. Copyright 2017, American Chemical Society. Spectral data of **32-31-32** are adapted with permission from ref. [92]. Copyright 2002, Wiley-VCH Verlag GmbH & Co. KGaA, Weinheim.

Its CD spectrum shows a positive couplet, which is in line with the *P*-helical aggregate determined by SEM (Figure 12c, left). However, the low g_{abs} of only about 10^{-5} is representative of these aggregates even though it is not discussed within the presented reports.^[88-91] The weak apparent excitonic chirality might be attributed to the issue that the supramolecular aggregation

will probably be dominated by the sugar moieties forming hydrogen bonds in high polar solvents rather than efficient π - π stacking induced by the PBI chromophores. The second concept of introducing a chiral bias into *bay*-aryloxy PBI-assemblies by a purely supramolecular approach was already realized in early 2002 and 2004. The *bay*-aryloxy PBI **31** was connected with chiral melamine **32** or chiral oligo(phenylene vinylene) **33** units by complementary hydrogen bond motifs leading to aggregates of the chiral dyads **32-31-32** and (**33-31-33**) with either H-^[92] or J-type^[93-94] coupling (Figure 12). The interpretation of the H-aggregate **32-31-32** upon its excitonic chirality is straightforward. A pronounced negative CD couplet arises around 550 nm, reaching a high g_{abs} of -9×10^{-3} , which was explained along a proposed model of an *M*-helical PBI geometry (Figure 12c, center). Besides, the fibrils of the **33-31-33** J-aggregate show a much more complex CD spectrum with an overall reduced dissymmetry. First, the absorption band around 450 nm and the corresponding negative couplet are assigned to the co-component **33** indicating a pronounced excitonic chirality of the PBI's co-assembly on its own even though their H/J-coupling type was not commented by the authors. In contrast, the J-band of the PBI does not show a distinct couplet but a very narrow band at 613 nm, 11 nm (300 cm^{-1}) redshifted to the maximum of the J-band. The authors excluded an excitonic contribution and proposed a chiral enrichment of *M*-enantiomers rigidified within their aggregate showing a monomeric chiroptical response.^[94] Figure 12c shows its *M*-PBIs ordering in a left-handed slip-stacked arrangement. This left-handedness was only rationalized by the negative PBI-assigned CD band. However, the AFM data revealed right-handed fibrils, which could not be adequately rationalized. Therefore, the proposed structural model might be incorrect and is right-handed instead. Such a right-handed slip-stacked 'creeper' geometry would not only corroborate the provided AFM data, but could also explain the negative couplet around 450 nm. Accordingly, **33** undergoes J-type coupling on its own within its 'creeper' type slip-stacked arrangement. Further on, the sharp and featureless CD band at 613 nm could be indeed the λ_+ band of a J-type couplet rather than a monomeric CD signature of the PBI transition even though the λ_- band is concealed, which is not uncommon for complex excitonic systems (see the following *Chapter 2.2.3*).

When going from the aforementioned twisted PBIs to planar PBIs, the design concept for chiral assemblies does not fundamentally differ. However, *bay*-unsubstituted PBIs show in general lower solubility, higher van-der Waals interactions of their planar π -scaffolds, higher charge transport properties in the solid state but also less chemical binding sides to control the supramolecular design. A prominent example is the planar PBI (see **34** and **35** Figure 13). The

benzamide functionalization in both imide positions of the PBI enforce strong π - π stacking with additional H-bond formation by the imide moieties. The achiral congener (not shown) can form H-type coupled stacking in both *P*- and *M*-helical fibers.^[95] Its rich polymorphism has also recently been addressed.^[96] In 2008, the system could be biased with a variety of chiral side chains. Even though the applied molecular changes might appear subtle by only changing two of six alkyl chains, the system could be tuned towards discrete H- or J-type assemblies of **34** and **35** (Figure 13).^[97-98] The interpretation of the chiroptical response can be fairly compared to the dyad co-assemblies of the twisted PBIs (Figure 12). For the H-type helix of **34**, a strong negative CD couplet arises around 475 nm with a g_{abs} of $\pm 4 \times 10^{-3}$.

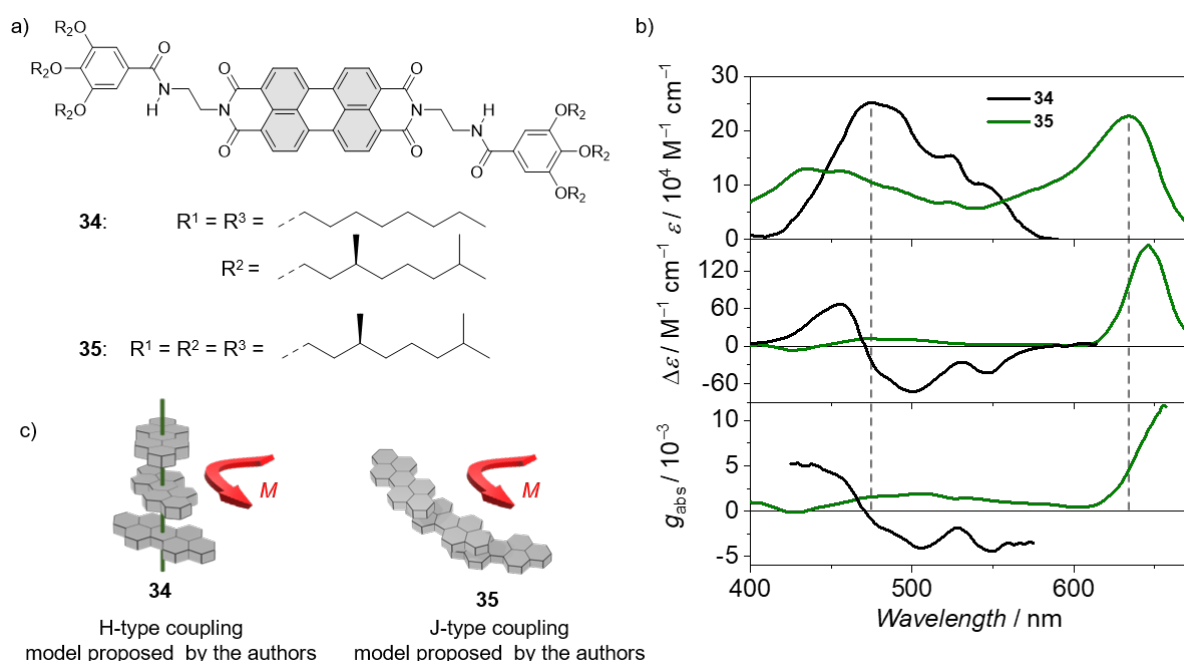


Figure 13. (a) Chemical structures of *bay*-unsubstituted PBIs **34**,^[97] and **35**^[98] forming H- or J-aggregates, respectively. (b) Chiroptical properties of the assemblies of **34** (black), and **35** (green) in CHCl_3 :MCH 80:20. (c) Structural models as proposed by the authors. Adapted with permission from ref. [97-98]. Copyright 2008, Wiley-VCH Verlag GmbH & Co. KGaA.

In contrast, the J-aggregate of **35** does not reveal a bisignate CD signal but a sharp positive CD band centered at 646 nm, again redshifted by 11 nm (270 cm^{-1}) to the absorption maximum. The high dissymmetry factor g_{abs} of around 8×10^{-3} at 611 nm strongly suggests excitonic chirality also in this case. Even if not discussed in the scope of excitonic chirality, the authors provided a structural model in ‘creeper’-geometry with left-handed helicity.^[97-98] Accordingly, this is the first pristine PBI-based literature example of this special helical J-type geometry. The second and only further report on a PBI-based ‘creeper’ J-aggregate was provided by Haino in 2012.^[99] It shows similar CD progression and even excimer-like CPL, but its various possible

H- and J-type contributions have not been thoroughly investigated.

Unlike the examples with J-type coupling, which remain exceptional, helical H-aggregates of planar PBIs are frequently reported. PBI-based H-type aggregates with manipulable self-assembly into either *P*- or *M*-helicenes^[100-102] have served as model compounds for understanding excitonic chirality.^[103] Like the twisted PBIs, also planar PBIs have thus been designed by linking the PBIs with chiral alkanes^[104] and biomolecules,^[105-108] or by co-assembly of an achiral PBI with a chiral inducer. This co-assembly can be achieved by H-bond-assisted aggregation,^[93, 109] the formation of ionic bonds,^[102, 110] metal coordination bonds,^[111] or even the dynamic covalent bonds.^[112] All examples show moderate CD couplets around the main transition of the PBI H-aggregate but do not surpass absorption dissymmetry factors of $\pm 10^{-3}$ in solution.

The concept of rigidified H-type geometries to increase excitonic chirality has not only been applied for cyclophanes, as discussed previously, but also for wedge-like bis-chromophores, which usually show pronounced CD couplets. Following early studies on NDIs,^[113] PBIs have been chirally linked by cyclohexane^[114] or binaphthalene (**36**). The bis-PBI **36** (Figure 14) has been presented in early 2007 as the first example of a CPL-active PBI. It revealed a decent g_{lum} value of $\pm 2 \times 10^{-3}$ as a monomolecular system even though its g_{abs} of $\pm 3 \times 10^{-4}$ was rather poor.^[115] This could be substantially improved by exploiting its self-assembly in 2014. Hence, **36** formed either nanoparticles or nanofibers, which both were investigated in solution as well as in PMMA matrix. Thus, the g_{lum} values could be drastically increased to $\pm 2 \times 10^{-2}$ for the fibers (see Figure 14).^[116-117] Alongside the H-type helical stacking of the bis-chromophores, electron microscopy revealed fibers of the corresponding *P*-helicity. This increase of an order of magnitude proves a successful switch from a molecular to a supramolecular chiral system. However, the increase highly depends on the molecular design and the corresponding excitonic nature of the chromophore coupling. Hence, the 1,2-cyclohexane linked congener (not shown here) remained at low dissymmetries of $\pm 1 \times 10^{-3}$ even in the aggregated state.^[114, 118]

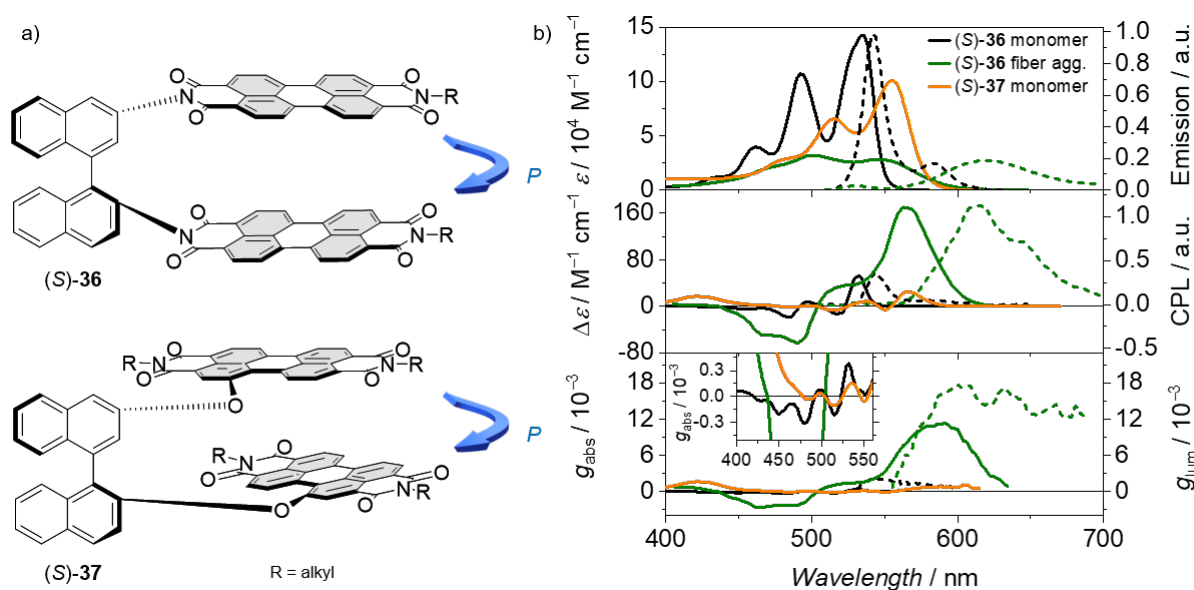


Figure 14. (a) Chemical structures of planar PBIs linked by a (*S*)-binaphthalene unit in imide (top) or *bay*-position (bottom) leading to a *P*-helical arrangement of the chromophores. (b) Chiroptical properties of the monomers of **36**^[115] (black), and **37**^[119] (orange) in toluene and TCE, respectively, as well as of the fiber aggregates of **36**^[120] (green) in a mixture of chloroform and methylcyclohexane (1:19).^[115, 119-120] The spectral data of the monomer of **36** are adapted with permission from ref. [115], copyright 2007, WILEY-VCH Verlag GmbH & Co. KGaA, Weinheim. The spectral data of the aggregated **36** as well as of **37** are adapted with permission from ref. [119-120]. Copyright 2014 and 2018, American Chemical Society.

A deep analysis of the excitonic coupling of PBI bis-chromophores has been provided in 2018 by the Würthner group.^[119] In contrast to **36**, the PBIs of **37** are *bay*-linked to the chiral binaphthalene spacer. To assess the excitonic coupling, both long-range Coulomb coupling as well as short-range charge-transfer coupling have been theoretically determined. This revealed contributions with opposing signs regarding H- and J-type coupling, respectively. When balanced, these contributions rendered the systems into the first so-called ‘null-aggregates’ at this time. For **37**, the obtained H-type coupling is slightly predominant. Hence, a positive CD couplet (Figure 14b) of the (*S*)-enantiomer is observed. This is congruent with its *P*-type chromophore arrangement induced by the (*S*)-binaphthalene spacer. Due to opposing H- and J-type contributions, the dissymmetry factor g_{abs} of the main band is accordingly remarkably small with values of only 1.5×10^{-4} .

All hitherto discussed systems have been designed for self-assembly in solution, in the liquid crystalline or the gel state, which requires large substituents for sufficient solubility. In contrast, for application in organic electronics, large solubilizing chains are usually avoided to ensure efficient charge-transport properties. Therefore, the chiral methylbenzyl (1-phenylethyl) moiety has been established as a synthon for rendering PBIs chiral, aiming for a low steric demand

since 2008.^[121-124] The CD spectra of the fibril-like aggregates of **38** in the spin-cast thin film are rather broad and do not show an apparent couplet (see Figure 15).

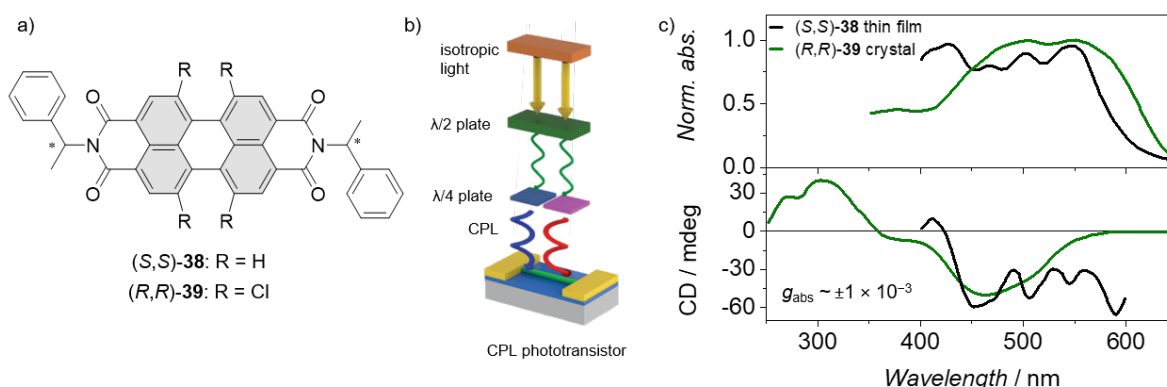


Figure 15. (a) Chemical structure of planar (**38**^[125]) or twisted (**39**^[126]) PBIs with chiral methylbenzyl units in imide-position. (b) Schematic setup of the utilized organic CPL phototransistor. (c) Chiroptical properties of a thin film of nanowires of (S,S)-**38** (black) and single crystal of (R,R)-**39** (green).^[125-126] Spectral data and (b) are adapted with permission from ref. [125], copyright 2017, WILEY-VCH Verlag GmbH & Co. KGaA, Weinheim and from ref. [126]. Copyright 2020, American Chemical Society.

Also, their dissymmetry g_{abs} of $\pm 1 \times 10^{-3}$ is rather modest. However, the aggregate could be successfully incorporated into the first PBI-based chiral organic phototransistors in 2017 and was able to discriminate between right and left-handed light.^[125, 127] Three years later, the authors could improve their molecular design from planar PBIs to *bay*-tetrachloro PBI **39** to change the material's morphology from dispersed aggregates to single crystals. Even though no dissymmetry factor is reported, a broad CD couplet could be observed. The low-energy branch was successfully used for the detection of CP light. A high charge carrier mobility of up to $1.0 \text{ cm}^2 \text{ V}^{-1} \text{ s}^{-1}$ and a photoresponsivity anisotropy factor of ~ 0.12 at 495 nm could be achieved. Up to now, this is the highest performance of a perylene-based detector for circularly polarized light so far.^[126] These examples highlight the demand not only for molecular dissymmetry but also suggest the packing properties to be equally important when designing an organic device for chiroptical sensing.

2.2.3 Bay-annulated Rylene Dyes

The design of PBI-based materials for organic electronics has been shifted from single-chromophore systems to multi-chromophore systems driven by the research in the field of non-fullerene acceptors for organic solar cells.^[128] Here, two design concepts have been established. First, the PBI chromophores are only connected by a single sigma bond with an optional aromatic spacer, which leads to twisted and flexible structures.^[129-130] Second, multiple PBIs are directly annulated, which leads to expanded conjugated π -scaffolds envisioning new

nanographene materials. For the second concept, major contributions have been made by the group of Wang and Nuckolls within the last years.^[131]

In this chapter, the chirality of fused PBI systems will be briefly discussed along the following scheme: 1) inherently chiral systems with resolvable atropoisomers, 2) systems requiring an additional chiral bias, and 3) the fusing of PBIs and carbo[n]-helicenes. The latter will include carbo[n]-helicene systems with either a single PBI or multiple embedded PBIs along their chiroptical properties. It should be noted that bisimides, which contain helical units^[132-133] but are no pristine rylene bisimides chromophores themselves, are beyond the scope of this work and will not be discussed here.

The first *bay*-fusion of PBIs was achieved by the Wang group in 2010, connecting the *bay*-positions of *bay*-tetrachloro PBIs by the Ullmann-coupling to obtain interconnected dimers, trimers, or tetramers **40–42** (see Figure 16).^[134-135] The bridging section between two PBIs is an eight-membered ring, which sustains the high core contortion with twist angles of exactly 90° as deduced from TD-DFT calculations.

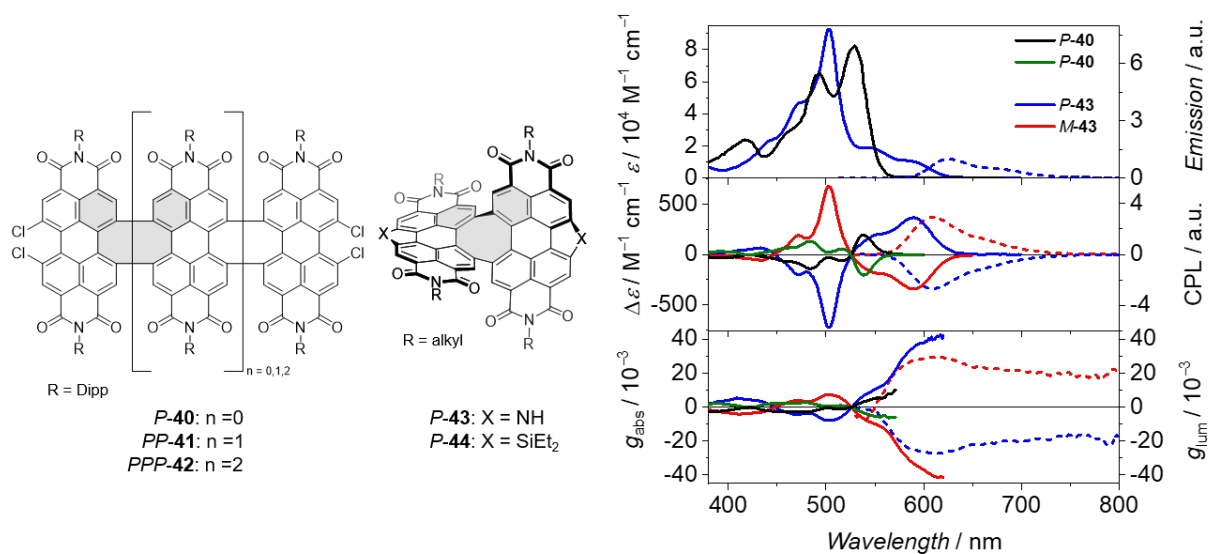


Figure 16. (a) Chemical structures of *bay*-annulated PBIs *P-40*, *PP-41*, *PPP-42*,^[134] as well as *P-43*^[136] and *P-44*^[137] along their (b) CD absorption (solid lines) and CPL spectra (dashed lines) of *P/M-40* (black and green) and *P/M-43* (blue and red) in chloroform and toluene solution, respectively.^[134, 136] The spectral data of **40** are adapted from ref. [134] with permission from the Royal Society of Chemistry. The spectral data of **43** are adapted with permission from ref. [136]. Copyright 2022, American Chemical Society.

The CD spectra show distinct couplets of the resultant S_0 – S_1 transition with a remarkable g_{abs} of about $\pm 4 \times 10^{-3}$. The signs obey the exciton chirality rule for H-type coupling. However, the authors did not assign the descriptors according to the common axial chirality. For the sake of consistency, the reported assignment has been adapted within the present thesis (see Figure 16).^[134] This fused eight-membered-ring-embedding PBI motif has been revived by the

same group in recent years by heteroannulation of nitrogen and silicon into the outmost PBI *bay*-positions to obtain **43** and **44** (see Figure 16).^[136-137] For the nitrogen-embedding **43**, the favorable D_2 symmetry and the high m due to the heteroannulation led to high dissymmetry factors g_{abs} and g_{lum} of up to 0.35 and 0.30, respectively. Moreover, its high fluorescence quantum yield of up to 41% resulted in a high B_{CPL} of $573.4 \text{ M}^{-1} \text{ cm}^{-1}$. To date, this is the highest dissymmetry and it is among the highest B_{CPL} values, which have been achieved for a single small organic molecule. The corresponding silicon heteroannulation in **44** even increased Φ_{FI} to up to 68% but, in turn also to a slightly diminished its chiroptical response ($g_{\text{abs}} = g_{\text{lum}}$) to 0.01, which resulted also in a lower B_{CPL} of $207.3 \text{ M}^{-1} \text{ cm}^{-1}$.^[137]

A second concept of *bay*-fusing for PBIs is to include a sp^2 -hybridized C2 unit into the annulated scaffold. This has been established by the Nuckolls group in 2014 by using Stille-coupling conditions and subsequent oxidative coupling.^[138] The corresponding architectures of the dimer **45** (see Figure 17) or of its higher oligomers have since then been widely applied as organic semiconductors^[139-142] or cathode materials.^[143] These PBI-based ‘twistacenes’ can be formally seen as carbo[4]helicenes, which do not endow stable inherent chirality but can be biased by the chirality of the PBI imide substituents. This concept was first reported for a similar PBI-acene hybrid ribbon, which used an N-bridged binaphthalene^[144] (not shown here). However, the first report of a pristine PBI *bay*-fused dimer **45** thereafter relied on small enantiopure side-chains such as methylbenzyl units attached to the PBI imide positions (see Figure 17)^[145] in a molecular ‘sergeants and soldiers’ principle.^[146] This approach leads to a decent chiroptical response in the magnitude of $g_{\text{abs}} \sim 10^{-3}$ of the exciton-coupled PBIs in *P*-**45**. The system can be considered a chiral switch due to the sensitivity of the molecular conformation on the choice of chiral imide substituent, the solvent and the applied temperature. However, no clear correlation was found between the end-group chirality and the imparted overall helicity of **45**. Even though the assigned descriptors of the fused dimers are ordinarily assigned, the TD-DFT predicted chiroptical response does not obey the exciton chirality rule. This is rather unusual but has not been further commented by the authors (see Figure 17).

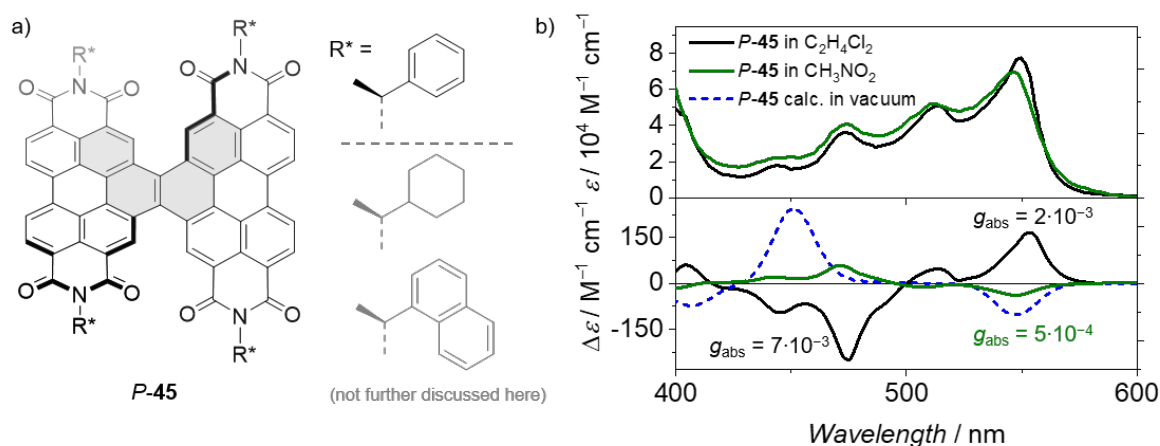


Figure 17. (a) Chemical structure of bay-annulated PP-45^[145] along the (b) chiroptical properties tetrachloroethane and nitromethane, respectively. The blue dotted line represents the TD-DFT calculated ECD spectrum of P-45 in vacuo with methyl as imide group with arbitrary scaling. The insets show the g_{abs} values at the respective local maxima. The spectral data of 45 are adapted with permission from ref. [145]. Copyright 2022, American Chemical Society.

The third concept discussed in this chapter is the fusion of pristine carbohelicenes to the bay-position of the PBI. The most straightforward example of a single PBI fused with either one or two pristine carbohelicene moieties has been described in 2020, leading to chiral derivatives with embedded double-helicenes 46 and 47 with $n = 4, 5$ ^[147] as well as 48 and 49 with $n = 8$,^[148] respectively (see Figure 18).

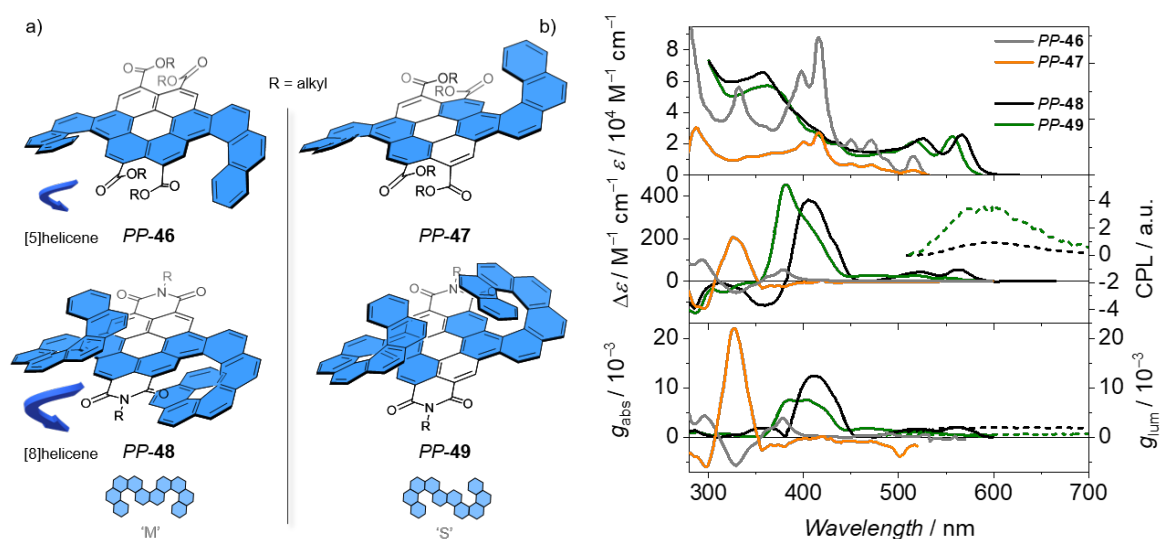


Figure 18. (a) Chemical structures of P-helical molecules based on a single perylene core that is bay-annulated with carbohelicene moieties resulting in either two P-carbo[5]helicenes (top) or two P-carbo[8]helicenes (bottom). The perylene peri-positions are either tetraester- (top) or bisimide- (bottom) functionalized. The mutual helicene orientation is either of 'M'-type (left) or 'S'-type (right). (b) Chiroptical properties of PP-46^[147] (gray), PP-47^[147] (orange), PP-48^[148] (black), and PP-49^[148] (green) in toluene solution. Absorption data are shown as solid lines, emission properties are shown as dashed lines. For better clarity, an artificial offset is applied to the CPL spectra.^[147-148] Spectral data are adapted with permission from ref. [147], copyright 2020, WILEY-VCH Verlag GmbH & Co. KGaA, Weinheim and from ref. [148]. Copyright 2020, American Chemical Society.

This structural plethora is rooted in the rich isomerism and even more non-chiral *meso* forms are reported. The double-helicenes are either in *P*- or *M*- handedness and are attached to the perylene core in either ‘S’- or ‘M’-configuration (for the chiral isomers see Figure 18).

The discussion will start with the carbo[5]helicene-embedded perylene tetraesters **46** and **47**. Due to the enlarged π -surface, these systems have also been termed ‘coronohelicene’, which is justified in the optical signature in the UV–vis absorption below 400 nm. However, upon the annulation, a distinct red shift is observed in the main S_0 – S_1 from 494 nm of the parent coronene bisimide^[149] to 543 nm. The molar extinction of the ‘M’-configuration of **46** is much more pronounced compared to the ‘S’-configured **47**. When analyzing the CD absorption spectra, two things become apparent. First, due to the planarity of the coronene π -plane, the S_0 – S_1 is almost completely CD silent, and the chiroptical properties are only governed by the helicene-assigned couplets below 400 nm. Second, the helicene-assigned CD bands of the ‘S’-shaped **47** are stronger by a factor of about four compared to **46**, reaching dissymmetries g_{abs} of $\pm 22 \times 10^{-3}$ versus $\pm 6 \times 10^{-3}$ at 330 nm. The compounds are emissive, but fluorescence quantum yields have not been reported.^[147] The overall chiroptical response, particularly the comparison of ‘S’ and ‘M’-configuration, is much different for the larger embedded carbo[8]helicenes **48** and **49**, respectively. These systems have a much more interlocked geometry with distinct through-space conjugation that rigidifies the π -scaffold. The chiroptical properties in **48** and **49** resemble more their parent perylene bisimide. Both derivatives now show rather equal extinction coefficients in the UV–vis absorption spectra and a pronounced monosignated CD signature for their respective S_0 – S_1 transition (see Figure 18). In contrast to the smaller [5]helicene-embedding systems **46** and **47**, now the ‘M’-configured **48** shows the highest dissymmetry. The authors claim that **48** has a ‘superhelicene’ architecture, which provides the most efficient π -conjugation.^[150] The dissymmetry factors of the monosignated S_0 – S_1 transition between 450–600 nm are $\pm 2 \times 10^{-3}$ (**48**) and $\pm 5 \times 10^{-4}$ (**49**). For the intense CD couplet around 380 nm, they reach $\pm 12 \times 10^{-3}$ (**48**) and $\pm 8 \times 10^{-2}$ (**49**). Both compounds show decent Φ_{FI} of approximately 30% and a g_{lum} corresponding to g_{abs} . The overall chiroptical response can be significantly enlarged when two or more PBI building blocks are *bay*-annulated to one or more carbohelicenes. This compound family and its chirality have been presented and investigated by the Nuckolls group starting in 2016. The most fundamental derivative **50** (see Figure 19) represents a carbo[6]helicene with two end-capping PBI chromophores.^[151] The PBI cores come in close proximity, inducing an intramolecular through-space excitonic coupling. This causes an increase in the 0–1 band of the vibronic progression of the main S_0 – S_1 transition

and to the appearance of multiple exciton couplets along the whole CD absorption spectrum. These couplets include the main PBI-assigned S_0 – S_1 absorption band and many high-energy transitions (see Figure 19). More profound studies in this PBI-helicene-PBI geometry have been conducted in recent years by converting the PBI imide positions of either one of the two PBI subunits (**51**) or those of both PBI subunits (**52**) into the respective perylene tetraester (PTE, see Figure 19).^[152]

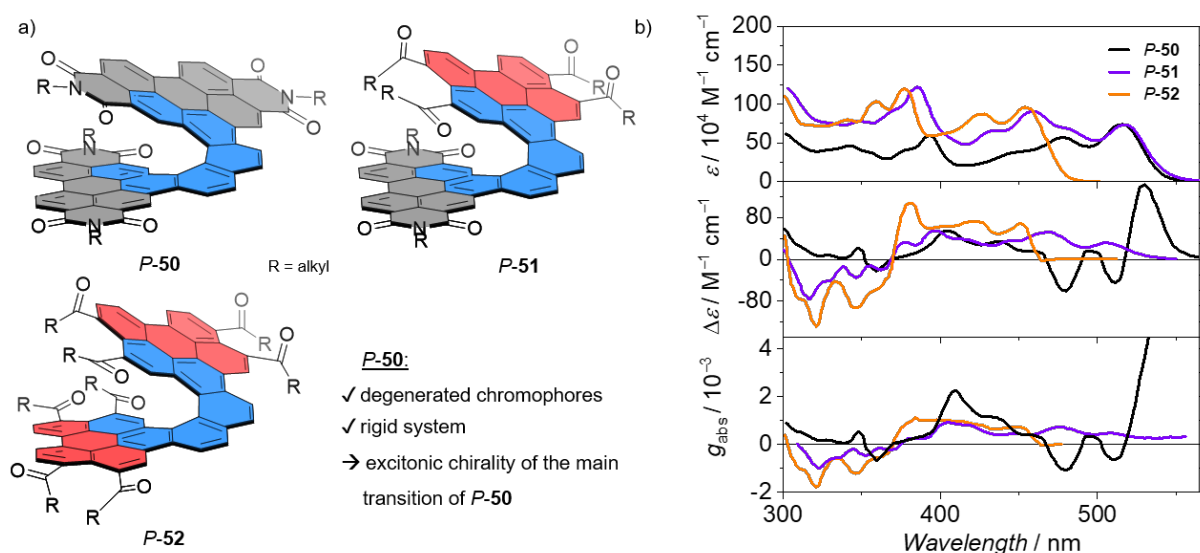


Figure 19. (a) Chemical structures of the *P*-enantiomers of the perylene derivative end-capped carbo[6]helicene scaffolds of **50**, **51**, and **52**.^[152] The π -scaffolds are highlighted in gray (PBI) or red (PTE). (b) UV–vis and CD absorption of the *P*-enantiomers of **50** (black), **51** (violet), and **52** (orange) in solution. The solvent was not reported by the authors. The spectral data are adapted with permission from ref. [152]. Copyright 2022, American Chemical Society.

For **51**, as a result of the non-equivalent perylene chromophores, no degenerative coupling occurs anymore, and the CD progression of the main S_0 – S_1 turns monosignated. Also, for **52**, the main transition no longer shows a CD couplet, and the high-energy transitions show fewer zero-crossings than **50**. The authors concluded a strong geometric distortion from the ester moieties, breaking the degeneracy between the PTEs in **52**. The dissymmetries therefore are highest for the exciton-coupled PBI-based **50** with an appreciable g_{abs} value of up to $\pm 4 \times 10^{-3}$ at 530 nm for the λ_{R-} band of the main CD couplet.

The dissymmetry of **50** could be significantly increased by enlarging the system by one further PBI unit. The resulting **53** is a superhelix combining three PBIs bridged by two carbo[6]helicenes.^[153] In this case, the CD intensity of the PBI-assigned S_0 – S_1 appears to turn monosignated (see Figure 20, orange spectra) while retaining its dissymmetry. However, the intensities of the carbohelicene-attributed CD couplets around 400 nm increase drastically, almost reaching a g_{abs} of 0.01. Hence, the authors concluded that the perylene units only serve

as promoters for the excitonic chirality of the carbohelicene-assigned CD couplet: 1) the PBI units increase the conjugation strength, which leads to an enhanced CD splitting. 2) The helicene-assigned couplet is redshifted more into the visible region. 3) The fluorescence quantum yields are drastically increased from 27% to 44%. The increase in the chiroptical response has been investigated in-depth in a comparative study of **50** and **53** in a subsequent study.^[154]

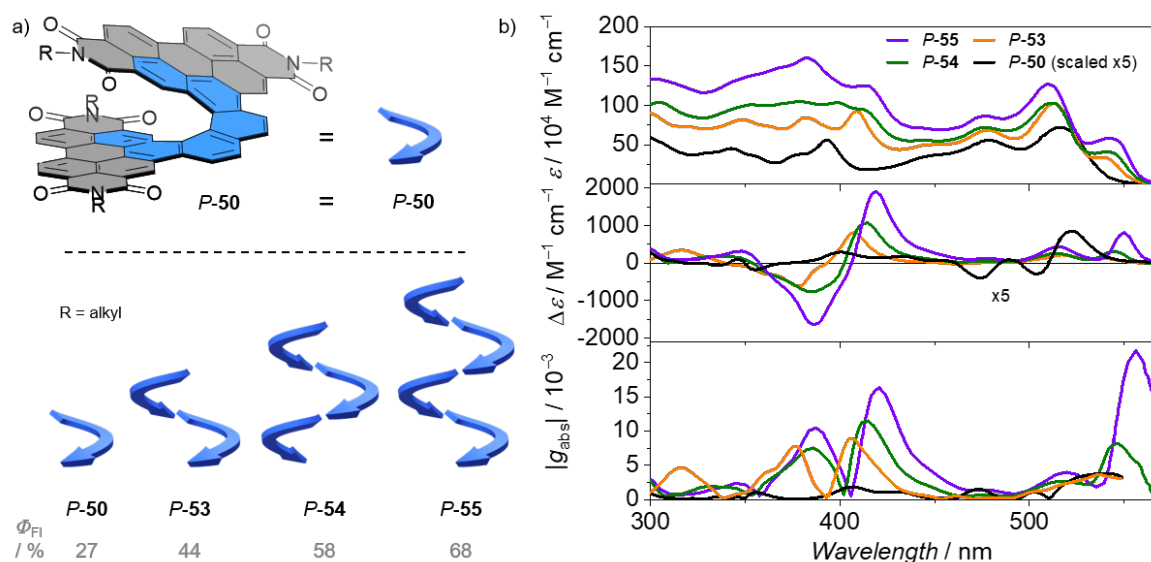


Figure 20. (a) Chemical structure and schematic representations of PBI-end-capped *P*-carbo[6]helicene scaffolds **50**,^[33] **53**,^[33] **54**,^[155] and **55**^[155] along their respective fluorescence quantum yields in THF shown in gray. The blue helical arrows represent the carbo[6]helicene scaffolds. The end-capping perylene bisimide chromophores are omitted in this representation. (b) UV-vis and CD absorption of the *P*-enantiomers in THF solution. The CD absorption spectrum of *P*-**50** has been multiplied by factor 5.^[33, 155] The spectral data are adapted with permission from ref. [155]. Copyright 2021, American Chemical Society.

The authors provided a detailed procedure on the theoretical calculations, including a fragmentation of the molecules to assess the role of each component independently and highlighted the exciton coupling of the helicene moieties in the region at around 400 nm. The computational results indicated that exciton coupling must indeed be also present for the main S_0 – S_1 transition even though its bisignation appeared to be concealed in the experimental spectra (see Figure 20, orange graph).^[33] This issue was further investigated in 2021. **50** was consequently expanded to the superhelicenes **54** and **55**. The most extended superhelix **55** comprises five PBI units connected by four carbohelicenes (see Figure 20).^[155] The results and their interpretation are in line with those of **50** but the dissymmetry of the main S_0 – S_1 transition drastically increased up to 0.023. Still, this PBI-assigned region from 500–550 nm appears monosignated in the experimental CD spectrum. It surpasses even the carbohelicene-assigned couplet around 400 nm with a $g_{abs} = 0.017$. It was concluded that the electronic states, which

contribute to the PBI-assigned region from 500–550 nm, are partially concealed. Hence the bisignation of the excitonic couplet transition is concealed, too, which could be rationalized by TD-DFT calculations.

This series of studies highlights the complexity of excitonic CD contributions and the importance of the proper molecular geometry. Minor structural deviations from the perfect helical geometry or the change from the superior ‘S’-configuration to ‘X’- or ‘M’-configuration of fused carbohelicenes^[27, 154] are crucial for synergistic effects of excitonic coupling to boost the chiroptical response. So far, these *bay*-fused hybrid helicene-PBI systems **54** and **55** show the highest chiroptical response among all PBI-based molecular systems and thus cross the benchmark of $g \sim 10^{-2}$, which is considered the range of chirally enhanced aggregates rather than monomeric organic molecules.^[34] This is indeed not surprising as its size and the number of involved chromophores approach the coherence length of dye aggregates. There are a few more recent examples of *bay*-fused PBI-helicene architectures. Still, they do not exceed the chiroptical properties of **55** nor show they a new trend for the chirality of *bay*-annulated PBIs (see Figure 21).

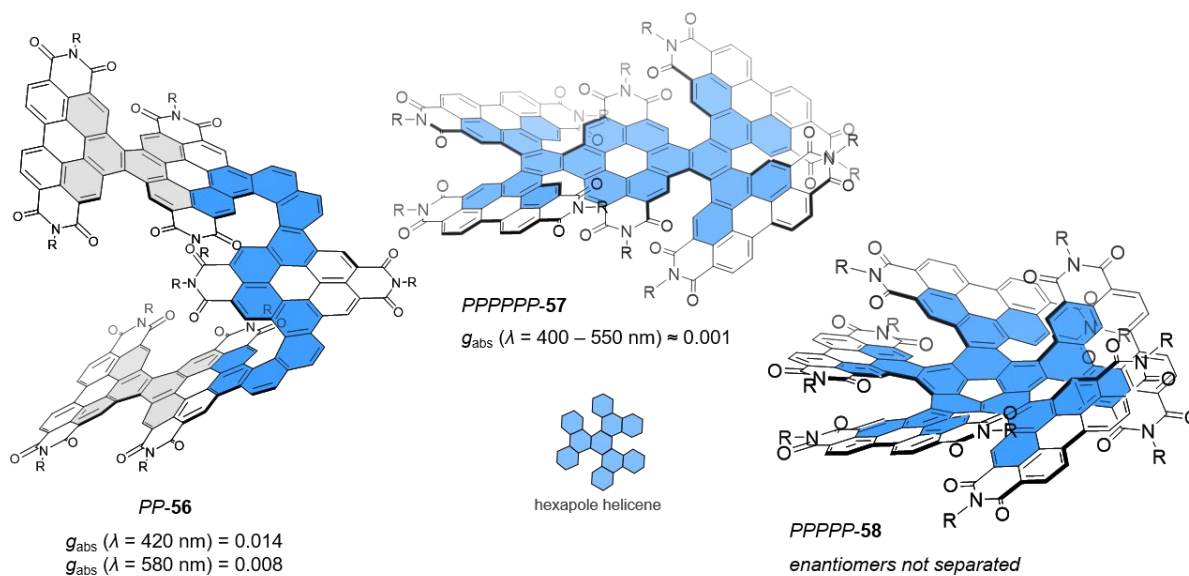


Figure 21. Chemical structures and schematic representation of the *P*-enantiomers of the PBI *bay*-fused *P*-helicene systems **56**,^[154] **57**,^[156] and **58**.^[157] Carbo[5]- and carbo[6]helicene motifs are highlighted in blue, and carbo[4]helicene motifs are highlighted in gray.

The wedge-like **56**^[154] is the combination of the PBI-carbo[6]helicene-PBI system **50** but with the C2-bridged bis-PBI as end-capping units (see **45**, Figure 17) instead of single PBIs (see Figure 21). Even though it has a low interconversion barrier of the terminal bis-PBI, its chiroptical response is comparable to that of **54**.^[154] Another recent PBI-helicene architecture resembles its parent hexapole helicene (see Figure 21). In both derivatives **57**^[156] and **58**,^[157]

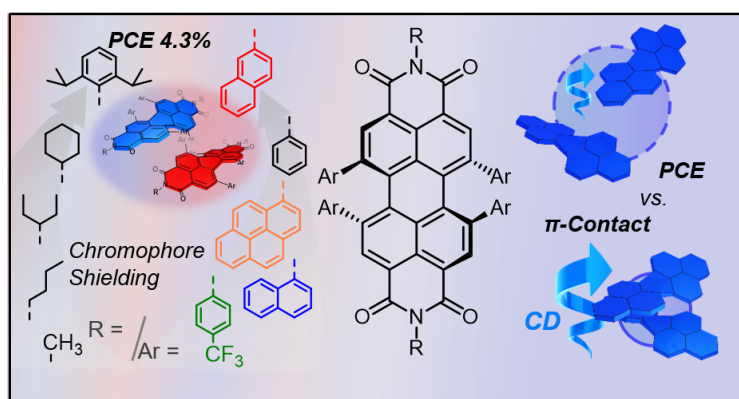
the *bay*-fused PBIs interlock each other in a propeller-like motif. **57** represents a fusion of two parent hexapole carbo[5]helicenes. The CD absorption shows strong couplets throughout the entire CD absorption spectrum, but the g_{abs} remains monomolecular only reaching $\pm 2 \times 10^{-3}$. The corannulene-based pentapole helicene **58** has not been obtained in enantiopure form yet but it shows promising properties as organic semiconductor. This molecule might be further investigated as chiral material in a sensing device.^[156-158]

Within this *Chapter 2.2*, a literature overview of research on chiral PBIs during the last 15 years was provided. This included the careful evaluation of chiral properties, which had not always been discussed by the authors of the respective original reports. First, the conceptual approaches towards the design of stable inherently chiral PBIs have been presented. Based on the theoretical quantities μ and m provided in *Chapter 2.1*, it could be shown in *Chapter 2.2.1* that the inherently chiral PBIs endow an appreciable chiroptical response already as monomer. In *Chapter 2.2.2*, the twisted PBI building block was then discussed for bischromophoric macrocycles as the smallest supramolecular entity. Here, the impact of geometry as well as monomeric chirality was discussed regarding their consequences for supramolecular chirality, which is based on excitonic coupling. The scope of this closed dimeric species was expanded to supramolecular H- and J-aggregates, which were discussed in two sections: First, the twisted PBIs (**1–5**, **15–19**, **21–31**) and second, the planar PBIs (**34–39**). For each section, the design strategies for maximizing the dissymmetry have been sketched. It could be shown that the chiroptical response of the PBI aggregates can be assessed within an excitonic picture and that the exciton chirality rule applies to almost all of the discussed examples. Even though the obtained dissymmetry factor of the presented examples does not surpass $\pm 10^{-2}$ in the aggregated state, it could be shown that the incorporation into a solid-state device can result in much higher electric anisotropy factors of up to 0.12 for **39**. In the last *Chapter 2.2.3*, extended scaffolds of *bay*-annulated PBIs **40–58** were discussed. These inherently chiral architectures show particularly high dissymmetry factors of up to 0.35 even in the monomeric state. The theoretical rationalization of these systems is much more challenging than for the hitherto mentioned examples. Thus, they are exclusively based on ab initio TD-DFT methods. However, for a qualitative impression, the chiroptical response can be assessed within the excitonic picture for most of the provided examples.

CHAPTER 3

—

Axially Chiral *Bay*-tetraarylated Perylene Bisimide Dyes as Non-fullerene Acceptors in Organic Solar Cells



This Chapter and the associated Supporting Information (*Chapter 8.1*) have been published in:ⁱ

B. Mahlmeister, R. Renner, O. Anhalt, M. Stolte, F. Würthner, *J. Mater. Chem. C* **2022**, *10*, 2581–2591 (<https://doi.org/10.1039/D1TC04116A>).

Adapted or reprinted with permission from ref. [159] with permission from the Royal Society of Chemistry.

Abstract. A series of twisted perylene bisimide (PBI) dyes bearing different imide substituents as well as various aryl substituents in 1,6,7,12 *bay*-positions inducing conformationally stable axial chirality are investigated as non-fullerene acceptors (NFAs) in organic solar cells (OSCs). A comprehensive study tests both imide and aryl substituent variations within a simple inverted bulk heterojunction (BHJ) architecture with donor polymer **PCE-10**. The results are

ⁱ Parts of the results have been described in: B. Mahlmeister, Master Thesis, Julius-Maximilians-Universität Würzburg, **2020** (ref. [193]).

rationalized by single crystal structure analyses revealing the importance of the sterical demand imparted by the substituents in both positions on the packing arrangements. Comparative studies of racemic and enantiopure samples of these axially chiral dyes showed that the enantiopurity only affects the OSC performance if the chromophore is not well shielded. In that case, intimate π - π stacking is disfavored for enantiopure compounds, thereby improving the OSC efficiency significantly by up to 24%. For a more shielded PBI bearing bulky 2,6-diisopropylphenyl (Dipp) substituents at imide and 2-naphthyl at *bay*-positions, a maximum power conversion efficiency (PCE_{max}) of 4.3% is achieved even for the racemate.

3.1 Introduction

Perylene bisimides (PBIs) opened up the field of non-fullerene acceptors (NFAs) in organic solar cells (OSCs) with the pioneering work of Tang at the very beginning of 1986.^[160] The embedding of a simple PBI derivative into a p-n junction not only demonstrated its utilization as a stable and electron-poor n-type semiconductor but also initialized the quest for vacuum-processable organic functional materials that are still of major interest when it comes to commercial large-scale applications.^[161] PBIs show outstanding photostability^[162] and chemical customizability, which allows for the tailoring of desired material properties.^[163] Thus, they found application in many parts of OSCs besides NFAs, such as interlayer dopants,^[164] cathode interlayers,^[165] and acceptor polymers.^[166] Even if the focus on current NFA research has moved towards solution-processable A-D-A structural motifs such as **ITIC**^[167-168] or **Y6**,^[169] PBIs still hold significant importance in this field.^[128, 170] Today's PBI-based NFAs are typically designed as twisted or star-shaped arrangements of multiple PBIs attached to each other by single or annulated bonding in *bay*, *ortho*, or imide position.^[130, 158, 171-174] This twisted geometry prevents strong aggregation of the planar PBI chromophores, enables good solubility, and allows the formation of an amorphous, three-dimensional packing arrangement.^[175-176] However, good solubility as well as twisted geometry, can also be achieved by twisting the PBI chromophore itself. This can be realized by the sterical congestion of four aryl *bay*-substituents directly attached to the PBI π -core resulting in a twist of the naphthalene subplanes against each other.^[177] As a result, the LUMO levels are lowered, a bathochromic shift of the absorption maximum is induced and the solubility is highly increased.^[22] This is of particular interest for solution-processed organic solar cells (OSCs) as the solubilizing alkyl chains can be omitted, which do not contribute affirmatively to charge transport properties anyway. The highly twisted

geometry itself and the steric demand of the four aryl substituents are effective tools to prevent the formation of large crystalline domains within the bulk-heterojunction (BHJ).^[67, 178] This was exploited by Sun and co-workers, who reached appreciable high efficiencies of up to 4.1% in a BHJ OSC using a *bay*-tetraphenyl PBI with cyclohexyl residues in imide position (**1d**, Figure 22a) combined with donor polymer **PCE-10**.^[21] The surprisingly simple synthesis to accomplish the fourfold arylation in the crowded PBI *bay*-area was pioneered in 2006 by Zhu and co-workers^[20] followed by the Hoffmann group in 2010^[65] who exploited different Suzuki cross-coupling routes. Applying this coupling chemistry, we recently synthesized a series of tetraarylated PBIs (Figure 22a) with aryl substituents ranging from phenyl and para-trifluoromethyl phenyl over 1- and 2-naphthyl up to 1-pyrenyl for, which for the first time we obtained the structural proof on its chirally twisted geometry via single-crystal structure analyses.^[22]

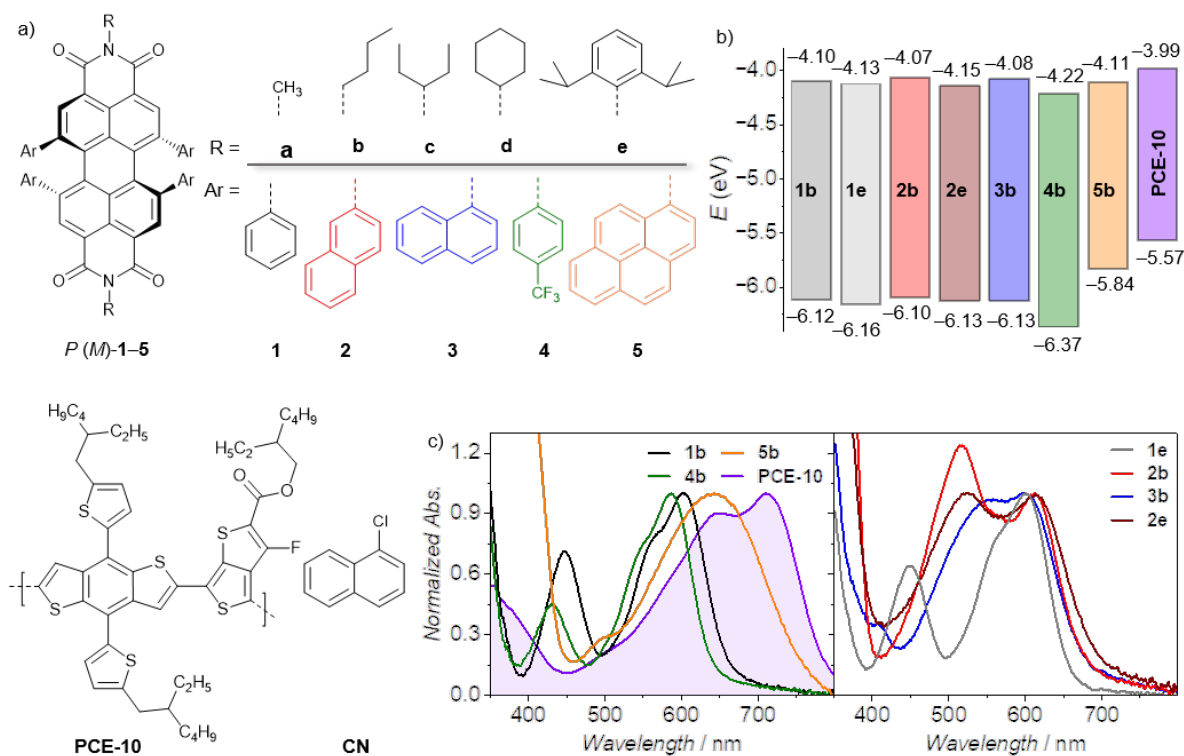


Figure 22. (a) Chemical structures of the *P*-atropo-enantiomer of PBI NFAs **1-5** (top) as well as donor polymer **PCE-10** and solvent additive 1-chloronaphthalene (CN) (bottom). (b) Schematic diagram of HOMO and LUMO energy levels of PBI NFAs^[22] as well as **PCE-10**.^[179] Literature reported **PCE-10** energy levels have been adjusted with respect to Fc/Fc^+ of 5.15 eV. (c) Normalized UV-vis-NIR absorption spectra of PBIs as well as **PCE-10** neat films on quartz spin-casted from a chloroform solution (10 mg mL^{-1}).

Based on early predictions on the formation of highly stable atropo-enantiomers for such tetraphenyl PBIs,^[60] first experimental investigation of tetraarylated PBIs chirality was done in 2014^[66] but did not find a way into a solid-state application so far unlike the closely related

ortho- π -extended PBI double-[7]heterohelicenes utilizing the chiral core twist for a circular polarized light detection device.^[64] Even if Sun and co-workers utilized the twisted geometry to design well-soluble and potent NFAs,^[21, 67] the impact of enantiopurity as well as the imide substituents remained so far unexplored. Indeed, there is only little investigation on morphological effects that are expected to significantly alter thin-film device performances while using either enantiopure species or their racemic mixtures. Within the few reported examples, no clear trends are yet provided by corresponding OSC and organic thin-film transistor (OTFT) devices. The impact of enantiopurity ranges from zero up to an increase in orders of magnitudes of the respective figures of merit.^[180-181] Among the important family of branched alkyl chains used in organic electronics,^[182] probably the one of the most investigated chiral residues is the branched 2-ethylhexyl chain. It is used in OSC donor polymers^[180] or diketopyrrolopyrroles (DPPs) for OSCs^[183] as well as OTFTs^[184] and single-crystal field-effect transistors (SCFETs).^[185] Smaller and more rigid chiral residues such as 2-methylbenzyl introduced on one or two sides of naphthalene diimides (NDIs) have also recently been investigated in thin-film devices.^[124, 186] Interestingly, even if key parameters such as charge carrier mobility or π - π stacking are assessed independently, the interpretation of their interplay within a final device is not always straightforward.^[124] Also, the proportion of the chiral moieties on molecular size is not solely decisive, as demonstrated by Itoh and co-workers by investigating a C₆₀ fullerene derivative with a small chiral methyl unit that changed the OSC performance significantly by a factor of two using either enantiopure species or their diastereomeric mixtures.^[187] Besides this point-chirality mediated by side chains, the π -scaffold can show inherent chirality itself. Thus, the investigation of packing effects upon enantiopurity is of major interest within the growing field of contorted polycyclic aromatic hydrocarbons (PAHs) for organic electronics and spintronics.^[5] Investigating carbon helicenes, the groups of Crassous^[188] and Fuchter^[189] thoroughly investigated their materials as NFAs in OSCs or as p-type semiconductors in OTFTs, respectively. Whereas the enantiopure NFA showed superior morphology, it was the racemic mixture of the 1-aza[6]helicenes enabling a favorable charge transport pathway in the OTFT devices. The chirality-functional-property relationship was also recently investigated within a phototransistor based on a polymer blend of chiral PBIs. Superior performance was again recorded for devices of the racemic mixture.^[190] However, similar investigations on twisted nanoribbons,^[191] chiral peropyrenes^[68] or perylene dyes^[192] are not yet reported.

Herein, we study the impact of both the aryl as well as imide substituents within two series of the recently reported twisted PBIs^[22] as NFAs (Figure 22a) in simple solution-processed OSCs.

Device efficiencies are correlated with molecular packing deduced from single-crystal X-ray structure analysis. Following our systematic study, we finally designed the new NFA **2e**, reaching highest efficiencies of up to 4.3% PCE_{max} in a simple inverted BHJ architecture. As these materials show inherent axial chirality, atropo-enantiomers of **1b** and **1e** could be successfully separated to investigate the impact of enantiopurity on device efficiency and its dependency on solvent additive 1-chloronaphthalene (CN). Single crystal X-ray analyses of enantiopure crystals then revealed major differences imparted by the flexibility of imide substituents and their ability to form supramolecular assemblies in the solid state guided by the sterical congestion of *bay*-substituents. This favorable interplay led to the formation of the hitherto highest PBI twist-angle of 38.3° of enantiopure **1b**. Circular dichroism (CD) spectroscopy not only proved the resemblance of chromophore packing in amorphous thin films with the single crystal structures but also identified a unique enhancement in the Cotton effect of this X-cross chromophoric dimer arrangement of enantiopure PBIs, which is further supported by TD-DFT calculations.

3.2 Twisted PBIs Designed as Non-fullerene Acceptors

To obtain comparable insights into their NFA applicability, all tetraarylated PBIs were initially tested using the donor polymer **PCE-10**^[179] in an inverted BHJ device architecture of ITO/ZnO/PBI:**PCE-10**/MoO₃/Al (Figure 23a). OSCs were fabricated and characterized under inert conditions and AM1.5 G irradiation. The optimized^[193] active layer blend consists of a 1:1 weight ratio of donor and acceptor material and was spin-cast from a 15 mg mL⁻¹ chlorobenzene (CB) solution. The NFAs were screened along two series varying either imide or *bay*-aryl-residues using 2% of CN as a solvent additive (Figure 23, Table 3 and Figure A2). Within the series of **1a–1e**, phenyl as the smallest aryl moiety was kept constant in *bay*-position and the imide substituents were varied.^[193] **1b** bearing flexible *n*-butyl chains reached a moderate maximum power conversion efficiency (PCE_{max}) of 3.31%.^[193] The overall high open circuit voltage (V_{oc}) of 0.84 – 0.88 V for these dyes indicated a low energy loss at around 0.6 V confirming **PCE-10** as the matching donor part. The obtained fill factors (FF) of about 40% are typical for single-core PBIs but lack behind some other oligomeric PBI-based NFAs that reach up to 80% due to the presence of enlarged π -surfaces with better intermolecular contacts. Accordingly, for these oligomers three-dimensional chromophore arrangement is achieved without sacrificing close edge-to-edge or edge-to-face PBI interactions to guarantee balanced

charge carrier mobilities within the BHJ.^[128, 158, 194] The obtained moderate short-circuit current densities (J_{SC}) of 9–11 mA cm² indicated a considerable PBI contribution to the generated overall photocurrent as corroborated by UV–vis–NIR^[193] and external quantum efficiency (EQE)^[193] measurements showing a complementary donor–acceptor absorbance over most of the visible range (Figure 22c, Figure 23c and Figure A2 see the appendix).

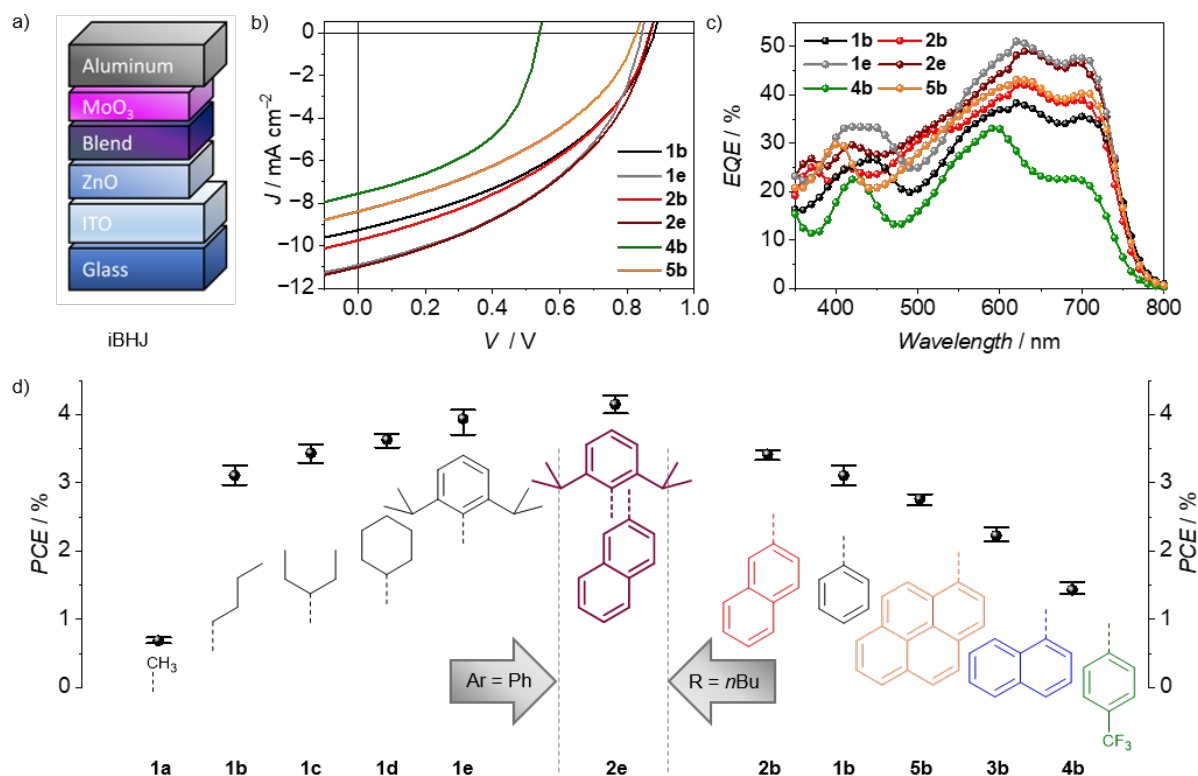


Figure 23. (a) Schematic device architecture of solution-processed inverted BHJ solar cells in ITO/ZnO/PBI:PCE-10/MoO₃/Al configuration. (b) J – V characteristics of a selection of the best PCE-10-based devices using racemic mixtures of PBIs as NFAs. The total blend concentration was 15 mg mL⁻¹ (16 mg mL⁻¹ for **2e**) in chlorobenzene (CB) with 1:1 donor/acceptor weight ratio for all devices (1.0:1.1 for **2e**). 2% of 1-chloronaphthalene (CN) was used as a solvent additive. (c) EQE spectra of the corresponding best devices displayed in (b). (d) OSC efficiencies of racemic PBIs used as NFAs along screening of imide (left: **1a–1e**) and aryl substituents (right: **1b–5b**) under optimized conditions of at least five independent devices. Error bars represent mean deviation. The solar cells were fabricated and characterized under inert conditions and AM1.5 G irradiation.^[193]

A proper film formation was observed by atomic force microscope (AFM), revealing a very smooth and homogeneous surface with a root-mean-squared roughness (R_q) of less than 1 nm that holds true for all of the properly working devices of **1b–1e** (Figure A4 in the appendix). In contrast, the low solubility of methyl functionalized **1a** hampers the formation of a homogeneous active layer due to strong phase separation (Figure A4 appendix), leading to a drop in all J – V characteristics and thus a low PCE_{max} of only 0.73%. By increasing the size and stiffness of the imide substituents from 3-pentyl (**1c**) to cyclohexyl (**1d**), the device performance

increases gradually from 3.53% to 3.72% and reaches even 4.07% PCE_{\max} for the 2,6-diisopropylphenyl (Dipp) substituted **1e**.^[193] The shielding of the PBI core by size and rigidity of the aryl as well as imide substitutes is in line with the NFA performance within this series.

Table 3. Photovoltaic parameters of J - V characteristics of solution-processed inverted BHJ OSC using a blend of the respective racemic mixture of tetraarylated PBIs **1a–e**, **2b–5b** as well as **2e** in combination with donor polymer **PCE-10** under optimized conditions. The blend consisted of a 1:1 (1.0:1.1 for **2e**) weight ratio using 2% of 1-chloronaphthalene (CN) as solvent additive. The cells in ITO/ZnO/PBI:PCE-10/MoO₃/Al configuration were fabricated and characterized under inert conditions and AM1.5 G irradiation.

NFA (<i>rac.</i>)	R, Ar	V_{oc} /V	J_{sc} / mA cm ⁻²	FF / %	PCE / %	PCE_{\max} / %
1a	Me, Ph	0.60 ± 0.01	-3.30 ± 0.11	35 ± 1	0.69 ± 0.02	0.73
1b	nBu, Ph	0.84 ± 0.01	-8.50 ± 0.24	44 ± 1	3.12 ± 0.11	3.31
1c	3-Pent, Ph	0.84 ± 0.01	-9.66 ± 0.24	42 ± 1	3.40 ± 0.08	3.53
1d	Cy, Ph	0.88 ± 0.01	-9.93 ± 0.14	42 ± 1	3.63 ± 0.06	3.72
1e	Dipp, Ph	0.84 ± 0.01	-10.77 ± 0.32	44 ± 1	3.94 ± 0.10	4.07
2b	nBu, 2-Naph	0.88 ± 0.01	-9.60 ± 0.21	41 ± 1	3.45 ± 0.03	3.48
3b	nBu, 1-Naph	0.76 ± 0.01	-7.42 ± 0.27	40 ± 1	2.23 ± 0.08	2.35
4b	nBu, PhCF ₃	0.60 ± 0.01	-5.49 ± 0.14	44 ± 1	1.43 ± 0.04	1.55
5b	nBu, 1-Pyr	0.80 ± 0.01	-8.77 ± 0.12	40 ± 1	2.76 ± 0.05	2.83
2e	Dipp, 2-Naph	0.84 ± 0.01	-11.17 ± 0.36	45 ± 1	4.15 ± 0.09	4.28

^a Average of at least five up to ten independent devices.

We like to note that Sun and co-workers accomplished a higher PCE_{\max} of 4.1% for **1d** and the same donor polymer **PCE-10** after optimization.^[21] Due to the variation of aryl substituents, both steric and electronic factors are affected within the second series. Thus, *n*-butyl as the most flexible imide substituent was kept constant within the series **1b–5b**, while the four aryl substituents were varied. Upon attaching electron-withdrawing *para*-trifluoromethyl units to the phenyl residues of **4b**, the device efficiency PCE_{\max} decreased significantly from 3.31% (**1b**) to 1.55%. The pronounced drop in V_{oc} to only 0.60 V is in line with its LUMO level lowered by 0.1 eV (Figure 22b).^[22] The concomitant loss in J_{sc} down to 5.49 mA cm² can be attributed to a significantly reduced donor contribution to the extracted photocurrent at 700 nm as the EQE^[193] (Figure 23c and Figure A2c in the appendix) reveals. However, as also the BHJ surface roughness is drastically increased ($R_q = 13.3$ nm,^[193] Figure A4 in the appendix), it is probable to consider both electronic and morphological factors for the low performance. Enlarging the phenyl substituent to its next homologue, the PBI isomers bearing 1-naphthyl (**3b**) or 2-naphthyl (**2b**) residues are obtained. Even if both NFAs show the same LUMO levels and exhibit comparable homogeneous thin films, the more laterally extended **2b** is highly superior in all OPV characteristics. Most prominent is the loss in V_{oc} from 0.88 V to 0.76 V for **3b**. Accordingly, while **2b** reaches a PCE_{\max} of 3.48%, for **3b** only 2.35% is achieved.^[193] Our

recent studies on conformational isomers in solution revealed low rotation barriers in **3b** for its 1-naphthyl residues and the presence of up to 14 stereoisomers in solution, while for **2b** this number is reduced to four, due to the intimate π -stacking of the 2-naphthyl substituents.^[22] Presumably, the multitude of present species of **3b** also in its amorphous spin-cast thin film will lead to a broadening of the density of states and hampers a uniform chromophore arrangement as well as a defined interface with the donor polymer. Appending 1-pyrenyl instead of 1-naphthyl, **5b** shows again slightly elevated PCE_{max} of up to 2.83% due to an increased V_{OC} of 0.80 V and higher PBI contribution to the photocurrent revealed by EQE (Figure 23c and Figure A2 in the appendix). This can be correlated with the broadened **5b** absorption due to the charge transfer (CT) character between electron-rich pyrene and electron-poor PBI within **5b**. The electron-donating character of the pyrene *bay*-substituents results in a localization of HOMO and LUMO on the pyrene units and PBI core, respectively.^[22] Combining the information from both the imide (**1a–1e**) as well as the aryl (**1b–5b**) substituent variation, we successfully designed a new derivative **2e** (for details see the appendix) consisting of the aryl (2-naphthyl) and imide groups (Dipp) that gave the highest PCEs within each respective series. By this systematic approach, we were able to enhance the J_{SC} as well as FF of the simple bulk-heterojunction solar cells further (Figure 23b, Table 3 and Figure 23, appendix). The optimized blend ratio of 1.0:1.1 resulted in the highest J_{SC} of 11.2 mA cm² with EQE of up to 49% at 640 nm (Figure 23c). An appreciable high FF of 45% was obtained to finally result in a PCE_{max} of up to 4.28%.^[193] This should result from the fusion of the discussed attributes such as its high degree of chromophore shielding while maintaining the conformational stability guided by the π -stacked 2-naphthyl units^[22] overall resulting in a homogeneous film forming of the **PCE-10** blend. To the best of our knowledge, this is the highest reported PCE value of a single-core PBI-based NFA without an extension of the π -system or embedding of heteroatoms.

3.3 Molecular Packing

To shed light on the influence of the chromophore arrangement by the variation of the imide and aryl substituents on device performance, a comprehensive analysis on the most relevant single-crystal structures from racemic mixtures of **1b**,^[193] **2b**,^[22] **1e**, and **2e** was performed. Single crystals of suitable size and quality could be obtained by slow-evaporation method out of either chloroform (**1b**) or chlorobenzene (**1e**, **2b**, **2e**) solution under optimized conditions

using methanol or *n*-hexane as co-solvent, respectively. They reveal an anisotropic arrangement of alternating *P*- and *M*-atropo-enantiomers within their respective unit cells (Figure 24).

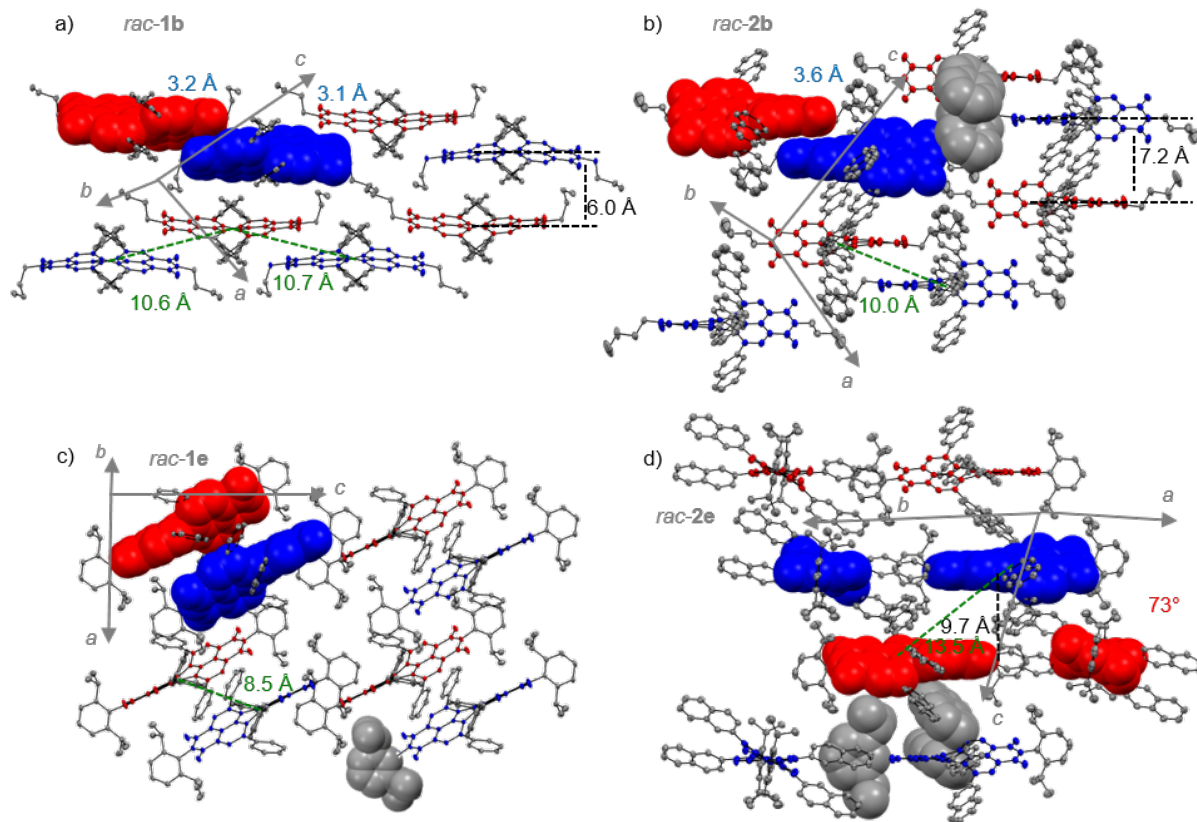


Figure 24. Molecular packing of PBIs *rac-1b*^[193] (a), *rac-2b*^[22] (b), *rac-1e* (c), and *rac-2e* (d) in their respective single crystal structures. PBI atropo-enantiomers are colored in blue (*P*) and red (*M*). The ellipsoids are set to 50% probability (C: gray). Disorder of the imide residues, hydrogen atoms as well as solvent molecules are omitted for clarity. Distances of closest π - π interactions (blue), the distance between the planes of adjacent chromophores (black) as well as twist angle between two chromophores (red), and distances between the centroids of the perylene cores (green) are indicated as well.

At this point, it should be noted that the activation barriers for the conversion between *P*- and *M*-atropo-enantiomers are rather high ($\Delta G^\ddagger \approx 120 \text{ kJ mol}^{-1}$).^[22] Accordingly, *P*- and *M*-atropo-enantiomers will not interconvert under our procession conditions. All crystal structures depicted here contain solvent molecules as well as the small disorder of the *n*-butyl chains, which is not depicted for clarity. Within this series, the flexible *n*-butyl residues of *rac-1b* allow the closest chromophore interactions between the PBI headland region, leading to a unique slip-stacked packing arrangement of alternating *P*- and *M*-atropo-enantiomers forming two isolated double strands within the unit cell of the $P\bar{1}$ space group (Figure A6, appendix). Even as the π - π distances between two stacked imide units of adjacent chromophores within one double strand can come as close as 3.1 Å, a large lateral displacement up to 10.7 Å (center-to-center distance) is introduced by the sterical congestion of the *bay*-substituents preventing the

chromophores from efficient excitonic Coulomb coupling (140 cm^{-1} and 156 cm^{-1}) along the double strand (see the Table A2, appendix).^[85, 193] As already mentioned, the sterical congestion of the aryl substituents leads to stable axial chirality due to the core twist of the PBI. Considering the PBI naphthalene subunits as individual planes, twist angles of about 32° are measured between them for *rac*-**1b**. This is within the range of our previously reported twisted PBIs (**1d**, **2b**)^[22] that is still below 37° as reported for the most contorted *bay*-tetrabromo PBIs due to the high van-der-Waals radii of its halogen *bay*-substituents.^[177] In contrast to the spherical heavy atoms, two adjacent aryl moieties align to each other mostly co-parallel. Their intramolecular π - π distance can be given by the distance between the respective centroids that is similar for all derivatives and ranges between 3.2–3.5 Å. The *rac*-**2b** single crystal structure was reported previously by us.^[22] By increasing the PBI lateral extension going from phenyl (*rac*-**1b**) to 2-naphthyl (*rac*-**2b**), the crystal symmetry and the packing motif of alternating *P*- and *M*-atropo-enantiomers are preserved but now the enlarged aryl substituents incur the guiding of chromophore arrangement and confine the number of interacting chromophores down to a number of two (Figure 24b). The closest π - π distance within the slip-stacked dimer arrangement is increased by 0.5 Å up to 3.6 Å, but the chromophore centers come slightly closer down to 10.0 Å. Apart from this entity further adjacent chromophores stay more distant compared to the chromophores in *rac*-**1b** crystal. Thus, the distance between planes of *P*- and *M*-atropo-enantiomers of the same unit cell is increased from 6.0 Å to 7.2 Å and the side-on neighbours of the same helicity in the *b*-axis direction are moved away from 12.6 Å to 14.5 Å. In summary, the strain imparted by the *n*-butyl-promoted slip-stacked arrangement combined with the steric demand of the 2-naphthyl units directly contacting the chromophore leads to this considerably higher core twist of up to 36.6° . It is noteworthy that our previous work on these twisted PBIs revealed a multitude of conformational isomers of **3b** in solution due to various possibilities for the arrangement of the aryl residues during the reaction that are similar in energy. This conformational variability was not as pronounced for **2b**, which might explain to the tremendous OSC performance differences for these two constitutional isomers (*vide supra*). By changing the imide substituent from flexible *n*-butyl to the stiff and bulky Dipp moieties, the isolation of the chromophore cores within the crystal lattice significantly increases. The single crystal structure of *rac*-**1e** (Figure 24c) reveals that intimate π - π stacking between adjacent chromophores is no longer possible and that the center-to-center distance is increased to 8.5 Å due to the steric demand of the Dipp residues. In contrast to the close arrangement promoted by the flexible *n*-butyl chain, the strain on the isolated PBI core of *rac*-**1e** is reduced, yielding a twist angle of 32.2° . The maximum in chromophore isolation was obtained for *rac*-**2e**

(Figure 24d). In contrast to the previous structures, **2e** has two pairs of enantiomers instead of one that are embedded within its unit cell of the $P21/c$ space group. The distance between adjacent P - and M -atropo-enantiomers in a slip-stack arrangement is large, revealing center-to-center distances of 13.5 Å or 9.7 Å between the planes of the respective chromophores. The two molecules at the exterior of the unit cell are rotated by 73° towards the inner pair of enantiomers that are evenly distant by 16.8 Å. It becomes apparent that the steric demand of the Dipp residue of the outmost molecules promotes the side-on orientation of two chromophores of the same helicity, whereas its 2-naphthyl units guide the distance within its heterochiral arrangement of the elementary cell. No chromophore interactions for *rac*-**2e** are possible, which further reduces the strain on its π -scaffold, leading to the smallest twist angle of only 30.9° within this series. While for each racemate, both P - and M -atropo-enantiomers are alternately arranged within the respective unit cell, only the flexible *n*-butyl chains of **1b** and **2b** allow for some minor face-to-face π -interactions between them but only at the expense of a substantial longitudinal displacement and accordingly large center-to-center distance.

3.4 Impact of Enantiopurity on Organic Solar Cell Performance

As the steric demand of both substituents highly affects the molecular packing of alternating P - and M -atropo-enantiomers in the solid state of the racemate, we expected a pronounced difference in the packing structure for enantiopure compounds. For the *bay*-phenyl derivatives **1b** (*n*-butyl) and **1e** (Dipp), the P - and M -atropo-enantiomers could be fully separated in sufficient quantity as well as purity using a semipreparative HPLC device equipped with a chiral stationary phase, showing perfect mirror images of the respective CD spectra (vide infra and see Figure A7, appendix).^[193] In contrast, a sufficient separation of the most potent NFA **2e** was not possible as a consequence of the effective shielding of the twisted core structure by the large 2-naphthyl and Dipp substituents that prevent sufficient chiral interactions with the stationary phase. OSCs of racemic mixtures as well as isolated P - and M -atropo-enantiomers of **1b** and **1e** (Figure 25a) as NFAs were fabricated either without solvent additive or with 2% of CN (Figure 25b, Table 4 and see Figure A3 in the appendix). The binary blends of *n*-butyl substituted **1b** show a significant increase in PCE by about 24% from 2.5% up to 3.1% upon the change from the racemic mixture to the enantiopure P - or M -atropo-enantiomers averaged over at least ten devices.^[193] The reduced efficiency of *rac*-**1b** based devices compared to enantiopure P -**1b** or M -**1b** (Figure 25b,c) solely derives from a reduced short-circuit current

density, while V_{OC} (0.84 V) and FF (40–41%) are almost unaffected. J_{SC} of the binary blend without additive decreases by more than 18% from up to 9.0 (*P/M*) down to 7.5 mA cm^{-2} (*rac*). The corresponding EQE shows its maximum of 40% at 620 nm and drops down to 34% upon the change from enantiopure to the racemic NFA, even while the overall thin film absorbance remains the same for all three active layers (Figure 25d).

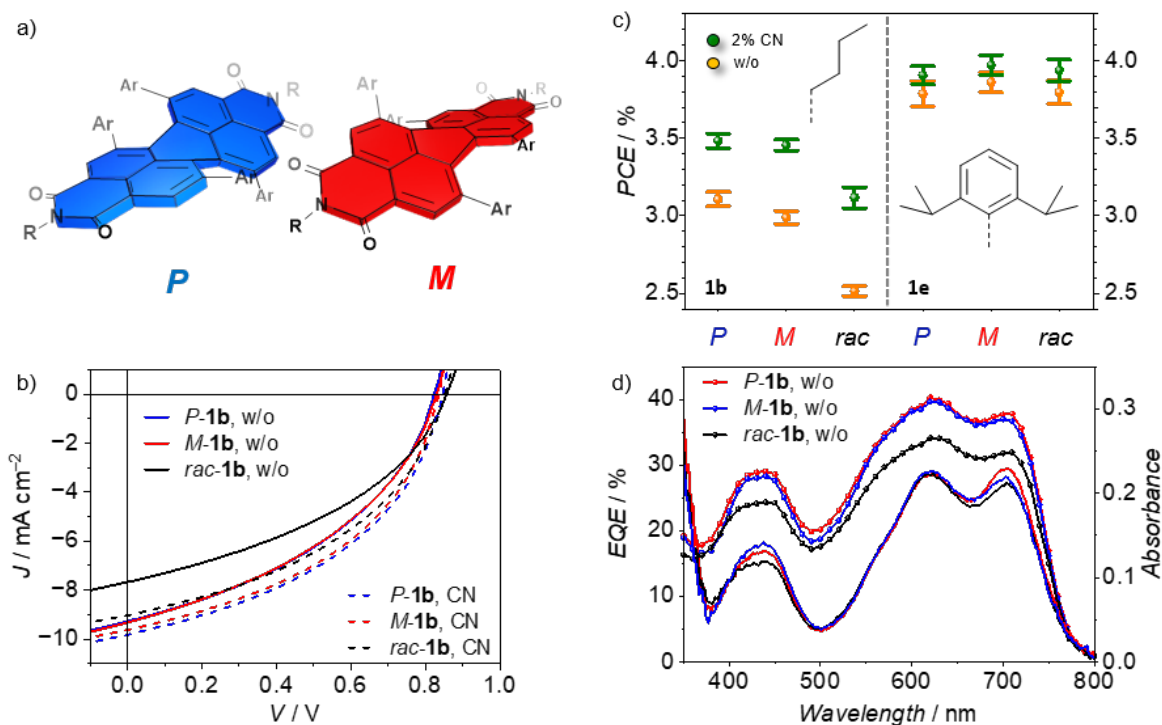


Figure 25. (a) Schematic illustration of *P*- (blue) and *M*- (red) atropo-enantiomers of chiral PBI **1**. (b) J - V characteristics of best OSC devices with inverted configuration of ITO/PCE-10:PBI/MoO₃/Al of **1b** without solvent additive (solid) and with 2% CN (dashed) as *P* (blue), *M* (red) or racemic (black) PBI species. The solar cells were fabricated and characterized under inert conditions and AM1.5 G irradiation. (c) Mean PCEs of **1b** (left) and **1e** (right) based OSCs with use of no solvent additive (orange spheres) or 2% CN (green spheres) of ten (**1b**) or five (**1e**) independent devices. Error bars represent mean deviation. (d) EQE (symbols) and UV-vis-NIR absorption (solid line) spectra of corresponding *P* (blue), *M* (red) or racemic (black) **1b**-based devices without solvent additive.^[193]

It is apparent that the extracted photocurrent of *rac*-**1b** is reduced equally within the entire spectral region and cannot be attributed to either the NFA region between 400–650 nm or the one of the donor polymer **PCE-10** with its maximum in absorbance at 700 nm. Thus, both ‘channel 1’ (hole) and ‘channel 2’ (electron) contribution to the photocurrent^[195] are affected by the different packing of the enantiopure and racemic chiral NFAs.^[193]

Space-charge limited current (SCLC) mobilities were evaluated according to literature known procedure^[196] and revealed an overall predominance in hole mobility over electron mobility by two orders of magnitude.^[193]

Table 4. Photovoltaic parameters of J - V characteristics of solution-processed inverted BHJ OSCs using a blend of polymer **PCE-10** and the respective PBI species in 1:1 weight ratio with optional use of 1-chloronaphthalene (CN) as solvent additive. The cells in ITO/ZnO/PBI:**PCE-10**/MoO₃/Al configuration were fabricated and characterized under inert conditions and AM1.5 G irradiation.^[193]

NFA	CN / %	V_{oc} / V	J_{sc} / mA cm ⁻²	FF / %	PCE / %	PCE _{max} / %
<i>P-1b</i>	–	0.84 ± 0.01	-8.96 ± 0.25	41 ± 1	3.11 ± 0.08	3.25
<i>M-1b</i>	–	0.84 ± 0.01	-8.91 ± 0.17	40 ± 1	2.99 ± 0.06	3.15
<i>rac-1b</i>	–	0.84 ± 0.01	-7.50 ± 0.09	40 ± 1	2.52 ± 0.05	2.65
<i>P-1b</i>	2	0.84 ± 0.01	-9.52 ± 0.17	44 ± 1	3.48 ± 0.07	3.68
<i>M-1b</i>	2	0.84 ± 0.01	-9.51 ± 0.18	43 ± 1	3.45 ± 0.7	3.59
<i>rac-1b</i>	2	0.84 ± 0.01	-8.50 ± 0.24	44 ± 1	3.12 ± 0.11	3.31
<i>P-1e</i>	–	0.84 ± 0.01	-11.45 ± 0.31	39 ± 1	3.79 ± 0.08	3.88
<i>M-1e</i>	–	0.84 ± 0.01	-11.35 ± 0.27	41 ± 1	3.86 ± 0.09	4.02
<i>rac-1e</i>	–	0.84 ± 0.01	-10.66 ± 0.31	43 ± 1	3.82 ± 0.10	4.05
<i>P-1e</i>	2	0.84 ± 0.01	-11.07 ± 0.25	42 ± 1	3.91 ± 0.09	4.02
<i>M-1e</i>	2	0.84 ± 0.01	-11.35 ± 0.24	42 ± 1	3.97 ± 0.08	4.09
<i>rac-1e</i>	2	0.84 ± 0.01	-10.77 ± 0.32	44 ± 1	3.94 ± 0.10	4.07

^a Average of at least ten (1b) or five (1e) independent devices.

Hole mobilities of 1.5 and $1.4 \times 10^{-3} \text{ cm}^2 \text{ V}^{-1} \text{ s}^{-1}$ were found for *P*- and *M-1b*, slightly higher than the $1.1 \times 10^{-3} \text{ cm}^2 \text{ V}^{-1} \text{ s}^{-1}$ for the corresponding *rac-1b* based device in ITO/PEDOT:PSS/**PCE-10:1b**/MoO₃/Al architecture (Figure A8 and Table A3, appendix).^[193] Interestingly, the electron mobility measured in a configuration of ITO/ZnO/**PCE-10:1b**/BCP/Al revealed elevated values of $13.9 \times 10^{-6} \text{ cm}^2 \text{ V}^{-1} \text{ s}^{-1}$ for the *rac-1b* based device compared to slightly lower mobilities of 9.4 and $9.7 \times 10^{-6} \text{ cm}^2 \text{ V}^{-1} \text{ s}^{-1}$ for the devices of the respective *P*- and *M*-atropo-enantiomers. This might show an improved forming of crystalline domains of the donor polymer in the presence of enantiopure *P/M-1b* PBIs whereas the elevated electron mobility of *rac-1b* is indicative of a more effective LUMO overlap of the chromophores in their racemic mixture, even if the SCLC differences cannot solely explain the significant differences in overall PCE. By applying 2% of the solvent additive CN on the **1b** based blends, device efficiencies show an overall increase up to 3.5% (*P*, *M*) or 3.1% (*rac*) in PCE, respectively. Thus, the relative difference between enantiopure and racemic material shrinks down to about 11%, but is still clearly discriminable. This indicates a partial reduction in the impact of enantiopurity in a molecular arrangement by the solvent additive. The overall rise in PCE observed in our studies for **1b**-based devices by CN solvent additive originates from an equal increase of J_{sc} and FF. This result slightly differs from observations reported for **1d**-based OSCs by Sun and co-workers^[21] who solely recorded an increase in FF. They attributed this improvement to the prolonged dwell time of the material in solution due to the higher boiling point of the CN with respect to the solvent. However, AFM analysis did not reveal significant changes in the overall smooth and homogeneous active layers, which matches

with our results for all blends of *P/M/rac-1b* with an R_q between 0.5–0.7 nm (Figure A4 and Figure A5, appendix). In contrast to **1b**, the Dipp-shielded **1e**-based OSCs do not show a PCE dependency on enantiopurity and likewise the impact of CN solvent additive is rather modest (Figure 25, Table 4). Overall higher PCE values of about 3.8–3.9% are recorded for the binary blends of *P/M/rac-1e* that only slightly increase to 3.9–4.0% when applying 2% of CN due to a subtle increase of FF by 1–3% to a maximum of 44%. Thus, for both, **1b** and **1e**, the additive promotes the device efficiency but with significantly less effect on **1e** regardless of its enantiopurity. It is reasonable to suggest the CN guiding the PBI arrangement for **1b** as it only shows little impact on the more shielded and isolated PBIs of **1e**. Thus, it can be followed that the CN additive promotes the donor/ acceptor interface or blend miscibility rather than improving the molecular order of the NFAs within their domains.

3.5 Chiral Packing in Single Crystals and Thin Films

The variation in PCE of OSCs of racemic and enantiopure NFA **1b** is solely attributed to changes in J_{sc} (Figure 25, Table 4), which cannot be easily explained by differences in thin-film UV–vis–NIR absorption or film morphology as these do not show significant alterations. To approach these morphological disparities in the sub-nanometer scale on the molecular level, we took the efforts to obtain the single-crystal structures of enantiopure *P-1b*^[193] and *M-1e*, revealing tremendous differences in molecular arrangement. The single crystal structures were obtained by slow evaporation method, likewise the racemates, from a chloroform or chlorobenzene solution, respectively, using methanol as a co-solvent. Similar to its racemic mixture, the flexible *n*-butyl chain of *P-2b* enables face-to-face π -stacking but now guides towards a unique twisted π -stacked dimer formation (Figure 26a). The chromophores in this X-cross arrangement^[197] are stacked perfectly on top of each other showing a relative twist angle of 73° with respect to the N,N' -axes with a close center-to-center distance of about 4.9 Å. Most interestingly, the two π -stacked phenyl substituents of each chromophore additionally stack on top of the neighboring naphthalene plane of the PBI within the dimer, therefore locking the molecular arrangement in a distinct conformation. Both molecules are distinguishable by a different torsional twist imparted by the sterical congestion of the phenyl substituents. Whereas the bottom PBI shows a twist angle of 34.2°, the topmost chromophore is twisted by 38.4°, supported by the helical stacking of its adjacent phenyl residues with the underlying naphthalene subunit of the bottom molecule.

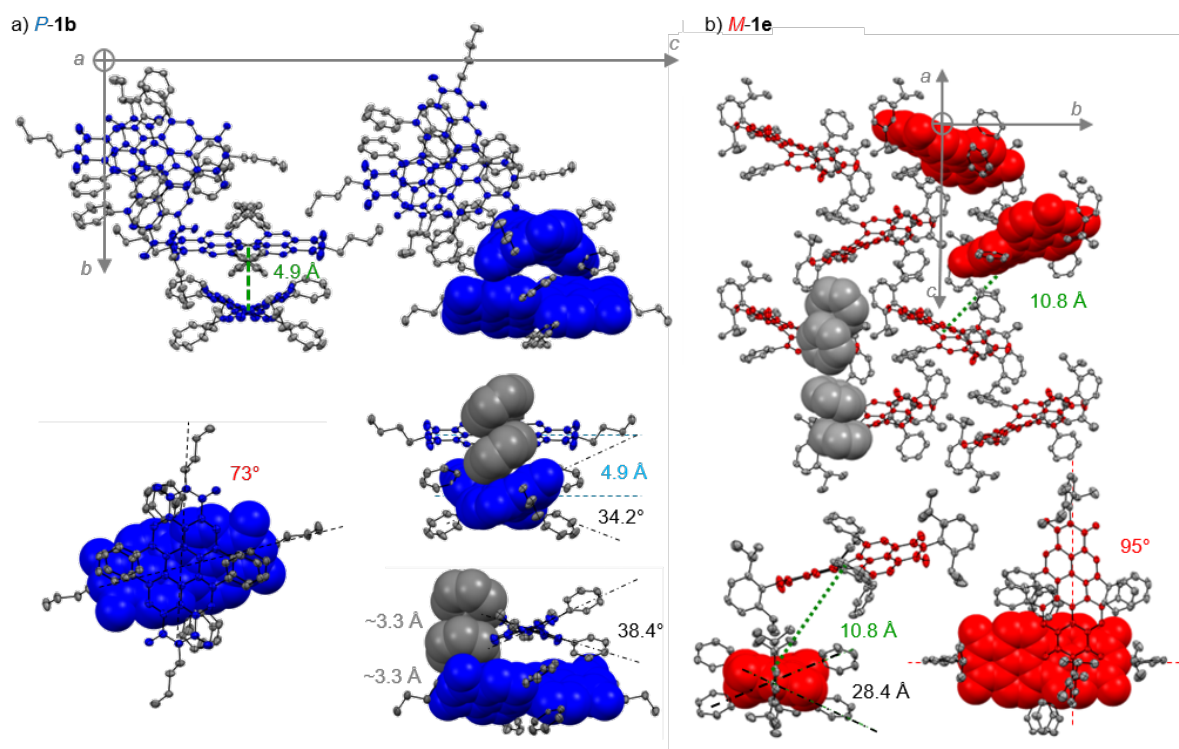


Figure 26. Molecular packing of PBIs *P-1b* (a) and *M-1e* (b) within their respective single crystal structures (top), top view onto dimeric chromophore arrangements and side view (bottom) as well as rotated side view (*P-1b*). PBI atropo-enantiomers are colored in blue (*P*) and red (*M*). Distances between centroids of adjacent perylene cores (green), distances between planes of adjacent chromophores (light blue) and closest π - π distances between centroids (gray) are indicated as well as twist angles of single chromophores (black) and twist angles between adjacent chromophores (red). The ellipsoids are set to 50% probability (C: gray). Disorder of the imide residues, hydrogen atoms as well as solvent molecules are omitted for clarity.

Within this three-part helix, short π - π contacts of 3.3 Å (between centroids) are determined. Thus, this supramolecular arrangement of *P-1b* guides its chromophore into the most twisted configuration of a PBI π -scaffold reported so far in the literature. This unique spherical dimeric entity arranges as isolated units in the large unit cell of the $P6_522$ space group consisting of twelve chromophores, six times larger than the close and unidirected packing in the racemic crystal of **1b**. The enantiopure species is assumed to allow for more isotropic growth, which might contribute to the superior OSC performance of enantiopure **1b** over its racemic species thereof. The comparison of single-crystal structures can also be correlated to the SCLC mobilities showing increased electron mobilities for the racemic **1b** with both a more intimate face-to-face π -stacking as well as a closer molecular network within its double strand compared to enantiopure *P/M-1b* (vide supra or see the Figure A6 in the appendix). Similar to the single crystal structure of the racemate of **1e** (Figure 24c), the Dipp-substituted enantiopure *M-1e* reveals isolated chromophores with relatively low twist angles of the chiral chromophores of only 28.4° within its single crystal (Figure 26b). The closest neighbor within its unit cell of the $P21$ space group resembles the dimeric arrangement of *P-1b* with a twist angle of 95° but with

the lack of any face-to-face π -stacking as the center-to-center distance of 10.8 Å reaches more than twice the value of *P-1b*. This is also significantly higher than the center-to-center distance of 8.5 Å found in the corresponding racemic crystal of **1e**. The long molecular axis of the chromophores are tilted by 25.2° towards each other and show a long-ranged edge-to-face orientation. Thus, no face-to-face π -stacking is present, and the PBIs of enantiopure *M-1e* can be considered as isolated chromophores contrasting the closed dimeric species of enantiopure **1b**. Accordingly, as no close chromophore–chromophore contacts are present, no significant difference in PCE is observable for *rac-1e* (4.0%) in comparison to *P/M-1e* (3.9%, vide supra, Figure 25, Table 4). To assess the resemblance of molecular arrangement in both, single crystal structures and amorphous thin films, the chiroptical properties of the neat thin films as well as BHJ with **PCE-10** were investigated and compared with corresponding spectra in solution with equal optical density (Figure 27 and Figure A7 in the appendix). Tetraarylated PBIs show overall broad and structureless absorption spectra in dichloromethane (DCM) solution.

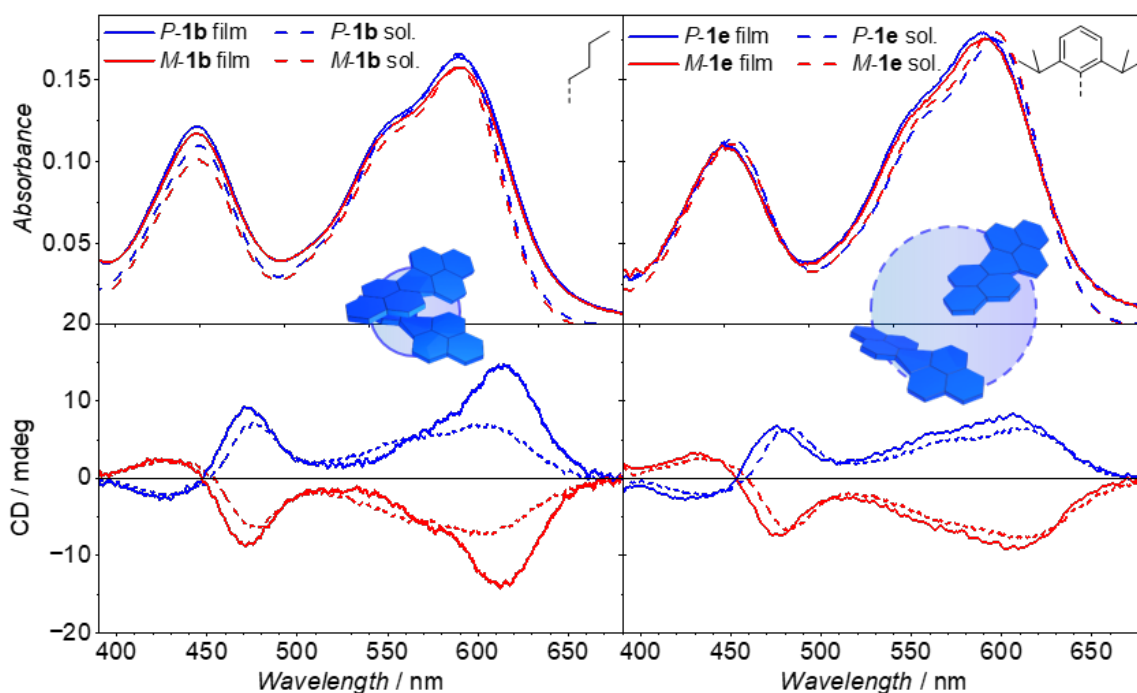


Figure 27. UV–vis–NIR absorption (top) and CD (bottom) spectra of *P*- (blue) and *M*- (red) atropo-enantiomers of **1b**^[193] (left) and **1e** (right) in thin film (solid lines) and DCM solutions (dashed lines) at room temperature. Neat films were spin-cast from CHCl₃ solution (10 mg mL⁻¹) onto quartz substrates. The schematic insets represent the dimeric chromophore arrangement of enantiopure *P-1b* and *P-1e* species found in the respective single-crystal structures.

Both spectral shape and position is mainly preserved also in the amorphous thin films of **1b** as well as of **1e** (Figure 27, top) with no significant difference to the respective solution spectra. Absorption maxima of **1b** are located at 603 and 420 nm for the S₀–S₁ and S₀–S₂ transition,

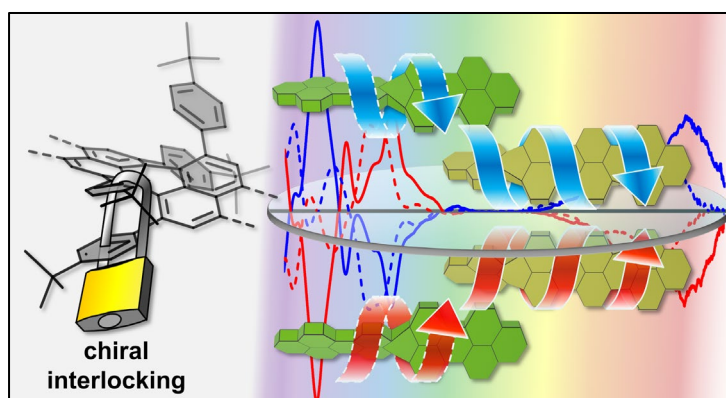
respectively. For **1e**, the main bands in the thin-film spectra are slightly blue-shifted by 7 nm from 610 to 603 nm, whereas the S_0 – S_2 maxima of both solution and thin film are located at 454 nm. Only the thin-film spectra of **1b** show a slightly increased S_0 – S_2 band compared to the main transition, indicative of molecular interactions (vide infra). Despite of these overall resembling UV/Vis absorption properties, the CD thin-film spectra of *P/M*-**1b** show a unique behavior contrasting all other remaining CD spectra in DCM solution (**1b**, **1e**) as well as the thin film of **1e**. Thus, the CD amplitude of the *P/M*-**1b** thin-film S_0 – S_1 transition is increased by a factor of two at 614 nm, whereas the CD signal is of lower amplitude at about 540 nm (Figure 27, bottom).^[193] To our understanding, this can be attributed to the helically twisted and π -stacked dimer entity of enantiopure **1b** found in its single crystal structure, giving rise to an excitonic Cotton effect. In contrast, **1e** only shows isolated chromophores with no supramolecular interaction in solution and single crystal as well as thin-film and the respective active layer of the OSCs (Figure A7, in the appendix). To rule out artifacts by anisotropy,^[64, 198] AFM images were recorded to show a homogeneous surface without oriented crystalline domains visible (Figure A5, in the appendix). By using the atomic coordinates obtained from the single crystal structure of either monomeric or dimeric *P*-**1b**, theoretical calculations on ω B97/def2SVP level of theory were performed to simulate the arising Cotton effect of the dimer structure of *P*-**1b** due to its chromophore coupling (Figure A9 in the appendix). It can be reasoned that the isolated chromophores of **1e** (4.05%) and **2e** (4.28%) show the highest performance as NFAs, followed by the isolated dimers of enantiopure *P/M*-**1b** (3.68%), whereas *rac*-**1b** (3.31%) allows intimate face-to-face π -interactions that diminish the OSC performance. The higher hole mobility of the isolated dimeric entities of enantiopure *P/M*-**1b** blends as well as the reduced dependency on the solvent additive for *P/M*-**1b** and *P/M/rac*-**1e** based devices suggests a more favorable formation of crystalline domains of the donor polymer **PCE-10** in the presence of the respective acceptor PBIs. Accordingly, the PBI enantiopurity only shows an impact on the OSC performance as long as the chromophores come into close vicinity and are not highly shielded by imide or *bay*-substituents.

3.6 Conclusion

In summary, we investigated two series of conformationally stable and heavily twisted *bay*-tetraarylated PBI dyes as NFAs in BHJ devices with donor polymer **PCE-10**. In a comprehensive study on the variation of both imide (**1a–1e**) and aryl (**1b–5b**) substituents, we determined 2,6-diisopropylphenyl (imide) and 2-naphthyl (aryl) as the best substituents for PBI-based NFAs. Thus, the corresponding derivative **2e** inheriting both substituents reached a peak performance of 4.3% PCE_{max} , that is, to the best of our knowledge, the highest OSC efficiency of a single core PBI without lateral π -extension or embedding of heteroatoms. Our OSC results were correlated with chromophore packing deduced by single crystal structure analysis of the PBIs in racemic mixtures. Interestingly, the more isolated chromophores **1e** and **2e** with almost no π - π interactions gave the highest device performance over 4% PCE_{max} . This reasoning was also corroborated by a comparison of devices built from either racemic or enantiopure PBIs. The effect was more pronounced for *n*-butyl-substituted PBI **1b** that assembles as pure enantiomers into isolated dimers rather than a close slip-stacked double-strand arrangement of the racemate as deduced from the respective single crystals. Thus, enantiopure PBIs of **1b** afforded higher PCEs. This contrasts with Dipp-substituted PBI **1e** whose π - π contacts are already prohibited by the bulky imide substituents and no difference in device efficiency is observed. Therefore, we conclude that isolated and shielded chromophores such as **1e** and **2e** are potent NFA candidates regardless of their enantiomeric purity. Instead, PBIs bearing small and flexible alkyl chains such as *n*-butyl chains, which allow for close π - π interactions that are detrimental for efficient OSCs show a dependency on enantiopurity because of their higher propensity for the formation of slip-stacked arrangements. Our study opens up several perspectives for future NFA material design: (1) utilization of the PBI core twist can be considered also as a viable strategy for multi-chromophore systems that constitute the currently most potent PBI-based NFAs.^[128] (2) In contrast, by enhancing close π - π interactions in the solid state as indicated for the still highly soluble *P*-**1b**, chromophoric coupling might introduce an excitonic Cotton effect. Thus, our materials with their appreciable semiconducting properties might be useful for detecting circularly polarized light in a phototransistor device. Recent progress in this field encourages research on enhancing chiroptical response towards the near-infrared spectral region.^[64, 199] (3) Lastly, the loose solid-state packing of this highly absorbing and electron deficient material will also allow for sublimation, which might enable the fabrication of entirely vacuum-deposited devices.

CHAPTER 4

—

Helically Twisted Nanoribbons Based on Emissive Near-Infrared Responsive Quaterylene Bisimides

This Chapter and the associated Supporting Information (*Chapter 8.2*) have been published
in:ⁱⁱ

B. Mahlmeister, M. Mahl, H. Reichelt, K. Shoyama, M. Stolte, F. Würthner *J. Am. Chem. Soc.* **2022**, *144*, 10507–10514 (<https://doi.org/10.1021/jacs.2c02947>).

Adapted and reprinted with permission from ref. [200]. Copyright 2022 American Chemical Society.

Abstract. Graphene nanoribbons (GNRs) have the potential for next-generation functional devices. So far, GNRs with defined stereochemistry are rarely reported in literature and their optical response is usually bound to the ultraviolet or visible spectral region, while covering the near-infrared (NIR) regime is still challenging. Herein, we report two novel quaterylene bisimides with either one- or twofold-twisted π -backbones enabled by the steric congestion of a fourfold *bay*-arylation leading to an end-to-end twist of up to 76° . The strong interlocking effect of the π -stacked aryl substituents introduces a rigidification of the chromophore

ⁱⁱ Parts of the results have been described in: M. Mahl, PhD Thesis, Julius-Maximilians-Universität Würzburg, **2021** (ref. [235]).

unambiguously proven by single-crystal X-ray analysis. This leads to unexpectedly strong NIR emissions at 862 and 903 nm with quantum yields of 1.5 and 0.9%, respectively, further ensuring high solubility as well as resolvable and highly stable atropo-enantiomers. Circular dichroism spectroscopy of these enantiopure chiral compounds reveals a strong Cotton effect $\Delta\epsilon$ of up to $67 \text{ M}^{-1} \text{ cm}^{-1}$ centered far in the NIR region at 849 nm.

4.1 Introduction

Graphene nanoribbons (GNRs) are one-dimensional cutouts of a parent sp^2 framework of carbon.^[201] Their electronic properties show critical dependence on the aspect ratio, width, and individual edge structures, which can be either zig-zag or armchair type.^[202] Tuning the ribbon in this way is feasible not only for overcoming the missing band gap in the pristine graphene layer but also for engineering spin-polarized edge and topological states.^[203-205] The study of extended nanoribbons in the condensed phase has been endowed by the pioneering bottom-up approaches of the Müllen group via polymerization and subsequent cyclodehydrogenation.^[206] With the emerging importance of curved polycyclic aromatic hydrocarbons (PAHs) for organic electronics and spintronics, warped GNRs have also become a subject of current research. These small and highly defined ribbons are built up from ‘zero-dimensional’ nanographene by exploiting established annulation chemistry. Thus, existing molecular motifs, which have been hitherto synthetically inaccessible, can be investigated within their novel geometries, leading to even expanded functionalities.^[72, 207-208] The family of acenes, as a ribbon-archetype, provides an impressive library starting from planar workhorse materials such as the hardly soluble pentacene and fourfold core-arylated rubrene.^[209-210] Increasing steric congestion of core substituents induces severe longitudinal backbone twists.^[211] This allows the isolation of helical ribbons, for example, pitched by up to 184° for a hexacene derivative.^[212] It also opens up synthetic pathways to expand the backbone by embedding heteroatoms or further aromatic moieties via benzannulation, such as with pyrene or even rylene bisimides, leading to impressive backbone lengths of up to 53 linearly fused ring units reported so far.^[141, 213-215] A defined chiral pitch for such nanoribbons was previously accomplished by chiral end groups that induce a predominant helicity.^[144] By this means, the helicity of flexible ribbons can be biased, which is a facile alternative compared to the separation of atropo-enantiomers formed statistically during the annulation of achiral building blocks. Nevertheless, the latter approach is still the method of choice for laterally extended and more rigid nanoribbons whose edge

functionalization defines whether stereoisomers can be isolated or not.^[138, 141, 144, 214-222] Thus, a variety of new molecular materials with a high chiroptical response have been realized, cumulating in the design of a supertwistacene by the Wang group in 2020,^[191] proving GNRs as a considerable alternative for pristine carbo[n]helicene backbones.^[27, 132, 155, 223-224]

Our group was the first to introduce stable axial chirality of perylene bisimides (PBIs) with the investigation of the core twist imparted by the steric congestion upon a fourfold *bay*-substitution by bromine, later on, improved by Zhu and the Hoffmann group with phenyl units.^[20, 60, 66] Until now, this strategy has been expanded to various aryl and benzannulated perylenes as well as peropyrene systems, which found applications within organic solar cells and circularly polarized light (CPL) detection devices.^[22, 64, 68, 159] Another family of core-twisted perylene-based nanoribbons has been realized by side-on annulation of multiple PBI cores into a helical oligomer showing a strong bisignated Cotton effect due to excitonic chirality in contrast.^[134, 225] Different from this earlier work, here, we expand the core-twisted one-chromophore system longitudinally from PBIs to quaterylene bisimides (QBIs, Figure 28).

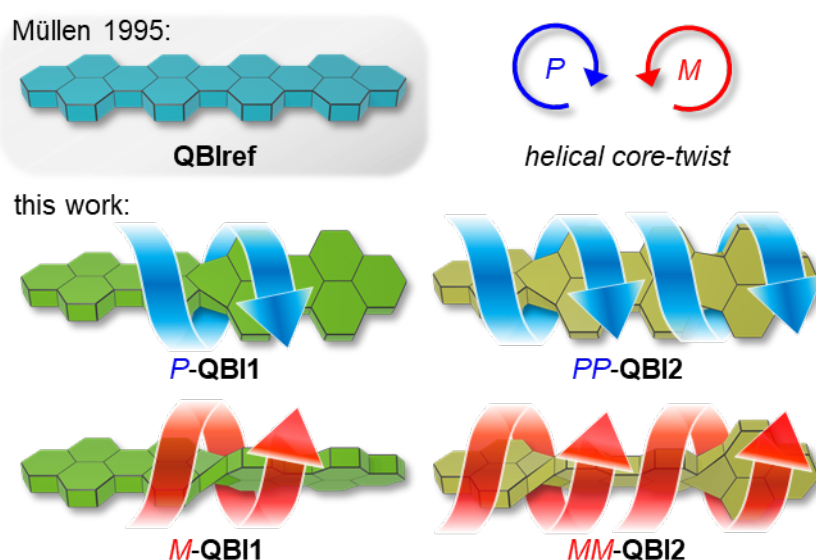
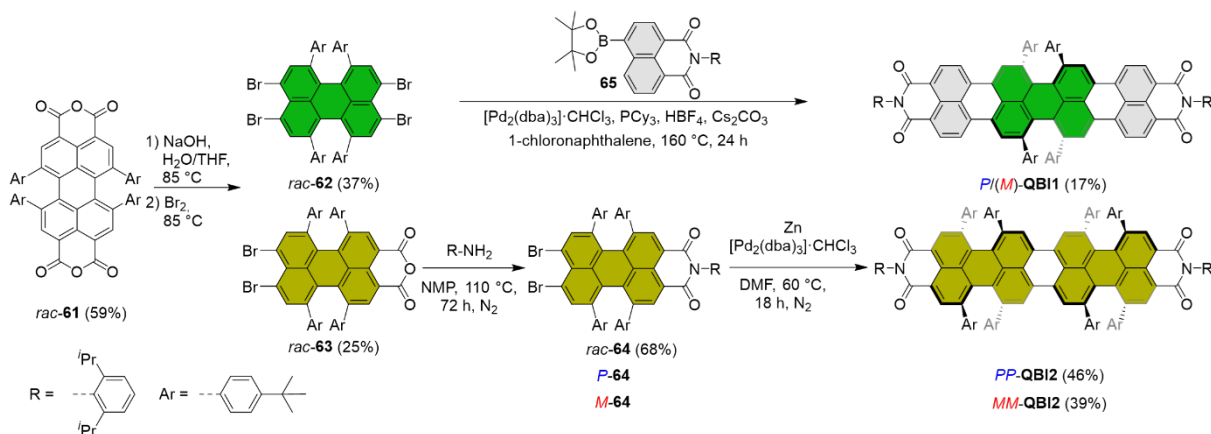


Figure 28. Schematic representation of previously reported^[226] planar and newly synthesized twisted QBI atropo-enantiomers in their molecular geometries.

These extended rylene dyes bearing four naphthalene subunits have been known since 1995 and show extraordinary thermal- and photostability, which allowed their use in organic electronics despite their poor solubility due to a strong pigment character.^[226-228] So far, only decent solubility could be achieved by extensive side chain decoration.^[229] Hitherto reported twisted higher rylene dyes did not allow for the isolation of stable atropo-enantiomers.^[230-233] Recent in-depth studies have focused on the singlet fission phenomenon of planar QBIs.^[234]

We now present **QBI1** and **QBI2** (Scheme 1) as two closely related novel *bay*-arylated QBIs, which are either one- or twofold twisted, respectively.



Scheme 1. Synthetic Route toward chiral **QBI1**^[235] and **QBI2**. For **QBI2**, the respective *PP*-enantiomer is depicted.

The chiral twist was unambiguously proven by X-ray crystallography. The compounds were further investigated by UV–vis–near-infrared (NIR) spectroscopy as well as circular dichroism (CD) spectroscopy and cyclic voltammetry. For the first time in the higher rylene chemistry, the axial chirality of **QBI2** was directly imprinted into the molecular fabric of the building blocks by enantiopure synthesis. This was made possible due to the final annulation reaction below the racemization temperature of the perylene monoimide precursor. This approach allows for the synthesis of large conjugated molecules that display strong absorption in the NIR region and paves the avenue toward nanoribbons with a stable helical pitch. This is now of particular interest as the presented QBIs are the first of their kind showing a strong chiroptical response far in the NIR regime, which is to date still rarely reported. As a further consequence of our core twist approach, a rigidification by the interlocked aryl substituents endows these dyes with improved fluorescence quantum yields compared to literature-known planar and unsubstituted QBI, which has been carefully evaluated via the direct excitation method and the relative determination of quantum yields using literature-known fluorescence standards.

4.2 Synthesis

The two newly designed twisted QBIs are synthesized in a straightforward approach using the same twisted precursors. The key reaction steps are either a palladium-catalyzed [3 + 3] annulation^[236-237] for the one-fold twisted **QBI1**^[235] or a zinc-mediated Ullmann-type

coupling^[238] for the twofold twisted **QBI2**. Scheme 1 shows the main synthetic steps starting with the racemate of fourfold *bay*-tetraarylated perylene bisanhydride **61**. For the overall synthetic route, see Supporting Information, Scheme A1. **61** was converted into carboxylate, whose decarboxylation was done by Hunsdieckertype tetrafold decarboxylative bromination.^[235,239] A large excess (40 equiv) of bromine afforded the fourfold *peri*-brominated perylene **62** (37%), the twofold *peri*-brominated monoanhydride **63** (25%), and reisolated starting material (20%). Single-crystal X-ray analysis of **63** revealed a twist angle of 42°, which is the highest degree of rotational contortion found for a *bay*-tetrasubstituted perylene core so far (for details, see appendix, Figure A18). The phenyl substituents were prevented from unselective bromination by their attached *tert*-butyl groups at the most reactive *para*-position.^[235] The final step toward **QBI1** is based on a twofold palladium-catalyzed [3 + 3] annulation reaction^[236-237] of **64** with 2.2 equiv of naphthalene dicarboximide boronic acid ester **65** affording the onefold twisted **QBI1** in a yield of 17% as a green solid.^[235] The remaining dibromo perylene monoanhydride precursor **63** was imidized to **64** (68%) and converted into the twofold twisted **QBI2** by a zinc-mediated Ullmann-type homocoupling reaction, which could be conducted at a moderate temperature of 60 °C, significantly below the enantiomerization barrier (*vide infra*). This is of particular interest as the homocoupling reaction using the racemic mixture of *rac*-**64** atropo-enantiomers afforded the *PP*-/*MM*-**QBI2** enantiomeric pair and the *PM*-**QBI3** *meso* derivative (for the ¹H NMR spectra of fractions isolated by the high-performance flash chromatography technique, see Figure A14). However, the separation of the three isomers was not perfectly accomplished by this approach. Accordingly, because our main interest was the helically chiral **QBI2** enantiopure *PP*- and *MM*-enantiomeric pair, we separated the enantiopure precursors *P*- and *M*-**64**, respectively, by high-performance liquid chromatography (HPLC) with a chiral stationary phase in 99.9% enantiomeric excess (*ee*) and subsequently coupled those to give enantiopure *PP*- and *MM*-**QBI2** in yields of 46 and 39%, respectively (for details, see the appendix, Figure A26). The racemization barrier (**QBI1**)^[235] or diastereomerization barrier (**QBI2**) is exceptionally high, for each about $\Delta G_{398\text{K}}^\ddagger = 125 \text{ kJ mol}^{-1}$, as determined by time-dependent CD spectroscopy at an elevated temperature of 125 °C (1,1,2,2-tetrachloroethane) utilizing the Eyring equation (for details, see the appendix Figure A27). The ΔG^\ddagger value slightly exceeds those for the tetraarylated PBIs (118 kJ mol⁻¹), tetrabromo-substituted PBIs (118 kJ mol⁻¹),^[60] tetrathioether-substituted PBIs (119 kJ mol⁻¹),^[240] and tetraaryl-substituted peropyrenes (121 kJ mol⁻¹).^[68, 241] Overall, the chiral contortion of the quaterrylene scaffold not only opens up rich stereochemistry but also introduces high solubility by preventing strong interchromophoric interactions, which is

remarkable for such extended π -scaffolds. **QBI1** is well soluble in chlorinated solvents and can even be dissolved in protic and dipolar aprotic ones (methanol and MeCN) for spectroscopic purposes ($c \sim 10^{-5}$ M) and non-polar solvents such as *n*-hexane despite the absence of long or branched alkyl chains. The solubility of **QBI2** is elevated up to $c > 8$ mM in dichloromethane (DCM). The compounds were fully characterized by NMR, UV–vis–NIR, and fluorescence spectroscopies as well as high-resolution mass spectrometry (see the appendix).

4.3 Structural Properties

Structural Properties. To gain insights into the structural features of the novel QBIs, a lot of effort was made to grow single crystals of a suitable size for X-ray diffraction analysis by the slow diffusion method of ethanol (*rac*-**QBI1**)^[235] or methanol (*PP*-**QBI2**) into a chloroform solution (Figure 29 and Figure A15). *Rac*-**QBI1** crystallizes in the centrosymmetric $P2_1/c$ space group as a 1:1 racemic mixture. Due to their spatial proximity, the adjacent aryl groups cause a strong distortion of the quaterrylene core, leading to a chiral π -scaffold with a dihedral angle of 39° between the two naphthalene subplanes of the central perylene moiety. The phenyl substituents interlock with each other in a rather rigid geometry at van der Waals distances of about 3.5 Å, thereby enforcing a rotational twist of the central part of the quaterrylene π -scaffold (Figure 29a,b). Similar features have been recently reported by us and others for the respective arylated PBIs^[22] or peropyrenes,^[68] which differ from the more common *bay*-functionalization of rylene bisimides by phenoxy groups, leading to a less twisted rylene scaffold usually not enabling the isolation of stable atropo-enantiomers. The racemic mixture of **QBI1** is organized in a π -stacked dimeric arrangement of *P*- and *M*-atropo-enantiomers within its crystal structure^[235] coming closest at a π – π distance of 3.5 Å, enforcing an additional torsional curving of the rylene scaffold (Figure 29 and for details, see Figure A15). This leads to a final end-to-end twist of about 59° measured between the outermost naphthalene planes. Besides, further intimate π – π contacts are prevented by both the steric shielding of the perpendicular geometry of 2,6-diisopropylphenyl (Dipp) imide and the demand of attached aryl substituents, leading to center-to-center distances of about 7.6 Å (Figure 29d and Figure A15). The absence of close packing of the dyes is also evident in the investigated single crystal of the enantiopure twofold twisted enantiomer *PP*-**QBI2**. The more complex crystal structure with the $P4_3$ space group contains high amounts of solvent molecules.

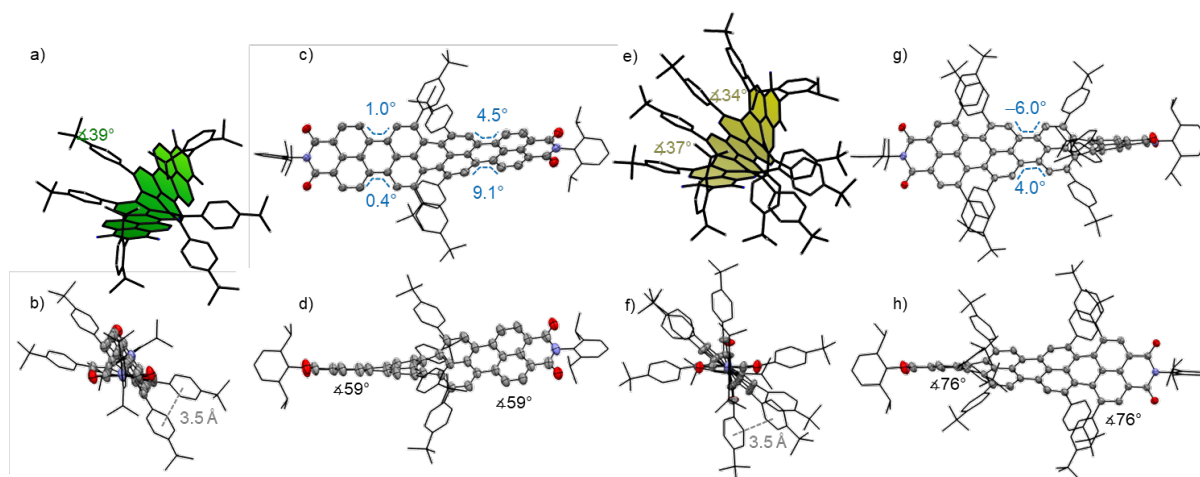


Figure 29. Molecular geometry of *P*-**QB11**^[235] (a–d) and *PP*-**QB12** (e–h) found in the single-crystal structures of racemic **QB11** and enantiopure *PP*-**QB12** from the top view (c,g), side view (d,h), and rotated side view (b,f). The ellipsoids are set to 50% probability (C: gray, N: red, O: blue). Disordered alkyl residues, hydrogen atoms, and solvent molecules are omitted for clarity. Twist angles between naphthalene subplanes interlocked by aryl substituents are shown in green (**QB11**) and dark yellow (**QB12**). Corresponding twist angles between the outermost naphthalene planes are shown in black. Torsion angles of the unsubstituted perylene *bay*-positions are shown in light blue. The closest π – π distances between centroids of the adjacent phenyl substituents scaffold (gray) are indicated as well.

These do not allow for intimate packing analysis but hereby highlights the more unimolecular character of the chromophore found in the crystal. The highly shielded scaffold reveals an end-to-end twist of an outstanding 76° , which is exactly twice as large as the central core twist of **QB11**. As no intimate π – π stacking is possible, showing only closest center-to-center distances of 10.6 \AA , no further significant packing-affected or torsional displacement is present as it is observed for **QB11**. Thus, the molecule has two individual twisted *bay*-areas (37 and 34°), which do not communicate as it is clearly visible by the almost-planar central perylene unit with only small contortion angles of about 6° of the central *bay*-areas (see Figure 29g and Figure A15). However, the distances between adjacent phenyl substituents are 3.5 \AA , equal in both twisted regions to those in **QB11**, suggesting that the additional strain of **QB11** is solely packing-induced. Recent reports on corresponding PBIs suggested an effect on the core twist by the individual stacking of attached aryl substituents, supramolecular chromophore arrangement, or the degree of planarization imparted by the *peri*-substituents. The latter one might account for the tremendous twist of 42° for the aforementioned precursor **63** (for details, see the appendix, Figure A18). The crystallographic analysis hereby unambiguously confirmed the twisted structures of **QB11** and **QB12** and their stereochemistry and further gave a perception of the high constraint due to the sterically crowded *bay*-positions.

4.4 Absorption Properties

The UV–vis–NIR, fluorescence, and CD properties of **QB11** and the enantiomeric pair of *PP*-/*MM*-**QB12** were studied in solution. For comparison, we also resynthesized the Dipp-substituted **QB1ref**.^[226-227] This parent compound shows an absorption maximum (λ_{\max}) at 766 nm (see Figure 30 and Table 5), assigned to the S_0 – S_1 transition of the rylene scaffold, while the S_0 – S_2 transition located below 400 nm has a significantly less intensity.

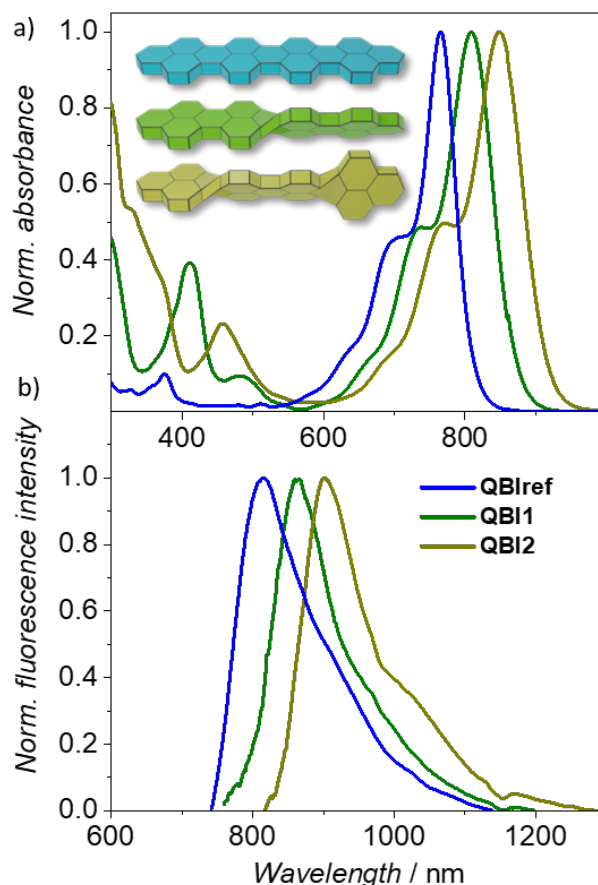


Figure 30. (a) Normalized UV–vis–NIR absorption and (b) fluorescence spectra of QBIs in a DCM solution at 295 K. Fluorescence data [$\lambda_{\text{ex}}(\text{QB1ref}, \text{rac-QB11}) = 740 \text{ nm}$, $\lambda_{\text{ex}}(\text{MM-QB12}) = 780 \text{ nm}$]. The schematic inset in (a) represents **QB1ref** (blue), **QB11** (green), and **QB12** (dark yellow).

The introduction of four (**QB11**) or eight (**QB12**) *tert*-butyl phenyl substituents at the respective *bay*-areas leads to a significant stepwise red shift from 766 (**QB1ref**) over 809 (**QB11**) to 849 nm (**QB12**) by 680 cm^{-1} each, while the overall spectral shape is mainly preserved (Figure 30a). The relationship of the spectral red shift to the frontier orbitals was further investigated by electrochemical measurements as discussed in the Supporting Information. The molar extinction coefficient (ϵ_{\max}) of **QB1ref** of $153000 \text{ M}^{-1} \text{ cm}^{-1}$ drops down by 38% to $95000 \text{ M}^{-1} \text{ cm}^{-1}$ for the onefold twisted **QB11** but then retains its intensity along the second

twist for **QBI2**, showing $98000 \text{ M}^{-1} \text{ cm}^{-1}$. The sharp **QBI1ref** absorption with a full width at half maximum (fwhm_{abs}) of 1020 cm^{-1} is only slightly broadened to about 1300 cm^{-1} for both twisted congeners, supporting the existence of a rather rigid π -scaffold for all three QBIs. Higher transitions of **QBI1** and **QBI2** gain intensity below 500 nm compared to those of **QBIref**, thereby suggesting the involvement of phenyl substituents, which could be rationalized by the analysis of natural transition orbitals (NTOs)^[242] based on time-dependent density functional theory (TD-DFT) at the $\omega\text{B97XD}/\text{def2-svp}$ level of theory (Figure A22 and Figure A23 in the appendix).

Table 5. Optical Properties of QBIs in DCM at 295 K.

	λ_{max}^a / nm	fwhm_{abs} / cm^{-1}	ϵ_{max} / $\text{M}^{-1} \text{ cm}^{-1}$	λ_{em}^a / nm	fwhm_{em} / cm^{-1}	$\Delta\tilde{\nu}_{\text{Stokes}}$ / cm^{-1}	Φ_{Fl} / %
QBIref	766, 376	1020	153000, 15400	815	1870	780	1.2 ± 0.1^b
QBI1^d	809, 482, ^d 411	1310	95000, 9000, 37000	862	1320	760	$1.5 \pm 0.1^{b,c}$
QBI2^e	849, ^b 458	1330	98000, 23000	903	1270	700	0.9 ± 0.2^b

^a $c_0 \approx 1 \times 10^{-5} \text{ M}^{-1}$. ^b Absolute Φ_{Fl} was determined by a calibrated integration sphere system via the direct excitation method; 1 cm cell thickness ($\text{OD} = 0.15 - 0.25$). The values were corrected for reabsorption. ^c Relative Φ_{Fl} was determined by the dilution method ($\text{OD} < 0.05$) with **Rh800** ($\Phi_{\text{Fl}} = 25\%$ in EtOH)^[243] as well as **QBI1** ($\Phi_{\text{Fl}} = 1.5\%$ in DCM). ^d The racemic mixture of **QBI1** was used for all reported measurements. ^e Both *PP*- and *MM*-enantiomers of **QBI2** were used for the reported measurements.

4.5 Fluorescence Properties

The fact that all of the discussed QBIs are endowed with high rigidity suggests little structural changes in the excited state, thereby promoting interesting fluorescence properties. In this regard, we would like to stress on the importance of the energy gap law^[244] that manifests an increased vibrational coupling between electronic states if they are energetically close. For this reason, it is indeed challenging to accomplish a decent NIR emission at wavelengths beyond 800 nm.^[229-234, 236-237, 239-241, 244-246] The fluorescence of planar **QBIref** has been previously investigated in chloroform solution, showing an emission maximum (λ_{em}) at 797 nm with an estimated quantum yield (Φ_{Fl}) by the Strickler–Berg analysis of about 5%.^[227] We took the effort to experimentally investigate all three QBIs in DCM with a state-of-the-art liquid-nitrogen-cooled NIR photomultiplier (with a good signal-to-noise ratio even in the NIR wavelength range) as well as a calibrated integration sphere setup. The emission maxima at 815 nm (**QBIref**), 862 nm (**QBI1**), and 903 nm (**QBI2**) with very low and surprisingly similar Stokes shifts ($\Delta\tilde{\nu}_{\text{Stokes}}$) of below 800 cm^{-1} for all three chromophores were obtained (Figure 30b), which, in contrast to PBIs,^[22] remain constant after the introduction of a core twist

(Table 5 for PBIs, see Table A8 and Figure A20). Moreover, fwhm_{em} narrows down from 1870 cm^{-1} (**QBIref**) to 1320 and 1270 cm^{-1} for **QBI1** and **QBI2**, respectively, corroborating the proposed rigidification of the twisted π -scaffold imparted by the interlocking aryl substituents (vide supra). Absolute Φ_{FI} determination by the direct excitation method and corrected for reabsorption yielded $1.2 \pm 0.1\%$ (**QBIref**), $1.5 \pm 0.1\%$ (**QBI1**), and $0.9 \pm 0.2\%$ (**QBI2**), respectively, which were additionally affirmed by relative Φ_{FI} measurements for **QBIref**^[243] and **QBI1**. Thus, considering the energy gap law, both core-twisted **QBI1** and **QBI2** are superior NIR emitters than the parent **QBIref**, presumably due to a rigidification imparted by the interlocked phenyl substituents. This interlocked arrangement counteracts fluorescence decays governed by molecular vibrations as a crucial loss pathway in the NIR region, again in contrast to the respective PBIs (Table A8 and Figure A20). Thus, the QBI quantum yields are in line with their preserved spectral shape in both absorption and emission upon core twist, and their fluorescence quantum yields can catch up with those of commercial cyanine dyes in the desired far-NIR spectral range utilized in NIR bioimaging and lasing applications exhibiting Φ_{FI} of 0.66% at 818 nm (indocyanine green)^[247] and 0.35% at 1011 nm (**IR-27**).^[248] The photostability, as a crucial issue for NIR dyes, has been verified for **QBI1** and **QBI2** in DCM solution after conducting long-lasting fluorescence measurements as well as under dark conditions after two weeks showing less than 1% decomposition.

4.6 Chiroptical Properties

The impact of the axial chirality introduced by a core twist on optical properties was investigated via CD spectroscopy (Figure 31), while CPL could unfortunately not be elucidated by our instrument due to the weak emission in the NIR spectral range. The *P*- and *M*-atropo-enantiomers of **QBI1** were separated using repetitive HPLC with a chiral stationary phase.^[235] Likewise, the *P*- and *M*-enantiomers of precursor *rac*-**64** were separated before their homocoupling reaction to obtain the pure *PP*- and *MM*-enantiomers of **QBI2**. This was possible due to the mild reaction temperature of $60\text{ }^{\circ}\text{C}$ (vide supra). The CD spectra of the enantiopure QBIs reveal a strong unisignated NIR band corresponding to the S_0 - S_1 transition of **QBI1** ($\Delta\varepsilon = 40\text{ M}^{-1}\text{ cm}^{-1}$) and **QBI2** ($\Delta\varepsilon = 67\text{ M}^{-1}\text{ cm}^{-1}$), respectively, as well as multiple higher energy bands below 500 nm with $\Delta\varepsilon$ up to $130\text{ M}^{-1}\text{ cm}^{-1}$ for **QBI2**. The CD spectra are in good agreement with TD-DFT calculations regarding the spectral shape and signs of the Cotton effect, further corroborating the results from single-crystal X-ray analysis.

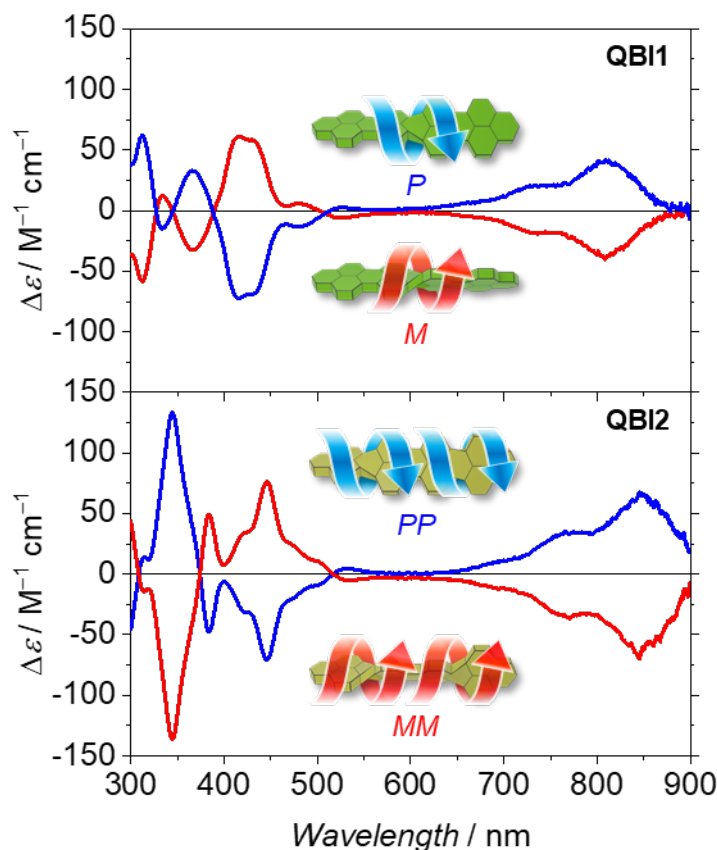


Figure 31. CD spectra of enantiopure **QB11** (top) and **QB12** (bottom) in DCM at 295 K. The insets show the corresponding molecular structures of *P*-/*PP*- (blue) and *M*-/*MM*- (red) atropo-enantiomers in green and dark yellow, respectively

NTO analysis (Figure A22 and Figure A23) highlights an involvement of the phenyl substituents in the sharp higher energy excitations with the strongest chiroptical responses, while the main NIR band only involves the S_0 – S_1 π -scaffold excitation. This difference can be rationalized by considering electric and magnetic transition dipole moments μ and \mathbf{m} (Figure A24) and their respective angle, being responsible for the magnitude of the CD signal. The higher energy excitations involving the attached phenyl substituents show only small μ corresponding to their minor oscillator strength but large \mathbf{m} . This opposes the perpendicular main S_0 – S_1 transition owing a high oscillator strength due to the highly electric-dipole allowed character but small magnetic transition dipole moment \mathbf{m} (for details, see the appendix, Table A9). As a result, the experimentally determined dissymmetry factors $g_{\text{abs}} = \Delta\epsilon/\epsilon$ for the S_0 – S_1 transitions of **QB11**^[235] (4.3×10^{-4}) and **QB12** (6.5×10^{-4}) are rather low (Figure S16).^[249] Considering that only the extended backbone is involved in the main transition, the molar ellipticity $\Delta\epsilon$ can be expressed by only using the molar mass of the rylene scaffold. This would change the increase in $\Delta\epsilon$ upon the core twist from **QB11** to **QB12** from a factor of 1.7 (40 to 67 $\text{M}^{-1} \text{cm}^{-1}$) to a factor of about 2.3 (93 to 212 $\text{M}^{-1} \text{cm}^{-1}$). This corroborates the

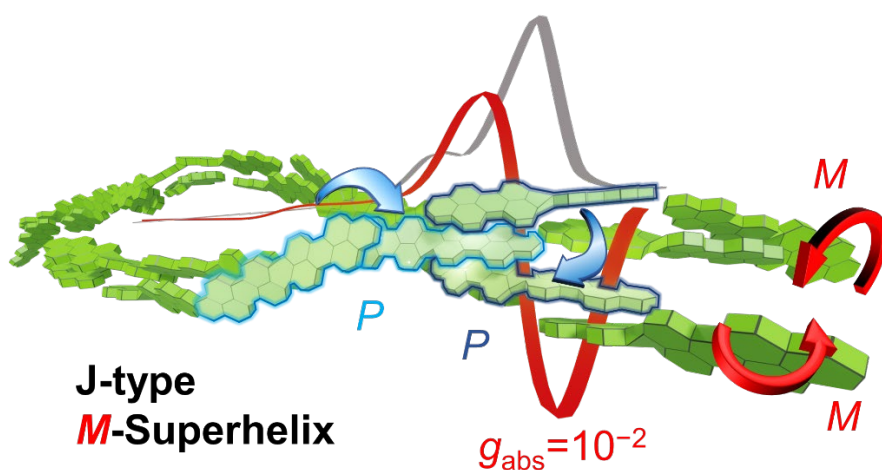
crystallographic findings, proving that two pristine core twists are present in **QBI2** as no saturation effect is observed, which can be seen as a result of the π -scaffold rigidification due to the steric constraint between the interlocked neighboring aryl groups.^[191]

4.7 Conclusion

In summary, we presented a straightforward synthetic route to the first two members of the new class of configurationally stable helically twisted nanoribbons based on the QBI scaffold. This has been accomplished by a recently developed palladium-catalyzed annulation protocol for electron-poor PAHs^[236] as well as a zinc-mediated Ullmann-type homocoupling reaction.^[238] Our core twist approach using an interlocking effect of adjacent aryl *bay*-substituents was inspired by the related PBIs but revealed unexpected and unique consequences for the core-enlarged class of QBIs. Thus, high solubility and an extraordinary configurational stability of the isolable atropo-enantiomers are the first consequences of this approach, which then guarantees the strong chiroptical responses in the NIR region. The twist-induced rigidification of the backbone was unambiguously proven by single-crystal X-ray analyses, showing a stable end-to-end twist of up to 76° for the twofold twisted **QBI2**. This accounts for the sharp emission with a small Stokes shift in the far NIR region at 862 nm (**QBI1**) and 903 nm (**QBI2**) as well as impressive fluorescence quantum yields of 1.5 and 0.9% for such small band gap chromophores, respectively. The large chiroptical response with a unisignated CD signal with $\Delta\epsilon$ of up to $67 \text{ M}^{-1} \text{ cm}^{-1}$ at 849 nm combined with reduction potentials comparable with well-established organic materials such as PBIs or fullerenes motivates the fabrication of chiral organic thin film devices encouraged by the high solubility.^[250]

CHAPTER 5

—

**Enantiopure J-Aggregate of Quaterrylene Bisimides for
Strong Chiroptical NIR-Response**

This Chapter and the associated supporting information (*Chapter 8.3*) have been published in:

B. Mahlmeister, T. Schembri, V. Stepanenko, K. Shoyama, M. Stolte, F. Würthner *J. Am. Chem. Soc.* **2023**, *145*, 13302–13311 (<https://doi.org/10.1021/jacs.3c03367>).

Adapted and reprinted with permission from ref. [251]. Copyright 2023 American Chemical Society.

Abstract. Chiral polycyclic aromatic hydrocarbons can be tailored for next-generation photonic materials by carefully designing their molecular as well as supramolecular architectures. Hence, excitonic coupling can boost the chiroptical response in extended aggregates, but is still challenging to achieve by pure self-assembly. Whereas most reports on these potential materials cover the UV and visible spectral range, systems in the near-infrared (NIR) are underdeveloped. We report a new quaterrylene bisimide derivative with a conformationally stable twisted π -backbone enabled by the sterical congestion of a fourfold *bay*-arylation. Rendering the π -subplanes accessible by small imide substituents allows for a slip-stacked chiral arrangement by kinetic self-assembly in low-polarity solvents. The well-dispersed solid-state aggregate

reveals a sharp optical signature of strong J-type excitonic coupling in both absorption (897 nm) and emission (912 nm) far in the NIR region and reaches absorption dissymmetry factors up to 1.1×10^{-2} . The structural elucidation was achieved by atomic force microscopy and single-crystal X-ray analysis, which we combined to derive a structural model of a fourfold stranded enantiopure superhelix. We could deduce that the role of phenyl substituents is not only granting stable axial chirality but also guiding the chromophore into a chiral supramolecular arrangement needed for strong excitonic chirality.

5.1 Introduction

Chiral polycyclic aromatic hydrocarbons (PAHs) are considered promising candidates for next-generation functional materials. The scope of applications ranges from displays,^[8] polarization-selective photodetectors,^[64, 126, 250, 252-253] security inks,^[254] or even spintronic devices^[204] and exploits the molecular chirality in both absorption and emission.^[255] A stable and high overall chiroptical response can be achieved on a molecular level by structural design. Rigid chromophores with extended π -scaffolds have to be transformed into a conformationally stable three-dimensional chiral geometry while maintaining the high tinctorial strengths and strong fluorescence properties of the parent PAHs.^[144, 191, 256] The required strain and contortion can be introduced into the π -scaffold in multiple ways. Common strategies include exploiting the sterical congestion of bulky substituents,^[22] fusing carbo[n]helicenes,^[27, 62] embedding non-planar elements such as five- and seven-membered rings^[257-258] or incorporating hetero atoms.^[259-261] The latter can affect the PAH electronically besides purely geometrical changes to enlarge the chiroptical response.^[136-137] However, the (dimensionless) molecular dissymmetry factors g_{abs} and g_{lum} of the vast majority of small organic molecules usually remain rather low in the range of 10^{-5} to 10^{-3} .^[16, 27, 221]

These dissymmetry factors can be significantly improved when tailoring small molecular systems into supramolecular architectures such as dimers^[116] or extended aggregates^[152] by utilizing the excitonic coupling of the self-assembled dyes.^[33-34, 262] The supramolecular design has to balance between both an efficient exciton coupling and a favorable chiral orientation between the chromophores.^[47-48] By this means, g -factors of 10^{-2} or even above could be realized for excimer-like aggregates^[263] or classical H-aggregates in both solution and solid state.^[255, 264] Most PAHs favor a co-facial supramolecular orientation.^[19] Hence, corresponding enantiopure H-type helical systems can be designed with relative ease.^[96, 265] In contrast, for

J-aggregates, it is much more demanding to meet the geometric requirements providing excitonic chirality. Thus, there are only a few reports on enantiopure J-aggregates of cyanine and squaraine dyes with strong chiroptical response of their main optical transition.^[266-267] J-type excitonic coupling with narrow absorption/emission bands as well as high fluorescence quantum yields is of particular interest when approaching the deep red or near-infrared (NIR) spectral region.^[268-269] Recent progress could be achieved however for J-aggregates of non-chiral dyes.^[73, 270-274] This research field becomes currently even more relevant regarding sensing applications in biomedical research, which highlights the desire for novel chiral J-type supramolecular materials.^[275]

J-aggregates based on tetra-*bay*-substituted perylene bisimides (PBIs) have been known since 2007.^[83] The sterical demand of the PBI's four aryloxy substituents introduces an axial chiral twist into the chromophore core, which imparts a right- or left-handed unidirectional helicity into the self-assembled cord-like aggregates (see Figure 32).^[86] The conformationally stable collinear alignment of the slip-stacked chromophores within these J-aggregates is ensured by dispersion forces of the overlapping π -surfaces. It is guided by hydrogen bonds between the self-complementary imide groups (Figure 32b). By this approach, helical J-aggregates are observed even from racemic mixtures due to a preferential homochiral self-assembly.^[85] However, the formation of actual enantiopure J-aggregates requires separable monomers with a racemization barrier ΔG^\ddagger higher than 90 kJ mol^{-1} , while fourfold *bay*-aryloxy PBIs only show values of about 60 kJ mol^{-1} at 270 K, which is too low for feasible enantiomer separation.^[59] This can be synthetically realized by rigidification approaches using bridging units^[60] or connecting adjacent *bay*-positions with biphenol units. By this means, the first chiral PBI J-aggregate built from stable axial chiral monomers could be realized in 2012 (Figure 32b).^[84] However, due to the perfect collinear arrangement of chromophores within the aggregate, no excitonic chirality of the main J-band (absorption/emission) could be detected, which would be needed to enhance the chiroptical response. To overcome this, in the present work, we follow our recent chiral interlocking approach by using directly arylated fourfold *bay*-substituted perylene cores (Figure 32). The corresponding *bay*-tetraarylated PBIs^[20, 22, 66] have been proven to show processability as efficient non-fullerene acceptors in organic solar cells.^[21, 159] The sterical congestion of the aryl substituents leads to a huge twist of the PBI core (up to 39°).

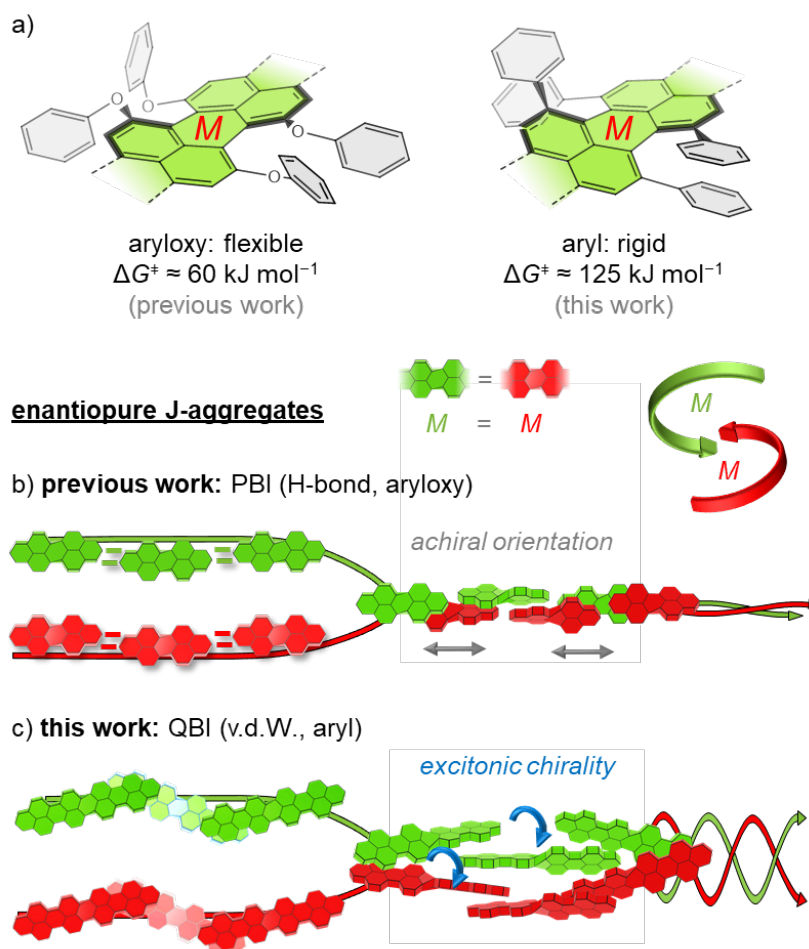


Figure 32. (a) Molecular structure of a tetraaryloxy (left) and a tetraaryl (right)-substituted helically twisted (*M*-)rylene core section along with their activation enthalpies for racemization. (b) Schematic depiction of H-bonded *M*-PBIs (red, green) forming a helical slip-stacked double strand with collinear (achiral) mutual orientation of the chromophores. (c) Schematic depiction of two kinked slip-stacked *M*-QBI double strands (red, green) forming an intertwined helical fourfold strand with chiral mutual orientation of the chromophores enabling excitonic chirality.

It imparts a high conformational stability (ΔG^\ddagger of about 120 kJ mol^{-1} at 383 K ^[22]) and rigidification. In this work, we could induce self-assembly of these axial-chiral molecules by expanding the π -scaffold into a core-twisted quaterrylene bisimide^[200, 226-227] (QBI) dye bearing only small methyl units in both imide positions. This allows self-assembly by pure van der Waals interactions even without H-bonding, which would facilitate an unwanted collinear (achiral) chromophore arrangement as for the *bay*-tetraaryloxy PBIs (Figure 32b). In our new work, the slip-stacked arrangement of the core-twisted enantiopure QBIs is guided into a chiral mutual orientation by the interlocking phenyl substituents^[200] (see Figure 32c). This results in the formation of two intertwining slip-stacked double-strands, which wrap up into a cord-like J-aggregate with strong excitonic chirality in the NIR. To the best of our knowledge, this is unprecedented for rylene bisimide dyes so far and opens up an avenue for new supramolecular chiral materials with strong dissymmetry factors.

5.2 Synthesis

The *peri*-brominated precursor **62** and the methyl-substituted naphthalimide boronic ester **67** are cross-coupled by a palladium-catalyzed 3 + 3 annulation to afford *rac*-QBI-Me as a racemic mixture of *P*- and *M*-atropo-enantiomers (see Figure 33a, for details see the appendix).

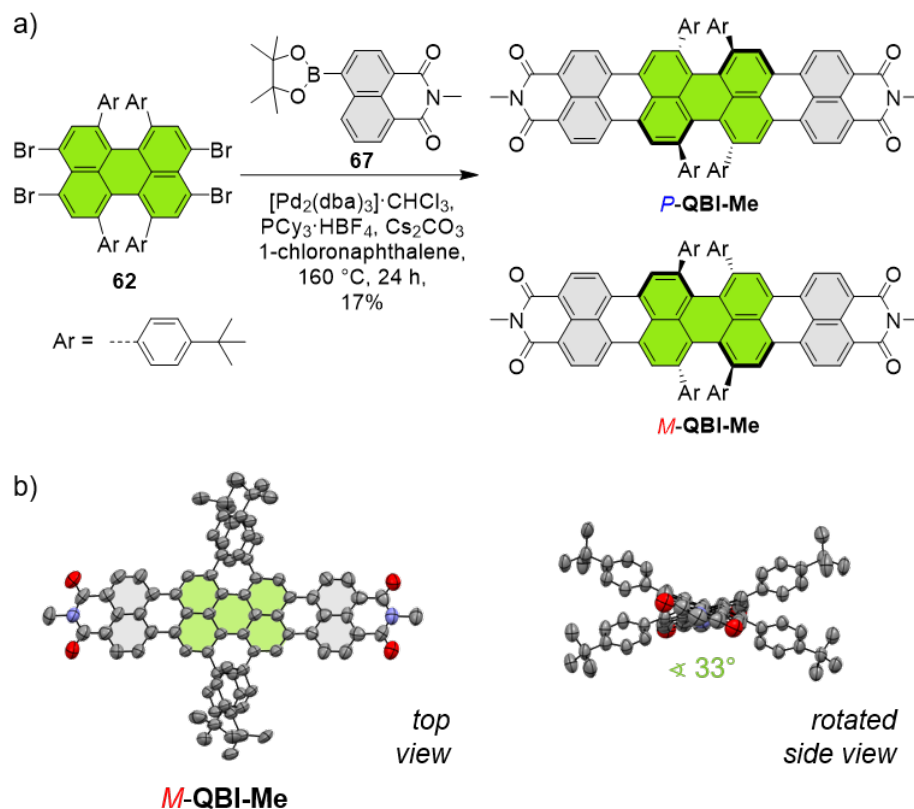


Figure 33. (a) Reaction scheme toward newly synthesized axial chiral (twisted perylene core highlighted in green) *rac*-QBI-Me. (b) Molecular geometry of the *M*-enantiomer found in the single-crystal structure in top view and viewed along the *N,N'*-axis. The ellipsoids are set to 50% probability. The twist angle between the central naphthalene subplanes is shown in green. Carbon (gray), nitrogen (blue), and oxygen (red) are indicated as well. Disordered alkyl residues and hydrogen atoms are omitted for clarity.

The enantiomers were separated using high-performance liquid chromatography with a chiral stationary phase. The QBI was fully characterized by NMR, UV-vis-NIR, and fluorescence spectroscopy as well as high-resolution mass spectrometry (appendix) and X-ray single-crystal analysis.

5.3 Optical Properties and Aggregation

First, the UV–vis–NIR absorption properties of the racemic (*rac*) as well as *P/M*-enantiopure species of **QBI-Me** were investigated in dichloromethane (DCM) solution revealing an equally strong NIR absorption of $\epsilon_{\max} = 99000 \text{ M}^{-1} \text{ cm}^{-1}$ of the main S_0 – S_1 transition at 800 nm (Figure A58 (DCM) in the appendix). This is in accordance with our previous report on the 2,6-diisopropylphenyl (dipp)-substituted monomeric **QBI1**.^[200] However, different from **QBI1**, a distinct difference is observed by switching the solvent from DCM to very unpolar aliphatic solvents such as *n*-hexane. For **QBI-Me** with its unshielded π -surfaces, *n*-hexane is barely able to dissolve it and precipitation occurs. The racemate of **QBI-Me** undergoes fast precipitation into small crystallites, whereas its enantiopure *P/M*-species slowly forms an amorphous and well-dispersed precipitate (for details, see Figure A59 in the appendix). This kinetic self-assembly process was optimized for *n*-hexane by adding 2 mL of a 5 mg mL⁻¹ DCM solution of *P/M*-**QBI-Me** into 50 mL of *n*-hexane to obtain the self-assembled species after 10 h at 8 °C. Decantation and subsequent addition of *n*-hexane led to the disappearance of monomeric species according to UV–vis–NIR spectroscopy. The spectroscopic measurements of this well-dispersed aggregate of enantiopure *P/M*-**QBI-Me** in *n*-hexane could be conducted using the transmission mode with a 1 mm cuvette after ultrasonication. In contrast, the racemic crystallites formed by fast precipitation were not suitable for measurements by this means. Experiments comparing racemic and enantiopure species, including emission data and structural investigation (*vide infra*), are presented in Figure A59 and Figure A64b in the appendix. To provide an appropriate monomeric reference to *P/M*-**QBI-Me**, a kinetically trapped monomeric *n*-hexane solution was prepared by dissolving the compound in boiling solvent and applying additional filtration using a 0.45 μm PVDF syringe filter, allowing measurements within a period of 1 h. The normalized UV–vis–NIR absorption and emission spectra of this monomeric reference and the self-assembled aggregates recorded in *n*-hexane at 295 K are presented in Figure 34a and summarized in Table A12 in the appendix. The monomeric reference shows its absorption maximum of the S_0 – S_1 transition at 778 nm with a bandwidth (the full width at half maximum; fwhm_{abs}) of 810 cm^{-1} measured in *n*-hexane. The absorption maximum of the aggregated species is strongly red-shifted by 1700 cm^{-1} (119 nm), showing a pronounced NIR absorption at 897 nm. The bandwidth narrows down significantly to 530 cm^{-1} (Figure 34a) and the vibronic progression is reduced, which leads to a single sharp absorption band. Both findings are strongly indicating a J-type excitonic coupling in the aggregated state.

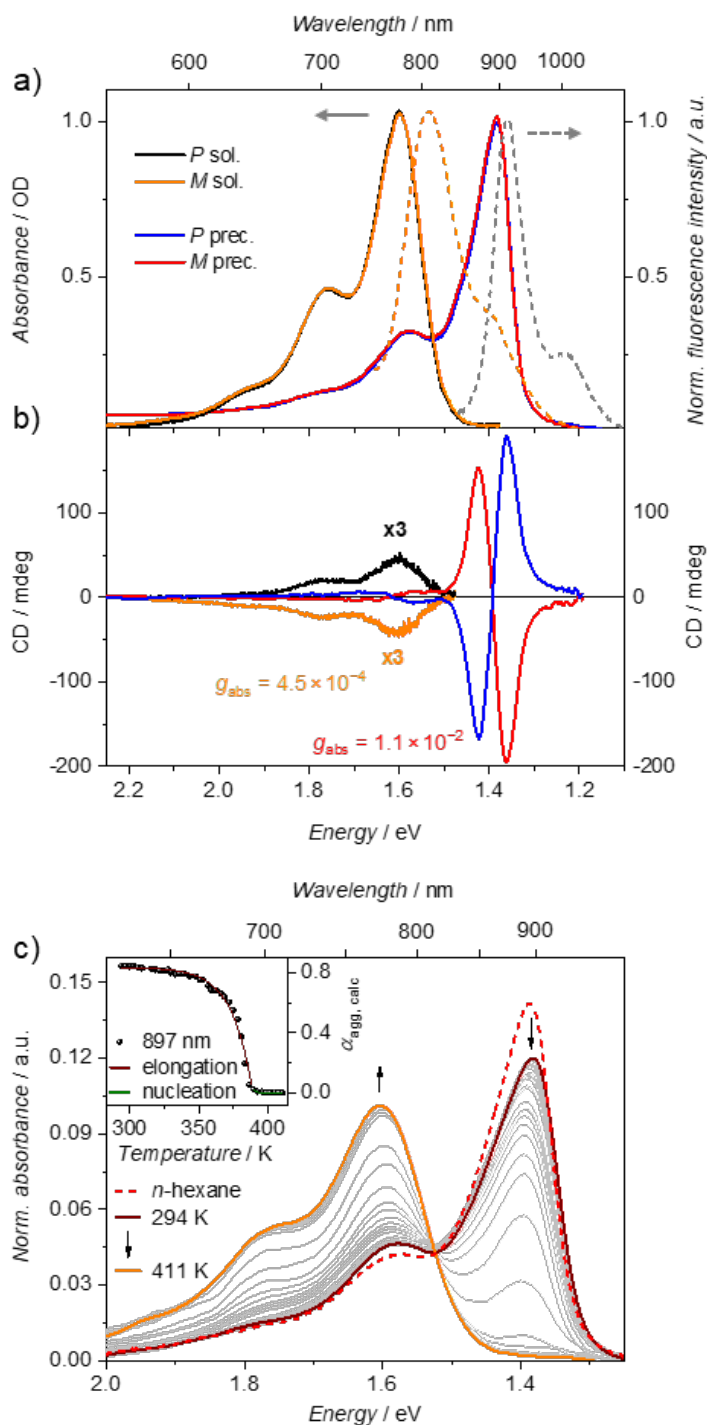


Figure 34. (a) UV-vis-NIR absorption (solid lines) and normalized emission (dashed lines) as well as (b) CD spectra of *P*- and *M*-QBI-Me in *n*-hexane at 295 K. The kinetically trapped monomeric solution [black (*P*) and orange (*M*)] is scaled by a factor of 3. Spectra of suspended J-aggregates are shown in blue (*P*) and red (*M*), (bottom), respectively. Absorption and emission measurements were conducted in the transmission mode and front-face setup, respectively [λ_{ex} (monomer) = 698 nm, λ_{ex} (J-aggregate) = 822 nm]. (c) UV-vis-NIR absorption spectra for the disassembly process of *M*-QBI-Me in paraffin oil were recorded with an optical microscope coupled into a CCD-spectrometer upon heating up to 411 K along with the reference species recorded in *n*-hexane (dashed red line). The inset shows the degree of aggregation $\alpha_{\text{agg, calc}}$ in paraffin oil at 897 nm along with the fitting curves (green, dark red) for nucleation and elongation, respectively.

To probe the conversion between monomer and aggregate, we chose to track the temperature-dependent disassembly due to the kinetic nature of the self-assembly process. To guarantee an artifact-free measurement of the solid-state aggregates, spatially resolved absorption and emission measurements were conducted by using an optical microscope coupled to a spectrometer in either the transmission mode on glass substrates (absorption) or the reflection mode on Si/SiO_x substrates (emission) upon blue light excitation (Figure 34c) and see Figure A60 in the appendix for the emission study and details). The aggregate was suspended in *n*-hexane and transferred into paraffin oil onto the respective substrates. Thereby, the system can be heated to temperatures above 400 K while entailing a similar solvent polarity as *n*-hexane to preserve the spectral position of the monomeric species. Probing this disassembly at a slow heating rate of 3 K min⁻¹ granted insights into the aggregation mechanism of the enantiopure *M*-QBI-Me. While the spatial confinement for spectral recording was kept constant during the heating process, the diffusion of molecules during disassembly could not be completely avoided. Hence, as an approximation, all spectra of the absorption study were corrected for equal total absorbance according to the Kasha exciton theory. This revealed a clear isosbestic point at 813 nm, proving an equilibrium between two defined species. The degree of aggregation $\alpha_{\text{agg,calc}} = 0.85$ in paraffin oil was determined by spectral comparison with the aggregated species in *n*-hexane (see Figure 34c) and Figure A60 in the appendix). We then could make use of the hereby obtained temperature-dependent UV-vis-NIR spectra at the absorption maximum of the aggregate by applying the cooperative nucleation-elongation model by Meijer, Schenning, and van der Schoot.^[276] This provided an accurate fit below the elongation temperature $T_e = 389 \pm 1$ K, revealing an enthalpy of $\Delta H = -83 \pm 3$ kJ/mol during the elongation process, quite similar to literature known H-bonded PBI J-aggregates.^[277] We were able to even estimate the equilibrium constant $K_a = 2.4 \pm 0.9 \times 10^{-4}$ of the activation step at T_e , indicating a high degree of cooperativity reasonable for the formation of extended aggregates. We like to note that the thermally induced disassembly occurs much faster than the racemization of the QBIs ($\Delta G^\ddagger \approx 125$ kJ mol⁻¹ in 1,1,2,2-tetrachloroethane at 398 K^[200]). Thus, the enantiopurity can be preserved after disassembly by fast heating to > 400 K (Figure A61 in the appendix).

J-aggregates have been proven to show sharp and intense emission bands, which are very desirable, particularly in the NIR spectral region.^[73, 83, 245, 270-271, 273] We were indeed able to observe sharp emission ($\text{fwhm}_{\text{em}} = 590$ cm⁻¹) of the suspended aggregate at 912 nm (Figure 34a). We chose a front-face setup to suppress reabsorption effects of the aggregate with

its small Stokes-shift ($\Delta\tilde{\nu}_{\text{Stokes}}$) of only 180 cm^{-1} . As a reference, we also recorded the emission of the monomeric *n*-hexane solution within the same sample geometry. We obtained the spectral signature of the kinetically trapped monomer, revealing the maximum at 811 nm, which showed a considerably larger $\Delta\tilde{\nu}_{\text{Stokes}}$ of 520 cm^{-1} with a doubled fwhm_{em} of 1080 cm^{-1} (see Table A12).

5.4 Chiroptical Properties

The high conformational stability of the axially chiral QBI monomers with a racemization barrier of about 125 kJ mol^{-1} at 398 K ^[200] allowed us now to investigate the transition from molecular to supramolecular chirality using circular dichroism (CD) spectroscopy. First, the monomer was investigated in DCM solution as well as in *n*-hexane as a kinetically trapped solution. Both monomeric species show a strong monosignated CD band of their S_0-S_1 transition following the spectral progression of the respective absorption measurement with maxima at 800 nm (DCM, $\Delta\epsilon \approx \pm 44\text{ M}^{-1}\text{ cm}^{-1}$, Figure A58) and at 778 nm (kinetically trapped *n*-hexane solution, $\theta \approx 15\text{ mdeg}$ at OD = 1, Figure 34b). As usual for chiral PAHs, a positive sign of the lowest-energy branch of the CD spectrum corresponds to the *P*-enantiomer (and a negative sign to *M*), which is confirmed by TD-DFT calculations (vide infra). For these monomeric spectra, absorption dissymmetry factors g_{abs} of 4.5×10^{-4} were calculated by $g_{\text{abs}} = \epsilon/\Delta\epsilon$ (DCM) or $g_{\text{abs}} = \theta/(32980 \times \text{OD})$ (*n*-hexane), respectively, and are within the typical range for small organic molecules.^[200] However, when forming the J-aggregate in *n*-hexane, the excitonic coupling gives rise to a bisignated CD signal (couplet) maximized at 871 and 911 nm with a conservative sign obeying the exciton-chirality rule. The dissymmetry factor is increased by almost 2 orders of magnitude to 7.0×10^{-3} (869 nm) and 1.1×10^{-2} (935 nm), respectively, while crossing zero at 903 nm close to the absorption maximum at 897 nm. To the best of our knowledge, this is the highest g_{abs} value for a chiral PAH molecule reported this far in the NIR regime. Due to strong J-type excitonic coupling, the vibrational progression is fairly suppressed, which becomes apparent around the zero-crossing of the vibrational shoulder at 767 nm.^[278] Despite the high absorption dissymmetry, circularly polarized luminescence could unfortunately not be elucidated by our instrument this far in the NIR spectral range.

5.5 Structural Properties

The structural elucidation of the J-aggregate was approached by a combination of atomic force microscopy (AFM), X-ray single-crystal structure analysis, and molecular modeling. For AFM measurements (Figure 35a), 60 μL of a freshly prepared aggregate suspension (500 μg of *P/M/rac*-QBI-Me added to 20 mL of *n*-hexane) was spin-cast onto a highly ordered pyrolytic graphite (HOPG) substrate.

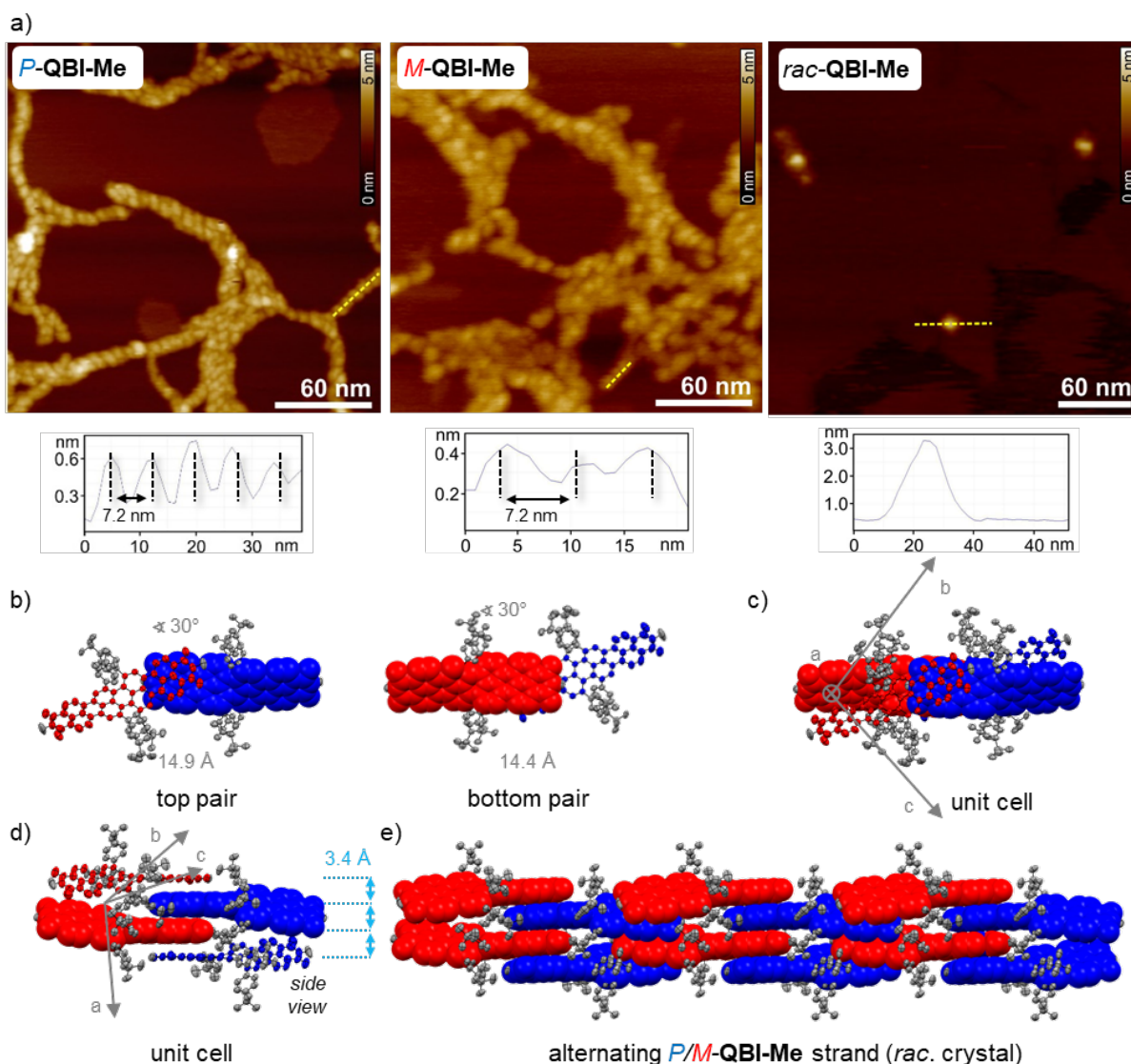


Figure 35. (a) AFM topography of self-assembled *P*- (left), *M*- (center), and *rac*- (right) QBI-Me after spin-casting on HOPG substrates. The insets show the cross-section analyses from yellow dashed lines in the corresponding AFM images. (b–d) Molecular arrangement of the *P*- and *M*-atropo-enantiomers as determined from the single-crystal structure obtained from their racemic mixture. Two pairs (bottom and top) of next neighbored *P*- and *M*-enantiomers (blue and red) are shown in top view (b). The entire unit cell is shown in (c,d). The infinite translation of the unit cells is shown in side view (d). Angles between the QBI's N_2N' -axes and unit cell axes are shown in gray. Center-to-center distances (gray) and closest distances between π -planes (light blue) are indicated as well. The ellipsoids are set to 50% probability. Disorder, hydrogen atoms, and solvent molecules are omitted for clarity.

Rod-like aggregates with a length of up to 200 nm and a diameter of 2.0 ± 0.2 nm were revealed for the enantiopure *P/M*-species. The enantiopure aggregate structures clearly reveal a right (*P*) or left (*M*) handed helicity, each with an identical helical pitch ($p/2$) of 7.2 ± 0.6 nm. At this point, we want to stress the kinetic hierarchical self-assembly. Thus, in *n*-hexane, the enantiopure aggregates undergo further aging (days to weeks) toward even more extended structures. AFM data of corresponding agglomerates reveal much more expanded rod-like structures with 12 nm diameter (see Figure A62 in the appendix). The AFM measurement of the racemate, in contrast, only shows small particles with diameters of 2.9 ± 0.2 nm (Figure 35a, right, Figure A63 in the appendix) with no signs of any further aging. We related these AFM observations to the molecular arrangement within the enantiopure J-aggregate by deducing the fundamental packing geometry obtained from single-crystal X-ray diffraction (XRD) analysis of single-crystals of *rac*-**QBI-Me** grown by the slow diffusion method of methanol into a chloroform solution. Unfortunately, we could not obtain enantiopure single crystals of sufficient size and quality for XRD. *Rac*-**QBI-Me** crystallizes as a 1:1 racemic mixture in a $P\bar{1}$ space group and its unit cell contains two *P*- and *M*-atropo-enantiomers, each. The molecular structure reveals a close spatial proximity of the two adjacent phenyl substituents at each side along the ribbon. These phenyl rings come as close as van der Waals distances of about 3.5 Å and interlock with each other entailing a rotational twist of the central part of the π -backbone (Figure 33 and Figure 35b–e). Hence, the two inner naphthalene subplanes enclose a large dihedral angle of 33° , while the outmost naphthalene subunits remain planar. This renders a large π -surface accessible to neighboring molecules to form the collinear slip-stacked geometry. By this means, two pairs of *P*- and *M*-enantiomers, top and bottom (Figure 35b), are present. The chromophores of these pairs include a 30° angle between corresponding QBI's *N,N'*-axes and are separated by equal center-to-center distances of 14–15 Å. When forming the unit cell by superimposing both pairs, the central QBIs are in perfect collinear alignment at the same center-to-center distance (Figure 35c,d). The outer naphthalene subplanes of all QBIs within the unit cell form a fourfold stack with overall equal π - π distances of about 3.4 Å.

Thus, the unit cell translates along the *cb*-axis orientation into a closely packed slip-stacked alternating fourfold strand (Figure 35e, for an overview see Figure A65). We could indeed correlate this to the precipitated microcrystallites, which were spin-cast on silicon wafers (Si/SiO_x, Figure A64a). The microcrystals of the racemate show birefringence as well as strong optical anisotropy as deduced from polarization-dependent microscopy.

Taking up this extended slip-stacked chromophore arrangement, we expected its underlying packing motif likewise for the enantiopure J-aggregates of *P*- or *M*-QBI-Me but with unidirectional helicity. Hence, we mimicked an enantiopure *M*-unit cell by mirroring the two *P*-enantiomers of the racemate (Figure 35d). The resulting unit cell was translated 20 times by 14.8 Å and rotated by 36° counterclockwise, each time. The resulting superhelix of 720° turn in total was then force-field optimized by using the COMPASS tool of Materials Studio software to eventually obtain a structural model of the J-aggregate built up from the four *M*-enantiomers A–D (Figure 36, for further details and reference computations, see Figure A66 in the appendix).

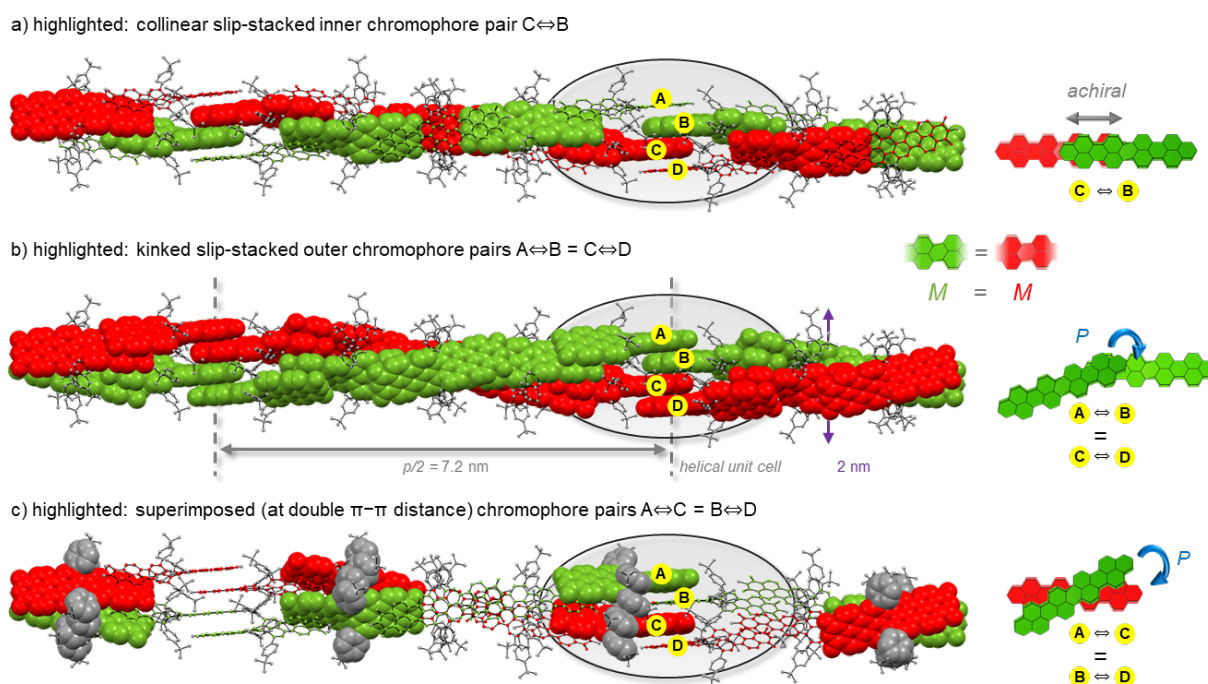


Figure 36. Structural model of the enantiopure *M*-superhelix built from *M*-QBI-Me chromophores derived from their molecular packing in the racemic crystal structure in three different representations (spacefill as well as ball and stick model, a–c, left) along additional schematic depictions of the corresponding pairs of QBI chromophores in the top view (a–c, right). QBIs are denoted in green and red, respectively, to guide the eye to the counterclockwise *M*-type propagation of the two intertwining slip-stacked double strands [highlighted in (a,b)] forming the fourfold strand. The clockwise orientation of top-stacked chromophores within their counterclockwise intertwining double strands is highlighted in (c). The helical unit cell indicating the individual chromophores A–D (highlighted with yellow) translates into the superhelix by incremental rotating of 36°. The shown structure represents the middle section (252°) of the 720° section, which was calculated in total. The structure optimization was done using the COMPASS tool of Materials Studio software. The helical half-pitch $p/2$ (gray, calculated with centroids) and the mean distance between the outmost carbon atoms of *tert*-butyl units (violet) are indicated as well as the mutual orientation of chromophore pairs in either clockwise (*P*, blue) or collinear (achiral, gray) arrangement.

The measures of this optimized fourfold-stranded *M*-superhelix are in excellent agreement with the AFM parameters of the freshly prepared aggregates. They reveal a helical half pitch ($p/2$) of 7.2 nm length and a diameter of 2 nm measured between the outmost carbon atoms of the

aryl *bay*-substituents within the presented model. The whole fourfold stranded J-aggregate can be displayed in three different representations, each highlighting a different dimeric packing motif of the four *M*-QBI-Me chromophores A–D, comprising the basic elongation unit. First, the slip-stacked chromophore pair C \leftrightarrow B (Figure 36a) forms the inner core structure of the fourfold strand by showing the strongest π – π -overlap among all other QBI pairs. This pair itself is in perfect (achiral) collinear alignment but imparts the *M*-type (counterclockwise) helicity into the superstructure by the core twist of each individual chromophore (see also Figure 32b). This supramolecular helicity now grows most prominent for the two equal slip-stacked outer pairs A \leftrightarrow B and C \leftrightarrow D (Figure 36b). The angles of the QBI's *N,N'*-axes of the respective pairs narrow down from 30° to 18° compared to the racemic packing (Figure 35d) and show an overall clockwise (positive, *P*) mutual orientation. The propagation of these two kinked slip-stacked pairs can be seen as two slip-stacked double strands (Figure 36b, green and red) intertwining each other in the counterclockwise (*M*) sense. Already within this depiction, it becomes apparent that the QBI pairs A \leftrightarrow C and B \leftrightarrow D, top-stacked at double π – π distance, are also in clockwise orientation likewise to the kinked QBIs A \leftrightarrow B and C \leftrightarrow D. This *P*-type handedness might be surprising but is a geometrical necessity for all *M*-intertwining double-strands that string up at small angles below 90°. Figure 36c shows these two pairs, A \leftrightarrow C and B \leftrightarrow D, in detail and highlights their π -stacked *bay*-phenyl substituents. Hence, the *P*-chiral arrangement of these superimposed QBI pairs is guided by the helical enclosing of four adjacent phenyl units. Therefore, the interlocking of the phenyl units of each chromophore not only grants stable monomeric axial chirality but also ensures the conformational stability of the overall *M*-superhelix of the J-aggregate. The elucidation of observed strong chiroptical signatures by theoretical means of all pairs of *M*-QBI-Me within an *M*-superhelix will be discussed in the following.

5.6 Theoretical Calculations of Chiroptical Response

Electronic circular dichroism (ECD) spectra were calculated by TD-DFT on a purely electronic approach on the ω B97XD/def2SVP level of theory. The obtained rotatory strength $R = \mathbf{m}\boldsymbol{\mu} \cdot \cos(\alpha)$ calculated from the magnetic (\mathbf{m}) and electric ($\boldsymbol{\mu}$) transition dipole moments and their respective angle (α) is rather sensitive to the geometrical distortion imparted by the chromophore packing in the J-coupled superhelix. Thus, we re-modeled the enantiopure unit cell with geometry-optimized monomers and adapted the crucial packing parameters (see

Figure A66c). The monomers were slightly simplified by replacing the *tert*-butyl units of the *bay*-substituents by hydrogen atoms. The corresponding monomeric ECD spectrum is in excellent agreement with the experiment (Figure A67 in the appendix). Next, the pairs of *M*-QBI-Me $C \leftrightarrow B$, $C \leftrightarrow D$, and $C \leftrightarrow A$ were simulated likewise (see Figure A68, Table A14 in the appendix for the following discussion). These ab initio calculations provide two low energy excitations each, which can be interpreted as coupled states along their respective *R* with coupling strengths of 660–780 cm^{-1} . Hence, the superimposed *P*-type pair $C \leftrightarrow A$, whose QBIs lie on top of each other, shows a bisignate ECD spectrum with a positive *R* for the low-energy branch. Its oscillator strength is mainly stored in the high-energy branch. Both would be reasonable for a H-type excitonic coupling. Besides, the kinked slip-stacked pair $C \leftrightarrow D$ ('creeper'-type^[47-48]) shows a strong negative Cotton-effect even though its clockwise +18° orientation. The collinearly aligned slip-stacked dimer $C \leftrightarrow B$ shows (almost) no bisignate ECD spectrum and only a single negative ECD band, hence correctly accounting for its achiral supramolecular orientation.

The opposite ECD signs of $C \leftrightarrow A$ and $C \leftrightarrow D$, even though both pairs' chromophores are in clockwise orientation, motivated for deeper analysis of the intermolecular coupling. Experimentally, the coupling strengths can be assessed by the maxima of the experimental CD bands, revealing a value of 500 cm^{-1} . For simulation of the excitonic coupling, however, ab initio TD-DFT calculations of multi-chromophore systems are rather unreliable (see the appendix).^[279-280] Thus, we determined the overall intermolecular coupling J_{total} by the combination of transition charge method accounting for long-range Coulomb-coupling as well as Amsterdam density functional calculations for charge-transfer-mediated short-range coupling (Figure 37a and Table A15 and Table A16 in the appendix), as established for PBI aggregates.^[119] We like to note that it is the large QBI transition dipole moment ($\mu_{\text{exp}} = 11.6 \text{ D}$), which maintains a sufficient Coulomb-coupling even at long center-to-center distances of almost 15 Å compared to similar PBIs.^[281] In total, reasonable J_{total} values of slip-stacked pairs of -807 cm^{-1} (100 meV, $C \leftrightarrow B$) and -404 cm^{-1} (50 meV, $C \leftrightarrow D$) as well as -258 cm^{-1} (32 meV) for the superimposing pair ($C \leftrightarrow A$) could be obtained. All dimers show a negative J_{total} and hence suggest J-type excitonic coupling. This might be surprising for the top-stacked $C \leftrightarrow A$ but could be clearly attributed to the twisted and displaced mutual orientation of the chromophores. When $C \leftrightarrow A$ is artificially parallelized into a perfectly superimposing arrangement, a positive J_{total} and hence H-type coupling was obtained in corroborating reference calculations (see Figure A70 and Table A17).

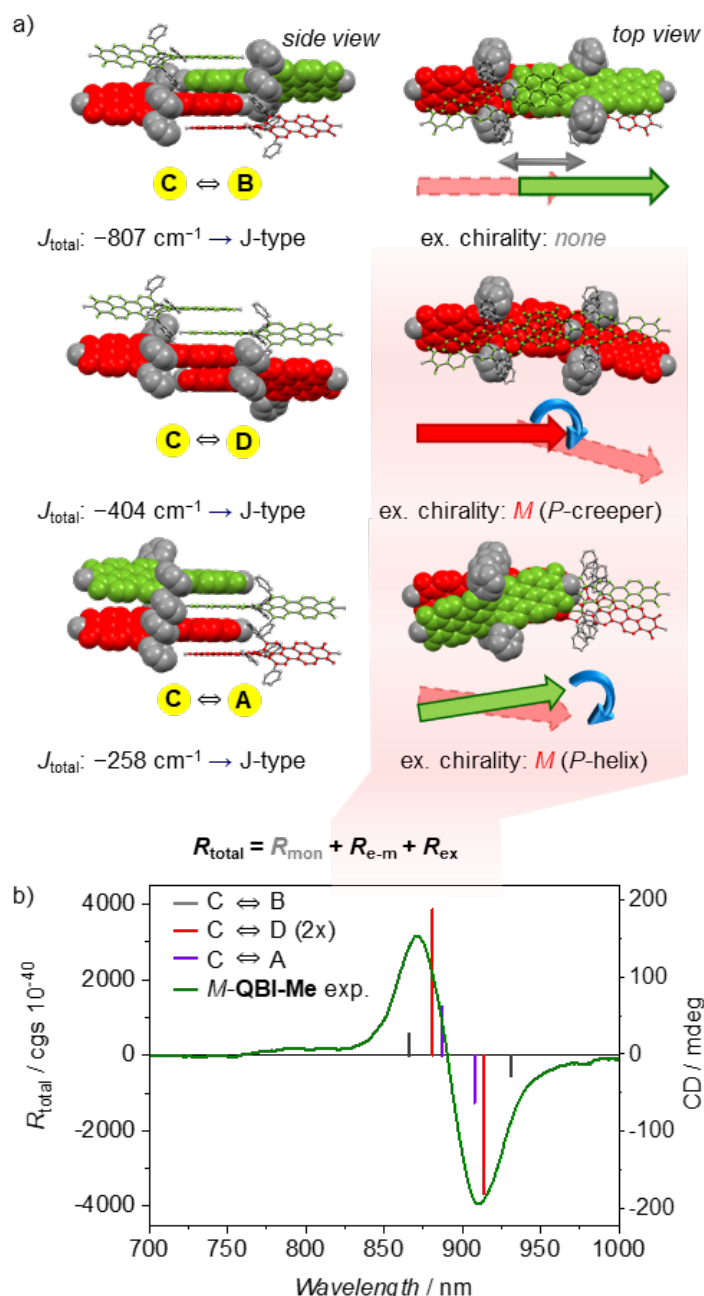


Figure 37. (a) Molecular geometries of dimers of *M*-QBI-Me (monomers DFT optimized) forming the core-unit of the modeled J-aggregate *M*-superhelix in side (left) and top (right) view. The arrows highlight the mutual chromophore orientation. (b) Experimental CD spectrum (green solid line) and calculated rotatory strengths of the three dimers derived from the modified Rosenberg equation.^[48] $C \rightleftharpoons D$ values are doubled to adequately represent the core unit of the infinite aggregate.

The simulated coupling strengths now allow us to interpret the mutual orientation of the chromophores. The clockwise *P*-handedness of the two chiral pairs of QBIs is indeed congruent with the common exciton chirality method^[46, 50] when considering their J-type coupling, which was just recently provided with theoretical understanding by Painelli and George Thomas and co-workers.^[47-48] Accordingly, attractive coupling interaction leads to a negative cotton effect

even though chromophores are in a right-handed arrangement. The alleged sign-flip arises from the inversion of excitation energies of the in-phase and out-of-phase combination for J- and H-type coupling, respectively.

Thus, we calculated R of the monomers and of all dimers by applying the expanded Rosenfeld equation as the sum of monomeric contribution (R_{mon}), electro-magnetic coupling ($R_{\text{e-m}}$), and excitonic contribution (R_{ex}) by using the monomeric \mathbf{m} and $\boldsymbol{\mu}$ as well as the geometric parameter from the enantiopure unit cell of the J-aggregate (Figure 37 and see the appendix for details). By this means, the contribution of the superimposing pair $C \Leftrightarrow B$ is restricted to R_{mon} and $R_{\text{e-m}}$ due to the perfectly collinear but achiral arrangement. In contrast, the slip-stacked pairs $C \Leftrightarrow D$ and $C \Leftrightarrow A$ are governed mainly by the excitonic contribution. For the low-energy branch, $R_{\text{total } \lambda^+}$ sums up to -544 ($C \Leftrightarrow B$), -1833 ($C \Leftrightarrow D$), and -1252×10^{-40} esu² cm² ($C \Leftrightarrow A$), respectively (see Table A16). The outer kinked collinear dimer $C \Leftrightarrow D$ ('creeper') is dominant due to its prominent charge-transfer coupling. Additionally, its contribution can be doubled by simple geometric considerations to account for the infinite extent of the core unit within the double strand (Figure 37b). Thus, even with this simple approach, we could successfully demonstrate that the interlocking phenyl *bay*-substituents serve two functions. They ensure the conformational stability of the individual molecules and guide the QBI's self-assembly into the required handedness of the entire J-aggregate to reach a strong chiroptical response in the NIR.

5.7 Conclusion

In summary, we presented the first enantiopure J-aggregate of a stable axial chiral rylene bisimide dye showing strong excitonic chirality of its main optical S_0 – S_1 transition. A strong CD couplet centered deep in the NIR region at 903 nm with high dissymmetry factors of up to 1.1×10^{-2} at 935 nm could be achieved. The high solubility of the tetra-arylated quaterrylene bisimide **QBI-Me** allowed for the cooperative self-assembly in low polarity *n*-hexane purely relying on weak van der Waals interactions enabled by the accessible large π -planes. Accordingly, we could successfully develop our concept of chiral interlocking phenyl *bay*-substituents from a molecular to a supramolecular level. Hence, the phenyl units attached to the chromophore cores not only grant conformational stability of the monomers but impart a supramolecular guiding into the helical J-aggregate. In our structural model of a slip-stacked intertwined fourfold-strand, we could highlight the geometrical necessity of *P*-type handedness of close pairs of QBI chromophores to form an overall *M*-superhelix. The high photostability, spectral position in the NIR, and accessibility in the solid state render our aggregate suitable for incorporation into active host materials for chiral sensing devices.

CHAPTER 6

—

Summary and Conclusion

Perylene bisimide (PBI) dyes combine a variety of both chemical and physical properties, which render them as highly versatile chromophores for tailor-made applications such as biomedical markers, fluorescence probes, or as molecular materials in organic electronics. PBIs show a high propensity for self-assembly due to their extended π -scaffold, enabling their utilization as supramolecular materials. The key characteristic of these PBI-based supramolecular assemblies is the possibility for strong excitonic coupling of multiple chromophores. This results in appreciable features like hypso-/bathchrommically shifted absorption/emission bands as well as improved exciton and charge transport. Besides the research field of organic chromophores, such excitonic coupling is also fundamental for the understanding of chirality, both molecular as well as supramolecular. The interest in the chiroptical properties of enantiopure materials has considerably grown within the last decade. However, materials from excitonically coupled inherently chiral PBIs are underdeveloped. This thesis aimed to investigate the chiral core-twisted fourfold *bay*-arylated perylene motif regarding its implementation into a series of PBI derivatives meant for use in organic thin-film devices. The prospect for thin-film devices made from chiral organic materials lies in their ability to selectively absorb or emit left- and right-circularly polarized light for applications such as photodiodes, phototransistors, and chiral OLEDs. Additionally, these materials hold promise for spintronic applications envisioned to differentiate electron spins. However, for realizing such sophisticated devices, it is indispensable to evaluate the fundamental material properties of new organic semiconductors, such as morphology forming and charge transport properties in a robust architecture such as a bulk heterojunction (BHJ) organic solar cell (OSC). The twist-imparted high solubility, broad absorption properties, and electronic tunability by chemical modification in both aryl and imide position renders these PBIs as ideal candidates for non-fullerene acceptors in combination with donor-polymers as active layers in OSCs.

In *Chapter 3*, two series of inherently chiral core-twisted *bay*-arylated PBIs were utilized as non-fullerene acceptors (NFAs) in combination with the donor polymer **PCE-10** within an inverted BHJ architecture by solution processions (Figure 38). In a comprehensive study on the

variation of either imide (**1a–1e**) and aryl (**1b–5b**) substituents, 2,6-diisopropylphenyl (imide) and 2-naphthyl (aryl) were determined as the best substituents for PBI-based NFAs. Thus, the corresponding derivative **2e** inheriting both substituents reached a peak performance of 4.3% PCE_{max} , that was at that time the highest OSC efficiency of a single core PBI without lateral π -extension or embedding of heteroatoms, so far. The OSC results were correlated with chromophore packing deduced by single crystal structure analysis of the PBIs in racemic mixtures. Interestingly, the more isolated and shielded chromophores **1e** and **2e** with almost no π - π interactions gave the highest device performance over 4.0% PCE_{max} (see Figure 38).

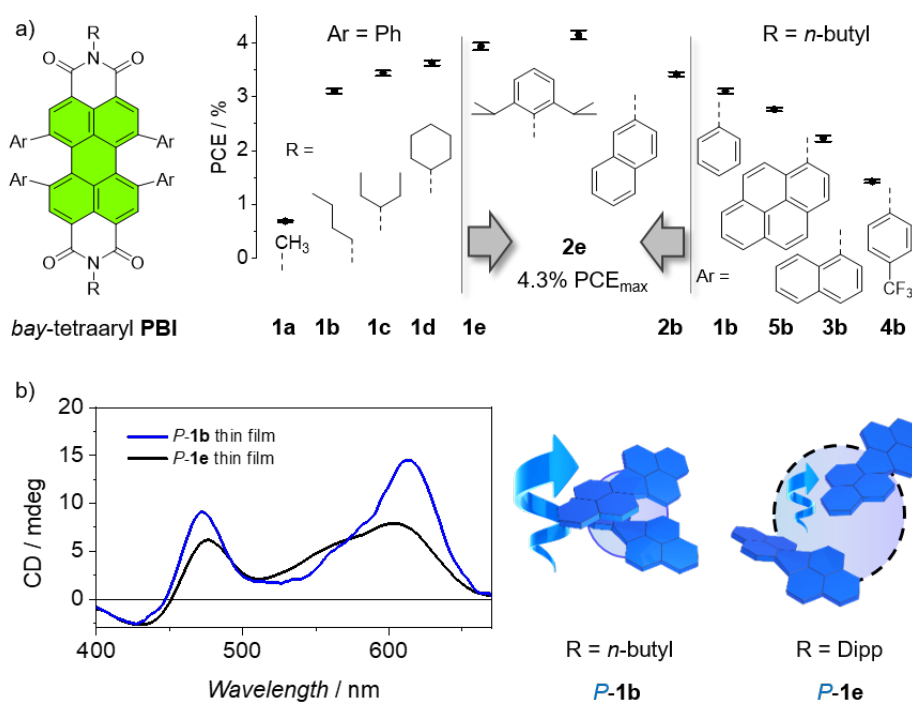


Figure 38. (a) Chemical structure of bay-tetraarylated PBIs along with their respective device performances of PCE-10-based iBHJ OSCs of racemic mixtures of **1a–1e** (left) and **1b–5b** (right). (b) CD absorption spectra of neat thin films of spin-cast *P-1b* (blue) and *P-1e* (black) along a sketch of their respective mutual chromophore arrangements as stacked dimers (*P-1b*) or isolated monomers (*P-1e*) as deduced by single-crystal X-ray analyses. The helical arrows represent the magnitude of chiroptical response.

In **2e**, the shielding of the chiral core twist by the substituents was most pronounced and did not even allow for the separation of the enantiomers. However, the effect of enantiopurity on the device performance could be investigated for the two bay-phenyl substituted **1b** and **1e** with either small *n*-butyl or bulky Dipp substituents, respectively. For **1e**, no difference in the device performance was observed for racemic mixtures or isolated enantiomers of **1e** due to similar overall isolated chromophores. In contrast, the *n*-butyl substituted **1b** revealed a relative performance increase of up to 20% when using the enantiopure instead of the racemic NFA. CD spectroscopy of the respective neat films and polymer blends revealed a unique signature

of upcoming positive excitonic coupling for *P*-**1b**, which corroborated its isolated dimeric entities of π -stacked chromophores that were found in the enantiopure single-crystal structure. In contrast, its racemic mixture shows a closely packed slip-stacked arrangement of alternating *P*- and *M*-chromophores resulting in a lower device performance.

In *Chapter 4*, the twisted π -backbone of the PBIs was expanded to the corresponding configurationally stable helically twisted quaterylene bisimides (QBIs). The first two members of this new class of nanoribbons show an either onefold (**QBI1**) or twofold (**QBI2**) twisted π -scaffold (Figure 39).

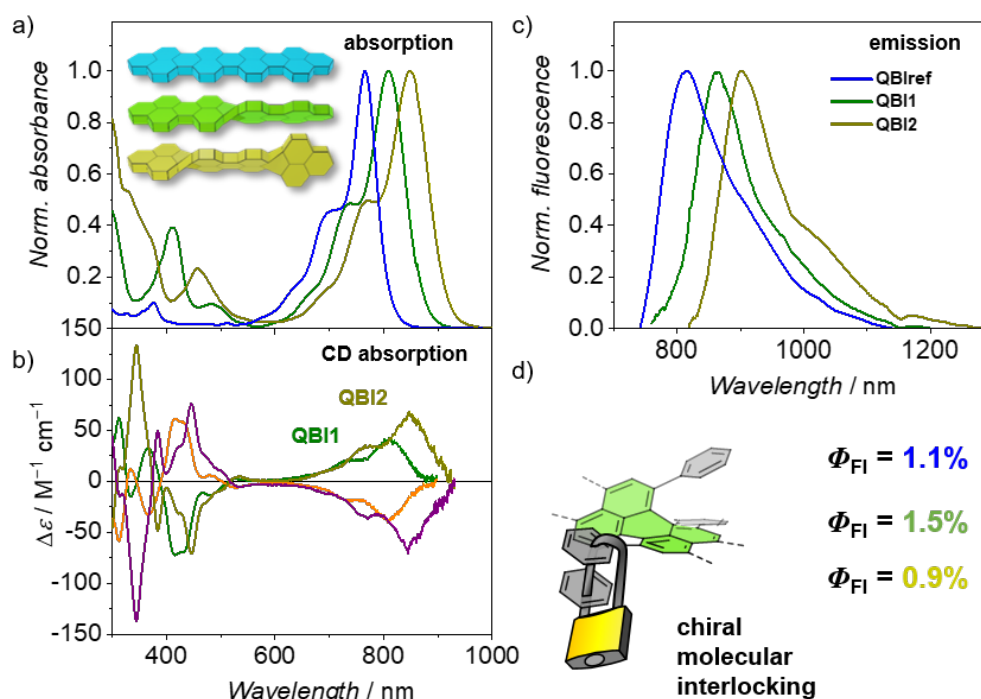


Figure 39. (a) UV–vis–NIR absorption, (b) CD absorption and (c) emission spectra of planar **QBIref** (blue), onefold twisted *P*-**QBI1** (green) and twofold twisted *P*-**QBI2** (dark yellow) in DCM at 295 K. The *M*-enantiomers of **QBI1** and **QBI2** are shown in (b) in orange and violet, respectively. (d) Sketch of the chirally interlocked perylene motif via their phenyl *bay*-substituents along the fluorescence quantum yields of **QBIref**, **QBI1** and **QBI2**.

This could be synthetically accomplished by either a palladium-catalyzed annulation^[236] (**QBI1**) or a zinc-mediated Ullmann-type homocoupling^[238] (**QBI2**) reaction, respectively. The high solubility and the extraordinary configurational stability of the isolable atropo-enantiomers of the QBIs are comparable to corresponding core-twisted PBIs. The twist-induced rigidification of the backbone was unambiguously proven by single-crystal X-ray analyses, showing a stable end-to-end twist of up to 76° for the twofold twisted **QBI2**. In contrast to the core-twisted PBIs, the conformational interlocking of the phenyl *bay*-substituents revealed an unexpected and unique consequence for the core-enlarged and near-infrared (NIR) responsive

QBIs. Thus, sharp emission bands with a small Stokes shift in the NIR region at 862 nm (**QBI1**) and 903 nm (**QBI2**) as well as impressive fluorescence quantum yields of 1.5 and 0.9% could be obtained for these small band gap chromophores, respectively. A large chiroptical response could be achieved for the monosignated S_0 – S_1 CD band with a $\Delta\epsilon$ of up to 40 or 67 $M^{-1} \text{ cm}^{-1}$ at 809 and 849 nm for **QBI1** and **QBI2**, respectively.

In *Chapter 5*, the onefold twisted QBI motif was substituted with small methyl units at its imide positions to enable self-assembly of the resulting **QBI-Me** facilitating excitonic coupling for strong chiroptical NIR response. Thus, the first enantiopure J-aggregate of a stable axial chiral rylene bisimide could be achieved, which showed strong excitonic chirality of its main optical S_0 – S_1 transition (see Figure 40).

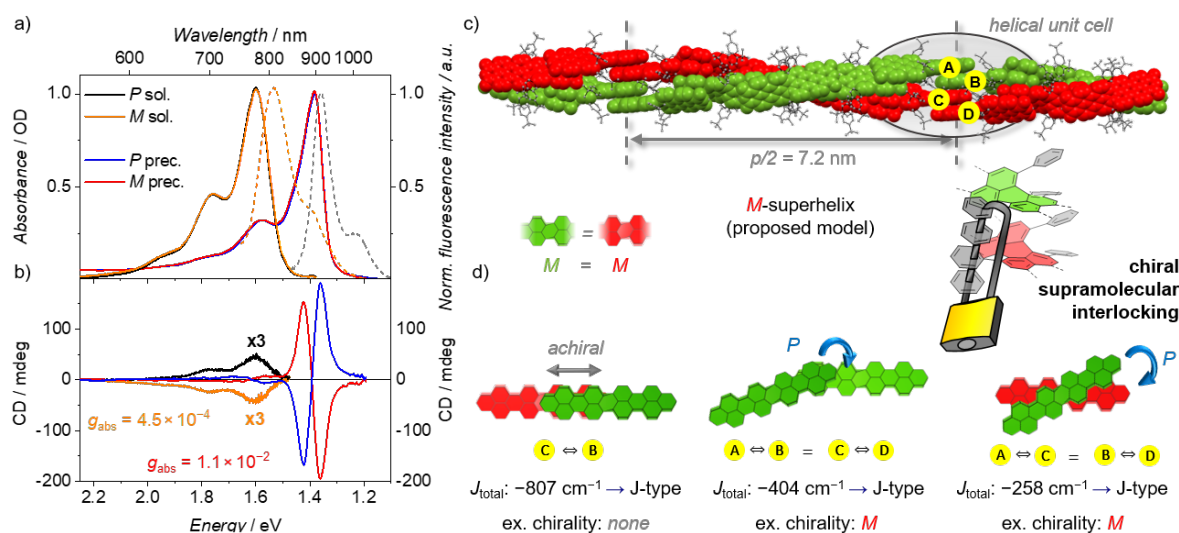


Figure 40. (a) UV–vis–NIR absorption (solid lines) and normalized emission (dashed lines) as well as (b) CD spectra of *P*- and *M*-QBI-Me in *n*-hexane at 295 K. The kinetically trapped monomeric solution [black (*P*) and orange (*M*)] is scaled by a factor 3. Spectra of suspended J-aggregates are shown in blue (*P*) and red (*M*), respectively. Absorption and emission measurements were conducted in the transmission mode and front-face setup, respectively. (c) Structural model of intertwined fourfold stranded *M*-superhelix as obtained by cooperative assembly of *M*-QBI-Me in *n*-hexane stabilized by chiral supramolecular interlocking of the phenyl *bay*-substituents. (d) Pairs of *M*-QBIs (green and red) and their mutual chromophore arrangement building up the *M*-superhelix as well as their calculated coupling energies and the resulting type of excitonic chirality.

Its CD couplet is centered deep in the NIR region at 903 nm and shows high dissymmetry factors of up to 1.1×10^{-2} at 935 nm. The twist-imparted high solubility of **QBI-Me** allowed for the cooperative self-assembly in low polarity solvents like *n*-hexane purely relying on weak van der Waals interactions enabled by the accessible large π -planes. Accordingly, the concept of the interlocked chirality of twisted perylene core was promoted from a molecular to a supramolecular level. The phenyl units attached to the chromophore cores now serve two purposes. First, they grant conformational stability of the inherently chiral monomers. Second,

they serve as a supramolecular guide of the chromophores into their mutual arrangement within the J-aggregate. For this J-aggregate, a structural model of a slip-stacked intertwined fourfold-stranded superhelix was rationalized. It highlights the geometrical necessity of *P*-type handedness of the mutual arrangement of close pairs of *M*-QBI-Me chromophores to form an overall ‘creeper’-type *M*-superhelix (and vice versa for *P*-QBI-Me) meeting the conformational demands for strong J-type excitonic chirality.

In summary, the chirality of the interlocked *bay*-arylated perylene motif was investigated upon its material prospect and the enhancement of its chiroptical response to the NIR spectral region. A considerable molecular library of inherently chiral PBIs was utilized as NFAs in OSCs to provide decent device performances and insights into the structure-property relationship of PBI materials within a polymer blend. For the first time in the family of core-twisted PBIs, the effects of enantiopurity on the device performance was thoroughly investigated. The extraordinary structural sensitivity of CD spectroscopy served as crucial analytical tool to bridge the highly challenging gap between molecular properties and device analytics by proving the excitonic chirality of a helical PBI dimer. The chirality of this perylene motif could be further enhanced on a molecular level by both the expansion and the enhanced twisting of the π -scaffold to achieve a desirable strong chiroptical NIR response introducing a new family of twisted QBI-based nanoribbons. These achievements could be substantially further developed by expanding this molecular concept to a supramolecular level. The geometrically demanding supramolecular arrangement necessary for the efficient excitonic coupling was carefully encoded into the molecular design. Accordingly, the QBIs could form the first J-type aggregate constituting a fourfold-stranded superhelix of a rylene bisimide with strong excitonic chirality. Therefore, this thesis has highlighted the mutual corroboration of experimental and theoretical data from the molecular to the supramolecular level. It has demonstrated that for rylene bisimide dyes, the excitonic contribution to the overall chiroptical response can be designed and rationalized. This can help to pave the way for new organic functional materials to be used for chiral sensing or chiral organic light-emitting devices.

CHAPTER 7

—

Zusammenfassung und Fazit

Perylenbisimid (PBI)-Farbstoffe vereinen eine Vielzahl chemischer und physikalischer Eigenschaften, was sie zu äußerst vielseitigen Chromophoren für maßgeschneiderte Anwendungen wie biomedizinische „Marker“, Fluoreszenzsonden oder molekulare Materialien in der organischen Elektronik macht. PBIs zeigen aufgrund ihres ausgedehnten π -Gerüsts eine hohe Neigung zur Selbstorganisation, was ihre Verwendung als supramolekulare Materialien ermöglicht. Das Schlüsselmerkmal von PBI-basierten supramolekularen Strukturen ist die Möglichkeit zur starken exzitonischen Kopplung mehrerer Chromophore. Dies führt zu bemerkenswerten Eigenschaften wie hypsochrom/bathchrom verschobenen Absorptions-/Emissionsbanden sowie verbessertem Exziton- und Ladungstransport. Neben dem Forschungsfeld organischer Chromophore ist eine solche exzitonische Kopplung auch für das Verständnis der Chiralität grundlegend, sowohl auf molekularer als auch auf supramolekularer Ebene. Das Interesse an den chiroptischen Eigenschaften enantiomerenreiner Materialien ist in den letzten Jahren erheblich gewachsen. Allerdings ist unter den untersuchten Materialien der Anteil von exzitonisch gekoppelten, inhärent chiralen PBIs noch vergleichsweise gering. In dieser Arbeit wurde das chirale, vierfach Bucht-arylierte und dadurch kernverdrillte Perylen-Motiv im Hinblick auf seine Umsetzung in einer Reihe von PBI-Derivaten für den Einsatz in organischen Dünnschicht-Bauelementen untersucht. Die Perspektive für Dünnschichtbauteile aus chiralen organischen Materialien liegt in ihrer Fähigkeit, links- und rechts-zirkular polarisiertes Licht selektiv zu absorbieren oder zu emittieren, was Anwendungen wie chirale Photodioden, chirale Phototransistoren und chirale organische Leuchtdioden (organic light-emitting diodes, OLEDs) ermöglicht. Zusätzlich versprechen diese Materialien Anwendungen im Forschungsfeld der Spintronik, die darauf abzielen, den Spin von Elektronen zu unterscheiden. Um solche anspruchsvollen Bauteilanwendungen zu realisieren, ist es jedoch unerlässlich, die grundlegenden Materialeigenschaften neuer organischer Halbleiter wie die Morphologiebildung sowie den Ladungstransport in einer robusten Bauteilarchitektur zu bewerten. Hierfür eignet sich die organische Solarzelle (organic solar cell, OSC) als Mischung einer Donor- und Akzeptorkomponente (Bulk-Heterojunction, BHJ), in der die PBIs als

Fulleren-ersetzende Akzeptoren (Non-Fullerene Acceptors, NFAs) eingesetzt werden. Die durch die Kernverdrillung verursachte hohe Löslichkeit, die breiten Absorptionseigenschaften, sowie die elektronische Abstimmbarkeit durch chemische Modifikation in Aryl- und Imidposition machen diese PBIs zu idealen Kandidaten für NFAs in Kombination mit Donor-Polymeren als aktive Schichten von lösungsprozessierten OSCs.

In Kapitel 3 wurden zwei Serien von chiral verdrillten Bucht-arylierten PBIs als NFAs in Kombination mit dem Donorpolymer **PCE-10** in einer invertierten BHJ-Architektur (iBHJ) durch Lösungsprozessierung verwendet (Abbildung 1).

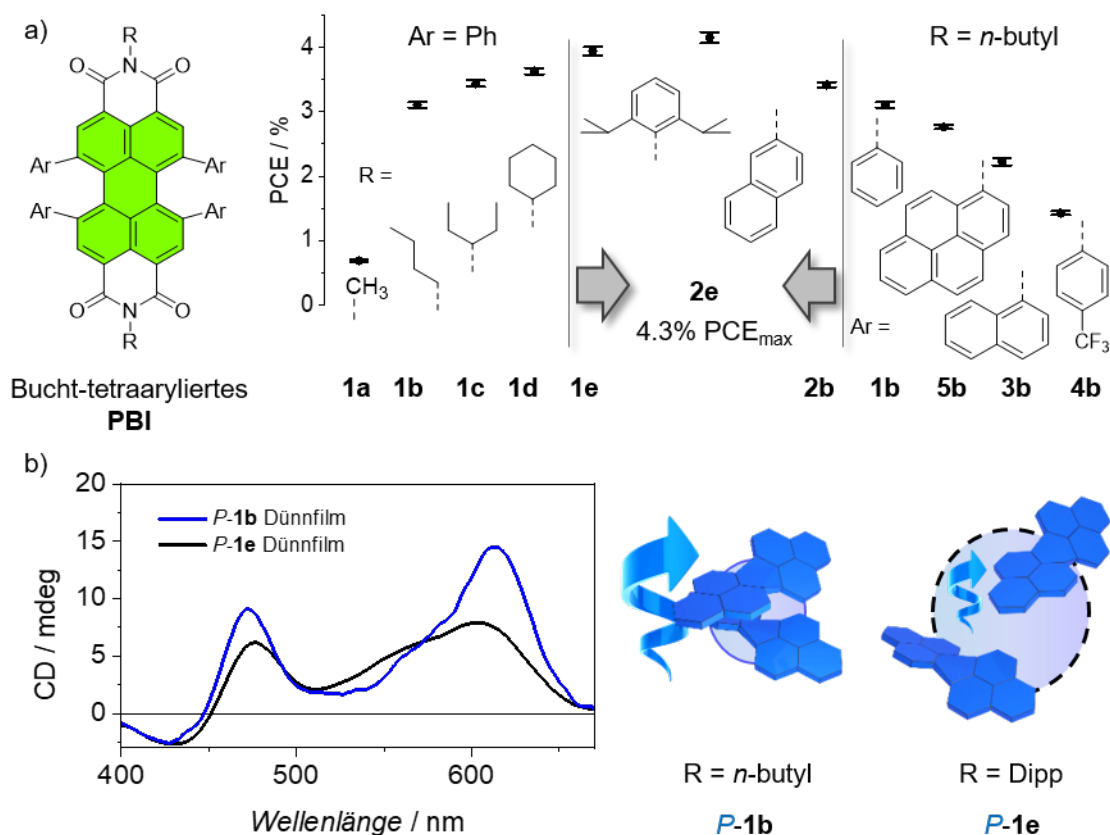


Abbildung 1. (a) Chemische Struktur von Bucht-tetraarylierten PBIs zusammen mit der Auflistung der Solarzelleneffizienzen der **PCE-10**-basierten iBHJs in Kombination mit den racemischen Mischungen von **1a–1e** (links), sowie **1b–5b** (rechts). (b) CD Absorptionsspektren der rotationsbeschichteten Dünnschichten der Reinsubstanzen *P-1b* (blau) und *P-1e* (schwarz) zusammen mit der schematischen Darstellung der jeweiligen Chromophoranordnungen als π -gestapeltes Dimer (*P-1b*) oder als isolierte Monomere (*P-1e*) entsprechend der Erkenntnisse der jeweiligen Einkristall-Röntgendiffraktometrien. Die helikalen Pfeile symbolisieren die Größen der chiroptischen Eigenschaften.

In dieser umfassenden Studie zur Variation der Imid- (**1a–1e**) und Aryl-Substituenten (**1b–5b**) wurden demnach 2,6-Diisopropylphenyl und 2-Naphthyl als beste Substituenten innerhalb der jeweiligen Serien der NFAs ermittelt. Somit erreichte das entsprechende neu synthetisierte Derivat **2e**, das beide Substituenten enthält, eine Spitzenleistung von 4.3 % PCE_{max}. Dies war

zu diesem Zeitpunkt der höchste Wirkungsgrad einer OSC mit einem PBI-Einzelkern als NFA ohne laterale π -Erweiterung oder Einbettung von Heteroatomen. Die OSC-Ergebnisse wurden mit der Chromophorpackung der entsprechenden PBIs korreliert, die aus der Röntgendiffraktometrie von Einkristallen der jeweiligen racemischen Mischungen erhalten wurden. Interessanterweise erzielten die stärker isolierten und sterisch abgeschirmten Chromophore **1e** und **2e** mit nahezu keinen π - π -Wechselwirkungen die besten Effizienzen von über 4.0 % PCE_{max} (siehe Abbildung 1). In **2e** war die Abschirmung des kernverdrillten chiralen Chromophors durch die Substituenten am ausgeprägtesten, was sogar die Auftrennung des Racemats in seine *P*- und *M*-Enantiomere verhinderte. Die Auswirkung der Enantiomerenreinheit auf die Bauteileffizienz konnte jedoch für die beiden Bucht-phenylsubstituierten **1b** und **1e** mit entweder den kleinen *n*-Butyl- oder den sterisch anspruchsvollen Dipp-Substituenten untersucht werden. Aufgrund der starken Isolierung der Chromophore wurde für **1e** kein Unterschied in der Effizienz zwischen racemischen Mischungen und isolierten Enantiomeren festgestellt. Im Gegensatz dazu zeigte das *n*-Butyl-substituierte **1b** eine relative Leistungssteigerung von bis zu 20 %, wenn die enantiomerenreine Spezies statt des Racemats als NFA verwendet wurde. Durch CD-Spektroskopie an den entsprechenden Dünnschichten der Reinsubstanz und Polymermischungen konnte in *P/M*-**1b** die optische Signatur von positiver exzitonischer Kopplung nachgewiesen werden. Dies bestätigte die π -gestapelte Chromophorpackung isolierter Dimere, die in der enantiomerenreinen Kristallstruktur gefunden wurden. Im Gegensatz dazu zeigt ihre racemische Mischung *rac*-**1b** eine kompakte, versetzt gestapelte Anordnung abwechselnder *P*- und *M*-Chromophore, womit deren geringere Solarzelleneffizienz erklärt werden konnte.

In *Kapitel 4* wurde das kernverdrillte π -Rückgrat der PBIs zu den entsprechenden konfigurationsstabilen, helikal verdrehten Quaterrylenbisimidinen (QBIs) erweitert. Die ersten beiden Vertreter dieser neuen Molekülklasse weisen entweder einfache (**QBI1**) oder zweifache (**QBI2**) Kernverdrillung auf (Abbildung 2). Dies konnte synthetisch einerseits durch eine Palladium-katalysierte Annulierungsreaktion^[236] (**QBI1**), sowie andererseits durch eine Zink-vermittelte Ullmannkupplung^[238] (**QBI2**) erreicht werden. Die hohe Löslichkeit und die außergewöhnliche Konfigurationsstabilität der isolierbaren Atropisomere der QBIs sind vergleichbar mit den entsprechenden kernverdrehten PBIs. Die durch die verzahnten Phenylsubstituenten induzierte Rigidisierung des π -Rückgrats wurde eindeutig durch Einkristall-Röntgenanalysen nachgewiesen. Diese führte beim zweifach verdrillten **QBI2** zu einer stabilen Ende-zu-Ende-Verdrillung von 76°.

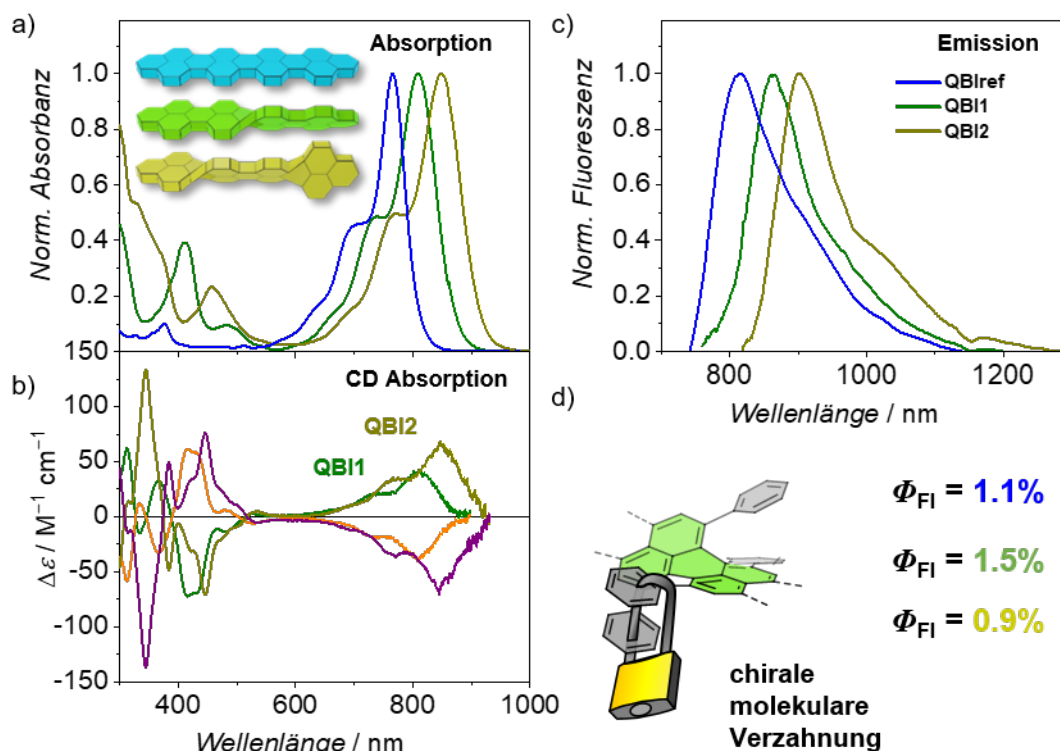


Abbildung 2. (a) UV-vis-NIR Absorptionsspektren, (b) CD Absorptionsspektren und (c) Emissionsspektren des planaren **QBIref** (blau), des einfach kernverdrillten **P-QBI1** (grün) und des zweifach kernverdrillten **P-QBI2** (dunkelgelb) in DCM bei 295 K. Die *M*-Enantiomere von **QBI1** und **QBI2** in (b) sind in orange bzw. violett, dargestellt. (d) Schematische Darstellung des durch Bucht-Substitution chiral verzahnten Perylenmotivs zusammen mit den Fluoreszenzquantenausbeuten von **QBIref**, **QBI1** und **QBI2**.

Im Gegensatz zu den kernverdrillten PBIs zeigte diese Konformationsverzahnung für die kernvergrößerten QBIs eine unerwartete und einzigartige spektrale Konsequenz im nahen Infrarotbereich (NIR). So konnten scharfe Emissionsbanden mit einer nur kleinen Stokes-Verschiebung im NIR-Bereich bei 862 nm (**QBI1**) und 903 nm (**QBI2**) sowie beeindruckende Fluoreszenzquantenausbeuten von 1.5 bzw. 0.9 % für diese Chromophore mit kleiner Bandlücke erzielt werden. **QBI1** und **QBI2** zeigen starke chiroptische Eigenschaften mit einer monosignierten S_0-S_1 CD Bande mit einem $\Delta\epsilon$ von bis zu 40 bzw. 67 $M^{-1} \text{ cm}^{-1}$ bei 809 und 849 nm.

In *Kapitel 5* wurde das einfach kernverdrillte QBI-Motiv an seinen Imid-Positionen durch kleine Methylgruppen substituiert, um eine über $\pi-\pi$ -Wechselwirkungen vermittelte Selbstorganisation des resultierenden **QBI-Me** zu erleichtern und exzitonische Kopplung für eine Verstärkung der chiroptischen NIR-Eigenschaften zu ermöglichen. Auf diese Weise konnte das erste enantiomerenreine J-Aggregat eines stabilen axialchiralen Rylenbisimids hergestellt werden, das eine starke exzitonische Chiralität seines optischen S_0-S_1 Übergangs aufweist (siehe *Abbildung 3*).

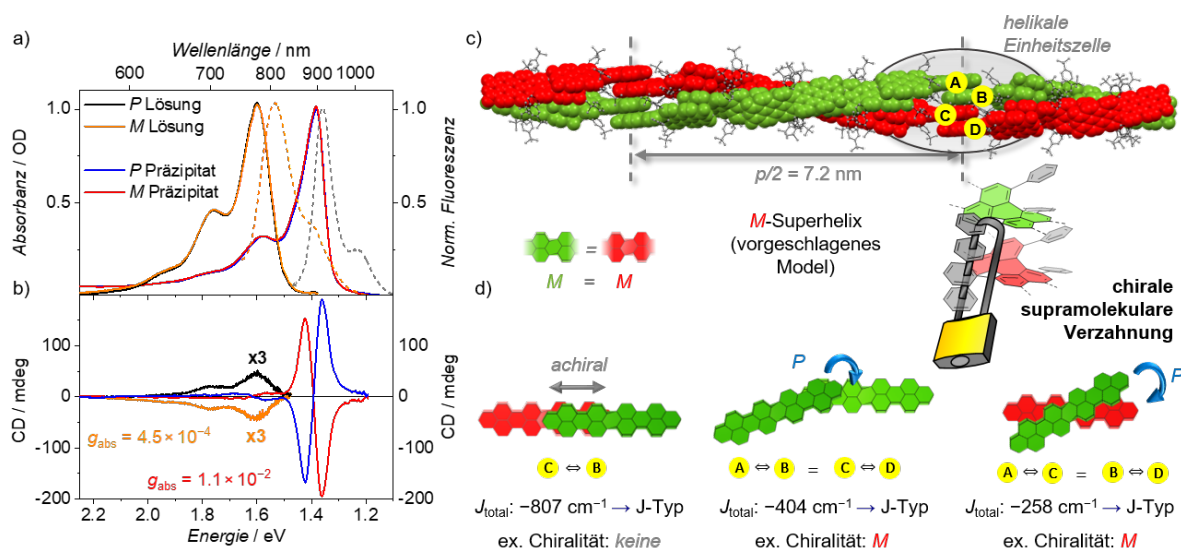


Abbildung 3. (a) UV-vis-NIR Absorptionsspektren (durchgezogene Linien) und normierte Emissionsspektren (gestrichelte Linien), sowie (b) CD Spektren von *P*- und *M*-QBI-Me in *n*-Hexan bei 295 K. Die kinetisch gefangenen monomeren Lösungen [schwarz (*P*) und orange (*M*)] sind um Faktor drei vergrößert dargestellt. Die Spektren des suspendierten J-Aggregats (Präzipitat) sind in blau (*P*) bzw. rot (*M*) dargestellt. Absorptions- bzw. Emissionsmessungen wurden in Transmissionsmodus bzw. Frontseitenaufbau gemessen. (c) Strukturmodell der verschlungenen *M*-Vierfachhelix, die durch kooperative Selbstorganisation von *M*-QBI-Me in *n*-Hexan erhalten wurde und durch chirale supramolekulare Verzahnung der Bucht-Substituenten zweier aufeinander π -gestapelter QBIs stabilisiert ist. (d) Paare von *M*-QBIs (grün und rot) und ihre gegenseitige Anordnung innerhalb der *M*-Superhelix sowie die berechneten Kopplungsenergien zusammen mit den daraus resultierenden Kopplungstypen.

Dessen CD Couplet ist weit im NIR-Bereich um 903 nm zentriert und zeigt hohe Dissymmetriefaktoren von bis zu 1.1×10^{-2} bei 935 nm. Die durch die Kernverdrillung bedingte hohe Löslichkeit des QBI-Me ermöglichte die kooperative Selbstorganisation in wenig polaren Lösungsmitteln wie *n*-Hexan, die ausschließlich auf schwachen van-der-Waals-Wechselwirkungen beruht, welche durch die zugänglichen großen π -Flächen ermöglicht werden. Dementsprechend wurde das Konzept der verzahnten Chiralität des verdrillten Perylenkerns von einer molekularen auf eine supramolekulare Ebene angehoben. Die an den Chromophoren angebrachten Phenylgruppen erfüllen nun zwei Zwecke. Erstens gewährleisten sie die Konformationsstabilität der inhärent chiralen Monomere. Zweitens führen sie auf supramolekularer Ebene zur richtigen gegenseitigen Chromophoranordnung innerhalb des J-Aggregats. Für dieses J-Aggregat konnte ein Strukturmodell erarbeitet werden, in dem sich vier versetzt aufeinander gestapelte Chromophore zu einer verschlungenen Superhelix fortsetzen. Es unterstreicht die geometrische Notwendigkeit der *P*-Händigkeit der gegenseitigen Anordnung enger Paare von *M*-QBI-Me-Chromophoren, um eine ‚Creepers‘ (dt. Schlingpflanze) -artige *M*-Superhelix auszubilden (entsprechend umgekehrt für

P-QBI-Me), die die konformativen Anforderungen für starke J-artig exzitonisch gekoppelte chiroptische Eigenschaften erfüllt.

Zusammenfassend wurde die Chiralität des verzahnten Bucht-arylierten Perylenmotivs im Hinblick auf seine Perspektive in der Materialanwendung sowie die Verstärkung seiner chiroptischen Eigenschaften im NIR-Spektralbereich untersucht. Eine umfangreiche Molekülbibliothek von inhärent chiralen PBIs wurde als NFAs in OSCs verwendet, um sowohl gute Solarzelleneffizienzen sowie Einblicke in die Struktur-Eigenschafts-Beziehung von PBI-Materialien innerhalb einer Polymermischung zu erhalten. Zum ersten Mal wurden für kernverdrillte PBIs die Auswirkungen der Enantiomerenreinheit auf die Effizienz von organischen Dünnschichtbauteilen untersucht. Die außerordentliche strukturelle Empfindlichkeit der CD Spektroskopie diente als entscheidendes Analysewerkzeug, um die hoch anspruchsvolle Lücke zwischen der Analytik molekularer Eigenschaften und der Bauteilanalytik zu schließen, indem die exzitonische Chiralität eines helikalen PBI-Dimers nachgewiesen wurde. Die Chiralität dieses Perylenmotivs konnte auf molekularer Ebene weiter verstärkt werden, indem das π -Gerüst sowohl erweitert als auch stärker verdrillt wurde, um wünschenswert starke chiroptische Eigenschaften im NIR-Bereich zu erzielen und so eine neue Molekülfamilie kernverdrillter QBIs zu definieren. Diese Errungenschaften konnten durch die Ausweitung dieses molekularen Konzepts auf eine supramolekulare Ebene noch erheblich weiterentwickelt werden. Die geometrisch anspruchsvolle supramolekulare Anordnung, die für die effiziente exzitonische Kopplung erforderlich ist, wurde sorgfältig in das molekulare Design kodiert. Dementsprechend stellt das präsentierte QBI in seiner vierfach versetzt gestapelten Superhelix das erste Rylenbisimid-J-Aggregat dar, welches eine starke exzitonische Chiralität zeigt.

Somit hat die Arbeit die gegenseitige Bestätigung von experimentellen und theoretischen Daten von der molekularen bis hin zur supramolekularen Ebene herausgestellt und gezeigt, dass für Rylenbisimid-Farbstoffe der exzitonische Beitrag zu den chiroptischen Eigenschaften konzipiert, synthetisch realisiert und quantenmechanisch verstanden werden kann. Dies kann den Weg für neue organische Funktionsmaterialien ebnen, die für chirale Sensoren oder Licht-emittierende Bauteile verwendet werden können.

CHAPTER 8

—

Appendix

8.1 Supporting Information for *Chapter 3*

The Supporting Information has been published in ref. [159]. For the sake of unity of this thesis, several formal editorial changes have been applied. Adapted or reprinted with permission from ref. [159] with permission from the Royal Society of Chemistry.

8.1.1 Materials and Methods

General

All chemicals, reagents and solvents were purchased from commercial suppliers and used after appropriate purification if not stated otherwise. *N,N'*-di(2,6-diisopropylphenyl)-1,6,7,12-tetrachloroperylene-3,4:9,10-bis(dicarboximides) and PBIs **1a–1e** as well as **2b–5b** were synthesized according to literature known procedures.^[66, 282] Toluene used for synthesis was of HPLC grade and was dried prior to use utilizing a *Pure Solv MD 7* system from Inert Technology. Dichloromethane (DCM) was distilled prior to use. Column chromatography was performed using commercial glass columns packed with silica gel 60 M (particle size of 0.04–0.063 mm from Merck KGaA) stationary phase. Normal phase HPLC was performed on a *JASCO* recycling semipreparative HPLC system equipped with a *VP 250/21 NUCLEOSIL 100-7* column from Macherey-Nagel. For chiral separation a *ReproSil 100 Chiral-NR 8 μm* column from Trentec (**1a–1e** as well as **2b–5b**) or *ReproSil Chiral-MIF 10 μm* column from Dr. Maisch (**2e** attempted) was utilized.

UV–vis–NIR spectroscopy

was carried out at room temperature on a *Jasco V770* spectrophotometer. Solution spectra were taken using 10 mm cuvettes (SUPRASIL[®], Hellma[®] Analytics, DCM spectroscopic grade). For thin-film spectra, the same spectrometer with an integration sphere was used. Neat films were prepared on quartz substrates (SUPRASIL[®], Hellma[®] Analytics) from a chloroform solution (spectroscopic grade). Spectra of blend films were taken using the respective thin-film device.

Fluorescence spectroscopy

was carried out on a *FLS980* fluorescence spectrometer from Edinburgh Instruments. Spectra were corrected against the photomultiplier sensitivity and the lamp intensity. Fluorescence quantum yields were determined using the dilution method ($OD < 0.05$) and Oxazine 1 in ethanol with 11% as reference.^[283] Fluorescence lifetimes were determined with EPL picosecond pulsed diode lasers ($\lambda_{ex} = 560$ nm) for time correlated single photon counting.

CD spectroscopy

was carried out using a customised *JASCO CPL-300/J-1500* hybrid spectrometer.

NMR spectroscopy

was performed using a Bruker *Avance III HD* 400 MHz NMR spectrometer relative to residual undeuterated solvent signals. Chemical shifts (δ) are listed in parts per million (ppm). The multiplicities for proton signals are abbreviated as *d* and *bm* for doublet and broad multiplet, respectively.

High resolution mass

spectra were measured by electron spray ionization (ESI) using an *ESI microTOF Focus* mass spectrometer from Bruker Daltonics GmbH.

Melting points were determined using a SMP50 from *Stuart Equipment*.

Cyclic voltammetry

was measured on an *EC epsilon* (BASi instruments, UK) potentiostat connected with a three-electrode single-compartment cell. A platinum disc electrode was utilized as working electrode, a platinum wire as counter electrode and an Ag/AgCl electrode as reference electrode.

Single-crystal X-ray diffraction

was measured on a Bruker *D8 Quest Kappa* diffractometer with a Photon II CMOS detector and multi-layered mirror monochromated $Cu_{K\alpha}$ radiation at 100 ± 1 K. The solved structures were obtained with Fourier techniques and the *Shelx* software package.^[284] Crystallographic data are deposited on the Cambridge Crystallographic Data Centre as supplementary publication no. CCDC 2106434 (*rac-1b*), CCDC 2106433 (*P-1b*), CCDC 2106436 (*rac-1e*), CCDC 2106435 (*M-1e*) and CCDC 2106437 (*rac-2e*).

AFM-Images

were obtained by *NT-MDT Next Solver System* in semi contact mode by using a SCOUT 350

RAI (Nu Nano Ltd) silicon cantilever (spring constant = 42 N m^{-1} , resonance frequency = 350 kHz).

Organic thin-film devices

(OSCs, SCLC) were prepared as organic solar cells in inverted bulk-heterojunction structure of ITO/ZnO/Blend/MoO₃/Al. SCLC-devices were fabricated in a structure of ITO/ZnO/Blend/BCP/Al (electron-mobility) or ITO/PEDOT:PSS/Blend/MoO₃/Al (hole mobility).

ITO-substrates (Soluxx GmbH) were cleaned with acetone (VWR, semiconductor grade), detergent, deionized water, and isopropanol (VWR, semiconductor grade) for 15 min each, followed by an ozone/UV treatment for 30 min.

The bottom layer was either ZnO or PEDOT:PSS. The ZnO-layer was deposited by static spin-casting ZnO nanoparticles^[285] on top of the substrates (3000 rpm, 30 s) followed by thermal annealing ($200 \text{ }^\circ\text{C}$, 1 h). PEDOT:PSS (solids content: 1.3 – 1.7%, PEDOT:PSS 1:6 w/w, Heraeus) was deposited analogously by spin-casting with 2500 rpm for 60 s and thermally annealing at $150 \text{ }^\circ\text{C}$ for 10 min.

The donor-acceptor blends were prepared by stirring a **PCE-10** (1-Material Inc.) polymer solution overnight in chlorobenzene (CB). This solution was then given to the respective PBI and stirred for 4 h at room temperature under inert conditions followed by dynamic spin-casting at 1000 rpm for 60 s (MBraun Intergas Systeme GmbH, UNIlab Pro, $c(\text{O}_2) < 1 \text{ ppm}$, $c(\text{H}_2\text{O}) < 1 \text{ ppm}$).

For vacuum deposition, the substrates were placed in the evaporation system (OPTIvap-XL, Creaphys GmbH). As top layers, either MoO₃ or BCP ($d = 10 \text{ nm}$, $r = 0.07 - 0.15 \text{ } \text{\AA} \text{ s}^{-1}$, $p < 10^{-6} \text{ mbar}$, rotation = 10 rpm) were deposited followed by aluminium ($d = 100 \text{ nm}$, $r = 1 - 2 \text{ } \text{\AA} \text{ s}^{-1}$, $p < 10^{-6} \text{ mbar}$) using shadow masks.

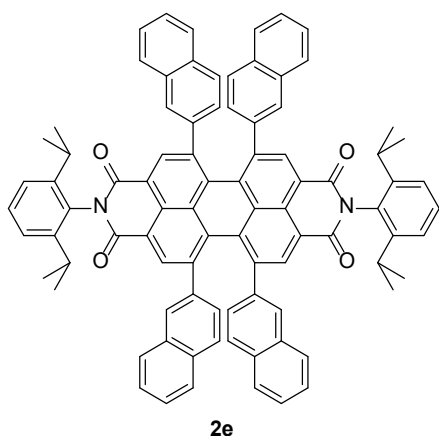
The device area was 7.1 mm^2 . J - V -characteristics were measured after calibration with a standard silicon solar cell with a KG filter (ISE Freiburg) under an AM1.5G *Oriel Sol3ATM* Class AAA solar simulator (Newport®) by a parameter analyser (Botest Systems GmbH).

SCLC measurements were recorded and evaluated using the protocol of Blakesley *et al.*^[196] applying Mott-Murgatroyd equation and a built-in-voltage of $V_{\text{bi}} = 0.6 \text{ V}$ (**PCE-10**, **1b**) and a relative permittivity of $\epsilon = 3.5$. Active layer thickness was determined via AFM.

EQE measurements were carried out with a Quantum Efficiency/IPCE measurement kit (Newport[®]) by using a 300 W Xe-lamp and a Cornerstone monochromator with a Merlin Lock-In Amplifier for detection.

TD-DFT calculations were performed with GAUSSIAN 09 software^[286] on ω B97/def2SVP level of theory. Molecule coordinates were taken from respective single-crystal structures without further geometry optimization.

8.1.2 Synthesis



N,N'-di(2,6-diisopropylphenyl)-1,6,7,12-tetrachloroperylene-3,4:9,10-bis(dicarboximide) (100 μmol), 2-naphthylboronic acid (2.00 mmol, 20 eq.), anhydrous potassium carbonate (145 mg, 1.05 mmol, 10.5 eq.) and tetrakis(triphenylphosphine)palladium (34.7 mg, 30.0 μmol , 0.3 eq.) were given in a Schlenk tube. Degassed toluene (3.2 mL), ethanol (0.6 mL) and water (1.6 mL) were added. The mixture was subjected to three freeze-pump-thaw cycles. After stirring for 26 h at 80 $^{\circ}\text{C}$, the mixture was extracted with dichloromethane and washed three times with water. The organic phases were combined, and the solvent removed under reduced pressure. The crude product was purified by column chromatography (hexane:dichloromethane 3:7) and HPLC (hexane:dichloromethane 1:2) to obtain 45.5 mg (37.4 mmol, 37%) of **2e** as purple solid.

^1H NMR (400 MHz, CD_2Cl_2 , 293 K): δ = 8.54 – 6.68 (bm, 38H), 2.91 (bm, 4H), 1.26 (d, 12H), 1.16 (d, 12H);

^{13}C NMR (100 MHz, CD_2Cl_2 , 293 K): δ = 164.4, 146.6, 143.2, 138.4, 134.9, 132.9, 132.6, 132.4, 131.7, 129.9, 128.5, 128.2, 127.9, 127.5, 127.0, 126.6, 124.5, 122.9, 29.5, 24.2;

HRMS (ESI-TOF, pos. mode, $\text{MeCN}/\text{CHCl}_3$): m/z calculated for $\text{C}_{88}\text{H}_{66}\text{N}_2\text{NaO}_4^+$ [$\text{M}+\text{Na}$] $^+$: 1237.4915, found 1237.4877; m.p. >390 $^{\circ}\text{C}$.

UV-Vis (CD_2Cl_2): λ_{max} / nm (ϵ / $\text{M}^{-1}\text{cm}^{-1}$) = 615 (23900), 536 (25300).

Fluorescence (CD_2Cl_2 , λ_{ex} = 600 nm): λ_{max} / nm (Φ_{F1} / %) = 670 (31),

M.p.: > 390 $^{\circ}\text{C}$.

8.1.2 UV-vis-NIR and Fluorescence

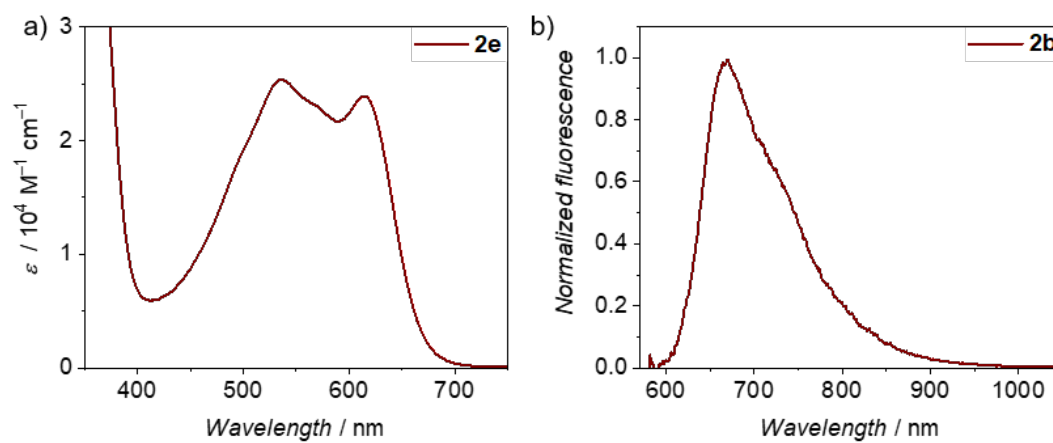


Figure A1. (a) UV-vis-NIR absorption spectra and b) normalized emission spectra of **2e** in DCM solution ($c_0 \approx 4 \cdot 10^{-6} \text{ M}$) at room temperature.

8.1.3 OPV

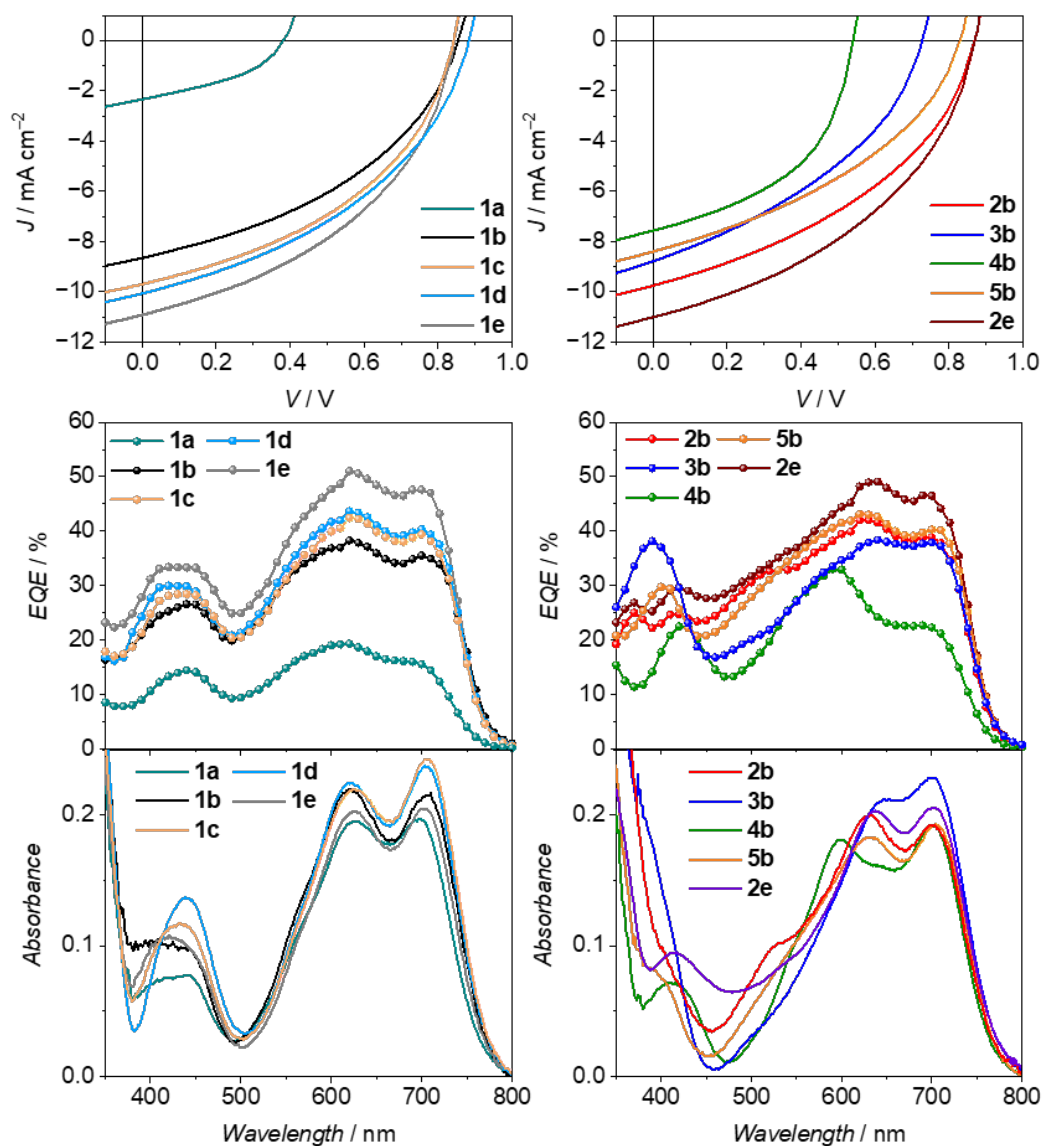


Figure A2. J - V characteristics (upper figures) as well as EQE (middle figures) and UV-vis-NIR absorption spectra (lower figures) of PCE-10 based devices of **1a–1e** (left) as well as **2b–5b** and **2e** (right). The total blend concentration was 15 mg mL^{-1} (16 mg mL^{-1} for **2e**) in chlorobenzene (CB) for all devices. D:A ratio was 1:1 (1.0:1.1 for **2e**) and 2% of 1-chloronaphthalene (CN) was used as solvent additive. The solar cells were fabricated and characterized under inert conditions and AM1.5 G irradiation.^[193]

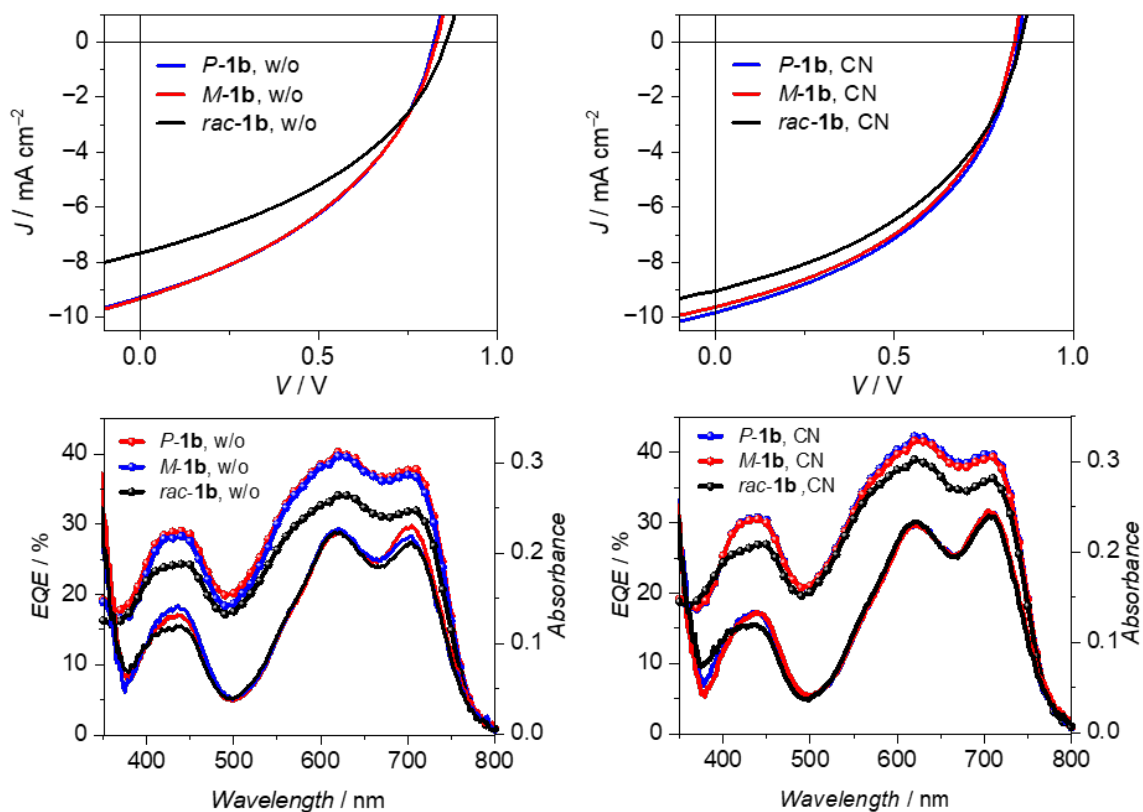


Figure A3. J - V characteristics (top) of best **1b**-based OSC devices with inverted architecture of ITO/PCE-10:**1b**/MoO₃/Al without solvent additive (left) or with 2% of 1-chloronaphthalene (CN, right). EQE and UV-vis-NIR absorption spectra of respective devices (bottom). The solar cells were fabricated and characterized under inert conditions and AM1.5 G irradiation.^[193]

8.1.4 AFM

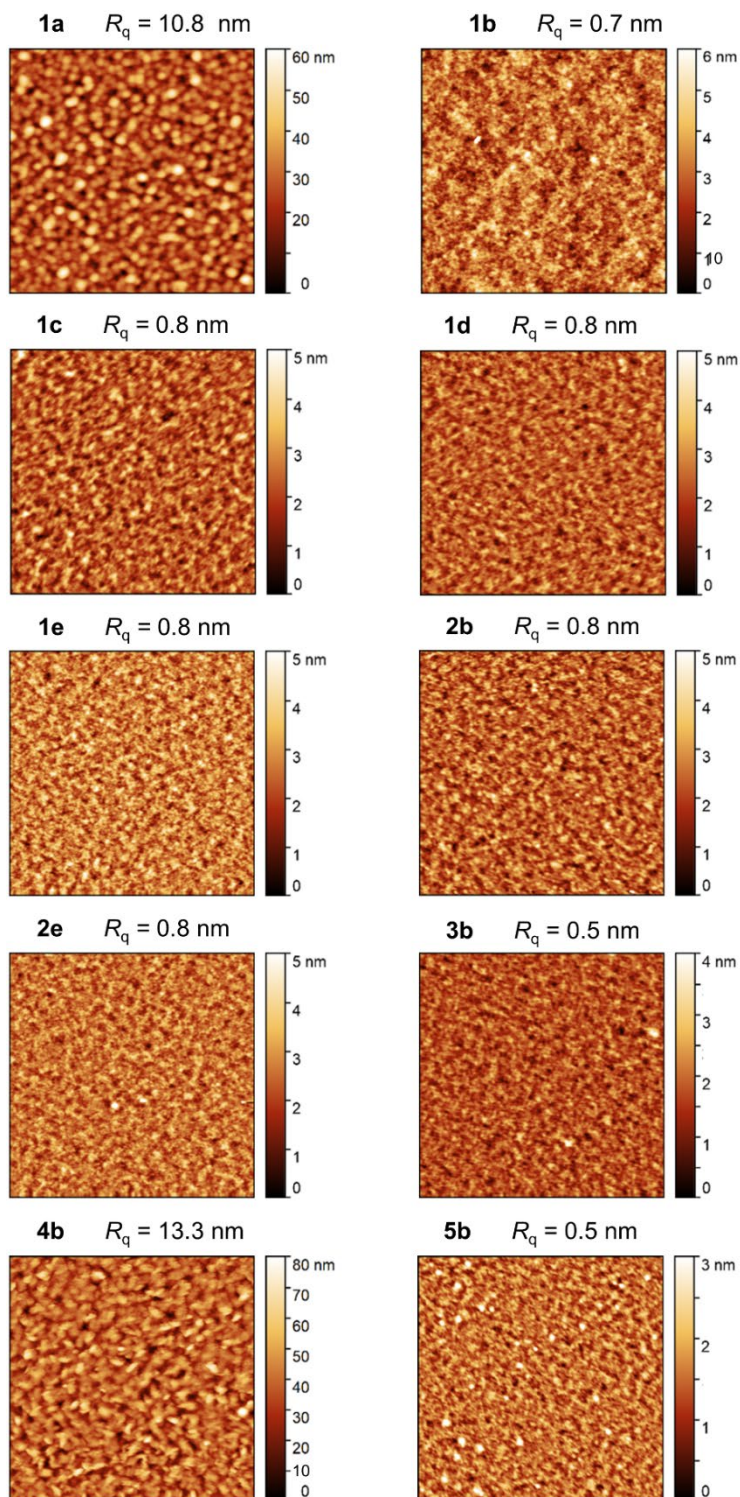


Figure A4. AFM-height images of all PCE-10-based PBI blends used as OSC device corresponding to Figure 23. Thin film devices were spin-coated on ITO/ZnO coated glass substrate at room temperature under inert conditions. $5 \times 5 \mu\text{m}^2$.

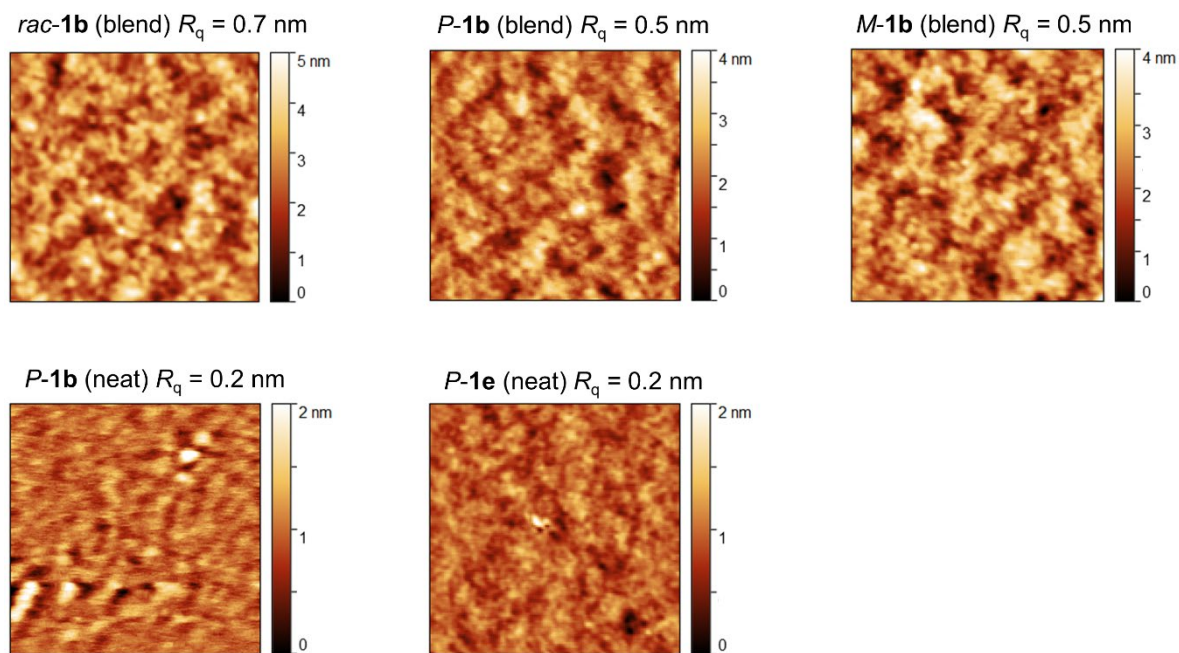


Figure A5. AFM-height images of **PCE-10**-based PBI blends of *P/M/rac-1b* used as OSC device corresponding to Figure 25 and Table 4 (top) as well as neat films of *P-1b* and *P-1e* (bottom) from a chloroform solution ($c = 10 \text{ mg mL}^{-1}$). Thin films were spin-coated on ITO/ ZnO coated glass substrate (blends) or quartz (neat films) at room temperature under inert conditions. $5 \times 5 \mu\text{m}^2$.

8.1.5 X-Ray

Table A1. X-ray structure characteristics for all tetraarylated PBI derivatives.

	<i>Rac-1b</i> ^[193]	<i>Rac-1e</i>	<i>Rac-2e</i>	<i>P-1b</i> ^[193]	<i>M-1e</i>
Empirical formula	C ₅₇ H ₄₃ Cl ₁₃ N ₂ O ₄	C ₇₉ H ₆₈ Cl ₁₂ N ₂ O ₄	C ₁₀₀ H ₇₆ Cl ₁₂ N ₂ O ₄	C ₅₇ H ₄₃ Cl ₁₂ N ₂ O ₄	C ₇₆ H ₆₀ Cl ₁₆ N ₂ O ₄
<i>M</i> _{empirical} (g mol ⁻¹)	926.28	1523.08	1440.52	888.08	1253.94
Wavelength (Å)	1.54178	1.54178	1.54178	1.54178	1.54178
<i>T</i> (K)	100	100	100	100	100
<i>Description of the crystal</i>					
Color	Red	Red	Red	Red	Red
Habit	Needle	Needle	Needle	Needle	Needle
Crystal System	Triclinic	Triclinic	Monoclinic	Hexagonal	Monoclinic
Space group	<i>P</i> $\bar{1}$	<i>P</i> $\bar{1}$	<i>P</i> 2 ₁ / <i>c</i>	<i>P</i> 6 ₅ 22	<i>P</i> 2 ₁
<i>Unit cell dimension</i>					
<i>a</i> (Å)	12.4343(7)	12.5786(9)	15.5844(10)	19.1064(9)	14.0489(10)
<i>b</i> (Å)	12.6105(7)	16.3365(12)	29.7802(17)	19.1064(9)	13.8721(10)
<i>c</i> (Å)	16.4663(10)	18.8231(14)	17.1937(10)	44.020(2)	16.7450(12)
α (°)	101.657(3)	74.006(3)	90	90	90
β (°)	90.456(3)	87.132(3)	110.767(3)	90	109.392(3)
γ (°)	118.044(3)	87.033(3)	90	120	90
Volume (Å ³)	2215.9(2)	3710.7(5)	7461.3(8)	13916.8(15)	3078.3(4)
<i>Z</i>	2	2	4	12	2
$\rho_{\text{alc.}}$ (g cm ⁻³)	1.388	1.363	1.282	1.272	1.353
<i>F</i> (000)	964	1573	3024	5561.3	1304
Range of θ (°)	2.760 – 72.452	2.443 – 72.498	2.986 – 72.624	2.670 – 72.141	2.797 – 72.567
Goodness of Fit	1.027	1.019	1.052	1.116	1.088
CCDC	2106434	2106436	2106437	2106433	2106435

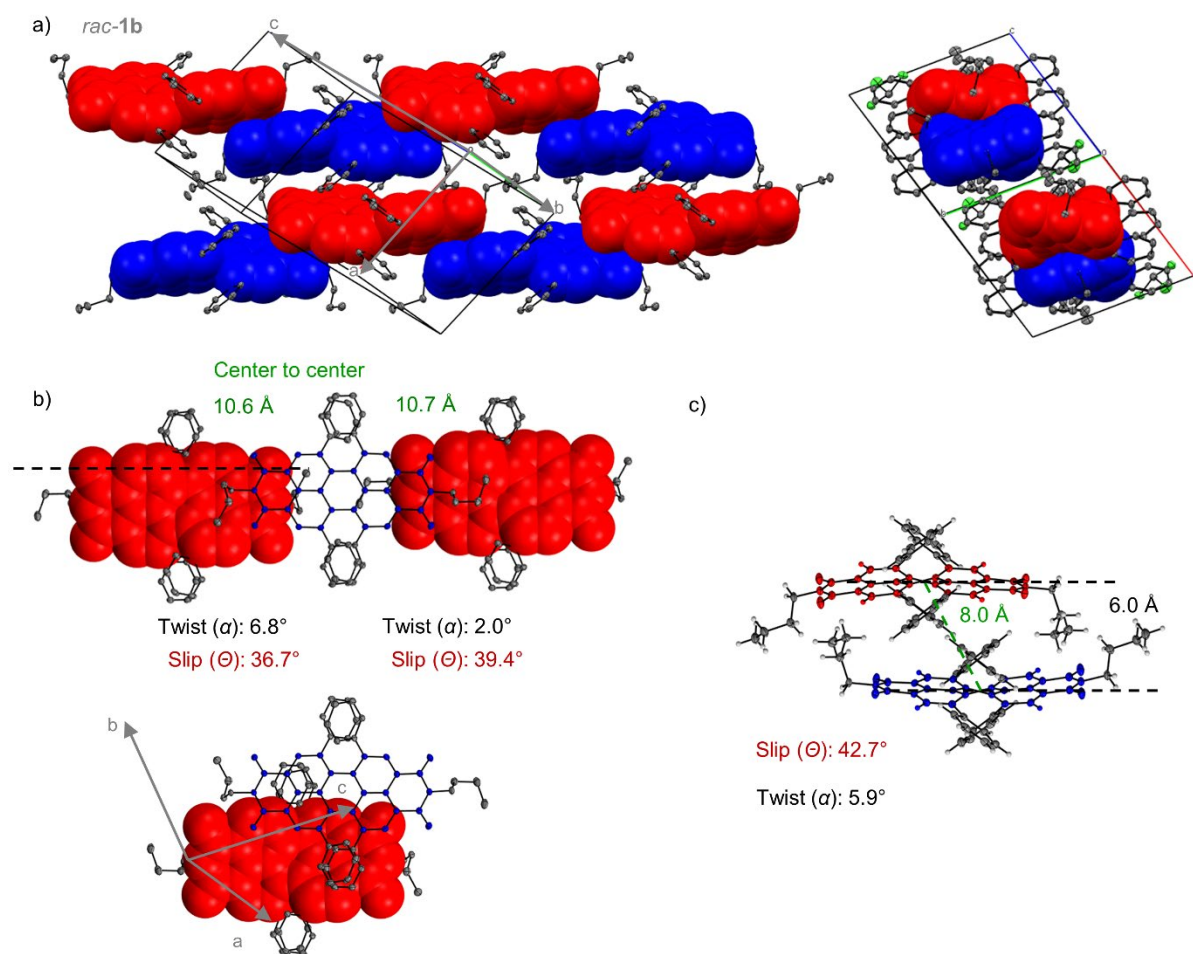


Figure A6. (a) Side view onto the unit cell of racemic PBI *rac-1b* (left) along the double stranded chromophore alignment within its single crystal structure (ellipsoids are set to 50% probability) as well as rotated side view (right). (b). Top view onto the chromophore slip-stack arrangement of one isolated double strand (top) as well as top view onto a pair of enantiomers within the same unit cell (bottom). c) Rotated side view onto the chromophores within their unit cell. PBI atropo-enantiomers are colored in blue (*P*) and red (*M*), respectively. The ellipsoids are set to 50% probability (C: gray). Disorder of the imide residues, hydrogen atoms as well as solvent molecules are omitted for clarity. The distance between the planes of adjacent chromophores (black) and distances between the centroids of the perylene cores (green), as well as twist angle α (black) and slip angle Θ (red) between two chromophores are indicated as well.^[193]

Table A2. Calculated Coulomb coupling between a *P-1b* atropo-enantiomer and its adjacent *M-1b* chromophores in either $-a$ -axis or c -axis direction (Figure A6b) within their racemic single crystal structure based on Kasha's molecular exciton theory.^[42, 193]

<i>rac-1b</i>	r_{c-c} / Å	μ_{eg}^a / D	α / °	Θ / °	J_{coul} / cm^{-1}
<i>P/M-1b</i> ($-a$ -axis direction)	10.6	6.4	6.8	39.4	-140.2
<i>P/M-1b</i> (c -axis direction)	10.7	6.4	2.0	36.7	-156.9

^a The transition dipole moment μ_{eg} was calculated from UV-vis-NIR absorption in DCM solution.

8.1.6 CD Spectroscopy

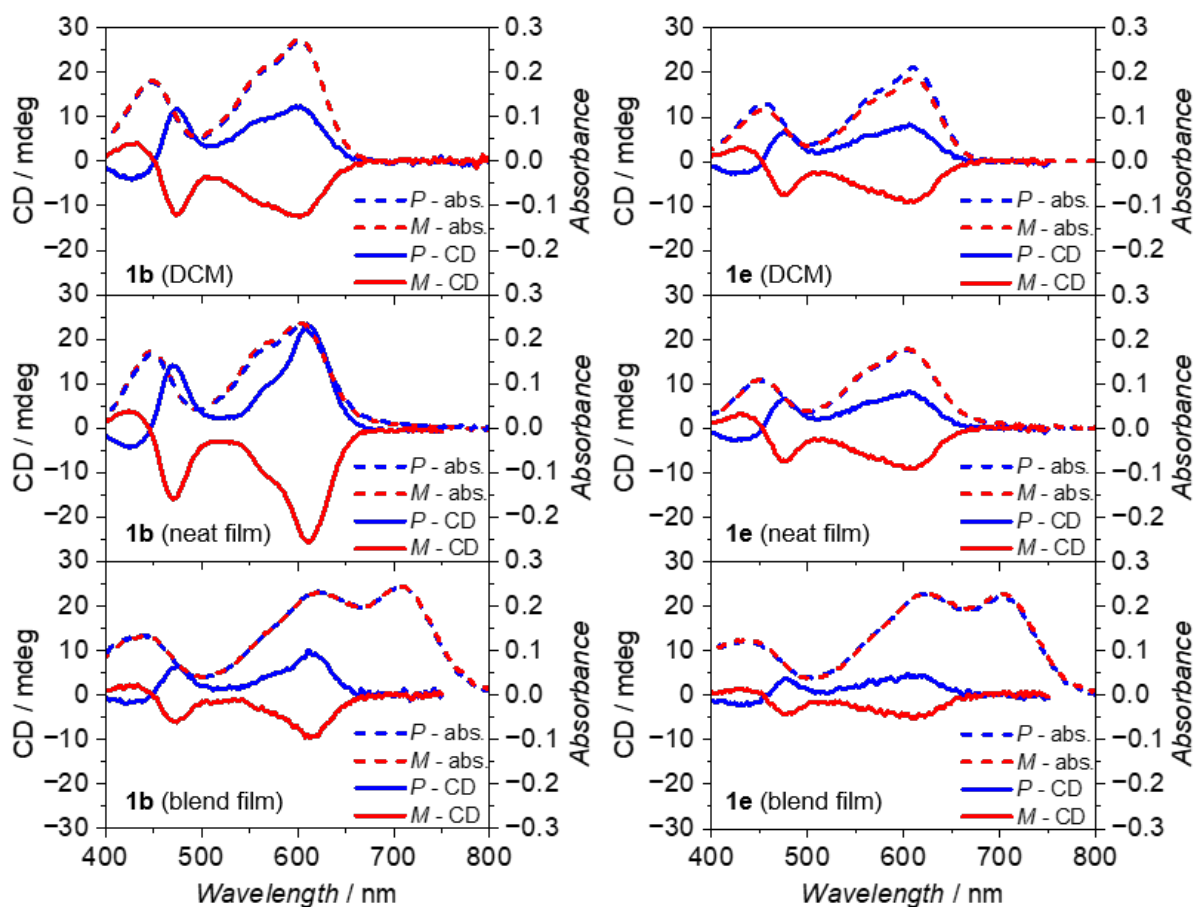


Figure A7. UV-vis-NIR absorption spectra (dashed lines) and CD spectra (solid lines) of *P*- (blue) and *M*- (red) atropo-enantiomers of **1b** (left) and **1e** (right). Spectra were taken in DCM solution (top) as well as spin coated neat film (center, from 10 mg mL^{-1} CHCl_3 solution on quartz) and OSC device (bottom, 15 mg mL^{-1} 1:1 PCE-10:PBI solution on ITO/ZnO).^[193]

8.1.7 SCLC

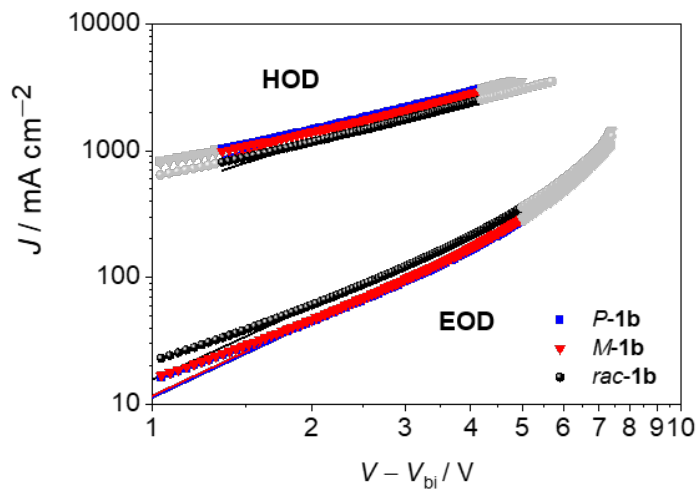


Figure A8. J - V curves of PBI **1b**-based SCLC devices including Mott-Murgatroyd fit. Electron only devices (EOD) and hole only devices (HOD) in structures of ITO/ZnO/PCE-10:PBI/BCP/Al (EOD) and ITO/PEDOT:PSS/PCE-10:PBI/MoO₃/Al (HOD) were fabricated and characterized under dark and inert conditions according to literature known procedure.^[193, 196]

Table A3. Extracted hole mobilities and electron mobilities μ of **1b** based SCLC devices. Electron only devices (EOD) and hole only devices (HOD) in structure of ITO/ZnO/PCE-10:PBI/BCP/Al (EOD) and ITO/PEDOT:PSS/PCE-10:PBI/MoO₃/Al (HOD) were fabricated and characterized under dark and inert conditions according to literature known procedure.^[193, 196]

Acceptor	$\mu_{\text{electron}}^{[a]}$ / $\text{cm}^2 \text{V}^{-1} \text{s}^{-1}$	$\mu_{\text{hole}}^{[a]}$ / $\text{cm}^2 \text{V}^{-1} \text{s}^{-1}$	$\mu_{\text{electron max}}$ / $\text{cm}^2 \text{V}^{-1} \text{s}^{-1}$	$\mu_{\text{hole max}}$ / $\text{cm}^2 \text{V}^{-1} \text{s}^{-1}$
<i>P-1b</i>	$8.9 \pm 0.3 \cdot 10^{-6}$	$1.4 \pm 0.1 \cdot 10^{-3}$	$9.4 \cdot 10^{-6}$	$1.5 \cdot 10^{-3}$
<i>M-1b</i>	$9.1 \pm 0.4 \cdot 10^{-6}$	$1.3 \pm 0.1 \cdot 10^{-4}$	$9.7 \cdot 10^{-6}$	$1.4 \cdot 10^{-3}$
<i>rac-1b</i>	$13.7 \pm 0.2 \cdot 10^{-6}$	$1.0 \pm 0.1 \cdot 10^{-4}$	$13.9 \cdot 10^{-6}$	$1.1 \cdot 10^{-3}$

^a Average of at least five independent devices.

8.1.8 TD-DFT

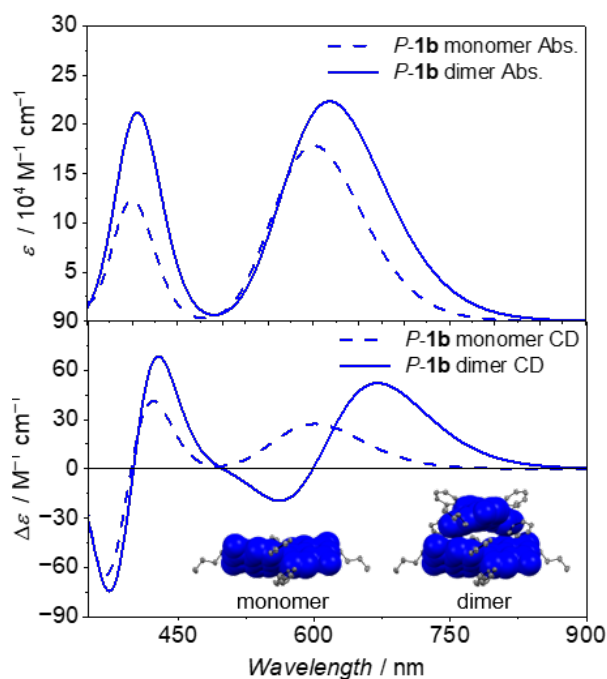


Figure A9. TD-DFT calculated UV/Vis (top) and CD spectra (bottom) of *P-1b* monomer (dashed lines) and dimer (solid lines) using molecular geometry obtained from single crystal X-ray structure analysis. For monomer calculation, the bottom chromophore of the dimer entity with the lower twist angle of 32.4° was used (see inset or Figure 26). Calculations were performed on ω B97/def2SVP level of theory and transition energies were shifted by 0.69 eV.

Table A4. Calculated UV–vis–NIR transitions for monomeric *P-1b* (topmost molecule of the dimeric entity) obtained from its single crystal structure.

Transition	Character /%	Wavelength / nm	Oscillator strength
212 → 213	100	449.64	0.4395
194 → 213	2.9		
204 → 213	4.3		
210 → 213	78.9	333.15	0.0534
211 → 214	5.6		
212 → 217	8.3		
197 → 213	6.5		
202 → 213	3.2		
210 → 214	8.7	326.12	0.2503
211 → 213	10.2		
212 → 216	11.4		
204 → 213	63.2		
210 → 213	2.7	305.04	0.0176
212 → 215	31.1		
203 → 213	17.0		
205 → 213	10.8	288.32	0.0105
212 → 214	72.1		
195 → 215	3.1		
197 → 213	11.0		
198 → 214	30.0		
198 → 228	4.3	275.62	0.0032
199 → 213	45.5		
199 → 219	6.2		
195 → 224	2.5		
196 → 215	2.7		
197 → 214	6.6		
198 → 213	52.7		
198 → 219	8.0	275.62	0.0003
198 → 227	3.3		
199 → 214	21.3		
199 → 228	2.9		
203 → 213	3.2		
203 → 216	2.7		
204 → 213	3.2		
205 → 216	2.4		
210 → 214	7.8	266.17	0.0780
210 → 229	2.4		
212 → 215	7.7		
212 → 227	70.6		
205 → 213	5.0		
219 → 213	83.2	263.87	0.0012
211 → 215	7.3		
212 → 224	4.6		
204 → 213	9.6		
205 → 216	4.9		
210 → 214	7.2	263.06	0.6960
210 → 229	7.0		
212 → 215	31.7		
212 → 227	39.5		

Table A5. Calculated UV–vis–NIR transitions for dimeric *P-1b* obtained from its single crystal structure.

Transition	Character / %	Wavelength / nm	Oscillator strength
423 → 425	18.4		
424 → 425	23.9	472.83	0.2182
212 → 426	60.2		
423 → 425	58.9		
423 → 426	22.0		
424 → 425	9.7	451.64	0.3446
424 → 426	9.4		
419 → 425	2.6		
419 → 426	14.7		
421 → 428	3.4		
422 → 425	28.9	342.65	0.0547
422 → 426	45.4		
424 → 434	5.0		
419 → 425	42.3		
419 → 426	9.1		
422 → 425	24.7	336.21	0.0812
422 → 426	17.0		
423 → 433	6.9		
420 → 426	14.5		
421 → 425	20.8		
421 → 426	37.0		
422 → 428	5.0		
424 → 425	7.7	332.86	0.1447
224 → 426	3.6		
224 → 431	5.5		
224 → 232	6.0		
393 → 425	3.2		
419 → 427	3.2		
420 → 425	25.9		
420 → 426	8.4		
421 → 425	25.3		
221 → 426	9.0	328.89	0.1444
222 → 427	3.0		
223 → 231	5.1		
223 → 232	4.5		
224 → 225	8.3		
224 → 226	3.2		
420 → 225	6.8		
421 → 226	6.3	324.80	0.0882
424 → 225	58.7		
424 → 426	28.2		
223 → 425	23.5	312.12	0.0248
223 → 426	76.5		
401 → 425	3.2		
401 → 426	10.8		
407 → 426	3.9		
409 → 425	3.8		
409 → 426	10.0		
410 → 425	7.1		
410 → 426	6.9	310.16	0.0076
412 → 425	6.4		
412 → 426	10.5		
424 → 227	2.8		
424 → 229	14.0		
424 → 430	20.4		
401 → 425	5.3		
404 → 425	17.0		
404 → 426	5.9		
407 → 425	6.6		
410 → 425	12.4		
410 → 426	8.2	306.80	0.0228
412 → 426	2.8		
414 → 425	5.1		
423 → 427	3.2		
423 → 229	23.4		
423 → 230	10.1		

8.1.9 Cyclic Voltammetry

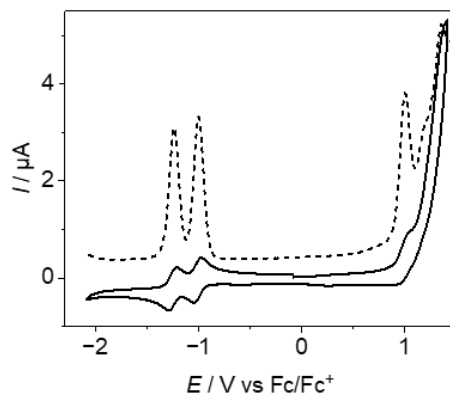


Figure A10. Cyclic voltammograms (solid lines) as well as square wave voltammograms (dashed lines) of PBI **2e** in DCM solution ($c_0 \approx 2 \cdot 10^{-4}$ M) at 293 K using tetrabutylammonium hexafluorophosphat (TBAHFP 0.1 M) as electrolyte. The scanning speed was 100 mV s^{-1} .

Table A6. Redox properties of **2e**. Half-wave potentials were determined by square wave voltammetry measured in DCM (0.1 M TBAHFP) vs. Fc^+/Fc at room temperature.

PBI	E_{red1} / V	E_{red2} / V	E_{ox1} / V	$E_{\text{HOMO}}^{[a]}$ / / eV	$E_{\text{LUMO}}^{[a]}$ / eV	E_{gap} / eV
2e	-1.00	-1.23	0.98	-6.13	-4.15	1.98

^a Calculated according to literature known procedure using the experimentally determined redox potentials ($E_{\text{HOMO}} = -[E_{\text{ox1}} + 5.15 \text{ eV}]$ and $E_{\text{LUMO}} = -[E_{\text{red1}} + 5.15 \text{ eV}]$) and the energy level of Fc^+/Fc with respect to the vacuum level (-5.15 eV).^[170]

8.1.10 NMR Spectra

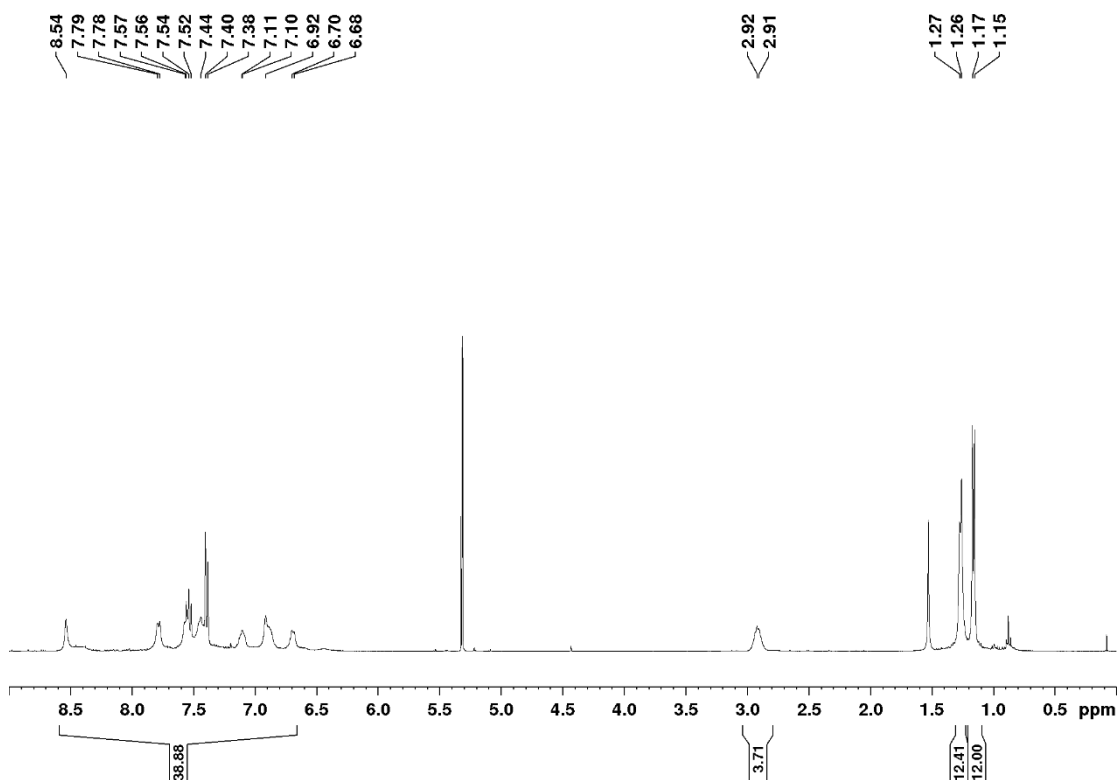


Figure A11. ^1H NMR spectrum (400 MHz) of **2e** in CD_2Cl_2 at 298 K.

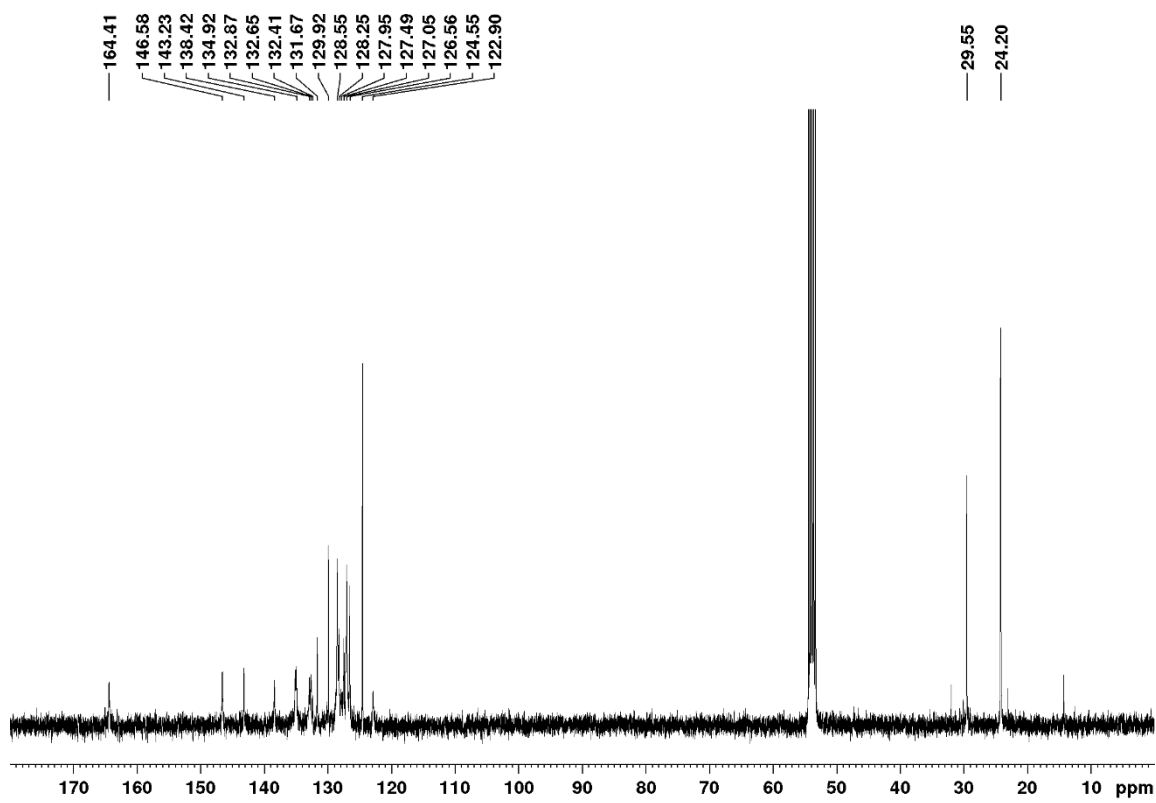


Figure A12. ^{13}C NMR spectrum (100 MHz) of **2e** in CD_2Cl_2 at 298 K.

8.2 Supporting Information for *Chapter 4*

The Supporting Information has been published in ref. [200]. For the sake of unity of this thesis, several formal editorial changes have been applied. Adapted and reprinted with permission from ref. [200]. Copyright 2022 American Chemical Society.

8.2.1 Materials and Methods

General

Unless otherwise noted, all chemicals, reagents and solvents were purchased from commercial suppliers and used without further purification after storing under conditions recommended by the commercial suppliers. The compounds **59**,^[66] **60**,^[65] **65**,^[287] $[\text{Pd}_2(\text{dba})_3] \cdot \text{CHCl}_3$ ^[288] and **QBiref**^[227] were synthesized and characterized according to literature reported procedures. Column chromatography and preparative thin-layer chromatography was performed on silica-gel 60M (particle size 0.040 – 0.063 mm) with freshly distilled solvents. Melting points were measured on an *Olympus* BX41 polarization microscope with the temperature regulator TP84 from *Linkam Scientific*. The reported values are uncorrected. Gel permeation chromatography was performed on a Prominence CBM GPC-device with recycling-mode from *Shimadzu*. Ethanol-stabilized chloroform (HPLC grade) was used as a solvent. Semi-preparative HPLC was carried out on a JAI LC-9105 HPLC-device from *Japan Analytical Industries* equipped with a VP 250/21 NUCLEOSIL 100-7 column ($\text{Ø} = 20$ mm) of Macherey-Nagel using HPLC grade solvents. For separation of enantiomers, the same HPLC device was used equipped with a semi-preparative Reprosil 100 Chiral-NR chiral column from *Trentec* ($\text{Ø} = 20$ mm). For separation of atropo-enantiomers by HPLC, a flow rate of 5-7 mL min⁻¹ was applied resulting in a column pressure of < 2 MPa. All measurements were carried out using spectroscopic grade solvents.

NMR Spectroscopy

¹H and ¹³C NMR spectra were recorded on a Bruker Avance HD III 400 or Bruker Avance HD III 600 spectrometer. The ¹³C NMR spectra are broad band proton decoupled. Chemical shifts (δ) are listed in parts per million (ppm) and are reported relative to tetramethylsilane and referenced internally to residual proton solvent resonances or naturally abundant carbon resonances. The coupling constants (*J*) are quoted in Hertz (Hz).

Mass Spectrometry

High-resolution MALDI-TOF mass spectra were measured with an ultrafleXtreme from *Bruker Daltonics GmbH* using *trans*-2-[3-(4-*tert*-butylphenyl)-2-methyl-2-propenylidene]malononitrile (DCTB) as a matrix material. DCTB and the chloroform solution of the compound ($c \approx 10^{-5}$ M) were mixed in 3:1 (v/v) ratio and then co-deposited. High-resolution mass spectra (ESI-TOF, APCI-TOF) were recorded on a microTOF focus instrument (*Bruker Daltonik GmbH*).

Optical Spectroscopy

UV–vis–NIR absorption spectra were recorded on a *Jasco V670, V-770-ST* or *Perkin Elmer Lambda950* spectrometer. Fluorescence steady-state and lifetime measurements were recorded on a *FLS980-D2D2-ST* *Edinburgh Instrument* fluorescence spectrometer and were corrected against the photomultiplier sensitivity and the lamp intensity. Fluorescence quantum yields were either determined by using the relative method and *Oxazine* ($\Phi_{\text{Fl}} = 11\%$ in EtOH)^[283] or *Rhodamine 800* ($\Phi_{\text{Fl}} = 25\%$ in EtOH)^[243] as a reference or via direct excitation method using a calibrated integration sphere measuring five independent samples of each compound following a literature known reported protocol.^[245] Circular dichroism spectra were recorded on a customized *Jasco CPL-300/J-1500 hybrid spectrometer*.

Electrochemistry

Cyclic voltammetry (CV) and differential pulse voltammetry (DPV) measurements were conducted out with a *BASi Epsilon* potentiostat connected to a microcell apparatus from *rhd instruments* involving a 1.6 mL sample container, a platinum counter- and pseudo-reference electrode as well as a glassy carbon working electrode.

Single Crystal X-ray Analysis

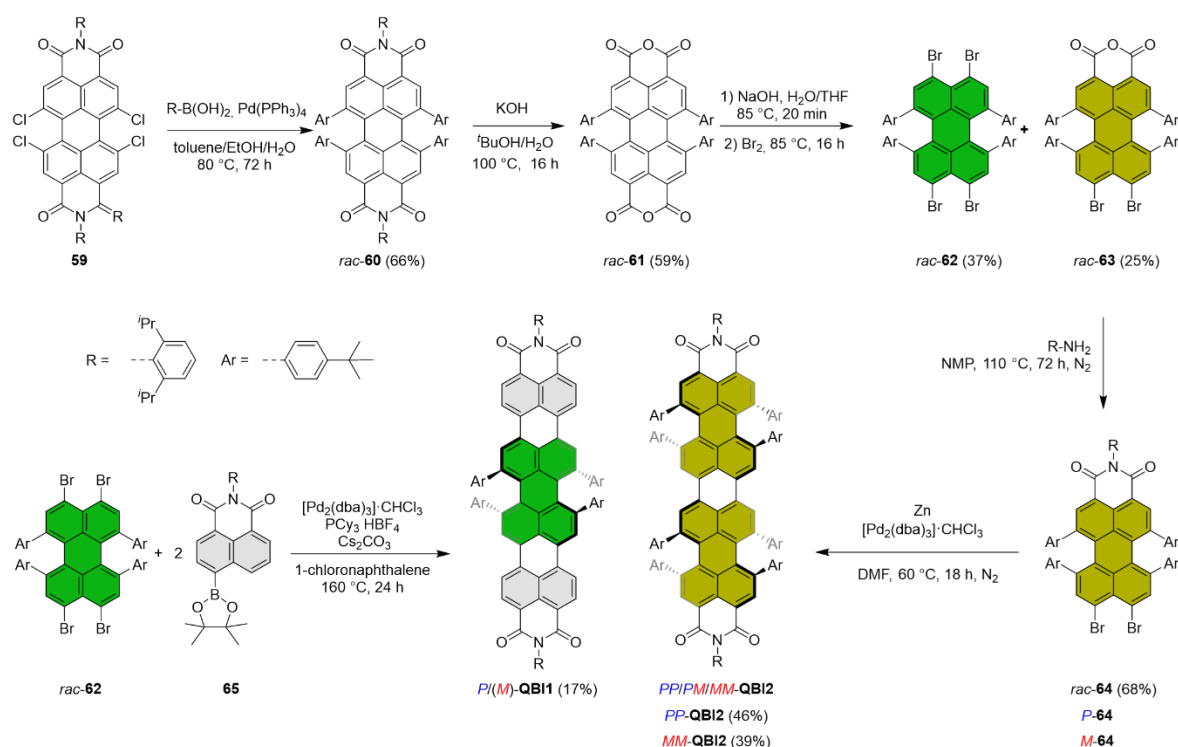
Single crystal X-ray crystallography was performed on a *Bruker D8 Quest* Diffractometer with a *PhotonII* detector using $\text{Cu K}\alpha$ radiation. The structures were solved using *SHELXT*,^[289] expanded with Fourier techniques and refined using the *SHELX* software package.^[284] Hydrogen atoms were assigned idealized positions and were included in the calculation of structure factors. All non-hydrogen atoms were refined anisotropically. Disordered *tert*-butyl groups are modelled with constrains and restrains using standard *SHELX* commands *RIGU*, *ISOR*, *SADI*, *DFIX*, and *EADP*. For the crystal structures of **63** and **QB11**, the electron density deriving from heavily disordered solvent molecules that could not be modelled satisfactorily

was removed using the SQUEEZE^[290] routine as implemented in the PLATON software.^[291] For the crystal structures of **QBI1** and **QBI2**, several Alert B were generated by CheckCIF routine^[292] regarding the absence of the acceptor of hydrogen bonds. This is due to the absence of the hydrogen-bond acceptor by the void generated by SQUEEZE or heavy disorder. For **QBI2** two more Alert B were generated for large difference of thermal factor of the same atom type in a residue. These Alerts were caused because the PLATON program considered that all disordered methanol molecules are in the same residue although they should be in separate residues.

Theoretical Calculations

DFT calculations were performed by Gaussian 16^[286] on ω B97XD/def2-svp level of theory.

8.2.2 Synthesis and Characterization



Scheme A1. Entire synthetic route toward chiral quaterrylene bisimides **QBI1**^[235] and **QBI2**.

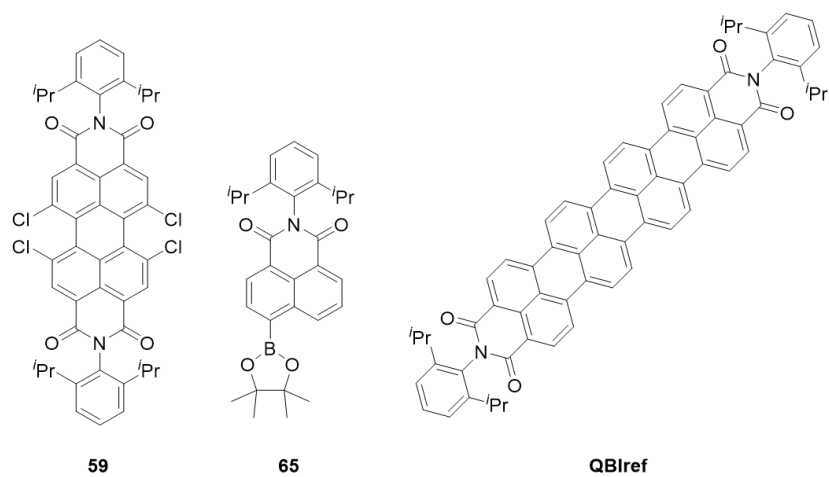
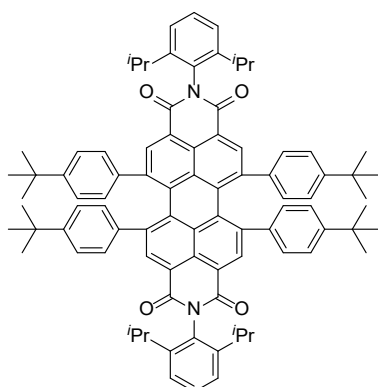


Figure A13. Literature known compounds used in this work.

Synthesis of Compound 60**60**

A Schlenk-tube was charged with tetrachloro PBI **59** (2.50 g, 2.95 mmol, 1.0 equiv), *para-tert*-butylphenylboronic acid (10.49 g, 58.92 mmol, 20.0 equiv), tetrakis(triphenylphosphine)palladium(0) [Pd(PPh₃)₄] (1.02 g, 0.88 mmol, 30 mol %), K₂CO₃ (4.27 g, 30.93 mmol, 10.5 equiv) under an inert atmosphere. Subsequently, 50 mL toluene, 10 mL ethanol and 25 mL water was added. All solvents were independently degassed prior to use. Then, freeze-pump thaw technique was applied to further degas the mixture. Thus, it was cooled to $-78\text{ }^{\circ}\text{C}$ and evacuated and backfilled with nitrogen three times. Subsequently, the reaction mixture was heated to $80\text{ }^{\circ}\text{C}$ for four days. After cooling down to room temperature, the reaction mixture was extracted with dichloromethane. The combined organic phases were dried over MgSO₄ and the solvent was removed under reduced pressure. The crude product was purified by column chromatography (gradient of dichloromethane/cyclohexane 1:2 to 1:1). The product was dried under high vacuum to obtain **60** as dark green solid (2.42 g, 1.95 mmol, 66%).

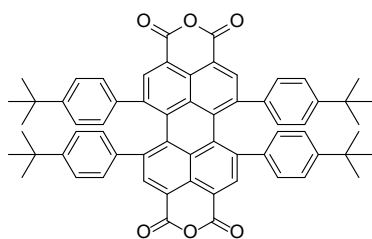
¹H NMR (CD₂Cl₂, 400 MHz, 295 K): δ/ppm = 8.23 (*s*, 4 H), 7.44 (*t*, $J = 7.72\text{ Hz}$, 2 H), 7.29 (*d*, $J = 7.72\text{ Hz}$, 4 H), 7.1–6.9 (*br*, 8 H), 6.9–6.4 (*br*, 8 H), 2.78 (*sep*, $J = 6.86$), 1.30 (*s*, 36 H), 1.15 (*d*, $J = 6.86$), 1.04 (*d*, $J = 6.86$).

¹³C NMR (CD₂Cl₂, 101 MHz, 295 K) δ/ppm = 164.4, 151.0, 146.6, 142.8, 138.5, 134.7, 132.7, 132.4, 131.7, 129.8, 128.4, 127.1, 125.1, 124.5, 122.4, 34.9, 31.4, 29.5, 24.3, 24.1.

MS (MALDI-TOF, negative mode, DCTB in chloroform): m/z : 1238.69099 [M][−] (calcd. for C₈₈H₉₀N₂O₄[−]: 1238.69006)

HRMS (ESI-TOF, positive mode, acetonitrile/chloroform): m/z : 1261.67807 [MNa]⁺ (calcd. for C₈₈H₉₀N₂NaO₄[−]: 1261.67928).

M.p.: 305–313 $^{\circ}\text{C}$.

Synthesis of Compound **61**^[235]**61**

Under an inert atmosphere, **60** (2.21 g, 1.8 mmol, 1.0 equiv) was suspended in 50 mL *tert*-butanol. Subsequently, 5.0 mL water and KOH, (100 g, 1.78 mol, 1000 equiv) was added and the mixture was heated to 95 °C for 16 h. After cooling down to room temperature, the reaction mixture was poured into 500 mL cold 10% aq. HCl and the resulting precipitate was collected and washed with water. The residue was dissolved in dichloromethane and washed with water, dried over MgSO₄ and the solvent was removed under reduced pressure. The crude product was purified by column chromatography (gradient of cyclohexane/dichloromethane 1:1 to 1:4; due to decomposition on the column, this step should be done fast) to give 976 mg (1.05 mmol, 59%) of **61** as a dark-green solid.

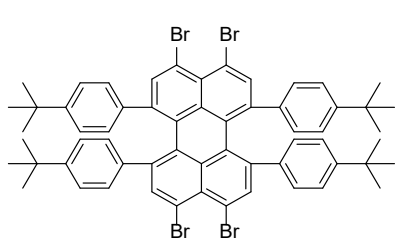
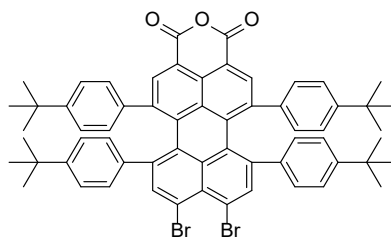
¹H NMR (CD₂Cl₂, 400 MHz, 295 K): δ /ppm = 8.28 (*s*, 4H), 7.21–7.01 (*br*, 8H), 6.78–6.43 (*m*, 8H), 1.37 (*s*, 36H).

¹³C NMR (CD₂Cl₂, 101 MHz, 295 K): δ /ppm = 160.7, 151.6, 143.0, 137.3, 135.8, 133.4, 132.4, 128.5, 128.4, 125.5, 118.8, 34.9, 31.3.

MS (MALDI-TOF, negative mode, DCTB in chloroform): *m/z*: 920.45 [M]⁻ (calcd. for C₆₄H₅₆O₆⁻: 920.4077)

HRMS (ESI-TOF, positive mode, acetonitrile/ chloroform): *m/z*: 943.3949 [MNa]⁺ (calcd. for C₆₄H₅₆O₆Na⁺: 943.3975).

M.p.: > 350 °C.

Synthesis of Compound **62** and **63**^[235]**62****63**

To a suspension of **61** (250.0 mg, 271 μmol, 1.0 equiv) in 25 mL water, an aqueous NaOH-solution (1.0 M, 1.63 mL, 1.63 mmol, 6.0 equiv) was added and the mixture heated to 85 °C.

Subsequently, THF was added carefully in small portions until a clear solution appeared (ca. 25 mL) and the reaction mixture was further heated to 85 °C for 20 min. Afterwards, bromine (1.73 g, 10.9 mmol, 40.0 equiv) was added in one portion and the mixture was stirred at 85 °C for 16 h. After cooling down to room temperature, the reaction mixture was poured into aq. HCl (10%, 100 mL), filtered and washed with water. The precipitate was dissolved in dichloromethane, washed with water and dried over MgSO₄. The crude product was purified by column chromatography (dichloromethane/cyclohexane 2:3) to yield **62** (111 mg, 101 μmol, 37%, red solid) and **63** (68.7 mg, 68.1 μmol, 25%, bluish green solid).

Characterization data of **62**:

¹H NMR (CD₂Cl₂, 400 MHz, 295 K): δ/ppm = 7.63 (*s*, 4H), 7.06–7.01 (*m*, 8H), 6.49–6.36 (*br*, 8H), 1.35 (*s*, 36H).

¹³C NMR (CD₂Cl₂, 101 MHz, 295 K): δ/ppm = 150.3, 140.8, 138.1, 137.6, 137.3, 128.6, 128.0, 127.2, 126.1, 119.5, 34.8, 31.4.

MS (MALDI-TOF, positive mode, DCTB in chloroform): *m/z*: 1096.17 [M]⁺.

HRMS (APCI-TOF, positive mode): *m/z*: 1092.1110 [M]⁺ (calcd. for C₆₀H₄₅Br₄⁺: 1092.1116)

M.p.: 272 °C.

Characterization data of **63**:

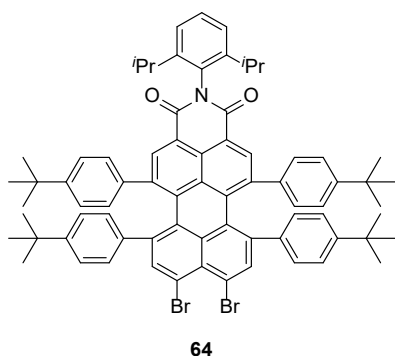
¹H NMR (CD₂Cl₂, 400 MHz, 295 K): δ/ppm = 8.21 (*s*, 2H), 7.72 (*s*, 2H), 7.12–7.01 (*m*, 8H), 6.70–6.30 (*br*, 8H), 1.37 (*s*, 18H), 1.35 (*s*, 18H).

¹³C NMR (CD₂Cl₂, 101 MHz, 295 K): δ/ppm = 161.2, 151.1, 150.8, 142.8, 140.9, 138.7, 137.5, 137.2, 137.1, 135.5, 135.2, 132.3, 128.7, 128.2, 127.9, 126.6, 122.3, 117.0, 34.8, 34.8, 31.4, 31.4.

MS (MALDI-TOF, positive mode, DCTB in chloroform): *m/z*: 1006.32 [M]⁺ (calcd. for C₆₂H₅₆Br₂O₃): 1006.2596)

HRMS (ESI-TOF, positive mode, acetonitrile/chloroform): *m/z*: 1029.2488 [MNa]⁺ (calcd. for C₆₂H₅₆Br₂O₃Na⁺: 1029.2494).

M.p.: > 350 °C.

Synthesis of Compound 64^[235]

A mixture of **63** (265 mg 263 μmol , 1.0 equiv) and 2,6-diisopropylaniline (743 μl 3.95 μmol , 15 equiv) in 2 mL acetic acid and 4 mL *N*-methyl-2-pyrrolidone was heated to 110 $^{\circ}\text{C}$ for 72 h. After cooling down to room temperature, the reaction mixture was poured onto water and extracted with dichloromethane. The combined organic phases were dried over MgSO_4 and the solvent removed under reduced pressure. The crude product was further purified by column chromatography (cyclohexane/dichloromethane 1:1) to obtain **6** as purple solid (208 mg, 178 μmol , 68%). The separation of *P*- and *M*-enantiomers was done by HPLC with chiral stationary phase (*n*-hexane/dichloromethane 1:1).

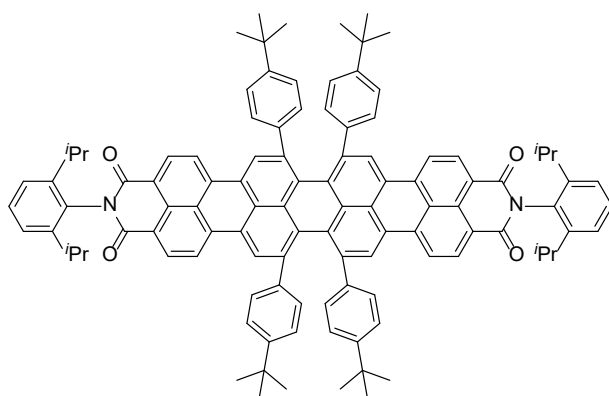
^1H NMR (CDCl_3 , 400 MHz, 295 K): δ/ppm = 8.25 (*s*, 2 H), 7.71 (*s*, 2 H), 7.51 (*t*, J = 7.8 Hz, 1 H), 7.36 (*d*, J = 7.8 Hz, 2 H), 7.11–7.05 (*m*, 8 H), 6.80–6.30 (*m*, 8 H), 2.86 (*sep*, J = 6.9 Hz, 2 H), 1.36 (*s*, 36 H), 1.22 (*d*, J = 6.9 Hz, 6 H), 1.13 (*d*, J = 6.9 Hz, 6 H).

^{13}C NMR (CD_2Cl_2 , 101 MHz, 295 K): δ/ppm = 164.6, 150.8, 150.5, 146.6, 142.6, 140.9, 138.9, 138.2, 137.6, 137.2, 134.0, 133.7, 132.4, 132.1, 129.7, 128.6, 128.4, 127.9, 127.2, 126.7, 124.4, 121.7, 121.0, 34.8, 34.8, 31.4, 31.4, 24.2, 24.1.

MS (MALDI-TOF, negative mode, DCTB in chloroform): m/z : 1167.45 [M]⁻.

HRMS (ESI-TOF, positive mode, acetonitrile/chloroform): m/z : 1188.3874 [MNa]⁺ (calcd. for $\text{C}_{74}\text{H}_{73}\text{Br}_2\text{NO}_2\text{Na}^+$: 1188.3906).

M.p.: 286–290 $^{\circ}\text{C}$.

Synthesis of **QB11**^[235]**QB11**

A Schlenk-tube was charged with **62** (15.0 mg, 13.5 μmol , 1.0 equiv), **65** (14.4 mg, 29.7 μmol , 2.2 eq.), tris(dibenzylideneacetone)dipalladium(0)-chloroform adduct ($[\text{Pd}_2(\text{dba})_3]\cdot\text{CHCl}_3$) (2.8 mg, 2.70 μmol , 20 mol %), tricyclohexylphosphine tetrafluoroborate ($\text{PCy}_3\cdot\text{HBF}_4$) (4.0 mg, 10.8 μmol , 80 mol %), Cs_2CO_3 (26.4 mg, 81.0 μmol , 6.0 equiv) and 1-chloronaphthalene (0.40 mL) as a solvent under an inert atmosphere at room temperature and stirred at 160 $^\circ\text{C}$ for 20 h. After cooling down to room temperature, the reaction mixture was filtered with cyclohexane over a pad of silica-gel to remove 1-chloronaphthalene and the crude product was eluted with dichloromethane. The crude product was purified by silica-gel column chromatography (gradient of dichloromethane/cyclohexane 1:1 to 1:0), followed by GPC and preparative thin-layer chromatography (dichloromethane/*n*-hexane 2:1). The product was dried under high vacuum to give 3.5 mg (2.35 μmol , 17%) of compound **QB11** as mixture of *P* and *M*-enantiomers as a light-green solid. The separation of atropo-enantiomers was accomplished using dichloromethane/*n*-hexane 2:1 as eluent.

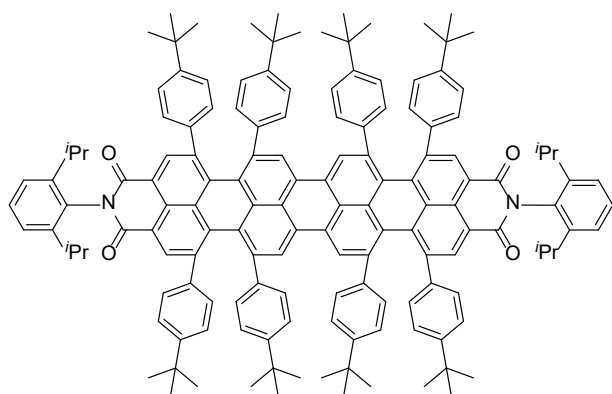
^1H NMR (CD_2Cl_2 , 400 MHz, 295 K): δ/ppm = 8.70 (*d*, J = 8.2 Hz, 4H), 8.63 (*d*, J = 8.2 Hz, 4H), 8.35 (*s*, 4H), 7.52 (*t*, J = 7.8 Hz, 2H), 7.37 (*d*, J = 7.8 Hz, 4H), 7.23–7.06 (*br*, 8H), 6.92–6.61 (*br*, 8H), 2.78 (*qui*, J = 6.8 Hz, 4H), 1.41 (*s*, 36H), 1.17–1.14 (*m*, 24H).

^{13}C NMR (CD_2Cl_2 , 151 MHz, 295 K): δ/ppm = 164.4, 150.5, 146.6, 142.2, 139.4, 137.3, 133.8, 132.1, 131.1, 130.3, 129.7, 129.1, 128.5, 127.6, 127.0, 125.7, 124.4, 121.4, 121.4, 34.8, 31.5, 30.1, 24.1.

HRMS (MALDI-TOF, positive mode, DCTB in chloroform): m/z : 1486.7558 $[\text{M}]^+$.

HRMS (ESI-TOF, positive mode, acetonitrile/chloroform): m/z : 1486.7517 $[\text{M}]^+$ (calcd. for $\text{C}_{108}\text{H}_{98}\text{N}_2\text{O}_4^+$: 1486.7527).

M.p.: > 350 $^\circ\text{C}$.

Synthesis of QB12

QB12

A Schlenk-tube was charged with 66.3 mg (56.8 μmol , 2.0 equiv) enantiopure **64** (either *P*- or *M*-enantiomer), 24.5 mg (374.5 μmol , 13.2 equiv) zinc powder, 4.7 mg (4.6 μmol , 12 mol %) *tris*(dibenzylideneacetone)dipalladium(0)-chloroform adduct $[\text{Pd}_2(\text{dba})_3]\cdot\text{CHCl}_3$. The mixture was evacuated and charged with nitrogen several times. Subsequently, 1 mL of anhydrous and degassed DMF was added under nitrogen atmosphere. The mixture was stirred at 60 $^\circ\text{C}$ for 18 h. After cooling down to room temperature the crude product was purified by column chromatography (dichloromethane/cyclohexane 4:1), followed by flash column chromatography, HPLC (dichloromethane/*n*-hexane 1:1) and GPC to obtain enantiopure *PP*- or *MM*-QB12 as olive green solid in yields of 46% (26.4 mg, 13.1 μmol) and 39% (11.2 μmol), respectively.

^1H NMR (CD_2Cl_2 , 400 MHz, 295 K): δ/ppm = 8.29 (*s*, 4H), 8.23 (*s*, 4H), 7.52 (*t*, J = 7.9 Hz, 2H), 7.38 (*d*, J = 7.9 Hz, 4H), 7.15–6.40 (*br*, 32H), 2.88 (*sep*, J = 6.6 Hz, 4H), 1.41 (*s*, 36H), 1.28 (*s*, 36H), 1.24 (*d*, J = 6.8 Hz, 12H), 1.14 (*d*, J = 6.9 Hz, 12H).

^{13}C NMR (CDCl_3 , 101 MHz, 295 K): 164.7, 150.4, 150.4, 146.6, 143.3, 140.7, 139.6, 139.0, 134.1, 133.9, 133.8, 132.4, 132.2, 131.3, 129.6, 128.7, 128.2, 128.1, 128.0, 127.7, 127.1, 126.4, 125.8, 124.4, 120.7, 34.9, 34.7, 31.5, 31.4, 29.4, 24.3, 24.1.

HRMS (MALDI-TOF, negative mode, DCTB in chloroform): m/z : *MM*-QB12: 2016.142 $[\text{M}]^-$ (calc. for $\text{C}_{148}\text{H}_{146}\text{N}_2\text{O}_4^-$: 2016.81).

HRMS (ESI-TOF, positive mode, acetonitrile/chloroform): m/z : *MM*-QB12: 2015.12771 $[\text{M}]^+$, *PP*-QB12: 2015.12771 $[\text{M}]^+$. (calcd. for $\text{C}_{148}\text{H}_{146}\text{N}_2\text{O}_4^+$: 2015.12826).

M.p.: (*PP*-QB12): >350 $^\circ\text{C}$.

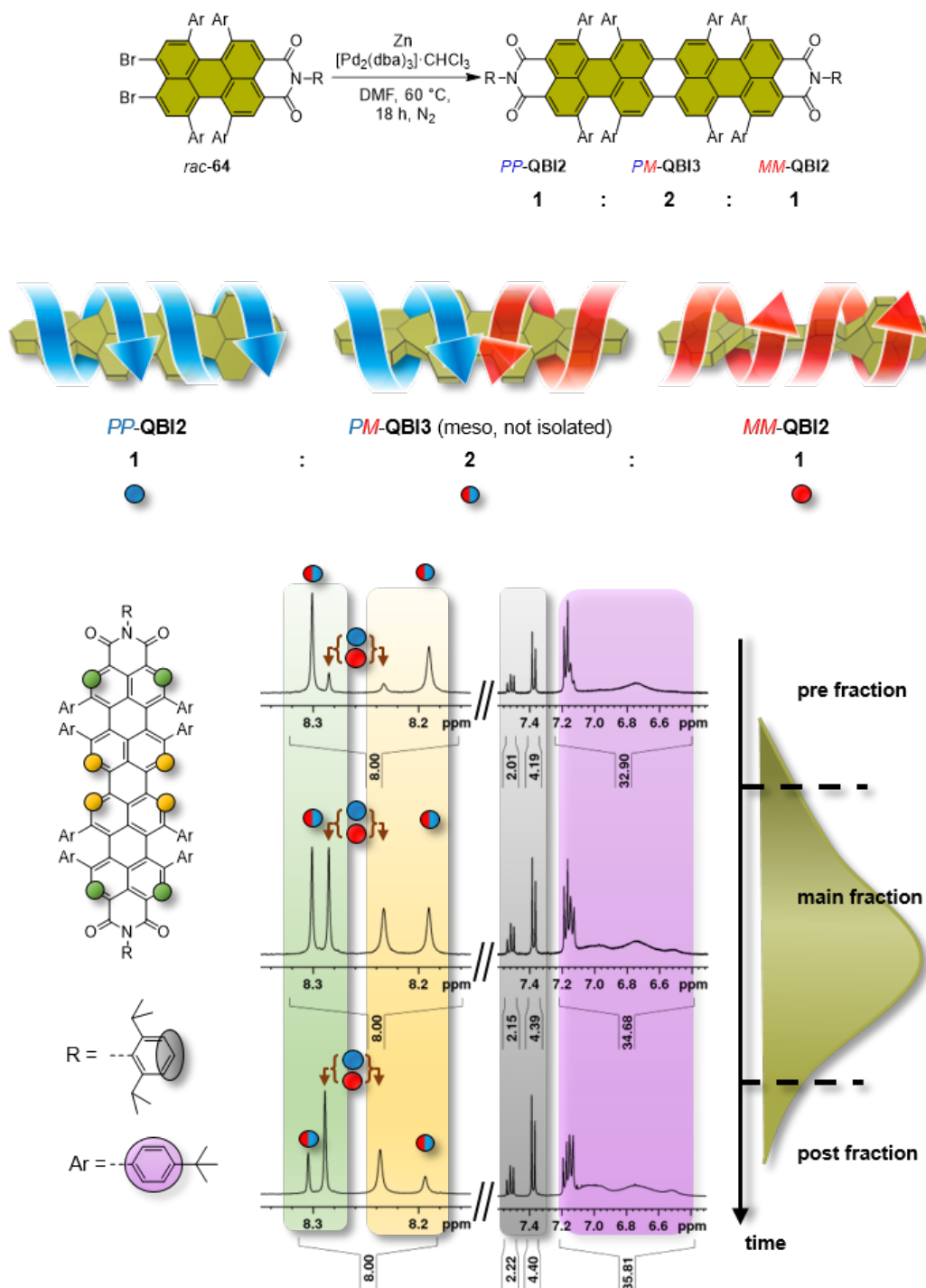


Figure A14. Schematic reaction overview of forming the isomeric mixture of the enantiomeric pair of *PP*- and *MM-QBI2* as well as the meso-form *PM-QBI3* in 1:2:1 ratio by using the racemic precursor *rac-64* (top) and the corresponding partial ^1H NMR spectra of product fractions (pre, main, post) obtained from high performance flash chromatography (dichloromethane/cyclohexane 1:1). For full NMR spectra of the pair of *PP*- and *MM*-enantiomers of QB12 see Figure A42 and Figure A44, respectively.

8.2.3 Single Crystal X-Ray Analysis

Table A7. Crystal data and structure refinement for *rac*-QBII, *PP*-QBII and 63.

CCDC	2057919 <i>rac</i> -QBII ^[235]	2151947 <i>PP</i> -QBII	2151946 <i>rac</i> -63 ^[235]
Empirical formula	(C ₁₀₈ H ₉₈ N ₂ O ₄), 0.283·(CHCl ₃), 0.717·(C ₂ H ₆ O)	2(C ₁₄₈ H ₁₄₆ N ₂ O ₄), 9.527·(C ₆ H ₅ Cl), 19.578·(CH ₄ O)	C ₆₂ H ₅₆ Br ₂ O ₃
Formula weight	1554.70	5732.71	1008.87
Temperature	100(2) K	100(2) K	100(2) K
Wavelength	1.54178 Å	1.54178 Å	1.54178 Å
Crystal system, space group	Monoclinic, <i>P2₁/c</i>	Tetragonal, <i>P4₃</i>	Monoclinic, <i>P2₁/c</i>
Unit cell dimensions	<i>a</i> = 18.4815(14) Å <i>b</i> = 18.4586(12) Å <i>c</i> = 30.406(2) Å <i>α</i> = 90 ° <i>β</i> = 101.598(5) ° <i>γ</i> = 90 °	<i>a</i> = 29.8923(13) Å <i>b</i> = 29.8923(13) Å <i>c</i> = 37.6557(18) Å <i>α</i> = 90 ° <i>β</i> = 90 ° <i>γ</i> = 90 °	<i>a</i> = 20.1055(15) Å <i>b</i> = 26.7587(19) Å <i>c</i> = 10.2202(8) Å <i>α</i> = 90 ° <i>β</i> = 103.474(4) ° <i>γ</i> = 90 °
Volume	10161.0(13) Å ³	33647(3) Å ³	5347.1(7) Å ³
<i>Z</i>	4	4	4
Calculated density	1.016 Mg/m ³	1.132 Mg/m ³	1.253 Mg/m ³
Absorption coefficient	0.669 mm ⁻¹	1.216 mm ⁻¹	2.253 mm ⁻¹
<i>F</i> (000)	3308.2	12259.4	2088.0
Crystal size	0.360 × 0.280 × 0.010 mm	0.407 × 0.306 × 0.300 mm	0.510 × 0.060 × 0.060 mm
Theta range for data collection	2.440 to 68.497 °	2.090 to 79.216 °	2.260 to 79.103 °
Limiting indices	-22 ≤ <i>h</i> ≤ 22, -22 ≤ <i>k</i> ≤ 22, -36 ≤ <i>l</i> ≤ 36	-37 ≤ <i>h</i> ≤ 37, -38 ≤ <i>k</i> ≤ 36, -47 ≤ <i>l</i> ≤ 47	-25 ≤ <i>h</i> ≤ 25, -34 ≤ <i>k</i> ≤ 28, -12 ≤ <i>l</i> ≤ 13
Reflections collected / unique	75812 / 18563 [<i>R</i> _{int} = 0.1428]	517164 / 72027 [<i>R</i> _{int} = 0.0536]	118040 / 11518 [<i>R</i> _{int} = 0.0555]
Completeness	99.6%	99.9%	99.9%
Absorption correction	Semi-empirical from equivalents	Semi-empirical from equivalents	Semi-empirical from equivalents
Max. and min. transmission	0.7531 and 0.5300	0.7542 and 0.6286	0.7542 and 0.5411
Refinement method	Full-matrix least-squares on <i>F</i> ²	Full-matrix least-squares on <i>F</i> ²	Full-matrix least-squares on <i>F</i> ²
Data / restraints / parameters	18563 / 231 / 1220	72027 / 6257 / 5109	11518 / 170 / 802
Goodness-of-fit	1.178	1.078	1.082
Final <i>R</i> indices [<i>I</i> > 2σ(<i>I</i>)]	<i>R</i> ₁ = 0.1162, <i>wR</i> ₂ = 0.2697	<i>R</i> ₁ = 0.0589, <i>wR</i> ₂ = 0.1623	<i>R</i> ₁ = 0.0560, <i>wR</i> ₂ = 0.1063
<i>R</i> indices (all data)	<i>R</i> ₁ = 0.1994, <i>wR</i> ₂ = 0.3297	<i>R</i> ₁ = 0.0600, <i>wR</i> ₂ = 0.1644	<i>R</i> ₁ = 0.0709, <i>wR</i> ₂ = 0.1176
Largest diff. peak and hole	0.381 and -0.279 e·Å ⁻³	0.419 and -0.331 e·Å ⁻³	1.478 and -1.195 e·Å ⁻³

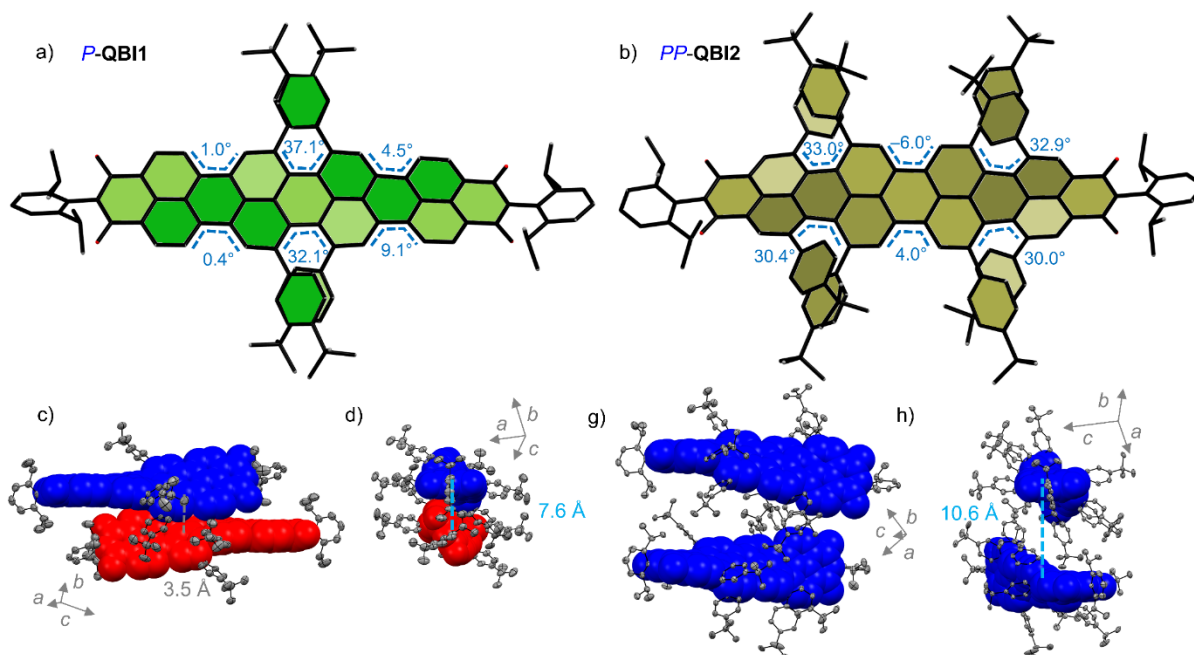


Figure A15. Top views (a,b) onto the molecular structure of the *P*-enantiomer of **QBI1**^[235] (left, green) and *PP*-**QBI2** (right, dark yellow) as well as molecular packing arrangement (c–h) found in their respective single crystal structures of the racemic mixture *rac*-**QBI1** or pure enantiomer *PP*-**QBI2** in side view (c,g) and front view (d,h). The torsion angles (blue) between four carbon atoms forming a *bay*-area are indicated (dashed line, light blue) as well as the topography of six-membered rings from top to bottom in increasing color brightness. Closest π -contacts (gray) and center-to-center distances (light blue) are indicated as well. The ellipsoids (c–h) are set to 50% probability (C: gray). Disorder of the alkyl residues, hydrogen atoms as well as solvent molecules are omitted for clarity.

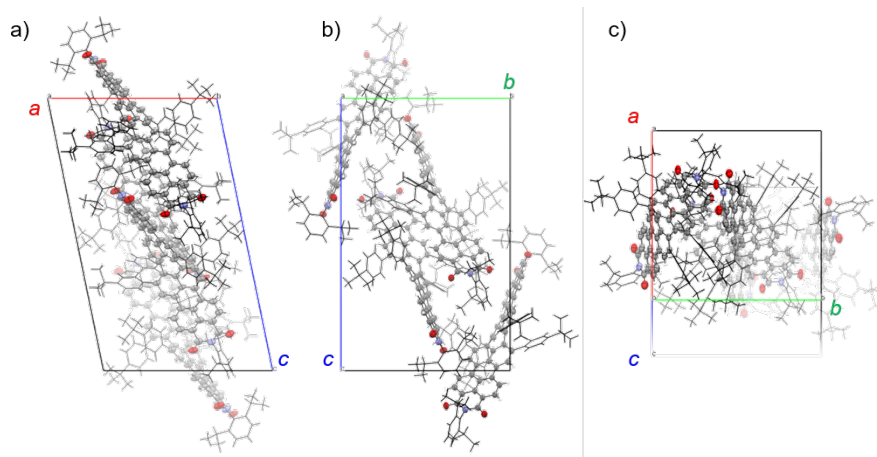


Figure A16. Unit cell of racemic *rac*-**QBI1**^[235] in the single crystal structure viewed along the (a) *b*-axis (b) *a*-axis and (c) *c*-axis. The ellipsoids are set to 50% probability (C: gray). Disorder of the alkyl residues, hydrogen atoms as well as solvent molecules are omitted for clarity.

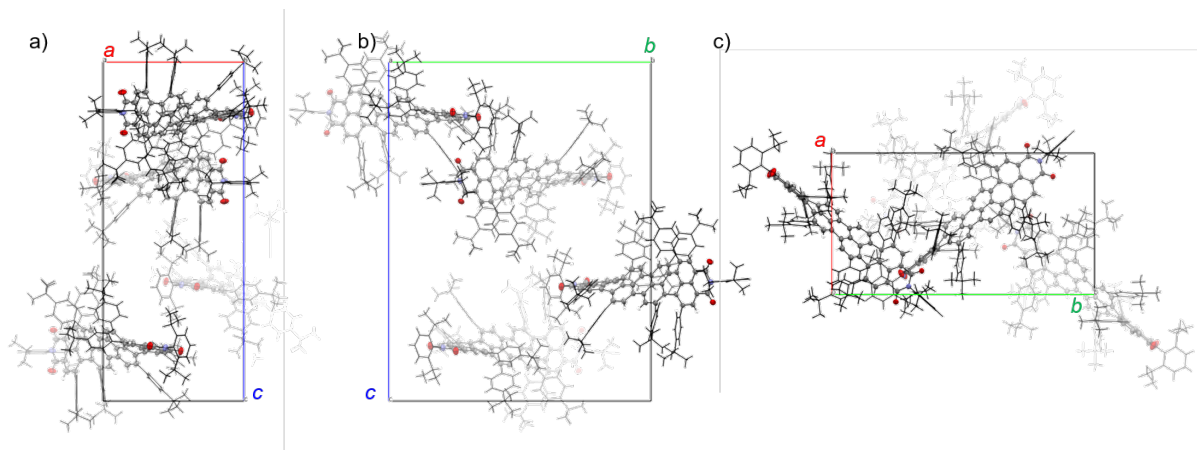


Figure A17. Unit cell of enantiopure *PP-QB12* in the single crystal structure viewed along the (a) *b*-axis (b) *a*-axis and (c) *c*-axis. The ellipsoids are set to 50% probability (C: gray). Disorder of the alkyl residues, hydrogen atoms as well as solvent molecules are omitted for clarity.

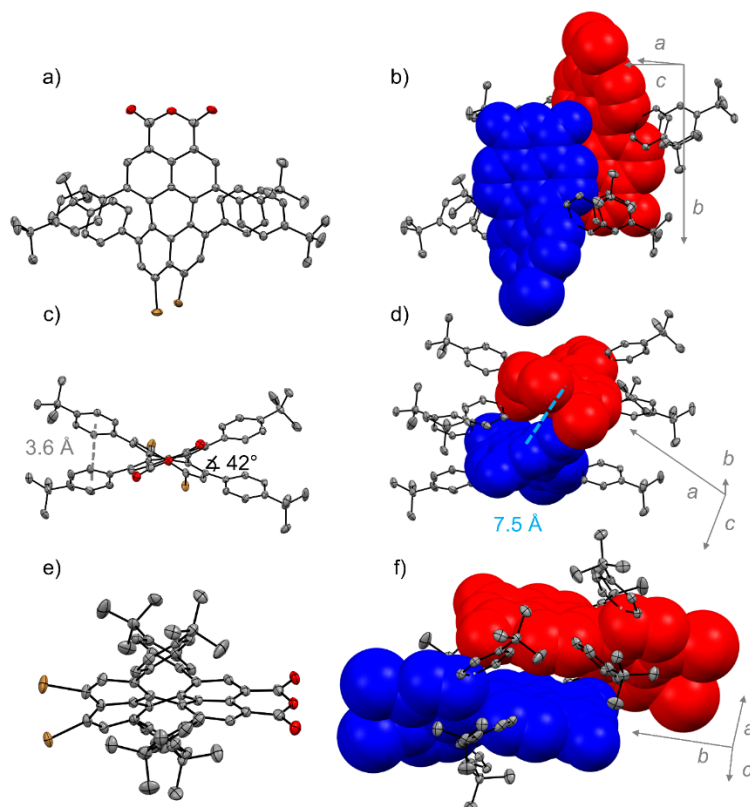


Figure A18. Molecular geometry of *P-63*^[235] (a,c,e) as well as a pair of *P-* and *M-* enantiomers (b,d,f) found in the single-crystal structures of racemic **63**. Molecules are shown within top-view (a,b), front-view (c,d) and rotated side-view (e,f). The ellipsoids are set to 50% probability (C: gray). Disorder of the alkyl residues, hydrogen atoms as well as solvent molecules are omitted for clarity. Twist angles between naphthalene subplanes interlocked by aryl substituents are shown in black. Closest π - π -distances between central centroids of chromophores (light blue) and adjacent phenyl-substituents scaffold (gray) are indicated as well.

8.2.4 Optical Properties

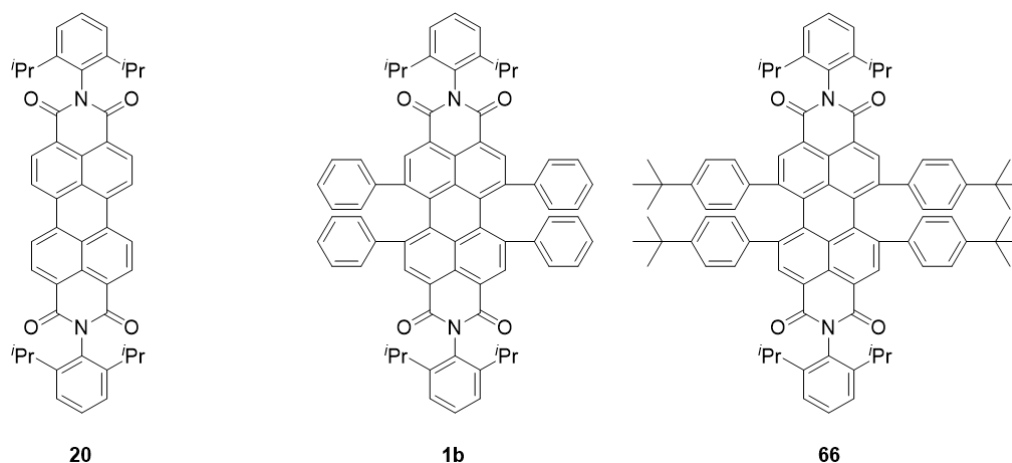


Figure A19. Chemical structures of PBI-based reference dyes.

The rigidification effect imparted by the sterical congestion of interlocking *bay*-aryl substituents of **QBI1** and **QBI2** is not accomplished in case of the respective PBIs showing significantly different behavior in both, absorption and emission (Table A8, Figure A20). Within the series of PBIs, the S_0 – S_1 transition of planar **20** undergoes both a dramatic redshift and broadening from 526 nm ($\lambda_{\max} = 96000 \text{ M}^{-1} \text{ cm}^{-1}$) to 602 nm (**1e**, $\lambda_{\max} = 24200 \text{ M}^{-1} \text{ cm}^{-1}$) additionally to the inductive effect of the attached *tert*-butyl units to 622 nm (**66**, $\Delta\lambda_{\max} = 23500 \text{ M}^{-1} \text{ cm}^{-1}$). Also the increase in S_0 – S_2 transition is much more pronounced as found for the respective QBIs. This differences are further pursued regarding fluorescence quantum yields of 100% (**20**) that drops down to 55% (**1e**) along the twist and further decreases to 37% (**66**) when attaching the *tert*-butyl units at the phenyl substituents. Thus, the rigidification approach only pays out for the extended QBIs emitting in the NIR region assuming the suppression of vibrational losses.

Table A8. Summary of optical properties of discussed PBI dyes in DCM at 295 K.

	λ_{\max}^a / nm	ϵ_{\max} / $\text{M}^{-1} \text{ cm}^{-1}$	λ_{em} / nm	$\Delta\tilde{\nu}_{\text{Stokes}}$ / cm^{-1}	Φ_{Fl} / %
20 ^[71]	527	93000	534	200	99±1
1e ^[22]	602, 449	24200, 14700	671	1740	55±1 ^c (Oxazine 1)
66	622, 452	23500, 20300	663	1500	37±1 ^c (Oxazine 1)

^a $c_0 \approx 1 \times 10^{-5} \text{ M}^{-1}$. ^b Absolute Φ_{Fl} was determined by a calibrated integration sphere system *via* direct excitation method,^[245] 1 cm cell thickness, OD = 0.15–0.25). The values were corrected for reabsorption. ^c Relative Φ_{Fl} was determined by dilution method (OD < 0.05) and Oxazine 1 ($\Phi_{\text{Fl}} = 11\%$ in EtOH).^[283]

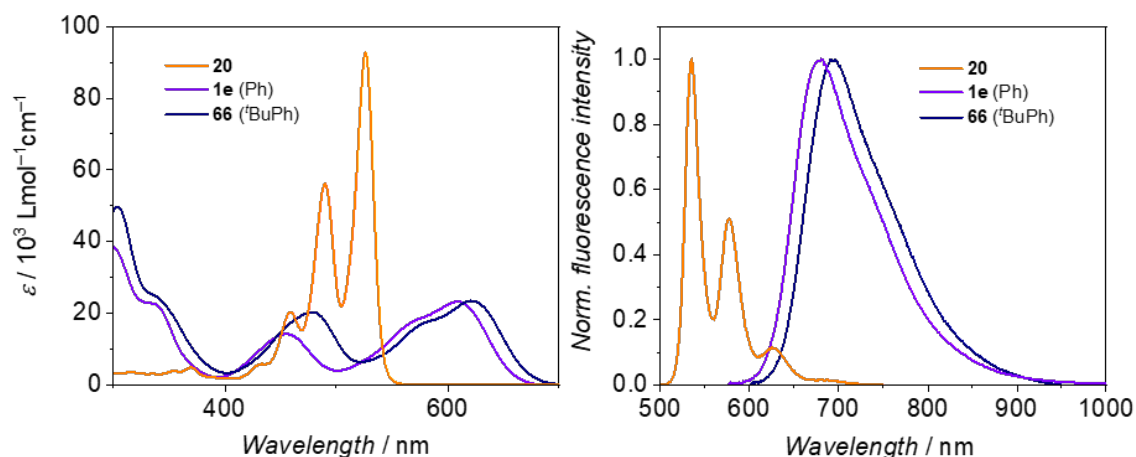


Figure A20. Absorption (left) and normalized emission (right) spectra of **20**,^[71] **1e**,^[22] and **66** in dichloromethane solution at 295K.

8.2.5 Theoretical Calculations

Absorption and electronic circular dichroism (ECD) spectra were calculated with the program Gaussian 16 using on ω B97XD/def2-svp level of theory. **QB11** and **QB12** were both simplified for the calculation by replacing the *tert*-butyl-phenyl units at the *bay*-areas by phenyl-rings and the diisopropyl groups at the Dipp imide substituents by methyl units.

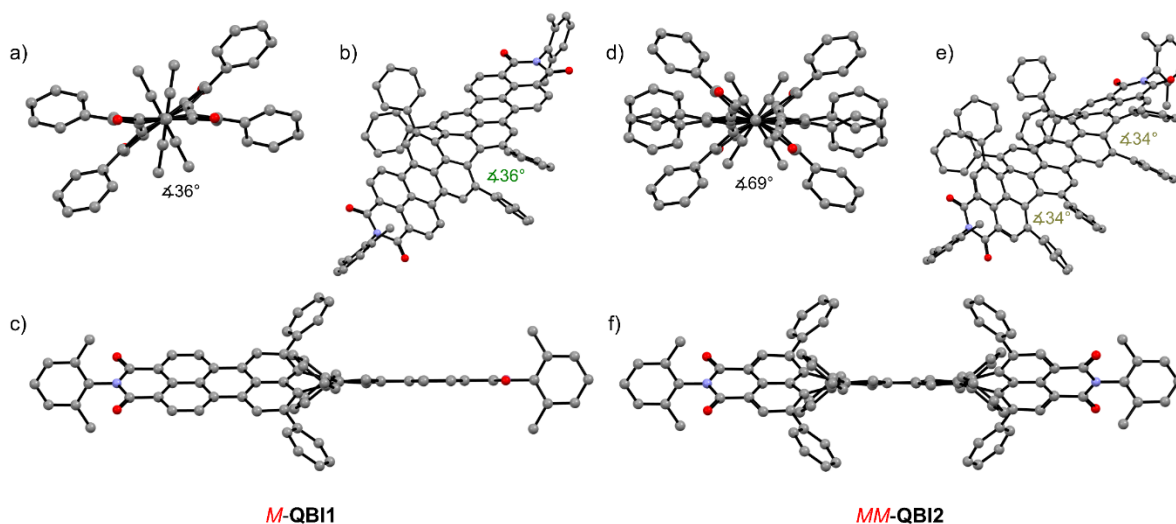


Figure A21. Calculated geometries of simplified **M-QB11** (a,b,c) and **MM-QB12** (d,e,f) in front view (a,d), bevelled side view (b,e) as well as even side view (c,f). Twist angles of the central naphthalene subplanes (green and dark yellow for **QB11** and **QB12**, respectively) are shown as well as twist angles between the outermost naphthalene subplanes.

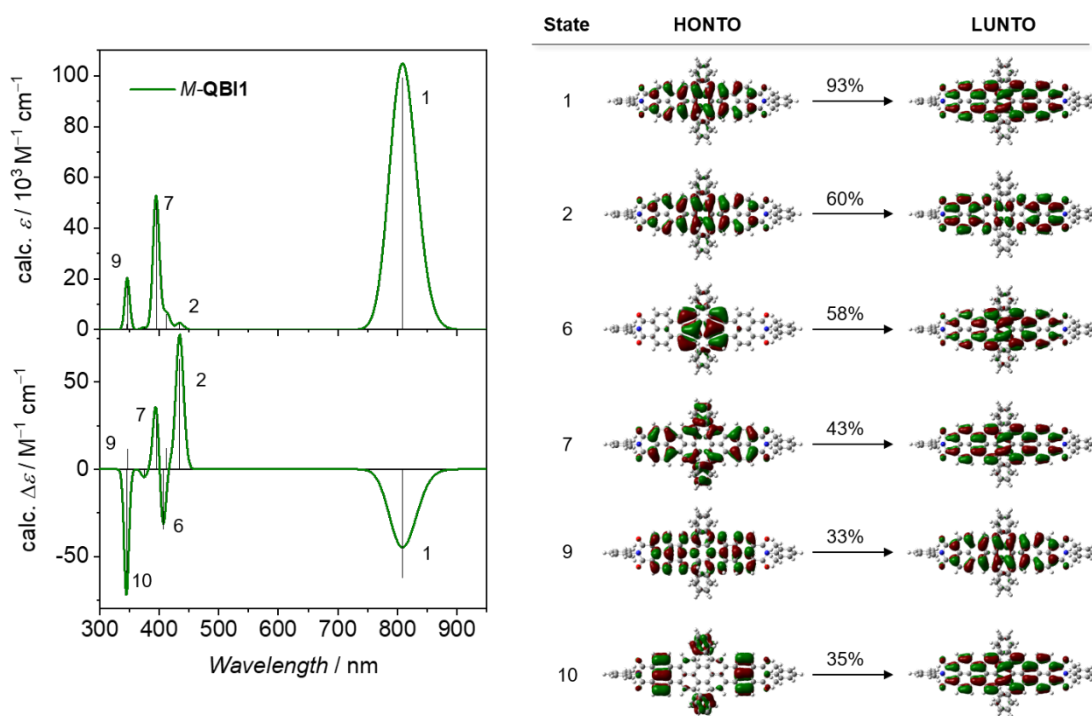


Figure A22. Left: Calculated UV–vis–NIR absorption (top) and ECD (bottom) spectra of simplified *M-QB11*. Vertical transitions are indicated as well as their respective NTO-representations^[242] (right) as HONTO (highest occupied natural transition orbital) and LUNTO (lowest occupied natural transition orbital) with iso-values of 0.02. Excitation energies are shifted by 0.353 eV scaled by factor 0.28 and convoluted with a phenomenological Gaussian with half width at half-maximum = 0.05 eV.

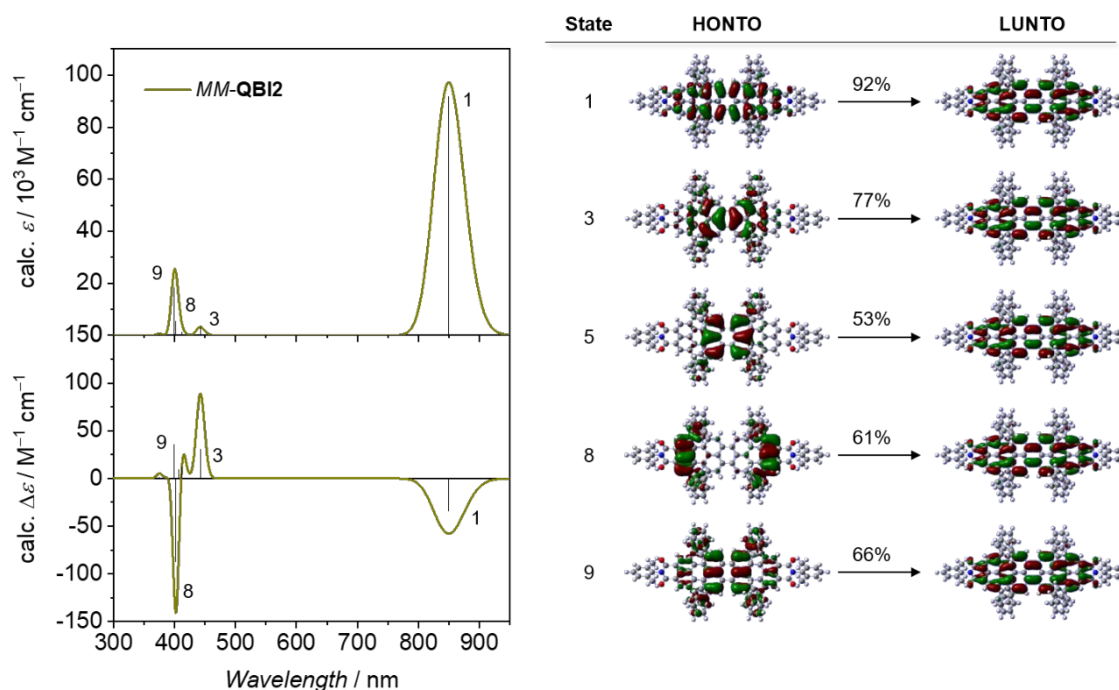
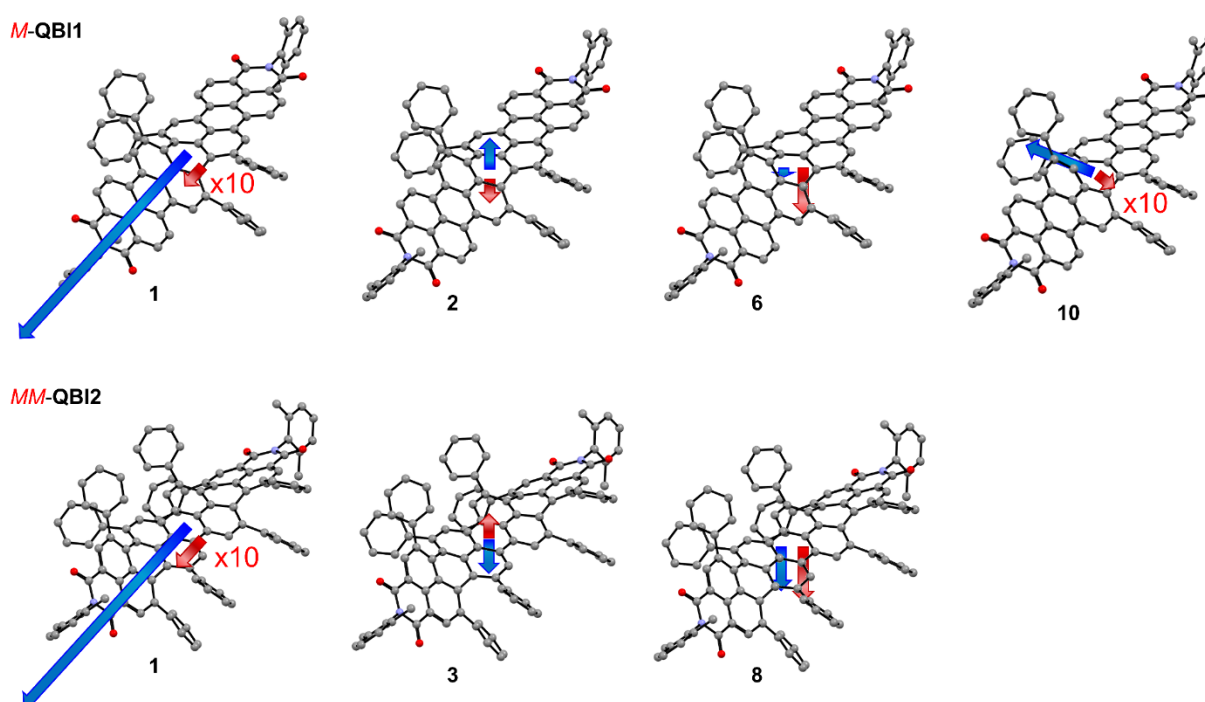


Figure A23. Left: Calculated UV–vis–NIR absorption (top) and ECD (bottom) spectra of simplified *MM-QB12*. Vertical transitions are indicated as well as their respective NTO-representations^[242] (right) as HONTO (highest occupied natural transition orbital) and LUNTO (lowest occupied natural transition orbital) with iso-values of 0.02. Excitation energies are shifted by 0.397 eV scaled by factor 0.28 and convoluted with a phenomenological Gaussian with half width at half-maximum = 0.05 eV.

Table A9. Ground to excited state transition electric dipole moments (μ) and ground to excited state transition magnetic dipole moments \mathbf{m} taken from TD-DFT calculations shown in Figure A22 and Figure A23.

	Excited State	$ \mu ^a$ / 10^{-18} esu cm $^{\square 1}$	$ \mathbf{m} ^a$ / 10^{-20} erg G $^{-1}$	$\angle(\mathbf{m}, \mu)$ / $^{\circ}$
<i>M-QBI1</i>	1	13.94	0.15	0.0
	2	1.69	1.30	179.7
	6	0.49	2.54	0.8
	10	4.02	0.12	154.5
<i>MM-QBI2</i>	1	13.60	0.21	0.0
	3	1.88	1.34	180.0
	8	2.43	3.03	0.0

^a The values obtained from Gaussian software were divided by $0.3934 \cdot 10^{-18}$ erg G $^{-1}$ and $1.0267 \cdot 10^{-20}$ esu $^{-1}$ cm $^{-1}$ to obtain the dipole moments in their common cgs units.^[35]

**Figure A24.** Schematic graphical representation of magnetic (\mathbf{m} , red) as well as electric (μ , blue) transition dipole moments of selected excited states of *M-QBI1* (top) as well as *MM-QBI2* (bottom) corresponding to Table A9 in cgs units.

8.2.6 Chiroptical Properties

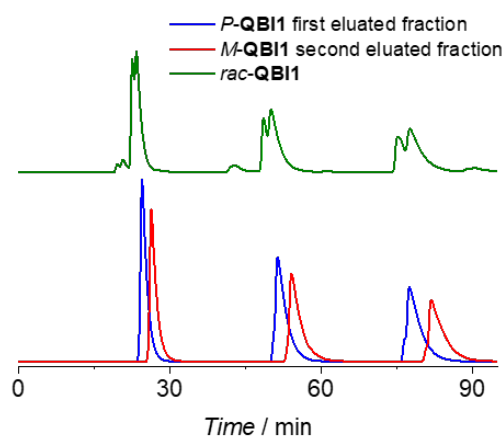


Figure A25. HPLC traces (semipreparative device) of racemic mixture (green) and of separated *P*- and *M*-enantiomers (blue and red) of QB11.^[235]

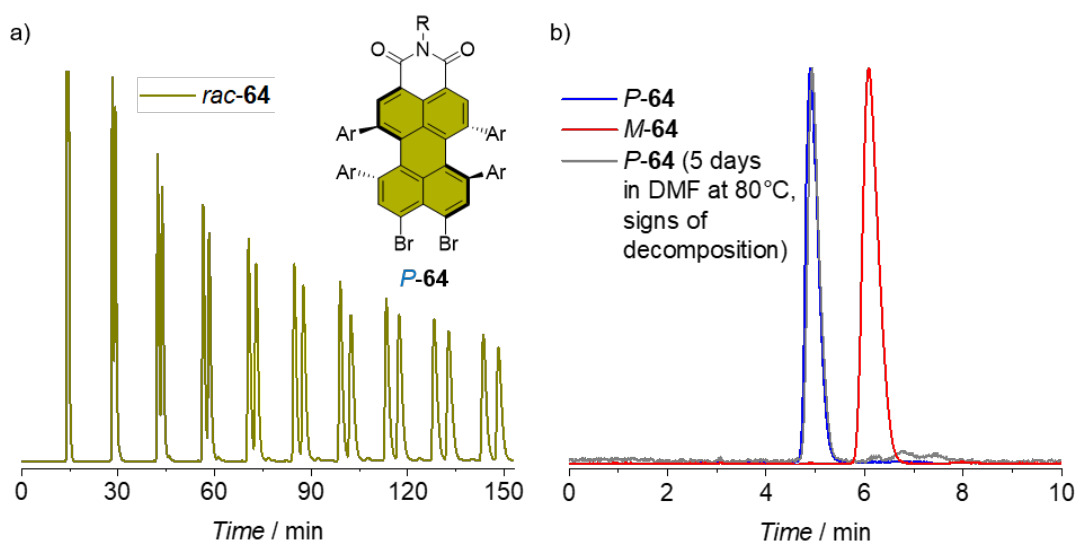


Figure A26. (a) HPLC elugram (semipreparative device) of precursor *rac*-64 as observed upon multicycle separation into the *P*- and *M*-enantiomers. (b) HPLC trace (analytical device) of the separated *P*- and *M*-enantiomers subsequently used for the synthesis of enantiopure QB12 as well as racemization experiment of *P*-64 ($c \approx 10^{-4}$ M) after 5 days in DMF at 80 °C (gray line) revealing signs of decomposition but no racemization.

The rate constant k_{rac} , half-life $t_{1/2}$ and free enthalpy for the activation of the racemization (QB11) and diastereomerization (QB12) ΔG^\ddagger are determined according to a literature procedure described by first order kinetic of equation 1.^[60] Time-dependent CD spectroscopy was carried out in 1,1,2,2-tetrachloroethane at 398 K to determine the rate constant k_{rac} of *P*-QB11 and *MM*-QB12 at 881 and 431 nm as well as at 848 and 448 nm, respectively.

$$A = A_0 \cdot e^{(-k_{rac} t)}. \quad (16)$$

The corresponding $t_{1/2}$ were determined according to Eq. 17:

$$t_{1/2} = \frac{\ln(2)}{k_{rac}}. \quad (17)$$

The free enthalpy for the activation of the racemization and diastereomerization ΔG^\ddagger was determined applying the Eyring equation (Eq. 18). Thereby, R represents the gas constant, h the Planck constant and k_B the Boltzmann constant. The transmission coefficient κ was either set to 0.5^[59] for the racemization of P -**QB11**^[235] or to 0.25 for the diastereomerization of MM -**QB12**. The obtained data for all fitted wavelengths are summarized in Table A10.

$$\Delta G^\ddagger = -RT \cdot \ln\left(\frac{h k_{rac}}{\kappa T k_B}\right). \quad (18)$$

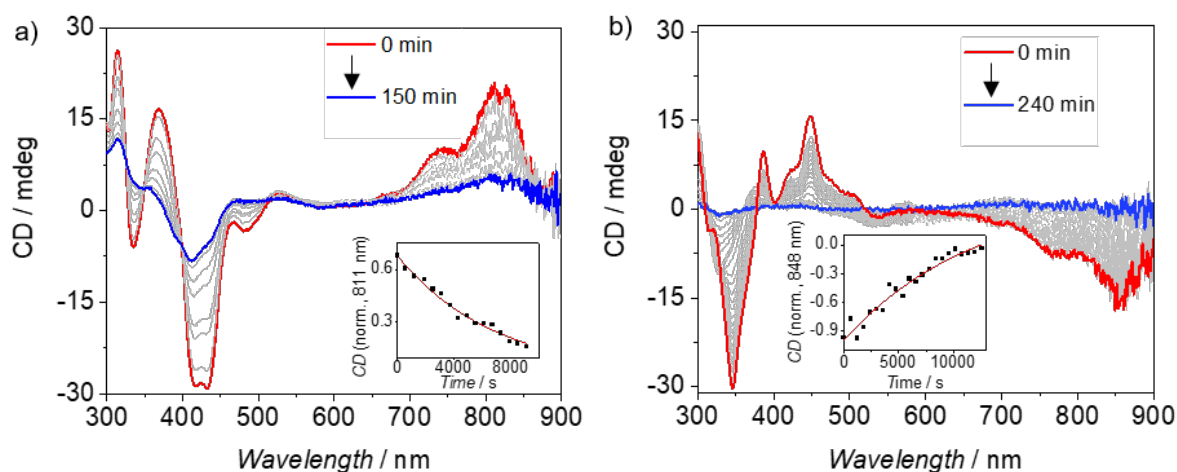


Figure A27. Exponential decay of the CD signal of P -**QB11**^[235] (a) and MM -**QB12** (b) in 1,1,2,2-tetrachloroethane at 398 K. The insets show the data points at maximum CD signal including exponential fit with $R^2 = 0.98359$ (**QB11**), $R^2 = 0.97486$ (**QB12**).

Table A10. Summary of the obtained data for the racemization process of *P-QBI1*^[235] as well as the diastereomerization process of *MM-QBI2* in 1,1,2,2-tetrachloroethane at 398 K.

	fitted wavelength	k_{rac}^a / s ⁻¹	$t_{1/2}^a$ / min	$\Delta G_{398\text{ K}}^\ddagger^b$ / kJ·mol ⁻¹
<i>P-QBI1</i>	431 nm	$1.4 \cdot 10^{-4} \pm 8.8 \cdot 10^{-6}$	81 ± 5	125.4 ± 1.6
	811 nm	$1.5 \cdot 10^{-4} \pm 5.6 \cdot 10^{-6}$	79 ± 3	125.4 ± 1.6
	average	$1.5 \cdot 10^{-4} \pm 5.2 \cdot 10^{-6}$	80 ± 3	125.4 ± 1.6
<i>MM-QBI2</i>	448 nm	$8.5 \cdot 10^{-5} \pm 1.8 \cdot 10^{-5}$	136 ± 28	124.9 ± 1.8
	848 nm	$8.4 \cdot 10^{-5} \pm 2.3 \cdot 10^{-5}$	138 ± 38	124.9 ± 1.9
	average	$8.5 \cdot 10^{-5} \pm 1.5 \cdot 10^{-5}$	137 ± 24	124.9 ± 1.7

^a Error of least square fit is assumed. Gaussian error propagation was calculated for $t_{1/2}$ and $\Delta G_{398\text{ K}}^\ddagger$.

^b Systematic error of ± 5 K was assumed.

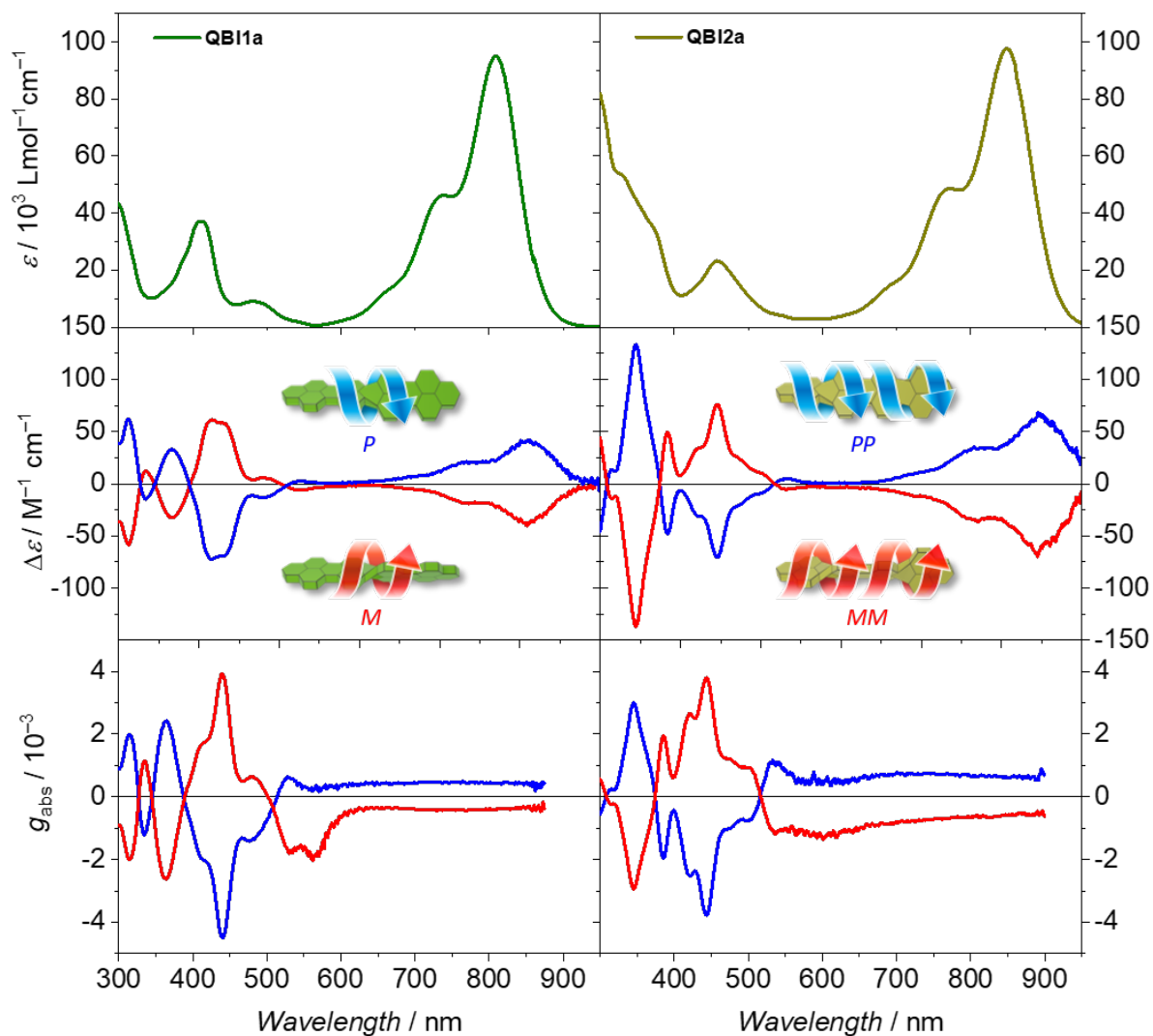


Figure A28. UV-vis-NIR absorption spectra (top) of QB11 (left) and QB12 (right), CD spectra (middle) and g_{abs} values (bottom) of their *P*/*PP*- and *M*/*MM*-atropo-enantiomers in blue and red, respectively. The insets show schematically the twisted π -scaffolds.

8.2.7 Electrochemical Properties

To relate optical to electrochemical band gaps for the twisted QBIs, cyclic voltammetry (CV) and differential pulse voltammetry (DPV) experiments were performed. Measurements were conducted in DCM at room temperature against Fc/Fc⁺ using tetrabutylammonium hexafluorophosphate (TBAHFP) as an electrolyte. The results are summarized in Table A1 and Figure A29.

Table A11. Summary of the obtained electrochemical properties in DCM at 298K.

	$E_{\text{red1}}^{\text{a}}$ / V	$E_{\text{red2}}^{\text{a}}$ / V	$E_{\text{ox1}}^{\text{a}}$ / V	$E_{\text{ox2}}^{\text{a}}$ / V	$E_{\text{gap, CV}}$ / eV
20 ^[71]	-1.02	-1.26	1.27	- ^b	2.49
1b ^[22]	-1.08	-1.29	0.99	1.29	2.07
66	-1.12	-1.36	0.92	- ^b	2.04
QBIfref ^[293]	-0.98 ^c	- ^b	0.42 ^c	- ^b	1.40
QBI1	-1.03	-2.16	0.38	0.73	1.41
QBI2	-1.08	-2.17	0.32	0.66	1.40

^aHalf-wave potentials were determined by cyclic or differential pulse voltammetry measured in DCM (0.1 M TBAHFP) vs. Fc/Fc⁺ at a scan rate of 100 mV s⁻¹. ^bNot observed. ^cLiterature reported half-wave potentials of CV measurement in CHCl₃/MeCN vs SCE potentials were converted to V vs. Fc/Fc⁺ by $E_{\text{Fc/Fc}^+} = E_{\text{SCE}} - 0.400$ V.

QBI1 and **QBI2** show two reversible oxidations as well as reductions each. Upon the second core twist from **QBI1** to **QBI2**, oxidation as well as reduction potentials are shifted similarly. The first oxidation potential decreases from 0.38 V to 0.32 V while the reduction potential undergoes a decrease from -1.03 V to -1.08 V thus resulting in an overall reduction of the electrochemically determined band gap ΔE_{CV} from 1.46 eV to 1.40 eV in accordance with the optical bandgap ΔE_{opt} showing 1.53 eV and 1.46 eV, respectively. The overall behavior of twisted QBIs follows the findings on hitherto reported planar rylene bisimides. Thus, uniquely the first reduction process shows a doubled intensity indicating a two-electron process assigned to the two imide subunits, which are decoupled over the extended π -scaffold.^[293] Moreover, the evolution from planar PBI over terrylene bisimide (TBI) to QBI had been revealed constant first reduction potentials whereas the spectral redshift is only assigned with the increase in oxidation potential.^[293-294] This trend now holds also true for the elongation of twisted congeners as the planar **20**, the twisted **1b** and **66** as well as the twisted QBIs. They all show overall very similar first reduction potentials of about -1.05 V, similar to many widely investigated n-type organic semiconductors such as C₆₀ fullerene^[170] while the major changes in this series are observed for their oxidation potential.

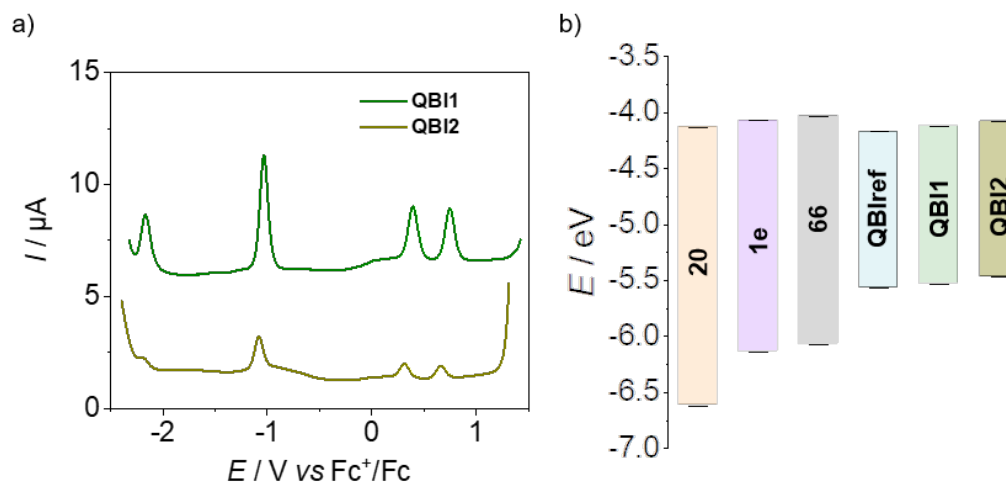
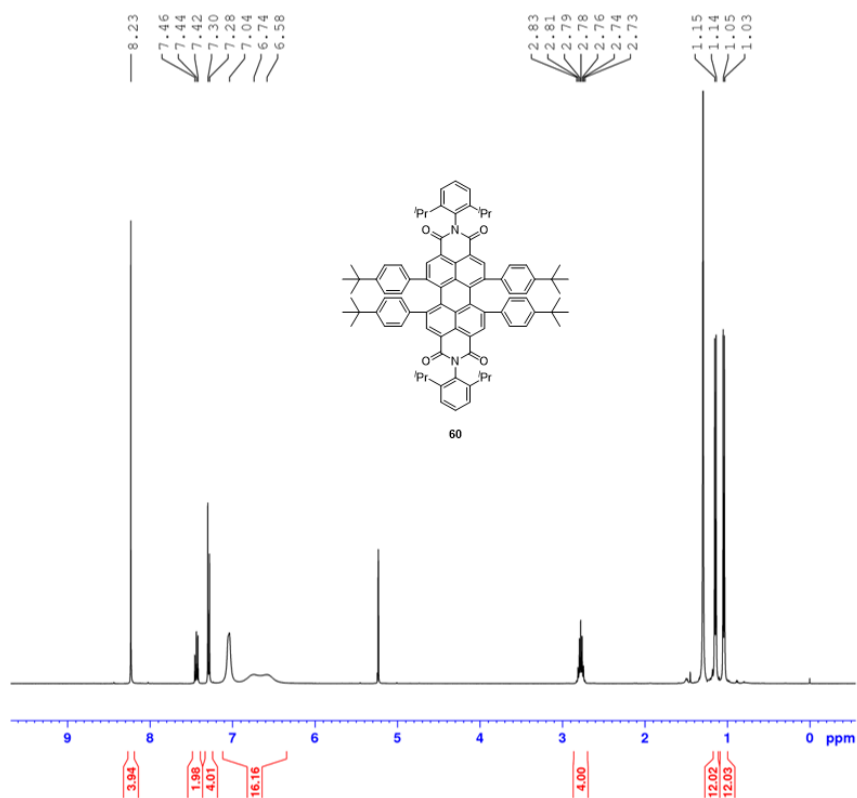
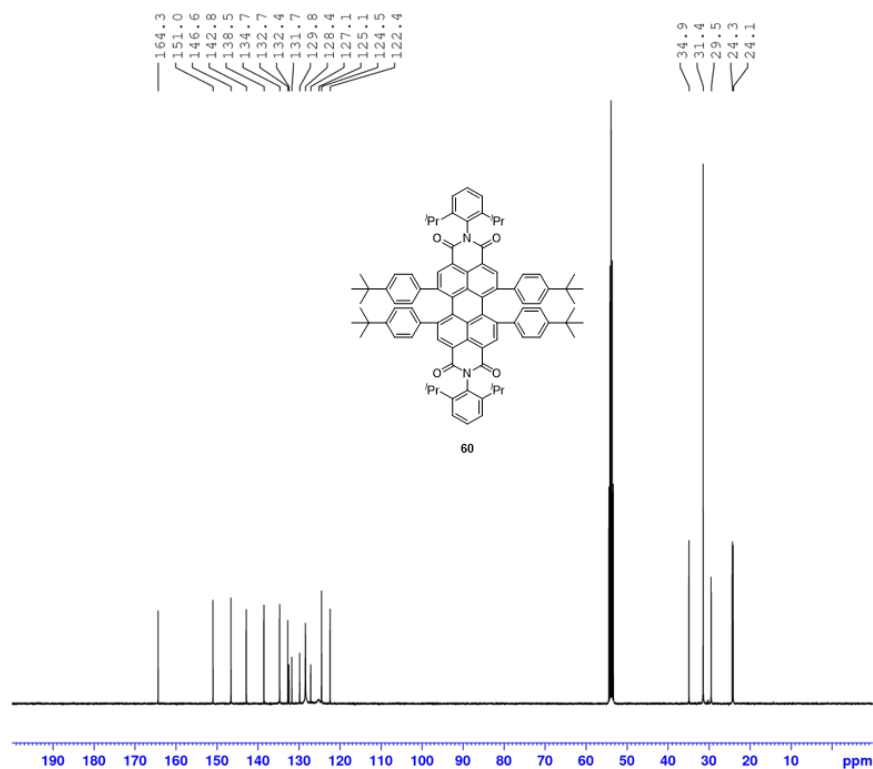


Figure A29. (a) Differential pulse voltammograms of *rac*-**QBI1** and *MM*-**QBI2**. Measurements were performed in DCM solutions ($c_0 \approx 10^{-4} \text{ M}$) at 293 K using TBAHFP ($c \approx 0.1 \text{ M}$) as electrolyte with a scan rate of 100 mV s^{-1} . (b) HOMO and LUMO levels corresponding to Table A11. Calculated according to literature known procedure^[170] using the experimentally determined redox potentials ($E_{\text{HOMO}} = -[E_{\text{ox1}} + 5.15 \text{ eV}]$ and $E_{\text{LUMO}} = -[E_{\text{red}} + 5.15 \text{ eV}]$) and the energy level of Fc/Fc^+ with respect to the vacuum level (-5.15 eV).

8.2.8 NMR Spectroscopy

Figure A30. ¹H NMR (400 MHz) spectrum of **60** in CD₂Cl₂ at 295 K.Figure A31. ¹³C NMR (101 MHz) spectrum of **60** in CD₂Cl₂ at 295 K.

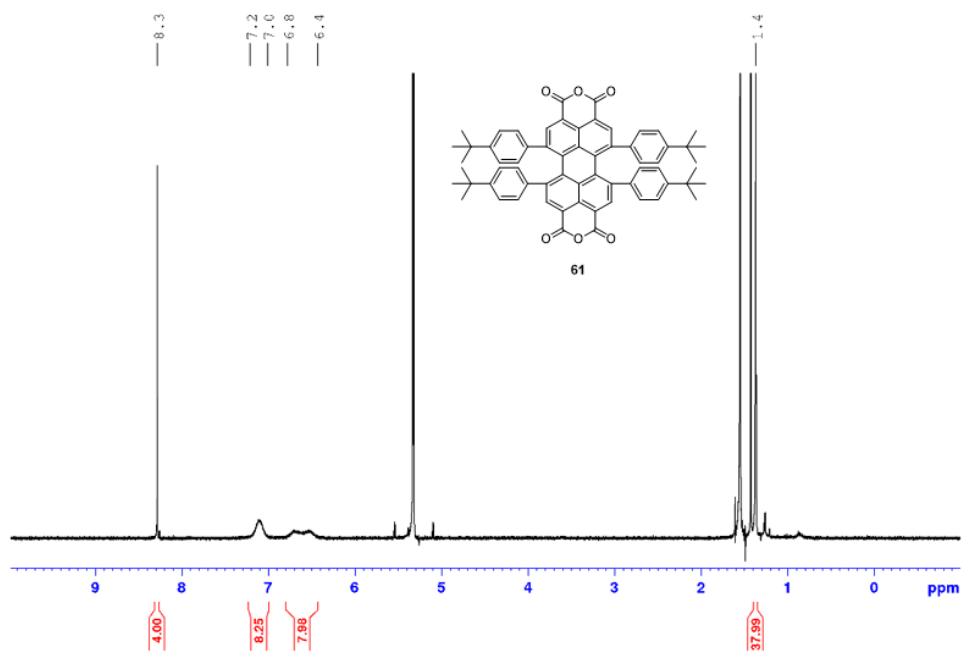


Figure A32. ^1H NMR (400 MHz) spectrum of **61** in CD_2Cl_2 at 295 K.^[235]

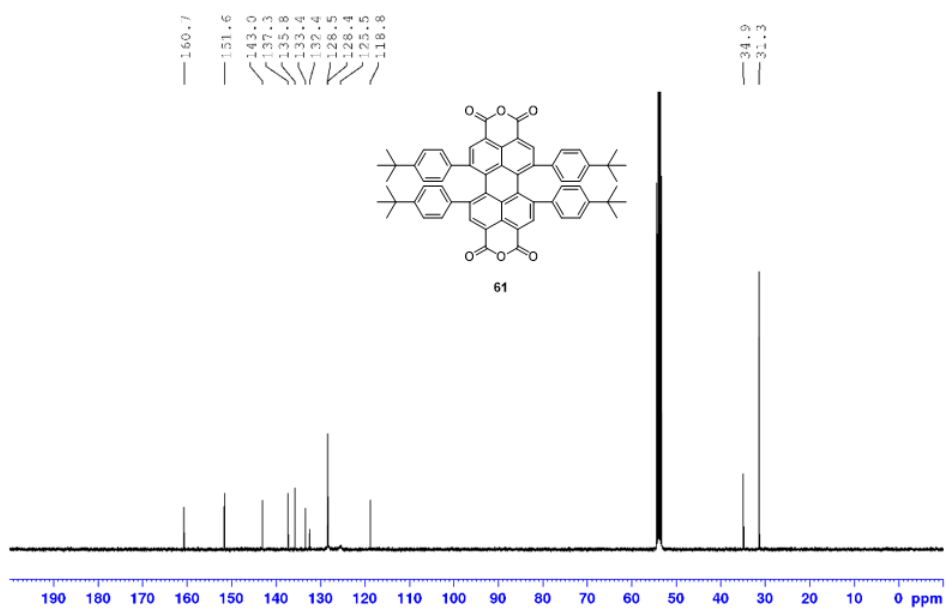


Figure A33. ^{13}C NMR (101 MHz) spectrum of **61** in CD_2Cl_2 at 295 K.^[235]

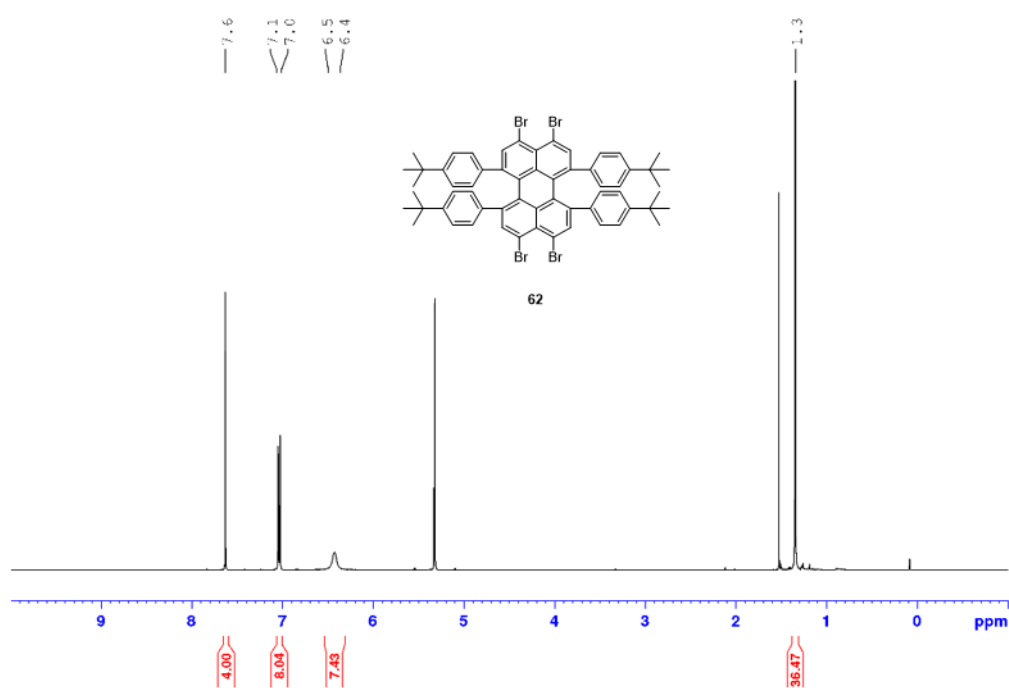


Figure A34. ^1H NMR (400 MHz) spectrum of **62** in CD_2Cl_2 at 295 K.^[235]

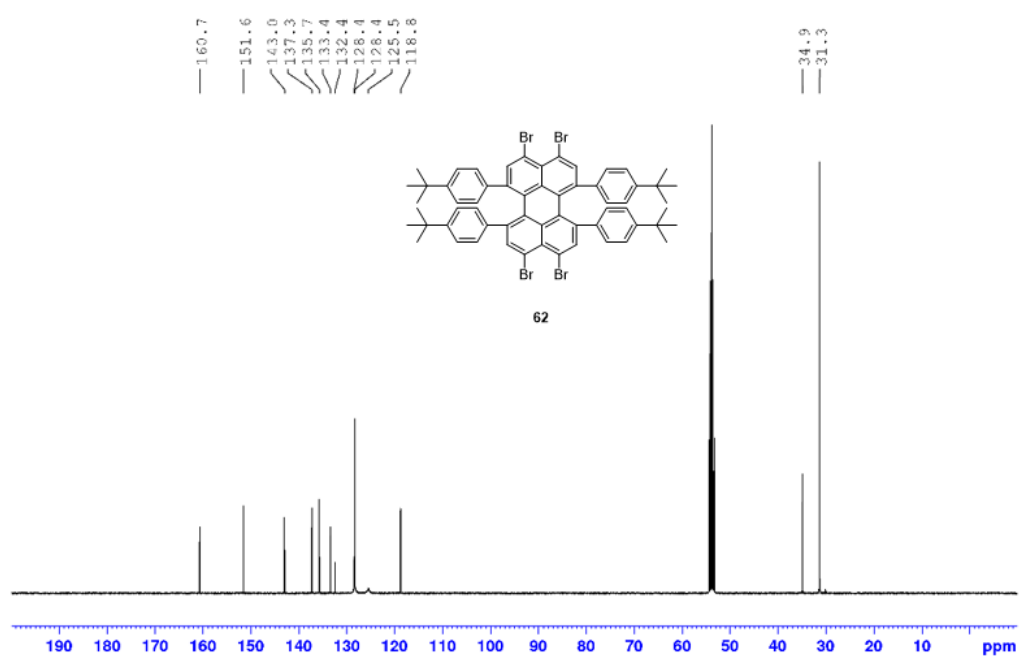


Figure A35. ^{13}C NMR (101 MHz) spectrum of **62** in CD_2Cl_2 at 295 K.^[235]

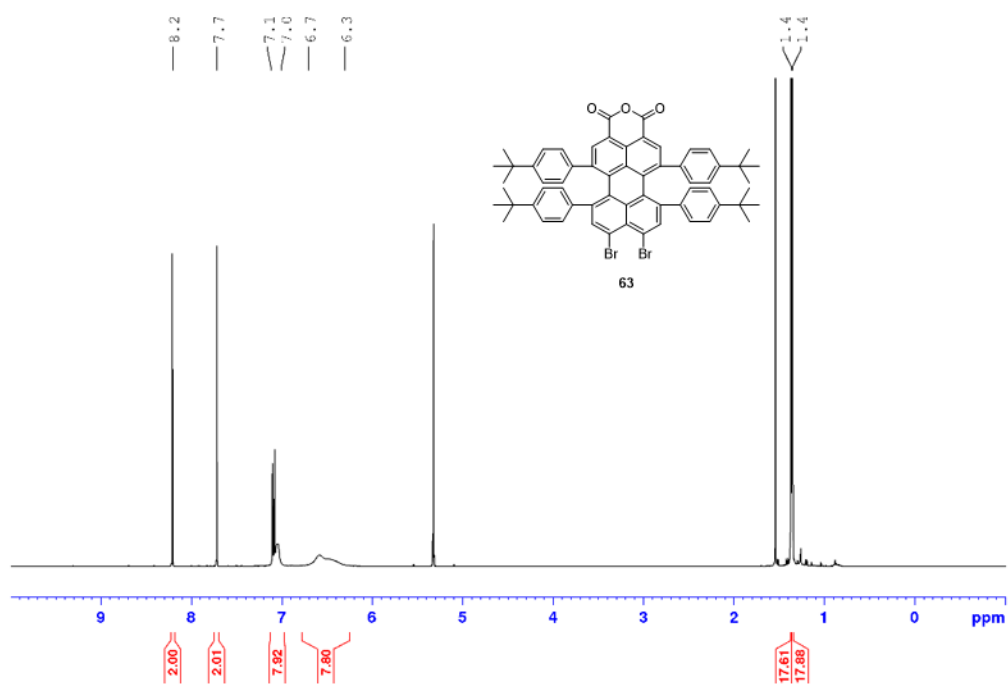


Figure A36. ^1H NMR (400 MHz) spectrum of **63** in CD_2Cl_2 at 295 K.^[235]

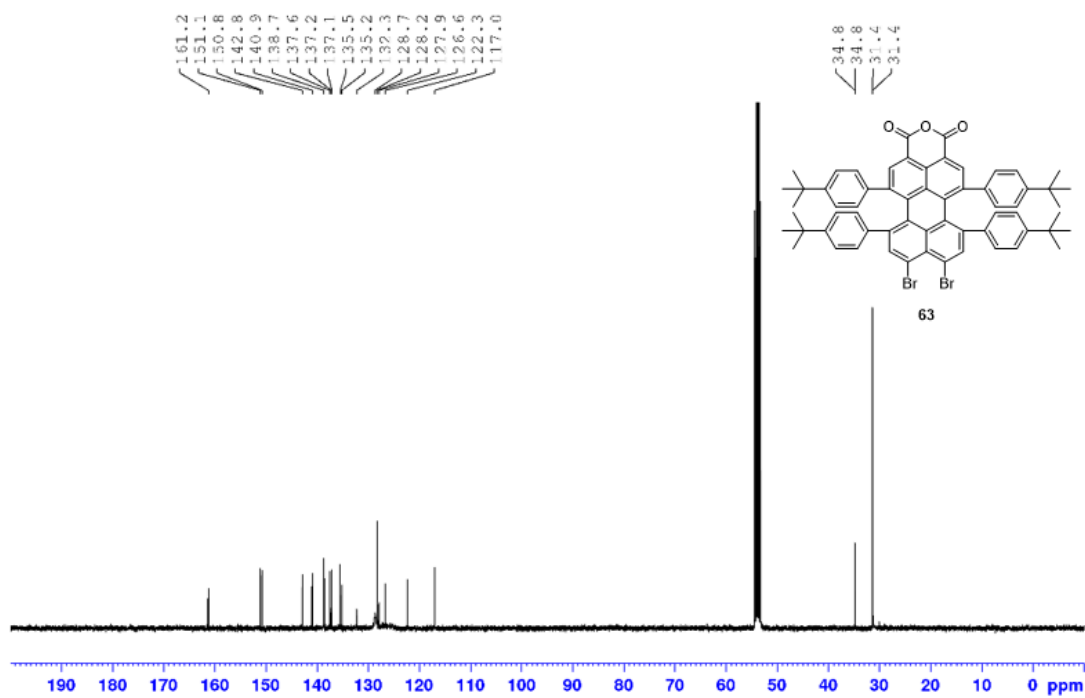


Figure A37. ^{13}C NMR (101 MHz) spectrum of **63** in CD_2Cl_2 at 295 K.^[235]

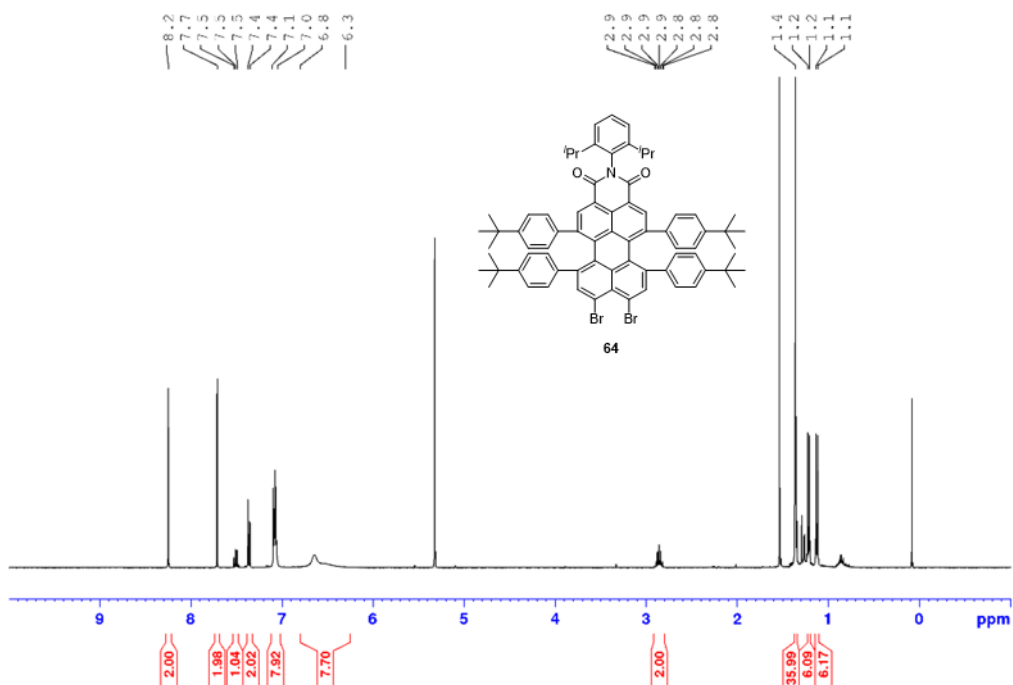


Figure A38. ¹H NMR (400 MHz) spectrum of **64** in CD₂Cl₂ at 295 K.^[235]

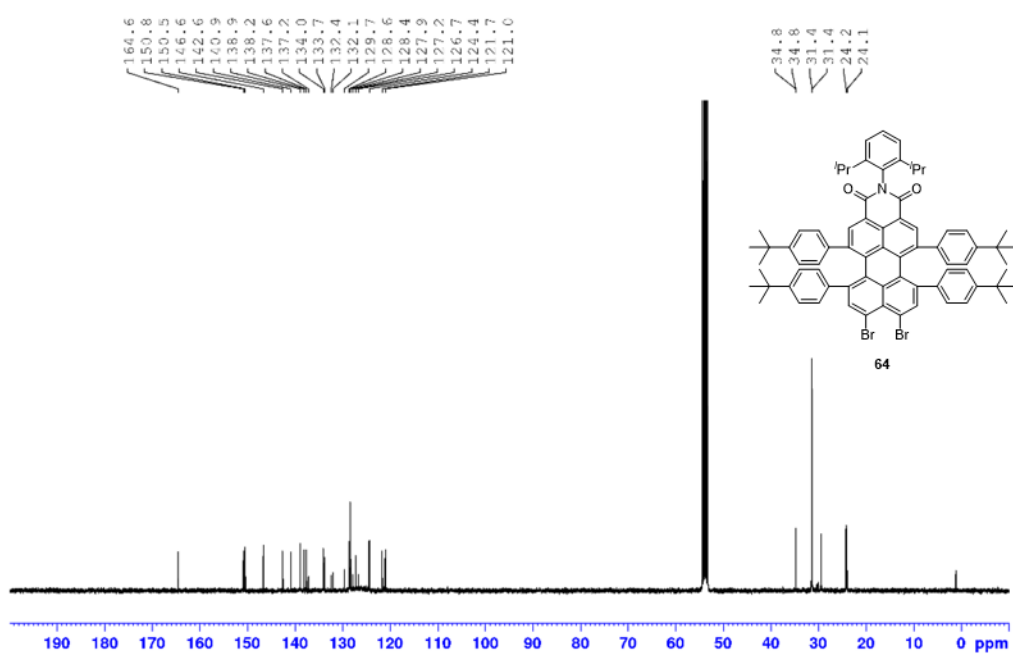


Figure A39. ¹³C NMR (151 MHz) spectrum of **64** in CD₂Cl₂ at 295 K.^[235]

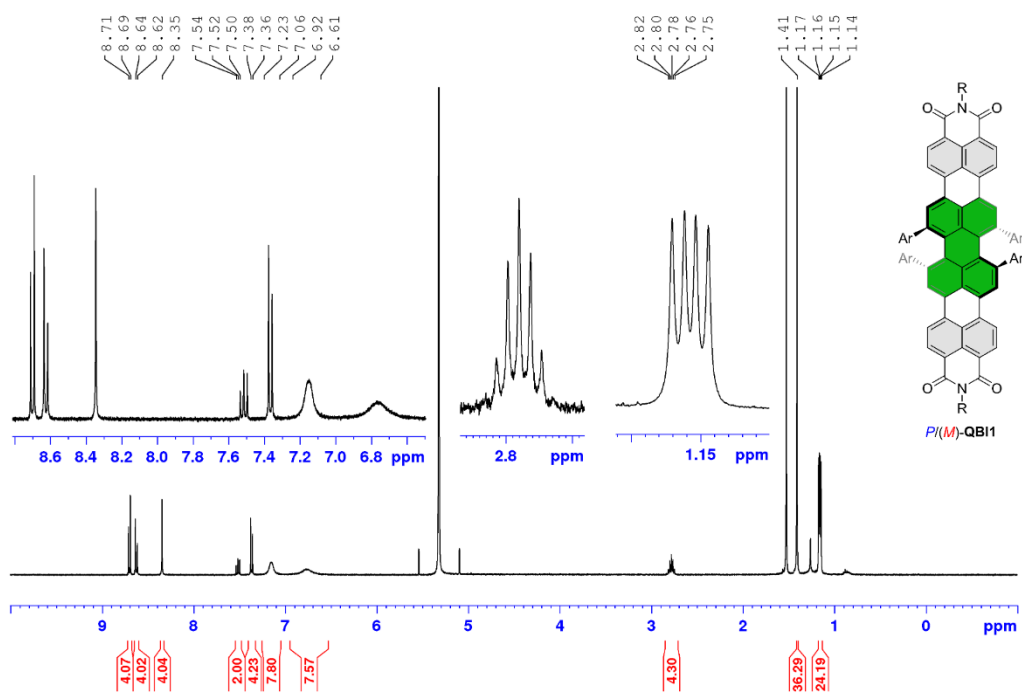


Figure A40. ¹H NMR (600 MHz) spectrum of QB11 in CD₂Cl₂ at 295 K.^[235]

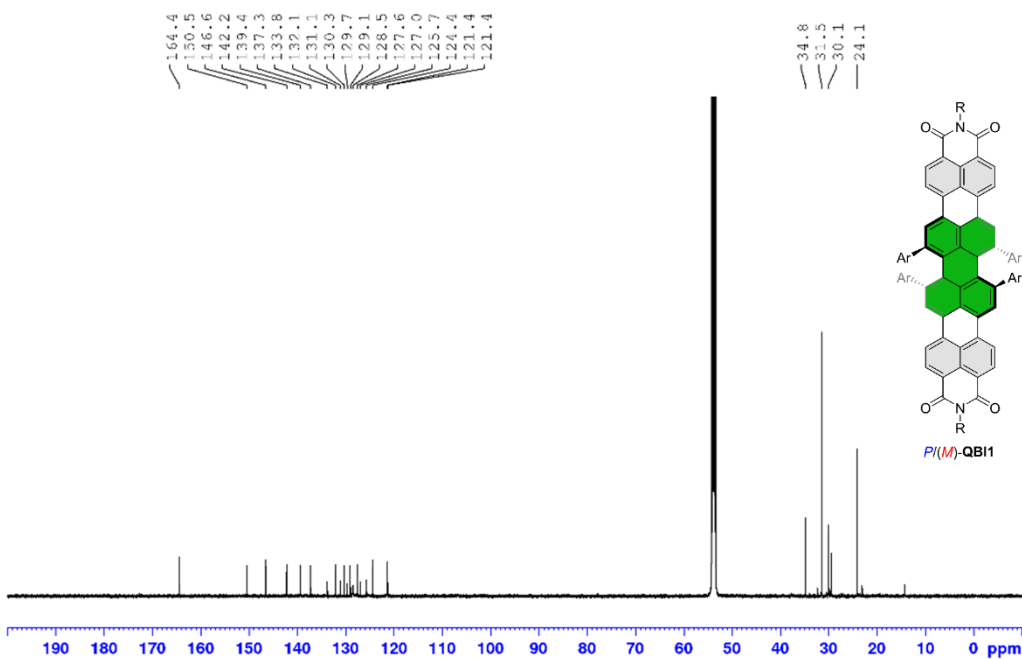


Figure A41. ¹³C NMR (151 MHz) spectrum of QB11 in CD₂Cl₂ at 295 K.^[235]

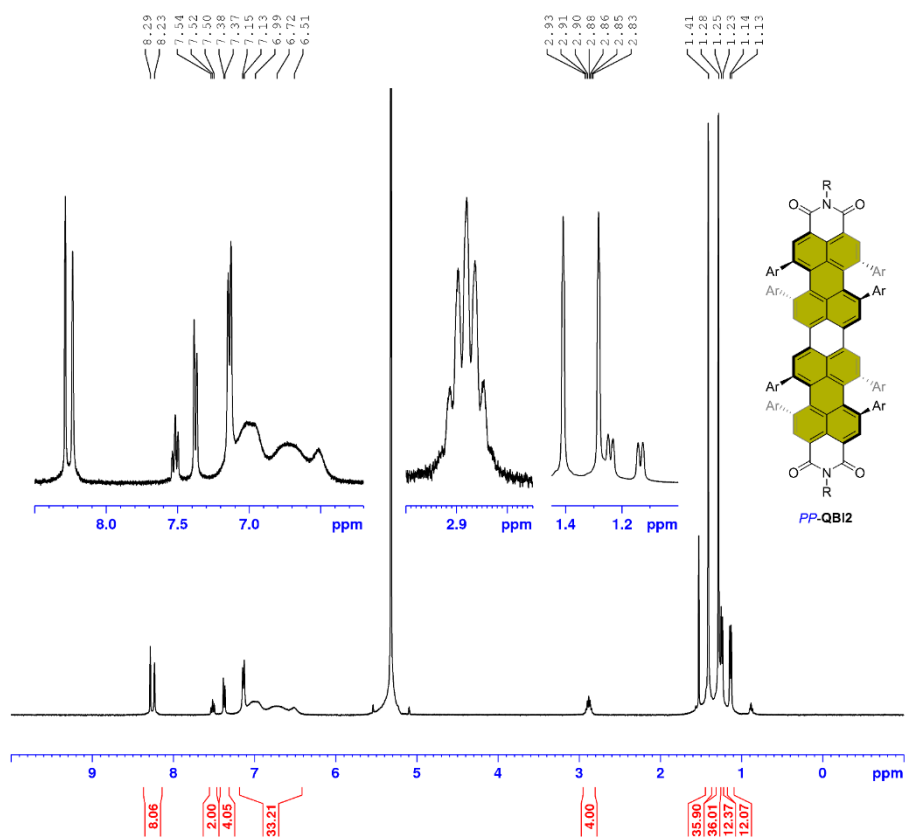


Figure A42. ¹H NMR (400 MHz) spectrum of *PP-QBI2* in CD₂Cl₂ at 295 K.

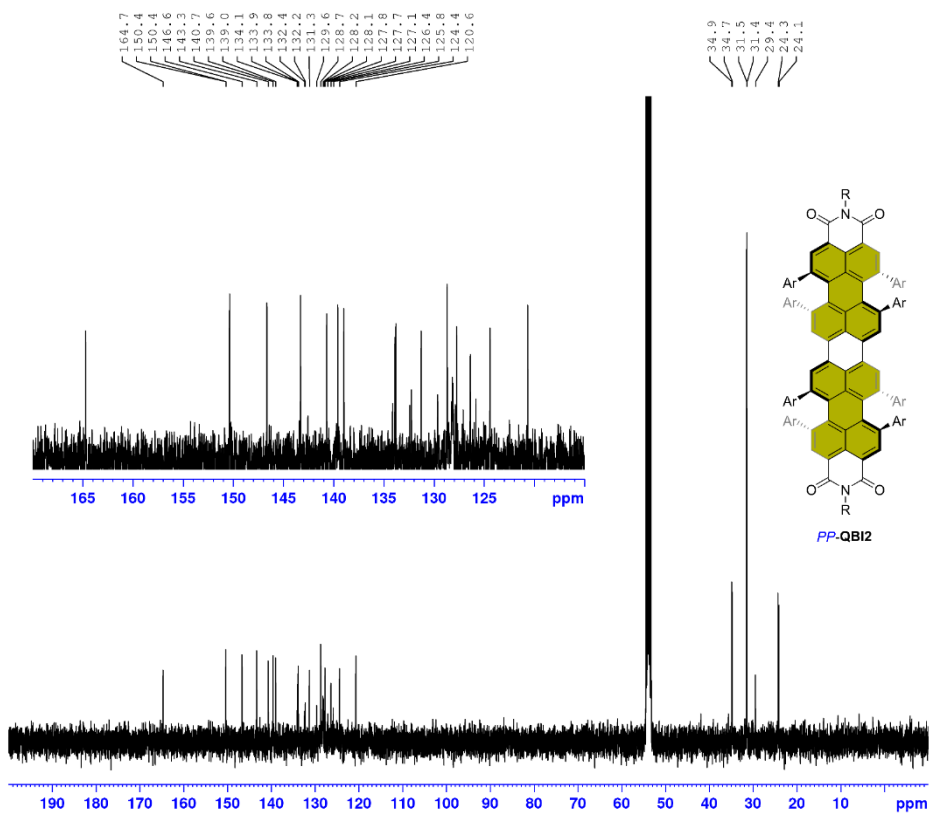


Figure A43. ¹³C NMR (101 MHz) spectrum of *PP-QBI2* in CD₂Cl₂ at 295 K.

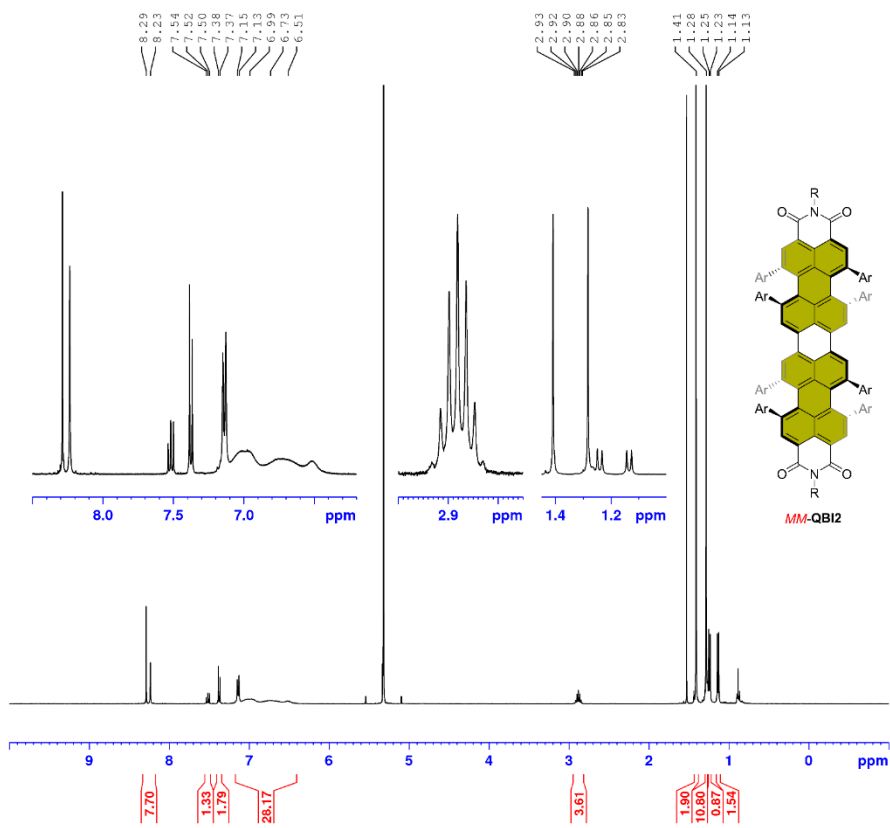


Figure A44. ¹H NMR (400 MHz) spectrum of *MM-QB12* in CD₂Cl₂ at 295 K.

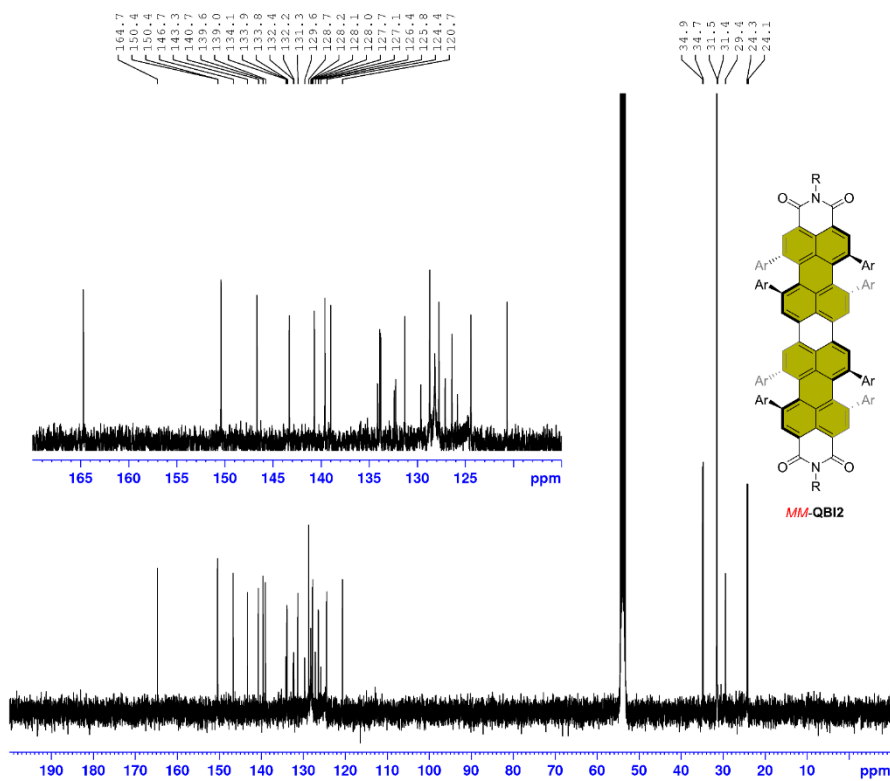


Figure A45. ¹³C NMR (101 MHz) spectrum of *MM-QB12* in CD₂Cl₂ at 295 K.

8.2.9 High-Resolution Mass-Spectrometry

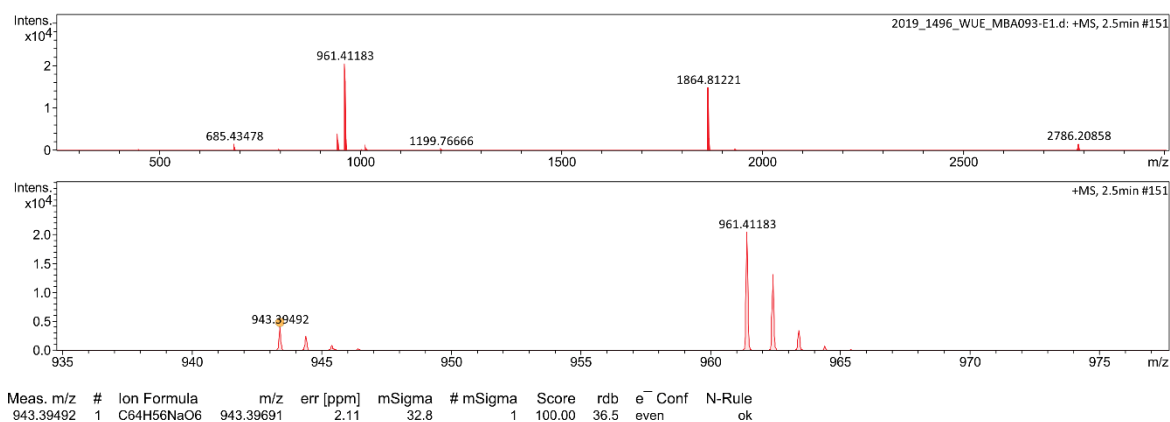


Figure A46. High resolution mass spectrum (ESI-TOF, pos. mode, CHCl₃/MeCN) of compound **60**.^[235]

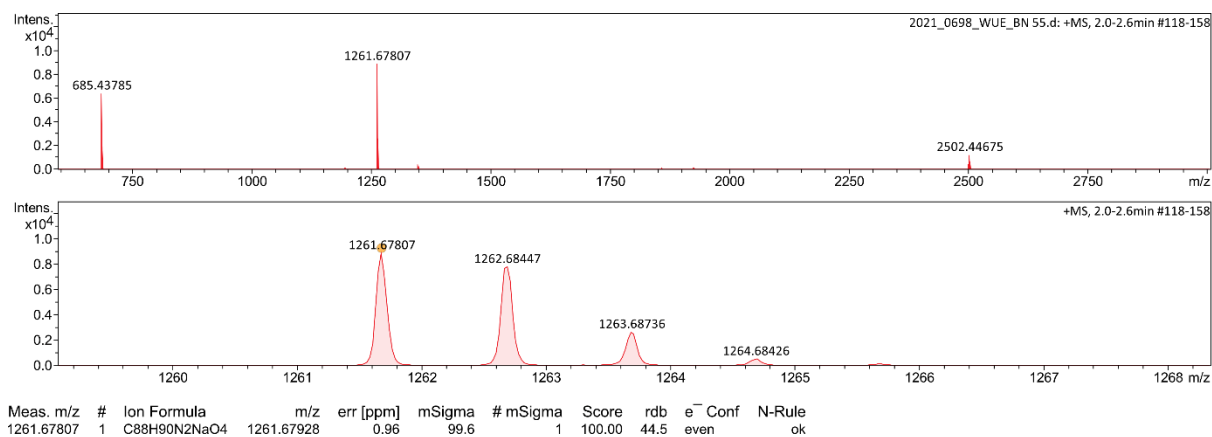


Figure A47. High resolution mass spectrum (ESI-TOF, pos. mode, CHCl₃/MeCN) of compound **61**.^[235]

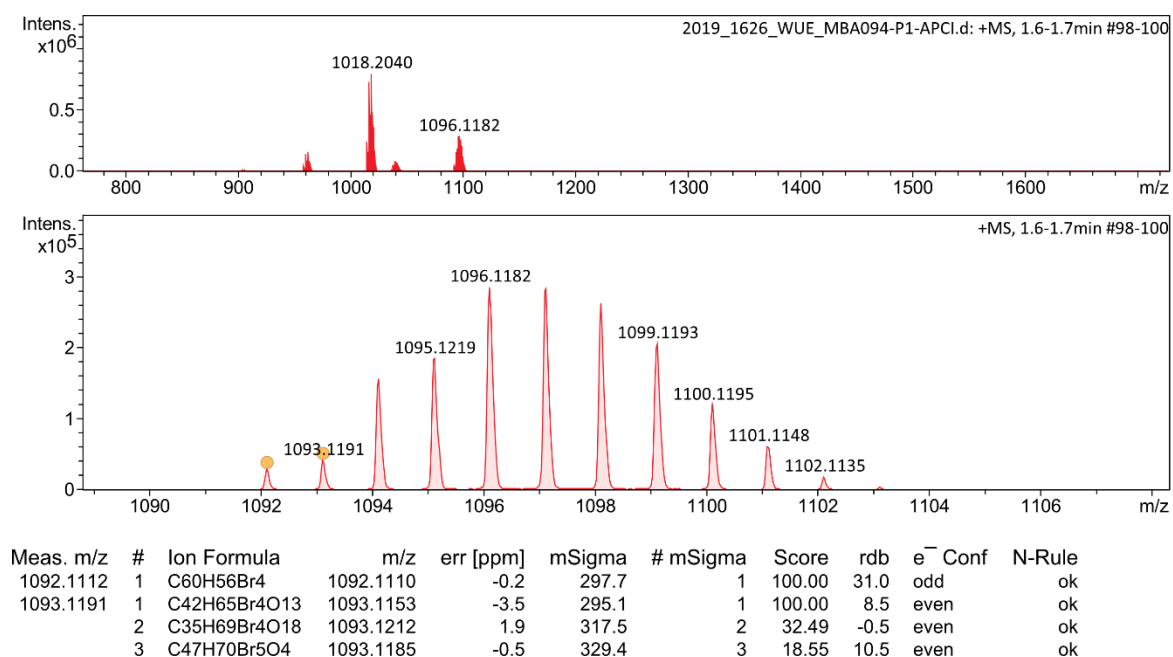


Figure A48. High resolution mass spectrum (APCI-TOF, pos. mode) of compound **62**.^[235]

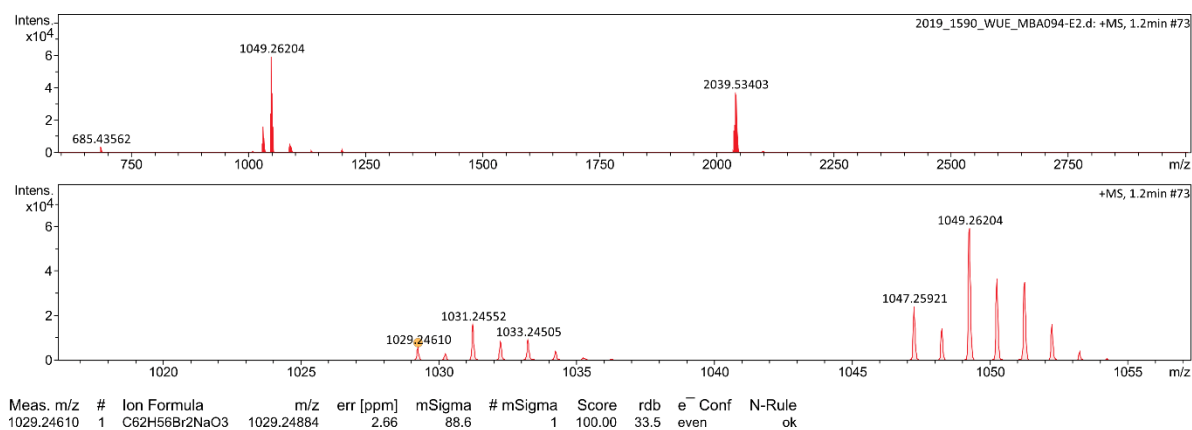


Figure A49. High resolution mass spectrum (ESI-TOF, pos. mode, CHCl₃/MeCN) of compound **63**.^[235]

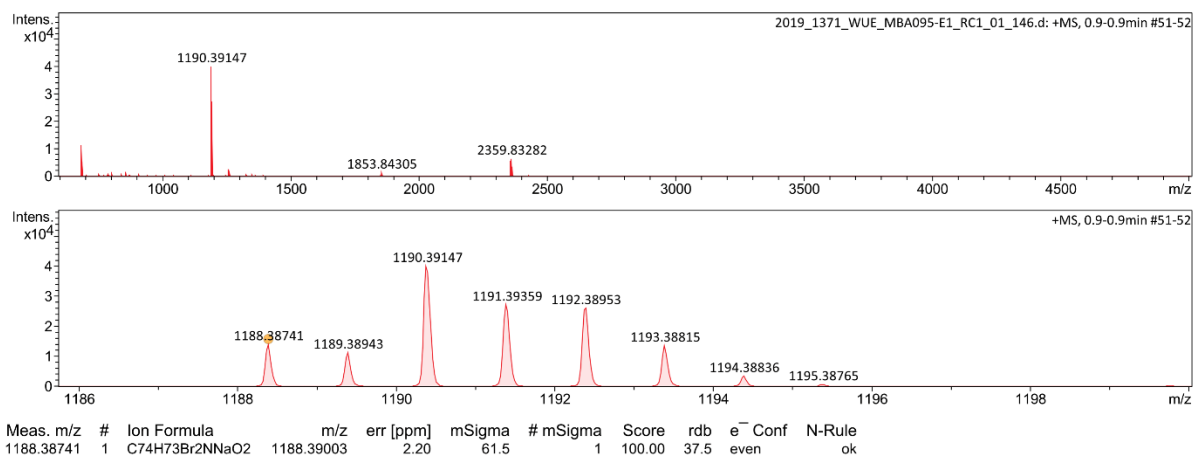


Figure A50. High resolution mass spectrum (ESI-TOF, pos. mode, CHCl₃/MeCN) of compound **64**.^[235]

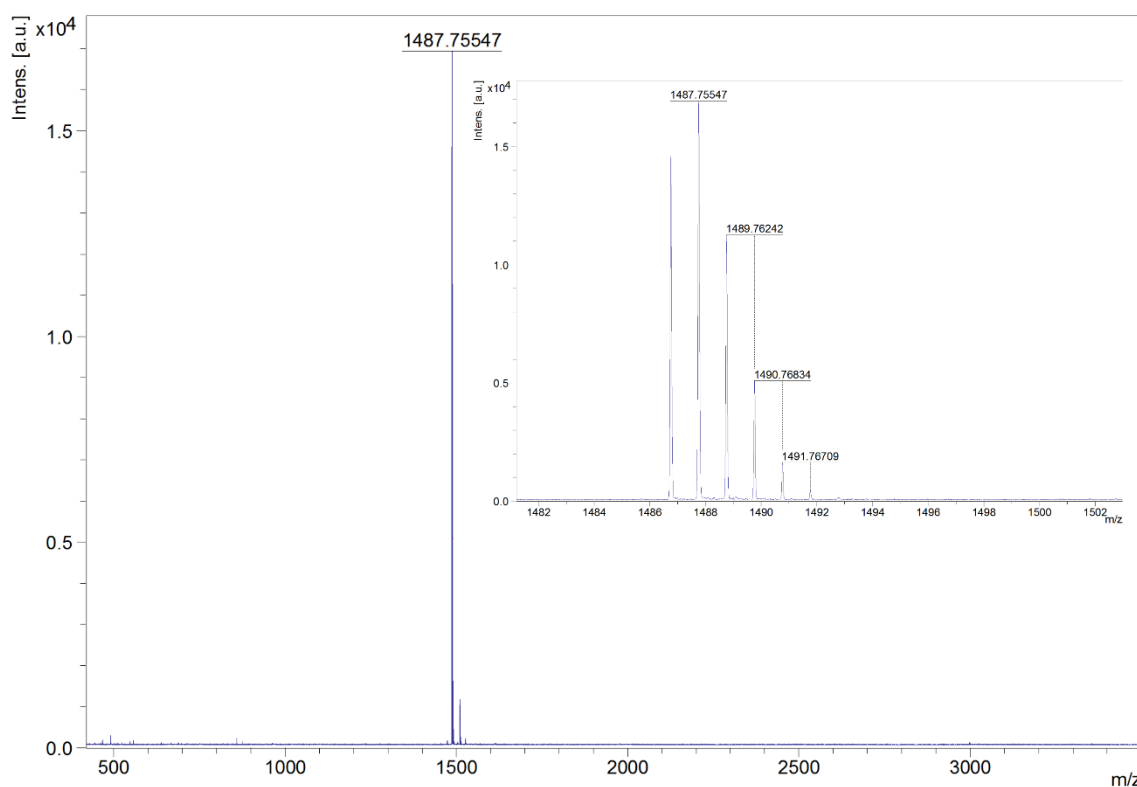


Figure A51. High resolution mass spectrum (MALDI-TOF, pos. mode, matrix: DCTB 1:3 in chloroform) of **QB11**.^[235]

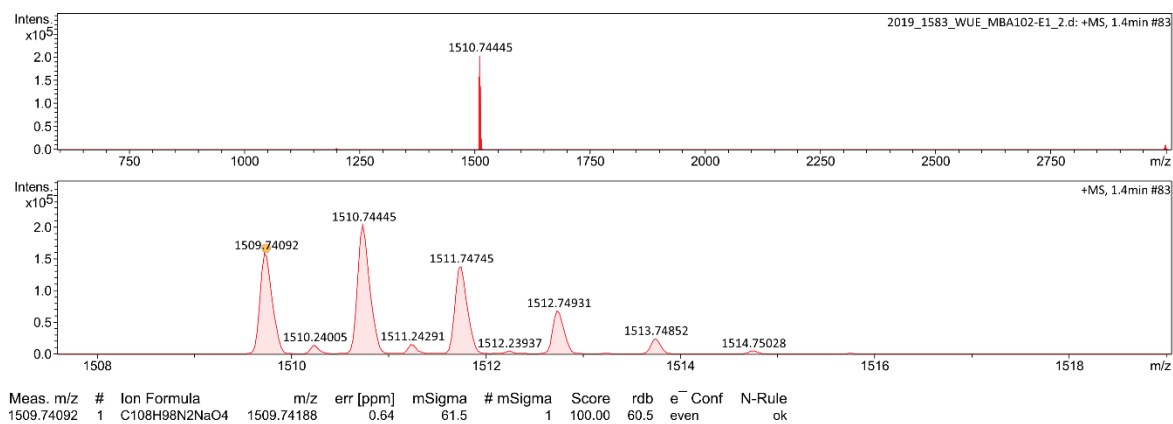


Figure A52. High resolution mass spectrum (ESI-TOF, pos. mode, CHCl₃/MeCN) of QB11.^[235]

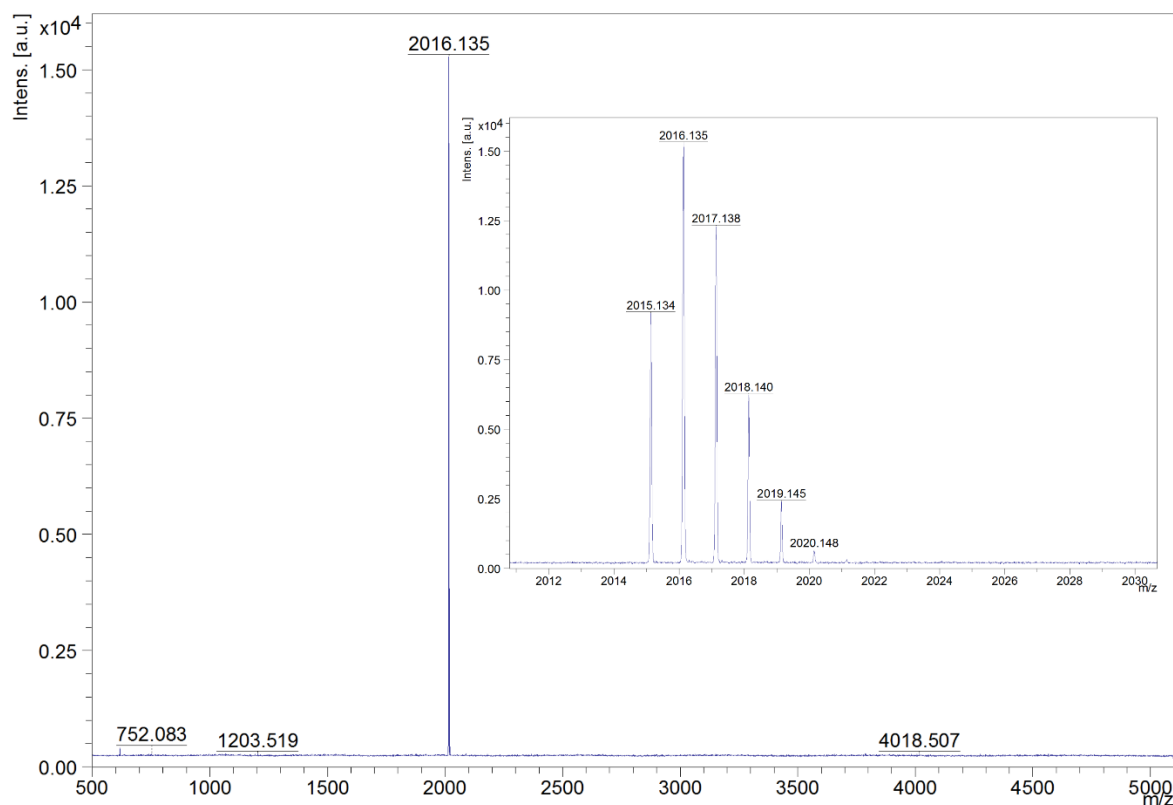


Figure A53. High resolution mass spectrum (MALDI-TOF, neg. mode, matrix: DCTB 1:3 in chloroform) of PP-QB12.

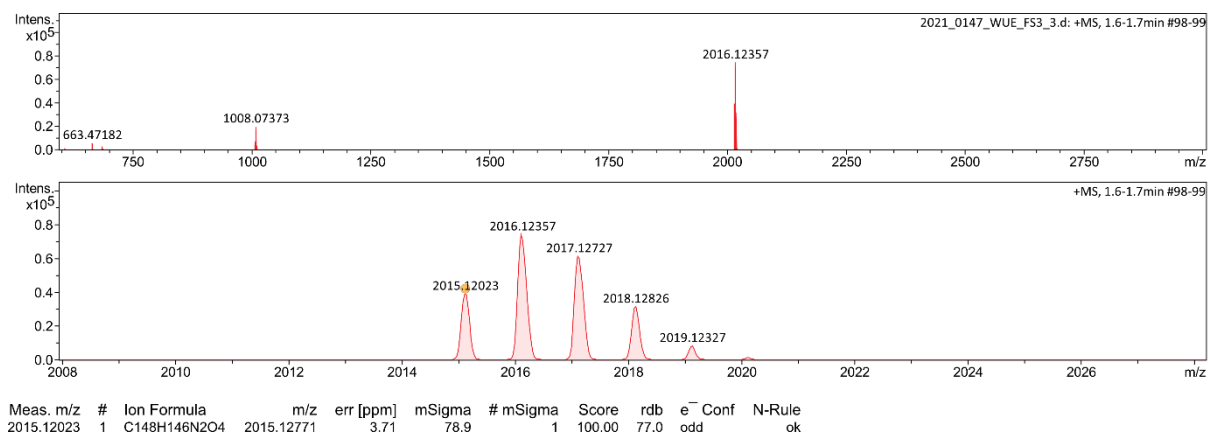


Figure A54. High resolution mass spectrum (ESI-TOF, pos. mode, CHCl₃/MeCN) of *PP-QBI2*.

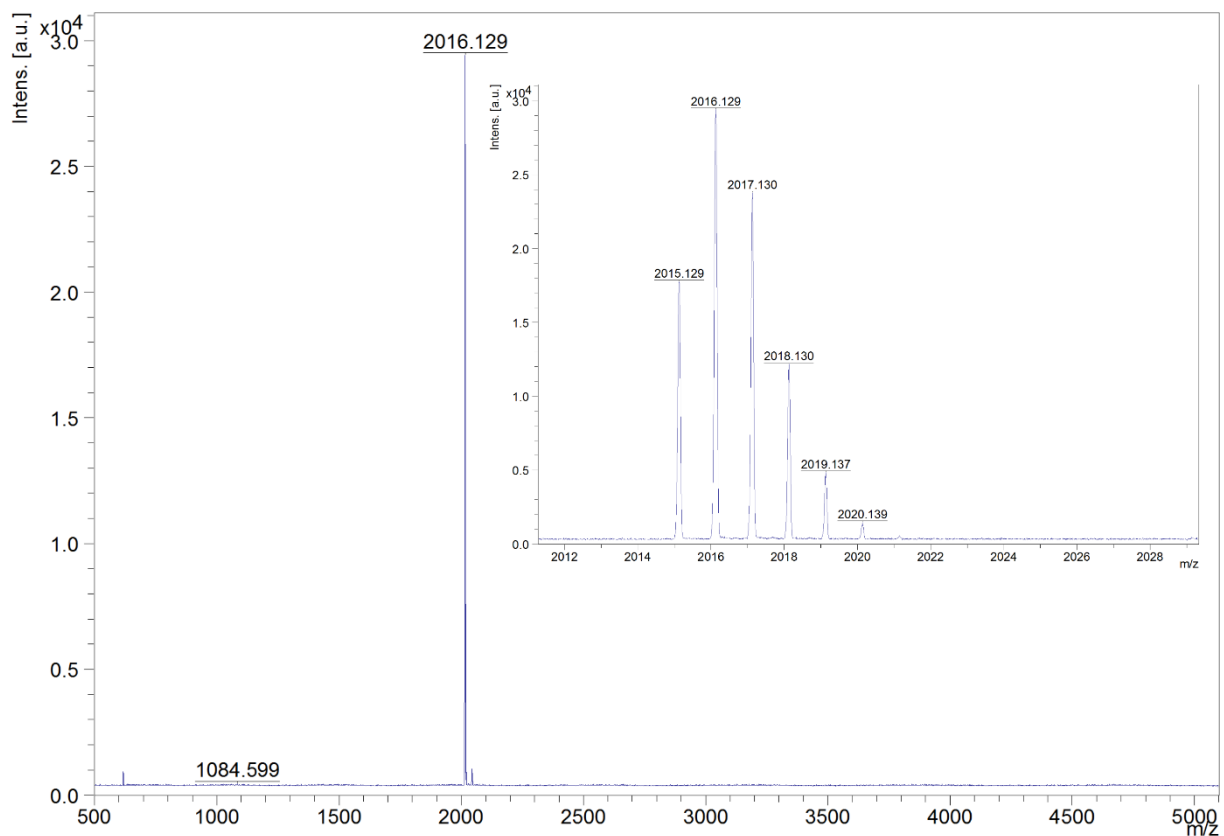


Figure A55. High resolution mass spectrum (MALDI-TOF, neg. mode, matrix: DCTB 1:3 in chloroform) of *MM-QBI2*.

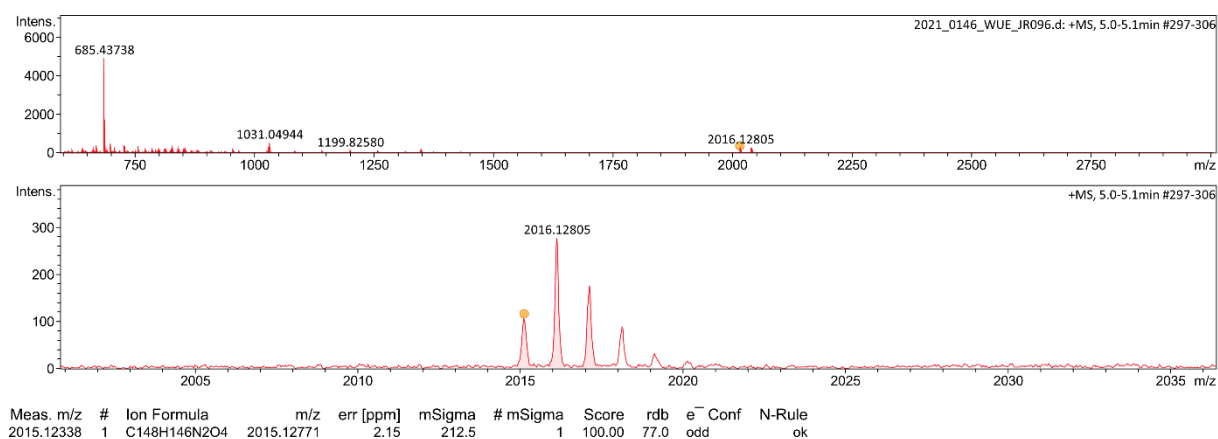


Figure A56. High resolution mass spectrum (ESI-TOF, pos. mode, CHCl₃/MeCN) of *MM-QBI2*.

8.3 Supporting Information for Chapter 5

The Supporting Information has been published in ref. [251]. For the sake of unity of this thesis, several formal editorial changes have been applied. Adapted and reprinted with permission from ref. [251]. Copyright 2023 American Chemical Society.

8.3.1 Materials and Methods

General

Unless noted otherwise, all chemicals, reagents and solvents were purchased from commercial suppliers and used without further purification after storing under conditions recommended by the commercial suppliers. The compounds **62**,^[200] **67**,^[295] and [Pd₂(dba)₃]·CHCl₃^[288] were synthesized and characterized according to literature reported procedures. Column chromatography was performed on silica-gel 60M (particle size 0.040 – 0.063 mm) with freshly distilled solvents. Melting points were measured on an *Olympus* BX41 polarization microscope with the temperature regulator TP84 from *Linkam Scientific*. The reported values are uncorrected. Semi-preparative high-performance liquid chromatography (HPLC) was carried out on a JAI LC-9105 HPLC-device from *Japan Analytical Industries* equipped with a VP 250/21 NUCLEOSIL 100-7 column (Ø = 20 mm) of *Macherey-Nagel* using HPLC grade solvents. For separation of enantiomers, the same HPLC device was used equipped with a semi-preparative Reprisil 100 Chiral-NR chiral column from *Trentec* (Ø = 20 mm). For separation of atropo-enantiomers by HPLC, a flow rate of 6 mL min⁻¹ was applied resulting in a column pressure of < 1.5 MPa. All measurements were carried out using spectroscopic grade solvents.

NMR Spectroscopy

^1H and ^{13}C NMR spectra were recorded on a Bruker Avance HD III 400. The ^{13}C NMR spectra are broad-band proton decoupled. Chemical shifts (δ) are listed in parts per million (ppm) and are reported relative to tetramethylsilane and referenced internally to residual proton solvent resonances or naturally abundant carbon resonances. The coupling constants (J) are quoted in Hertz (Hz).

Mass Spectrometry

High-resolution MALDI-TOF mass spectra were measured with an ultrafleXtreme from *Bruker Daltonics GmbH* using *trans*-2-[3-(4-*tert*-butylphenyl)-2-methyl-2-propenylidene]malononitrile (DCTB) as matrix material. DCTB and the chloroform solution of the compound ($c \approx 10^{-5}$ M) were mixed in 3:1 (v/v) ratio and then co-deposited. High-resolution mass spectra (ESI-TOF) were recorded on a microTOF focus instrument (*Bruker Daltonik GmbH*).

Optical Spectroscopy and Optical Microscopy

UV–vis–NIR absorption spectra were recorded on a *Perkin Elmer* Lambda950 spectrometer. Fluorescence steady-state measurements were recorded on a FLS980-D2D2-ST *Edinburgh Instruments* fluorescence spectrometer and were corrected against the photomultiplier sensitivity and the lamp intensity. Circular dichroism spectra were recorded on a customized *Jasco* CPL-300/J-1500 hybrid spectrometer. All samples of aggregated dispersions were ultrasonicated for 5 s prior to optical measurements. Absorption- and emission spectroscopy as well as light-microscopic investigations of crystallites and precipitates of *rac*/*M*-**QBI-Me** were conducted on a Carl Zeiss Axio Imager A2m optical polarization microscope equipped with a Hg arc lamp (excitation) and a Zeiss Peltier-cooled CCD array customized by *A.S. & Co. GmbH* or and MAYA2000-Pro diode array spectrometer from *Ocean Optics*.

Single-Crystal X-ray Analysis

Single-crystal X-ray diffraction data for *rac*-**QBI-Me** were collected at the P11 beamline at DESY. The diffraction data were collected by a single $360^\circ \phi$ scan at 100 K. The diffraction data were indexed, integrated, and scaled using the XDS program package.^[296] In order to compensate low completeness due to single-axis measurement two data sets were merged using the XPREP program from *Bruker*.^[297] The structure was solved using SHELXT,^[289] expanded with Fourier techniques and refined using the SHELX software package.^[298] Hydrogen atoms were assigned at idealized positions and were included in the calculation of structure factors. All non-hydrogen atoms in the main residue were refined anisotropically. Disordered solvent

molecules were modelled with restraints using standard SHELX commands DFIX, FLAT, SAME, SADI, DELU, SIMU, CHIV, ISOR, and RIGU. The crystal structure of *rac*-**QBI-Me** was solved as twins using HKLF5 data generated by the TwinRotMat function implemented in the PLATON software package.^[291]

AFM Microscopy

AFM measurements were performed under ambient conditions using a Bruker Multimode 8 SPM system operating in tapping mode in air. Silicon cantilevers (OMCL-AC240TS, Olympus) with a resonance frequency of ~ 70 kHz and a spring constant of ~ 2 Nm^{-1} were used. The AFM samples were prepared by spin-casting onto highly oriented pyrolytic graphite (HOPG) or silicon wafer (SiO_x) with 2000 rpm.

Theoretical Calculations

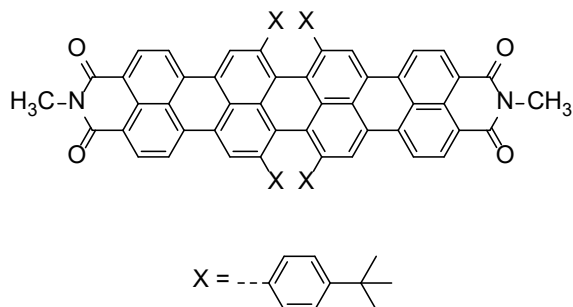
Density-functional theory (DFT) calculations were performed by Gaussian 16^[286] on the ω B97XD/def2-svp^[299-300] level of theory. Quantum chemical calculations for determining the different types of chromophore coupling were conducted with the Gaussian 09 package^[301] similarly to those previously reported for perylene bisimide foldamers^[119] using the three respective dimer structures as shown in Figure 37 of the main manuscript. Time-dependent DFT (TD-DFT) with the long-range corrected hybrid density functional ω B97X-D^[299] and the def2-SVP basis set^[300] was also used for calculating the Coulomb-coupling J_{Coulomb} . The resulting transition density was projected onto atomic transition charges by a Mulliken style electron excitation analysis for the first excited state (= main transition) using the Multiwfn software package^[302] and J_{Coulomb} finally calculated using the transition charge method.^[303] The short-range charge-transfer coupling J_{CT} was calculated at the perturbative limit^[304] for, which the effective electron and hole transfer integrals t_e and t_h , respectively, were determined using the Amsterdam Density Functional (ADF) program^[305-306] with the PW91 functional^[307] and a TZP basis set^[308] within the unique fragment approach.^[309] The effective transfer integrals were calculated according to Wen *et al.*^[310]. The resulting total coupling J_{total} was calculated as the sum of J_{Coulomb} and J_{CT} .

Electrochemistry

Cyclic voltammetry (CV) and differential pulse voltammetry (DPV) measurements were conducted with a BASi Epsilon potentiostat connected to a microcell apparatus from *rhd instruments* involving a 1.6 mL sample container, a platinum counter- and pseudo-reference electrode as well as a glassy carbon working electrode.

8.3.2 Synthesis and Characterization

Synthesis of *rac*-QBI-Me



Five reactions were carried out in parallel: A Schlenk-tube was charged with **1** (20.0 mg, 18.2 μmol , 1.00 equiv), **62** (19.4 mg, 40.1 μmol , 2.20 equiv), *tris*(dibenzylideneacetone)dipalladium(0)-chloroform adduct $[\text{Pd}_2(\text{dba})_3]\cdot\text{CHCl}_3$ (3.8 mg, 3.65 μmol , 30.0 mol %), tricyclohexylphosphine tetrafluoroborate $\text{PCy}_3\cdot\text{HBF}_4$ (5.4 mg, 15 μmol , 80 mol %), Cs_2CO_3 (35.7 mg, 109 μmol , 6.00 equiv) and 1-chloronaphthalene (0.8 mL) as a solvent under an inert atmosphere at 160 °C for 24 h. After cooling down to room temperature, the reaction mixtures of the five reaction batches were combined. The combined mixture was filtrated with cyclohexane over a pad of silica-gel to remove 1-chloronaphthalene and the crude product was eluted with dichloromethane. This was followed by HPLC chromatography (dichloromethane/ethyl acetate = 95:5). The product was dried under high vacuum to give a dark-green solid (total yield: 18.5 mg, 15.5 μmol , 17%).

$^1\text{H-NMR}$ (CD_2Cl_2 , 400 MHz, 298 K): δ/ppm = 8.70 (*d*, J = 8.2 Hz, 4 H), 8.63 (*d*, J = 8.2 Hz, 4 H), 8.35 (*s*, 4 H), 7.52 (*t*, J = 7.8 Hz, 2 H), 7.37 (*d*, J = 7.8 Hz, 4 H), 7.22–7.07 (*br*, 8 H), 6.92–6.60 (*br*, 8 H), 2.78 (*qui*, J = 6.8 Hz, 4 H), 1.41 (*s*, 36 H), 1.18–1.14 (*m*, 24 H).

$^{13}\text{C-NMR}$ (CD_2Cl_2 , 101 MHz, 295 K): δ/ppm = 164.4, 150.3, 142.0, 139.4, 136.8, 133.8, 131.5, 130.1, 129.0, 128.5, 127.3, 126.7, 125.6, 121.3, 121.3, 34.8, 31.5, 27.1.

UV–vis–NIR (CH_2Cl_2 , $\lambda_{\text{max}} / \text{nm}$ ($\epsilon / \text{M}^{-1} \text{cm}^{-1}$)) = 800 (99000).

Fluorescence (*n*-hexane, $\lambda_{\text{ex}} = 698 \text{ nm}$): $\lambda_{\text{max}} / \text{nm} = 811$.

M.p.: > 350 °C.

MS (MALDI-TOF, negative mode, DCTB in chloroform): *m/z*: Calculated for $\text{C}_{86}\text{H}_{70}\text{N}_2\text{O}_4$: 1194.53030; found: 1194.53030 $[\text{M}]^+$.

HRMS (ESI-TOF, positive mode, acetonitrile/chloroform): *m/z*: Calculated for $\text{C}_{86}\text{H}_{70}\text{N}_2\text{O}_4$: 1194.53301; found: 1194.53582 $[\text{M}]^-$.

8.3.3 Chiroptical Properties

After the purification of the racemic mixture of *rac*-**QBI-Me**, the enantiomers were separated by semi-preparative HPLC using a chiral stationary phase (see Materials and Methods). For both of the collected fractions, an additional HPLC run was conducted to ensure purity as well as enantiopurity. The handedness of the fractions was assigned by CD spectroscopy and determined by TD-DFT calculations.

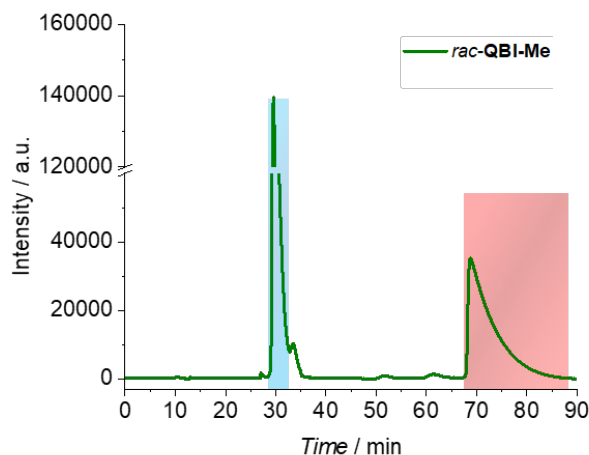


Figure A57. HPLC traces (semipreparative device) of racemic mixture (green line) and of separated *P*- (blue area) and *M*- (red area) enantiomers of **QBI-Me** using a solvent mixture of DCM/ethyl acetate in 95:5 *v/v* ratio.

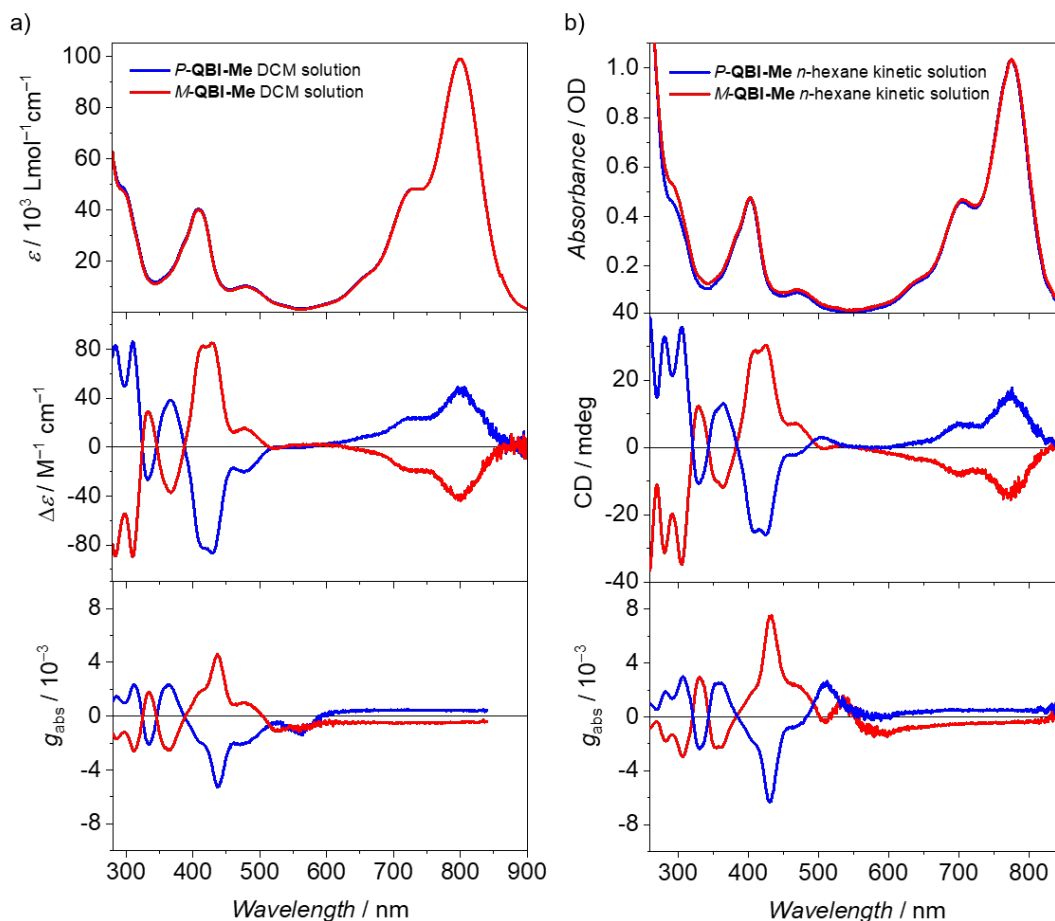


Figure A58. UV–vis–NIR absorption (top) and CD spectra (center) as well as g_{abs} values (bottom) of the monomers of *P/M*-QBI-Me enantiomers in blue and red, respectively in (a) DCM and (b) *n*-hexane at 295 K. The absorption coefficient ϵ in DCM was calculated by averaging three independent samples within error margins of $\pm 2000 \text{ L mol}^{-1} \text{ cm}^{-1}$.

Table A12. Optical properties of *P/M*-QBI-Me in *n*-hexane at 295 K.

	λ_{max}^a / nm	$\text{fwhm}_{\text{abs}}^{a,b}$ / cm^{-1}	$\lambda_{\text{em}}^{b,c}$ / nm	$\text{fwhm}_{\text{em}}^c$ / cm^{-1}	$\Delta\tilde{\nu}_{\text{Stokes}}^c$ / cm^{-1}
monomer ^d	778	810	811	1080	520
J-aggregate	897	530	912	590	180

^a Absorption measurements were conducted in transmission mode using 1 mm cuvettes (bandwidth 2 nm, OD = 1).

^b The fwhm was derived as twice the distance between the absorption/ emission maximum to the closest edge at half maximum towards higher/ lower wavelengths of the unsymmetrically shaped absorption/ emission bands, respectively, to prevent falsification by overlapping transitions.

^c Emission measurements of (1 cm cuvettes, OD > 0.15) were conducted in front face setup using bandwidths of 6 nm for both excitation and emission.

^d The monomer species was investigated as kinetically trapped state before its self-assembly into aggregates.

8.3.4 Photographs of Precipitates

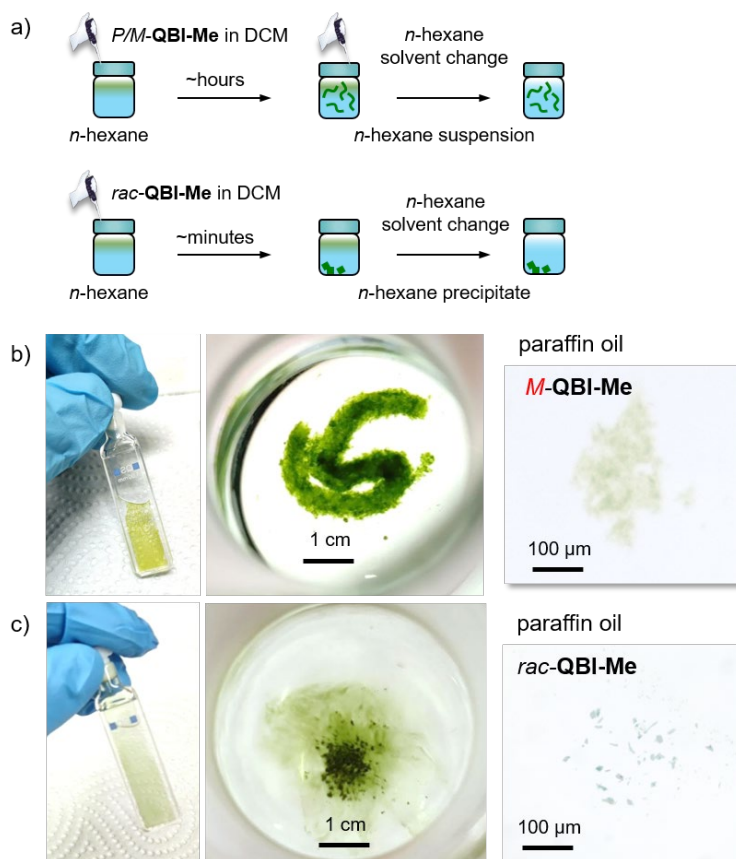


Figure A59. (a) Schematic depiction of the preparation of solid-state J-aggregates by using enantiopure *P/M-QBI-Me* (top) or the racemic mixture (bottom). Photographs of (b) *M-QBI-Me* and (c) *rac-QBI-Me* in 1 mm cuvettes (left) as well as 50 mL flask in top view (middle) as obtained from slow precipitation after 1 week under ambient light along with the optical microscope images under transmitted light (right).

The self-assembly of enantiopure *P/M-QBI-Me* was achieved by adding 2 mL of a 5 mg mL⁻¹ DCM solution of *P/M-QBI-Me* into 50 mL of *n*-hexane (Figure A59a). After 10 hours at 8 °C, the solvent mixture was decanted three times and replaced by pure *n*-hexane each time to fully suppress possibly remaining monomeric species dissolved by a fractional amount of initial DCM. The same procedure was applied for the racemate but resulted in a fast precipitation under the same conditions. The enantiopure aggregate forms a well-dispersed precipitate, which resembles natural algae (Figure A59b). The racemate precipitates as fine powder (Figure A59c). For deeper analysis under the light microscope, the *n*-hexane precipitates were suspended in paraffin oil on a microscope slide (Figure A59b,c, right). After stored at room temperature for 24 h under ambient conditions to reduce the amount of *n*-hexane by evaporation, the samples were topped with a microscope glass cover. The light-microscopic images taken under white

light in transmission mode corroborate the macroscopic differences between well-dispersed enantiopure aggregates and the small crystallites of the racemate (Figure A59b,c right).

8.3.5 Disassembly Studies

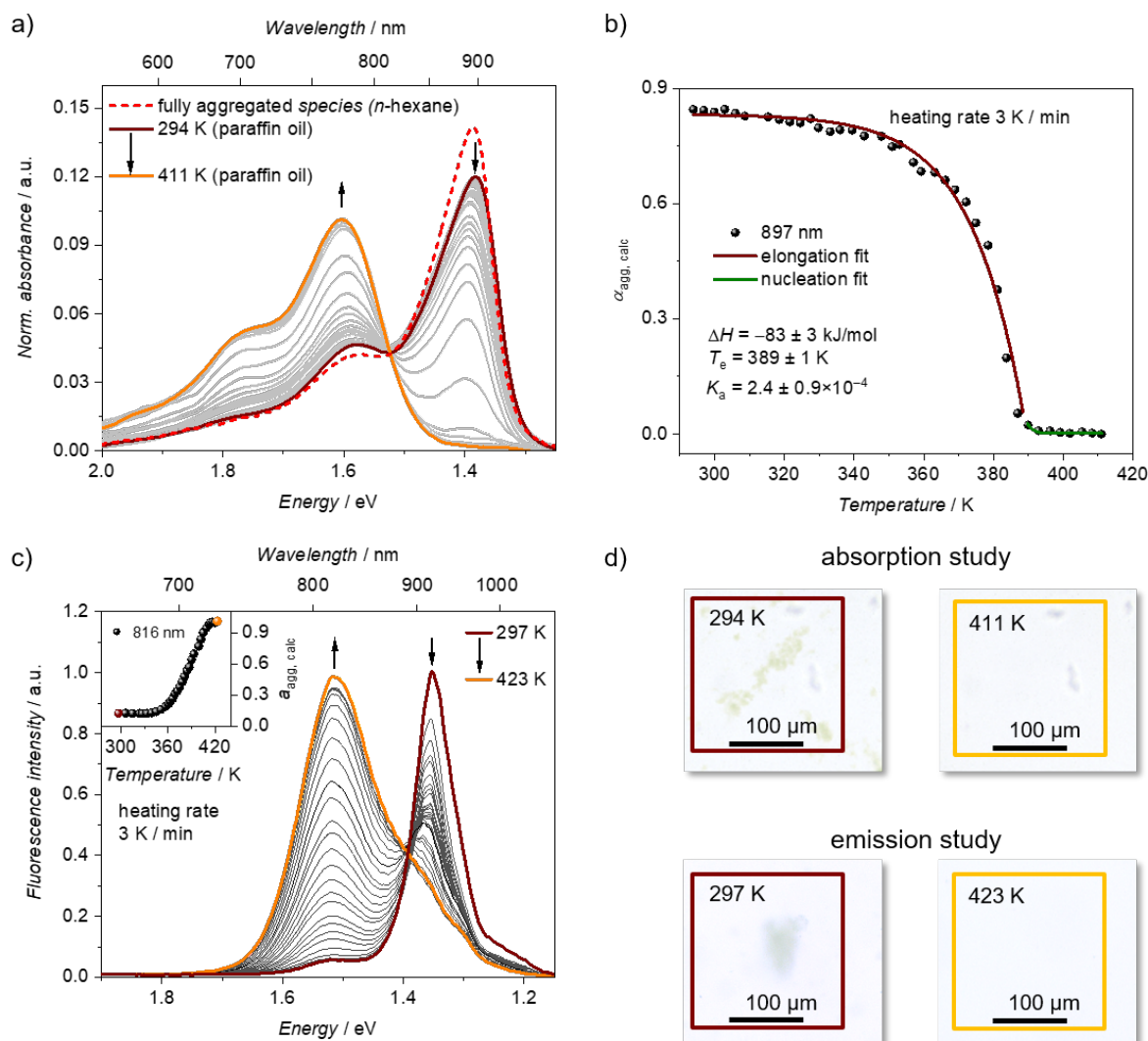


Figure A60. Temperature-dependent UV-vis-NIR absorption (a,b) and emission (c) studies of *M-QBI-Me* dispersed in paraffin oil between 294 K or 297 K up to 411 K or 423 K investigated under a polarizing optical microscope equipped with a spectrometer (dark red) (orange) for absorption and emission, respectively. The paraffin oil suspensions were investigated on glass in transmission mode (absorption) and on Si/SiO_x substrate in reflection mode (emission) upon blue light excitation. The arrows (a,c) indicate the spectral changes with increasing temperature. The spectra of the absorption study (a) are normalized between 1.54 and 2.0 eV (S_0 - S_1 transition) assuming a constant transition dipole moment. (b) Plot of fractions of aggregates in the area-normalized absorption study at 897 nm against temperature fitted with the nucleation-elongation model, in green and dark red, respectively. (d) Optical transmission microscopic images of the sample in paraffin oil investigated during the thermal disassembly. The regions of interest, which were integrated for spectral analysis are marked in dark red (start) and orange (end), respectively.

The enantiopure J-aggregate of *M*-QBI-Me suspended in paraffin oil (see previous chapter) was spectroscopically investigated under the light microscope in transmission mode upon heating by coupling the light microscope into a CCD spectrometer (Figure A60). In contrast to the enantiopure aggregate, the precipitate of the racemate did not allow for transmission absorption spectroscopy due to the large extent of the macroscopic crystallites (Figure A59c, right). The racemization barrier of the twisted QBIs is very high with activation barriers ΔG^\ddagger of about 125 kJ mol^{-1} . In 1,1,2,2-tetrachloroethane, we observed half-life times of about 80 minutes at 398 K.^[200] In contrast, disassembly of our enantiopure J-aggregate is much faster (see Figure A61). Accordingly, the enantiopurity is retained for at least two hours at temperatures of up to 368 K (below the racemization temperature) or shorter times at very high temperatures of 413 K. We deduced this from the equivalent monomeric dissymmetry factor g_{abs} of about 4×10^{-4} in paraffin oil after disassembly of the QBI's J-aggregate upon heating.

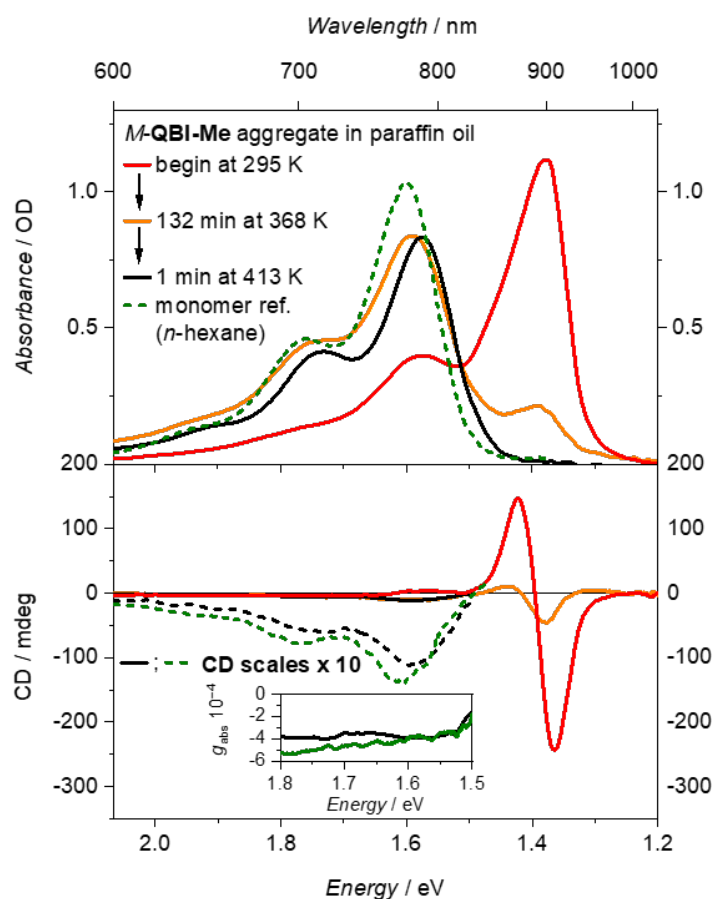


Figure A61. UV-vis-NIR absorption (top) and CD (bottom) spectra of enantiopure *M*-QBI-Me J-aggregates dispersed in paraffin oil upon heating up to 413 K (solid lines) as well as a kinetically trapped monomeric *n*-hexane solution as reference (green dashed line). The CD spectra of the monomeric species are scaled by factor 10. Their respective absorption dissymmetry factors g_{abs} around their absorption maxima are shown in the inset.

8.3.6 AFM Microscopy

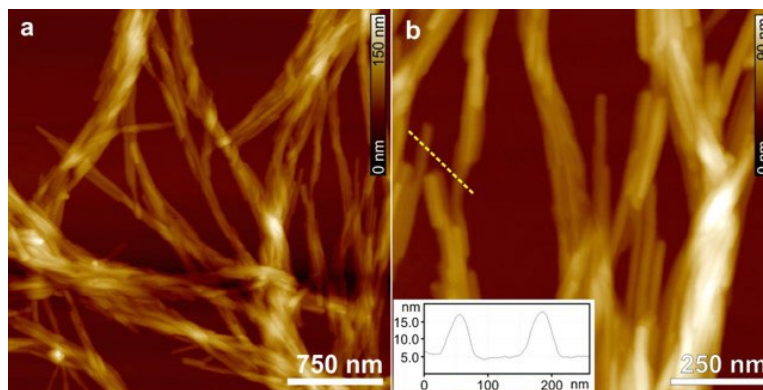


Figure A62. AFM topography images of an aged sample of *M*-QBI-Me on silicon wafer (SiO_x). Z scale is 150 nm (a) and 90 nm (b). The inset shows the cross-section analysis from the yellow dashed line in image (b). The sample was prepared by dropcasting the aged enantiopure precipitate suspended in *n*-hexane see (Figure A59) after 30 s of ultrasonication.

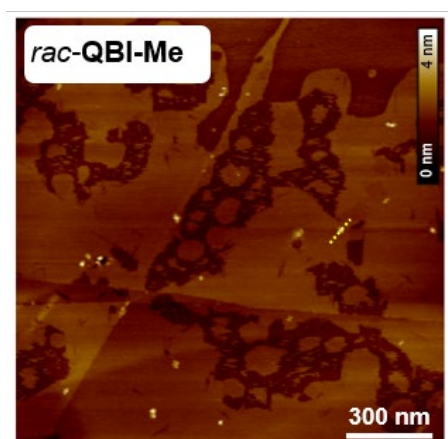


Figure A63. Full sized AFM topography image of *rac*-QBI-Me nanoparticles on HOPG substrate (see Figure 35 of the main manuscript). Z scale is 4 nm. The sample was prepared by spin-casting the freshly prepared *n*-hexane precipitate after 30 s of ultrasonication.

8.3.7 POM Investigation

The microcrystals of the racemic species *rac*-**QBI-Me** could be investigated on a Si/SiO_x substrate (silicon wafer) with a polarizing optical microscope showing strong birefringence as well as strong optical anisotropy (Figure A64). The large extend of the racemic crystallites did not allow for transmission absorption spectroscopy of the suspension in paraffin oil (see Figure A59) but it was possible to probe the NIR emission of the precipitates of *rac*/*M*-**QBI-Me** dispersed in paraffin oil on Si/SiO_x substrates (Figure A64b). The overall matching of emission profiles of microcrystals of the racemate *rac*-**QBI-Me** and the enantiopure species *M*-**QBI-Me** (Figure A64b) hence proved the equivalence of chromophore packing on the molecular level.

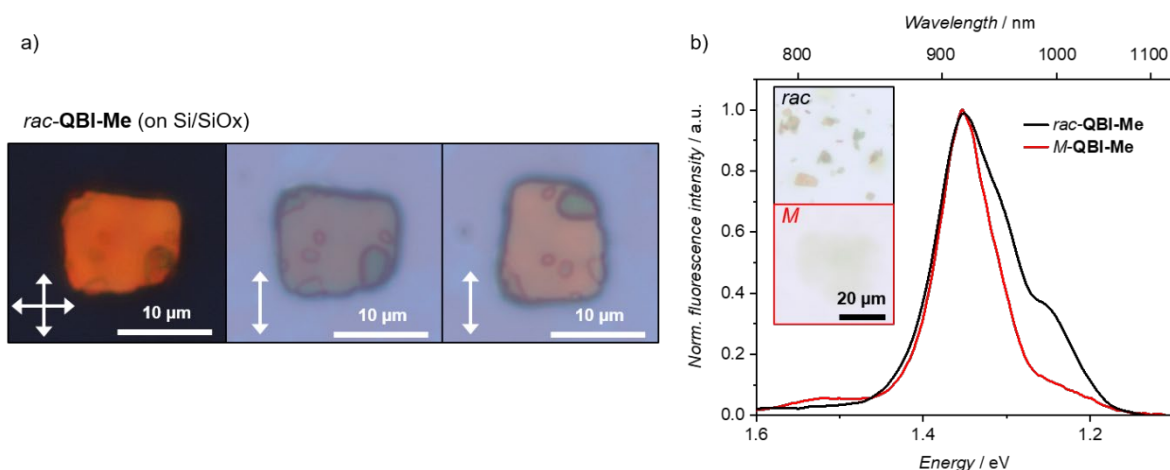


Figure A64. (a) Polarized optical microscopy images of microcrystals of *rac*-**QBI-Me** under cross polarization (left) and for different orientations of the crystals (0° and 90°) to the polarization axis of incident light (scale bar 10 μm). The samples were spin-cast on a Si/SiO_x substrate. (b) Normalized emission spectra of *rac*-**QBI-Me** (black) and *M*-**QBI-Me** (red) suspensions in paraffin oil on Si/SiO_x substrates. The insets show the regions of interest, which were integrated for spectral analysis (scale bar 20 μm).

8.3.8 Single-Crystal X-Ray Analysis

Table A13. Crystal data and structure refinement for *rac*-QBI-Me.

CCDC	2252806	
Empirical formula	C _{103.47} H _{81.69} Cl _{12.34} N ₂ O _{7.44}	
Formula weight	1554.73	
Temperature	100(2) K	
Wavelength	0.61992 Å	
Crystal system	Triclinic	
Space group	<i>P</i> $\bar{1}$	
Unit cell dimensions	<i>a</i> = 16.957(10) Å	α = 95.342(14)°.
	<i>b</i> = 23.156(11) Å	β = 110.991(16)°.
	<i>c</i> = 23.344(15) Å	γ = 103.526(14)°.
Volume	8161(8) Å ³	
<i>Z</i>	4	
Density (calculated)	1.265 g/cm ³	
Absorption coefficient	0.108 mm ⁻¹	
F(000)	3262.6	
Crystal size	0.100 × 0.100 × 0.100 mm ³	
Theta range for data collection	0.804 to 21.803°	
Index ranges	-20 ≤ <i>h</i> ≤ 18, -27 ≤ <i>k</i> ≤ 27, -27 ≤ <i>l</i> ≤ 27	
Reflections collected	28838	
Independent reflections	28838 [<i>R</i> (int) = 0.1518]	
Completeness to theta = 21.803°	98.1 %	
Absorption correction	None	
Refinement method	Full-matrix least-squares on <i>F</i> ²	
Data / restraints / parameters	28838 / 3195 / 2846	
Goodness-of-fit on <i>F</i> ²	1.172	
Final <i>R</i> indices [<i>I</i> > 2 σ (<i>I</i>)]	<i>R</i> ₁ = 0.1399, <i>wR</i> ₂ = 0.3859	
<i>R</i> indices (all data)	<i>R</i> ₁ = 0.1996, <i>wR</i> ₂ = 0.4417	
Extinction coefficient	n/a	
Largest diff. peak and hole	0.431 and -0.402 e ⁻ Å ⁻³	

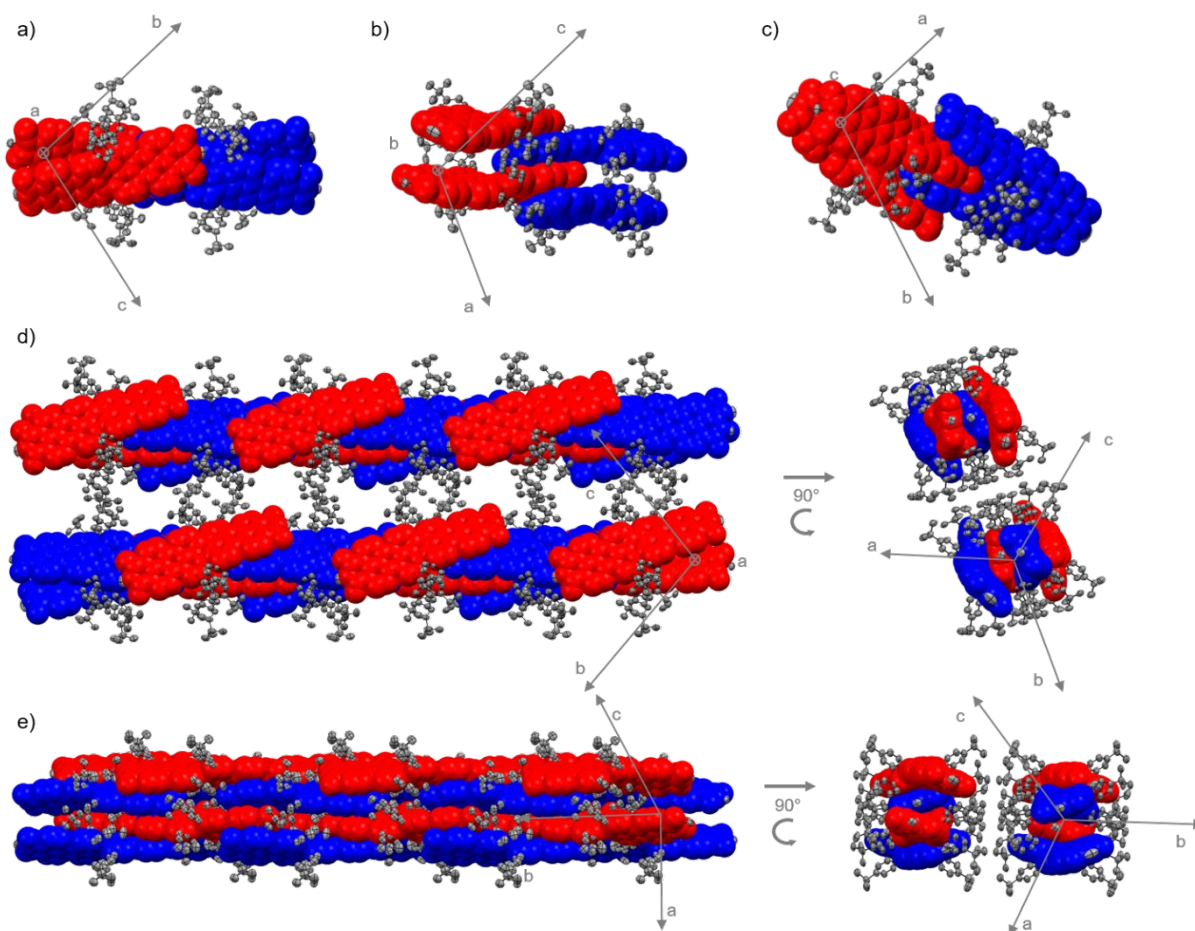


Figure A65. Molecular arrangement of the *P*- (blue) and *M*- (red) atropo-enantiomers of *rac*-QBI-Me as determined from the single-crystal structure obtained from their racemic mixture. The unit cell (*a*–*c*) containing two pairs of *P*- and *M*-atropo-enantiomers is shown along their *a*- (*a*), *b*- (*b*) and *c*- (*c*) axis. Two fourfold strands, each built up from four unit cells propagating along the *bc*-direction, are shown in top (*d*) and side view (*e*). The ellipsoids are set to 50% probability. Carbon, oxygen and nitrogen atoms of the QBI chromophore are shown in spacefill model. Disorder, hydrogen atoms, and solvent molecules are omitted for clarity.

8.3.9 Molecular Modelling

The modelling of the enantiopure *M*-superhelix (*J*-aggregate) will be elucidated in the following along with Figure A66.

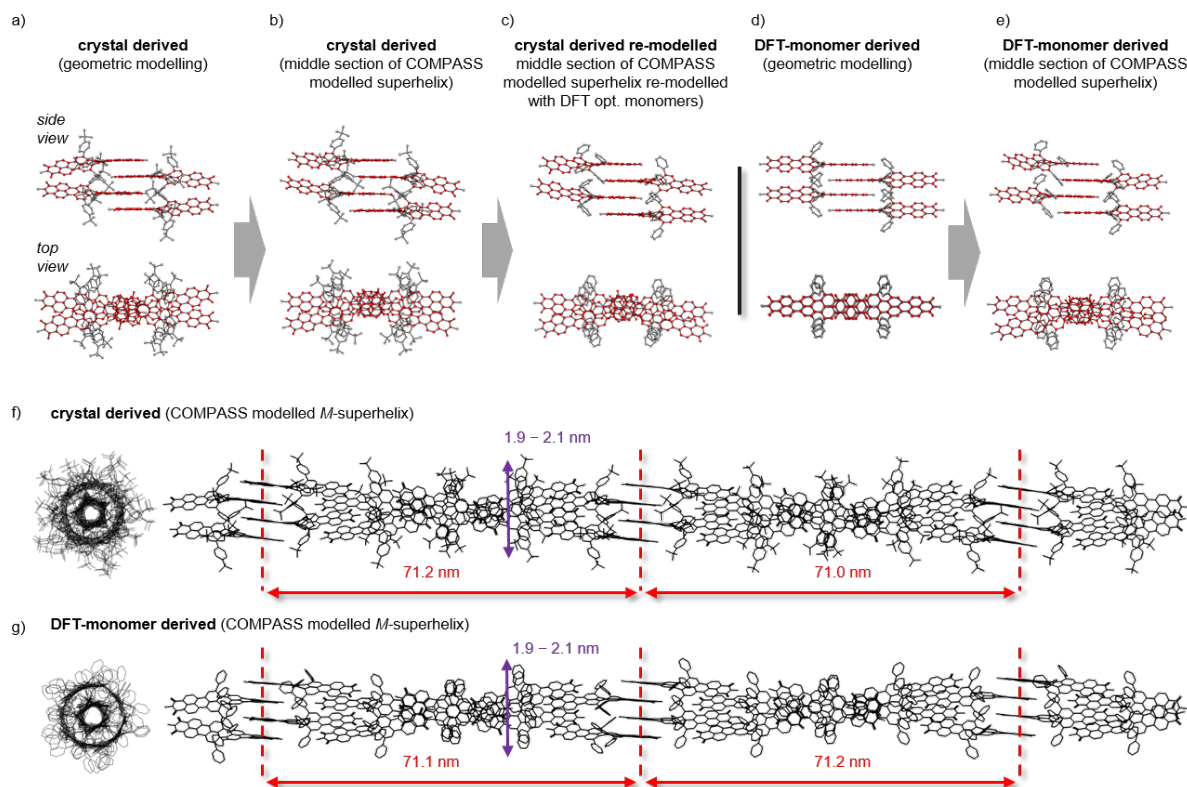


Figure A66. Conceptual overview on conducted molecular modelling. (a–e) Unit cells of *M*-QBI-Me showing different packing geometries before and after COMPASS optimization using *Materials Studio*. (f,g) Cutoffs of the COMPASS-optimized *M*-superhelicenes viewed along the helix axis (left) and in side view (right). The resultant $p/2$ helical half-pitch (red) as well as mean diameter of the four-fold strand (violet) are displayed as well. The total translation of the respective unit cells (f,g) was until a 720° turn.

The *P*-enantiomers of the unit cell of the racemic crystal structure were inverted to obtain an enantiopure unit cell (a). This unit cell was incrementally both translated by 14.8 \AA and rotated by 36° counterclockwise in propagation direction to obtain an *M*-superhelix in total rotation of 720° (not shown). This helix was then structure-optimized using the COMPASS tool of *Material Studios*. The central section of 332° total turn is presented in (f). The unit cell in the center of this superhelix (b) was then taken for the reference ab-initio dimer calculations (Table A14, Figure A68b) and was re-modelled with DFT-optimized simplified monomers by applying the crucial packing parameters (c). This unit cell was taken for all calculations shown in Figure 37, Figure A67, Figure A68a Figure A69, as well as Table A14, Table A15, Table A16, Table A17. We want to note, that as further reference, also the DFT-optimized monomers have been arranged in perfect collinear slip-stacked geometry at 3.4 \AA distance

between the π -planes (d). This unit cell was then analogously geometry-optimized to obtain the *M*-superhelix (g) and its central unit cell (e) revealing the same chromophore packing as the *M*-superhelix derived from the single crystal structure of the racemate (b).

8.3.10 Theoretical Calculations

The chiroptical response of extended PAHs can be estimated by time-dependent density functional theory (TD-DFT) calculations using functionals that are corrected for long-range coupling (LC) interactions such as CAM-B3LYP or ω B97XD even for higher energy transitions.^[280] However, ab-initio calculations usually fail at simulating exciton-coupled systems. Recent progress could be achieved by modifying the LC-parameters of these functionals^[280] or by exploiting double-hybrid density functional or configurational interaction methods, which are unfortunately rather unhandy for extended PAHs.^[279] Accessing the chiroptical signature of excitonic systems remains still challenging but can be approached by applying the Rosenfeld equation using the critical parameters of monomeric fragments derived from TD-DFT calculations.^[50, 52, 280]

In this work, theoretical absorption and electronic circular dichroism (ECD) spectra of *M*-**QBI-Me** were calculated with the program Gaussian 16 using TD-DFT on ω B97XD/def2-svp level of theory. All presented UV–vis–NIR and ECD spectra refer to the structure optimized and simplified QBI as A, B, C and D, where its *tert*-butyl units of the aryl *bay*-substituents are replaced by hydrogen. For reference calculations, also the packing contorted non-simplified QBIs (Figure A66b) were used, which are denoted as A', B', C' and D'. Rotational strengths were calculated by using the dipole velocity formula. Hence, both, oscillator strengths and rotational strengths were corrected for the applied shift in transition energy. The origin of Cartesian coordinates of the ab-initio calculations of pairs of QBIs (Figure A67) were set to the respective center of mass to minimize effects of the origin-dependent magnetic transition dipole moment. For the same reason, also the individual DFT-optimized monomers within their rebuilt enantiopure unit cell were origin-centered for their monomeric calculations (Table A15).

For conversion between atomic units and SI units following relations have been used:

$$\text{Bohr-electron:} \quad 1 \text{ a.u.} = 254.1746 \cdot 10^{-20} \text{ esu cm}$$

$$\text{Bohr Magneton:} \quad 1 \text{ a.u.} = 0.9274 \cdot 10^{-20} \text{ erg G}^{-1}$$

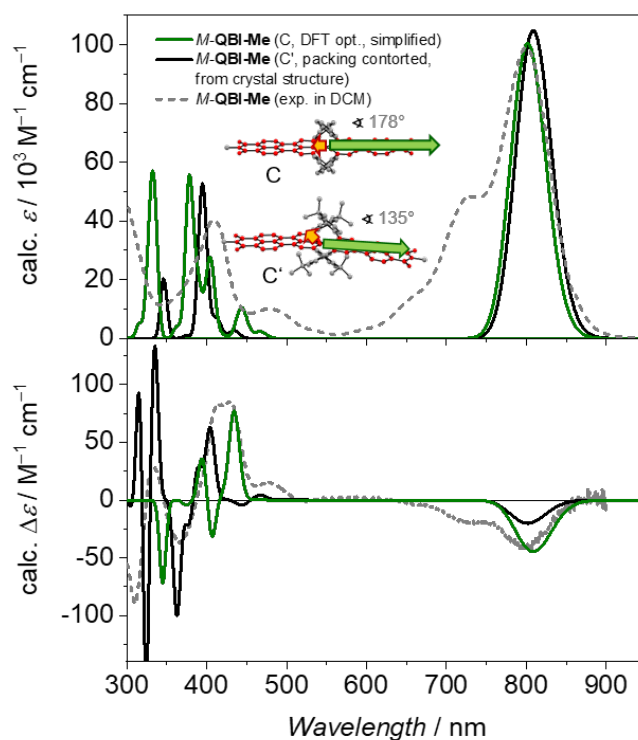


Figure A67. Calculated UV-vis-NIR absorption (top) and ECD (bottom) spectra of simplified and DFT geometry-optimized *M-QBI-Me* (green) as well as packing-contorted *M-QBI-Me* (derived from packing-optimized superhelix, see Figure A66b) along the corresponding experimental spectra recorded in DCM (see Figure A58). Excitation energies are shifted by 0.35 eV and 0.10 eV, respectively. Intensities of vertical transitions (not shown) were scaled by factor 0.28 and 0.40, respectively and convoluted with a phenomenological Gaussian with fwhm = 0.05 eV.

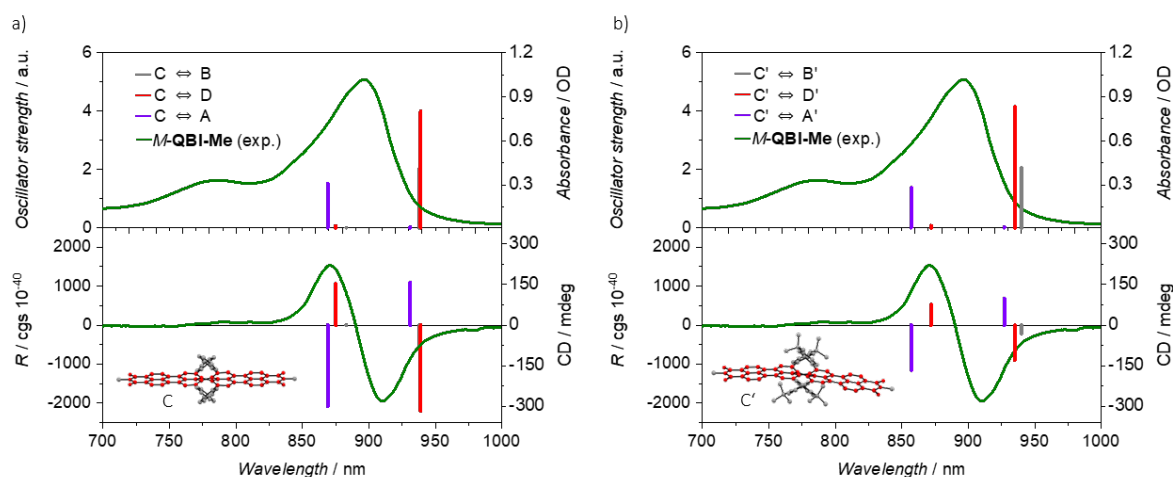


Figure A68. Experimental UV-vis-NIR and CD spectra (green) as well as ab-initio TD-DFT calculated vertical transitions of *M-QBI-Me* dimers either using the geometry-optimized and simplified monomers (a) or the packing-affected monomers (b), corresponding to Figure A66c and Figure A66b, respectively. The insets show the molecular geometry of monomer C and C', respectively. Transition energies are shifted by 0.50 eV (a) and 0.08 eV (b), respectively.

Insights into the reliability of the ab-initio calculations (Figure A68a, red) could be obtained by natural transition orbital^[242] analysis of the C↔D QBI pair (Figure A69) revealing that the main

excitations remain almost localized on the monomers, hence failing to distribute the oscillator strength evenly, which would be necessary to properly assess the chiroptical response of the entire dimer. Thus, the *ab-initio* calculations can be estimated rather unreliable for interpretation of the excitonic coupling, which motivated for the more elaborated approach including the transition charge method as well as Amsterdam Density Functional (ADF) into the Rosenfeld equation.

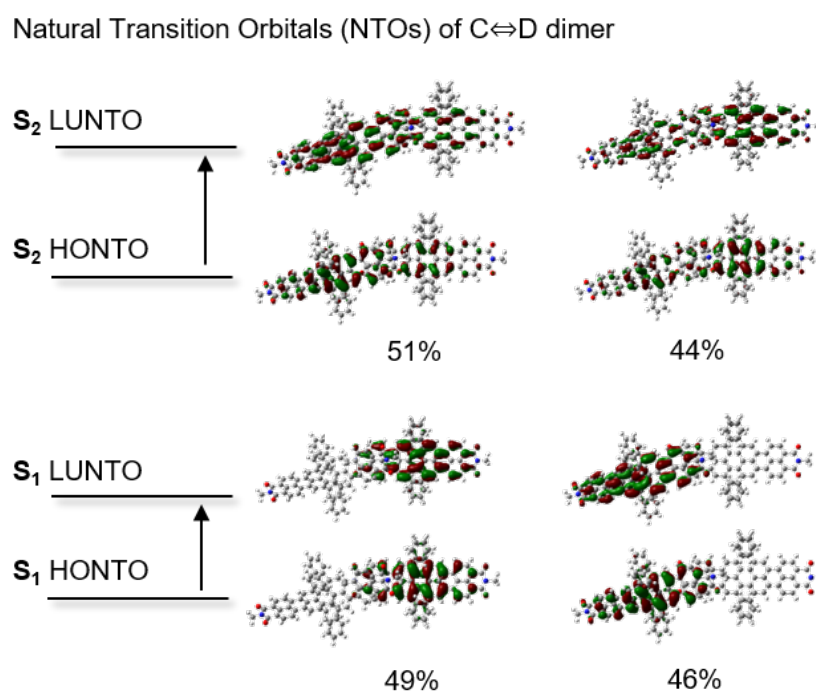


Figure A69. Natural transition orbitals (NTOs) of the first two excitations of the slip-stacked QBI pair C \rightleftharpoons D of *M-QBI-Me* as HONTO (highest occupied natural transition orbital) and LUNTO (lowest occupied natural transition orbital) with iso-values of 0.02.

Table A14. Chiroptical properties obtained from ab-initio TD-DFT calculations of pairs of *M*-QBI-Me either with geometry optimized monomers (top) or as packing-contorted pairs (bottom) within the modelled *M*-superhelix.

Pairs of <i>M</i> -QBI-Me	Excitation energy / nm (eV)	$ \mu $ / 10^{-20} esu cm	R / 10^{-40} esu cm erg G^{-1}	g_{abs}^a
C \leftrightarrow B	(938) 1.3220	2801	-519	$-2.6 \cdot 10^{-4}$
	(888) 1.4039	3	-3	$-9.2 \cdot 10^{-1}$
$2 \times$ C \leftrightarrow D	(939) 1.3201	5579	-1104	$-2.8 \cdot 10^{-4}$
	(875) 1.4169	670	528	$9.4 \cdot 10^{-3}$
C \leftrightarrow A	(931) 1.3317	348	1101	$3.6 \cdot 10^{-2}$
	(869) 1.4268	2299	-2073	$-1.6 \cdot 10^{-3}$
C' \leftrightarrow B'	(940) 1.3196	2178	-213	$-1.8 \cdot 10^{-4}$
	(872) 1.4223	44	-5	$-1.1 \cdot 10^{-2}$
$2 \times$ C' \leftrightarrow D'	(935) 1.3255	2156	-447	$-2.0 \cdot 10^{-4}$
	(872) 1.4214	273	266	$7.1 \cdot 10^{-3}$
C' \leftrightarrow A'	(927) 1.3376	285	683	$3.4 \cdot 10^{-2}$
	(857) 1.4460	1706	-1153	$-1.6 \cdot 10^{-3}$

$$^a g = 4R / |\mu|^2$$

Table A15. Calculated coupling strengths of pairs of *M*-QBI-Me including Coulomb-coupling and charge-transfer coupling as well as calculated rotatory strengths.

Pairs of <i>M</i> -QBI-Me	r_{ij} / Å	J_{Coulomb}^a / meV	$ t_e ^b$ / meV	$ t_h ^b$ / meV	J_{CT}^c / meV	J_{total} / meV	R_{mon}^d / 10^{-40} esu ² cm ²	$R_{\text{e-m}}^d$ / 10^{-40} esu ² cm ²
C \leftrightarrow B	14.88	-30	35	24	-70	-100	-271	-271
C \leftrightarrow D	14.93	-31	18	12	-19	-50	-271	-260
C \leftrightarrow A	7.22	-33	1	21	-1	-32	-271	259

^a Transition charge scaling factor = $\mu_{\text{eg}}(\text{exp.}) / \mu_{\text{eg}}(\text{TD-DFT}) = 11.6 / 13.1 = 0.885$.

^b Calculated using ADF.

^c Calculated as $'-2 \times |t_e| \times |t_h| / (E_{\text{CT}} - E_{\text{S1}})'$ with $|(E_{\text{CT}} - E_{\text{S1}})| = 1600 \text{ cm}^{-1} = 198 \text{ meV}$, – taken from the assumption for PBIs from C. Kaufmann *et al.*^[119, 311]

^d The monomeric transition energy was set to 1.3822 eV (897 nm). $R_{\text{mon},ij} = -(\mu_i \cdot \mathbf{m}_i + \mu_j \cdot \mathbf{m}_j)$; $R_{\text{e-m},ij} = -(\mu_i \cdot \mathbf{m}_j + \mu_j \cdot \mathbf{m}_i)$.

Table A16. Calculated transition energies and rotatory strengths of pairs of QBIs along their calculated coupling strengths.

Pairs of <i>M</i> - QBI-Mc	λ_-^a / nm	λ_{\max}^a / nm	λ_+^a / nm	J_{total}^b / meV	$R_{\text{ex}\lambda_-}^c$ / $10^{-40} \text{ esu}^2 \text{ cm}^2$	$R_{\text{ex}\lambda_+}^c$ / $10^{-40} \text{ esu}^2 \text{ cm}^2$	$R_{\text{total}\lambda_-}^d$ / $10^{-40} \text{ esu}^2 \text{ cm}^2$	$R_{\text{total}\lambda_+}^d$ / $10^{-40} \text{ esu}^2 \text{ cm}^2$
C \Leftrightarrow B	866	897	931	-100	3	-2	545	-544
C \Leftrightarrow D	881	897	914	-50	1400	-1302	1931	-1833
C \Leftrightarrow A	887	897	908	-32	756	-722	1286	-1252

^a The monomeric transition energy was set to 1.3822 eV (897 nm). For the presented J-type excitonic states, the excitation wavelengths λ_+ and λ_- refer to the lower and higher energetic transition, respectively.

^b J_{Total} is used from Table A15.

^c R_{ex} was calculated according to K. Swathi *et al.*^[48]

^d $R_{\text{total}} = R_{\text{mon}} + R_{\text{e-m}} + R_{\text{ex}}$. Note: The sign of $R_{\text{e-m}}$ of C \Leftrightarrow A was inverted to account for change in the relative mutual spectral positions of λ_- and λ_+ due to the J-type coupling.^[51]

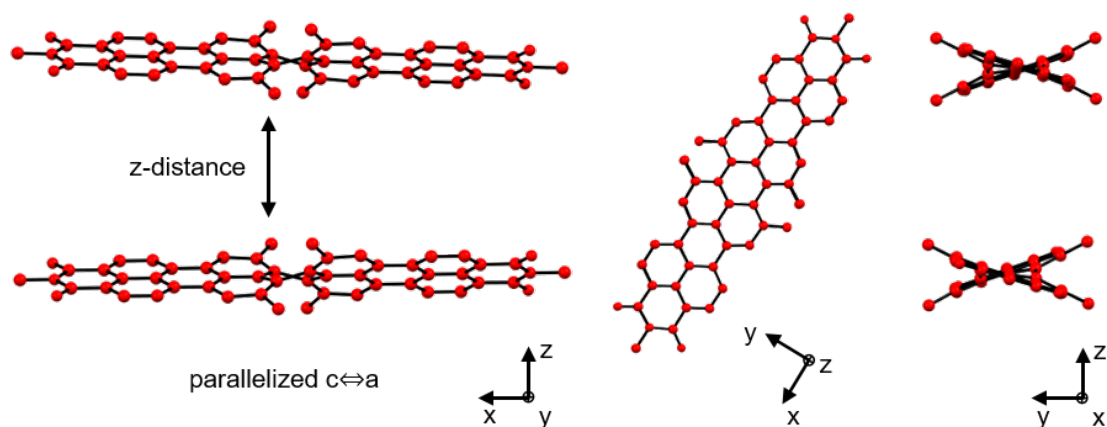


Figure A70. Reference structures of the parallelized pair of simplified *M-QBI-Me* $C \leftrightarrow A$ where phenyl moieties have been substituted by methyl units and hydrogen atoms have been omitted for clarity. The presented *z*-distance measured between the centroids of the central hexagon is 9 Å.

Table A17. Reference calculations of coupling strengths of pairs of QBIs. The phenyl moieties have been substituted by methyl units (see Figure A70).

Pairs of <i>M-QBI-Me</i>	J_{Coulomb}^a / meV	$ t_c ^b$ / meV	$ t_h ^b$ / meV	J_{CT}^c / meV	J_{total} / meV
$C \leftrightarrow B$ (Ph→Me)	-30	40	28	-91	-121
$C \leftrightarrow D$ (Ph→Me)	-31	20	14	-23	-54
$C \leftrightarrow A$ (Ph→Me)	-37	2	2	-0	-37
$C \leftrightarrow A$ (Ph→Me, parallelized z-distance = 7 Å)	+43	1	1	-0	+43
$C \leftrightarrow A$ (Ph→Me, parallelized z-distance = 9 Å)	+30	0	0	-0	+30

^a Transition charge scaling factor = $\mu_{\text{cg}}(\text{exp.}) / \mu_{\text{cg}}(\text{TD-DFT}) = 11.6 / 14.5 = 0.800$.

^b Calculated using ADF.

^c Calculated as “ $-2 \times |t_c| \times |t_h| / (E_{\text{CT}} - E_{\text{S1}})$ ” with “ $(E_{\text{CT}} - E_{\text{S1}}) = 1600 \text{ cm}^{-1} = 198 \text{ meV}$,” – analogous to the assumption for PBIs from C. Kaufmann *et al.*^[119, 311]

8.3.11 Electrochemical Properties

Cyclic voltammetry (CV) and differential pulse voltammetry (DPV) experiments were performed. Measurements were conducted in DCM at room temperature against Fc/Fc⁺ using tetrabutylammonium hexafluorophosphate (TBAHFP) as an electrolyte. The results are summarized in Table A18 and Figure A71.

Table A18. Redox properties of *P/M-QBI-Me* in DCM at 298 K.

	$E_{\text{red1}}^{\text{a}}$ / V	$E_{\text{red2}}^{\text{a}}$ / V	$E_{\text{ox1}}^{\text{a}}$ / V	$E_{\text{ox2}}^{\text{a}}$ / V
<i>rac</i> -QBI-Me	-1.08	-2.18	0.37	0.75

^aHalf-wave potentials were determined by cyclic or differential pulse voltammetry measured in DCM (0.1 M TBAHFP) vs. Fc/Fc⁺ at a scan rate of 100 mV s⁻¹.

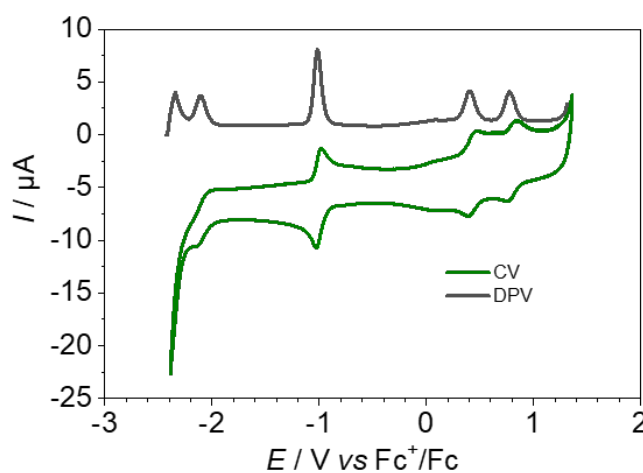


Figure A71. Differential pulse (DPV, gray) and cyclic voltammetry (CV, green) of *rac*-QBI-Me. Measurements were performed in DCM solutions ($c_0 \approx 10^{-4}$ M) at 293 K using TBAHFP ($c \approx 0.1$ M) as electrolyte with a scan rate of 100 mV s⁻¹.

8.3.12 NMR Spectroscopy

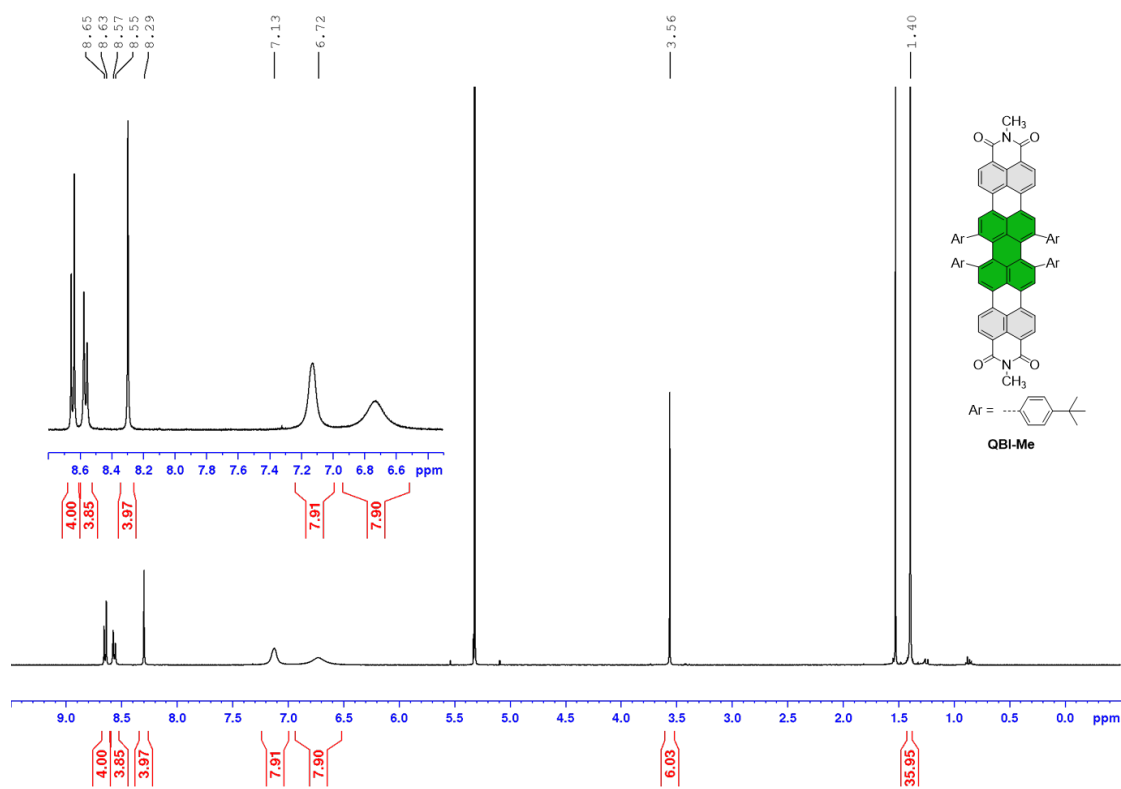


Figure A72. ¹H NMR (400 MHz) spectrum of *rac*-QBI-Me in CD₂Cl₂ at 295 K.

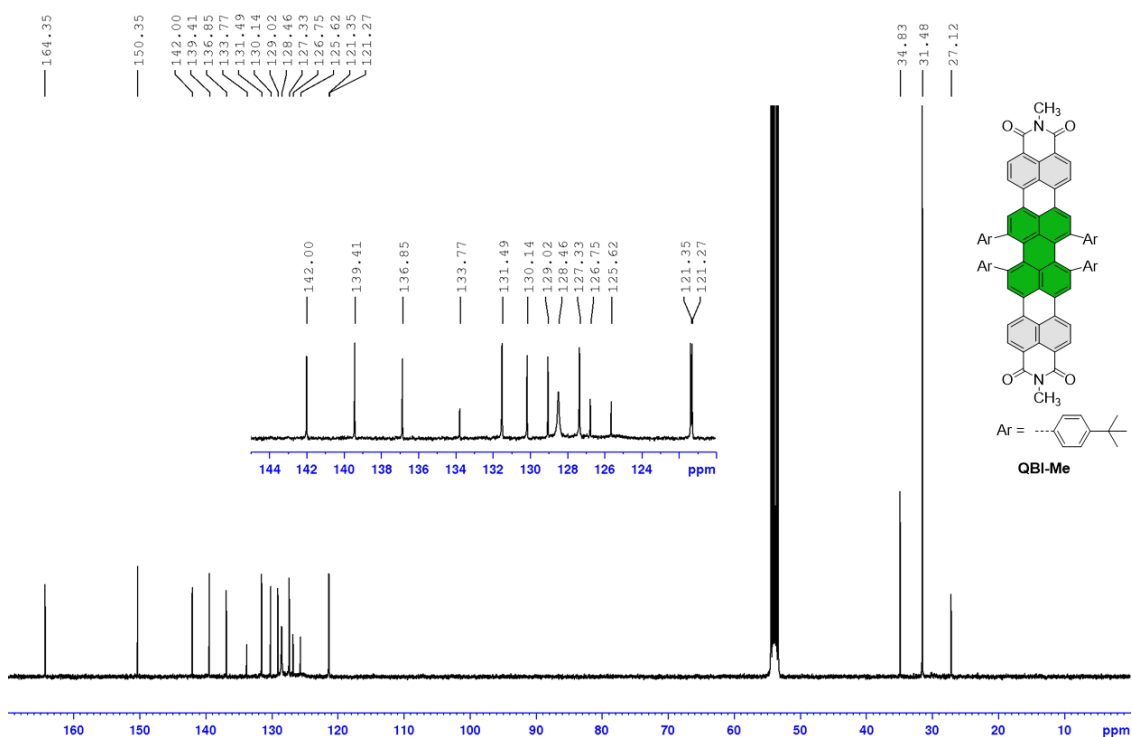


Figure A73. ¹³C NMR (131 MHz) spectrum of *rac*-QBI-Me in CD₂Cl₂ at 295 K.

8.3.13 High-Resolution Mass-Spectrometry

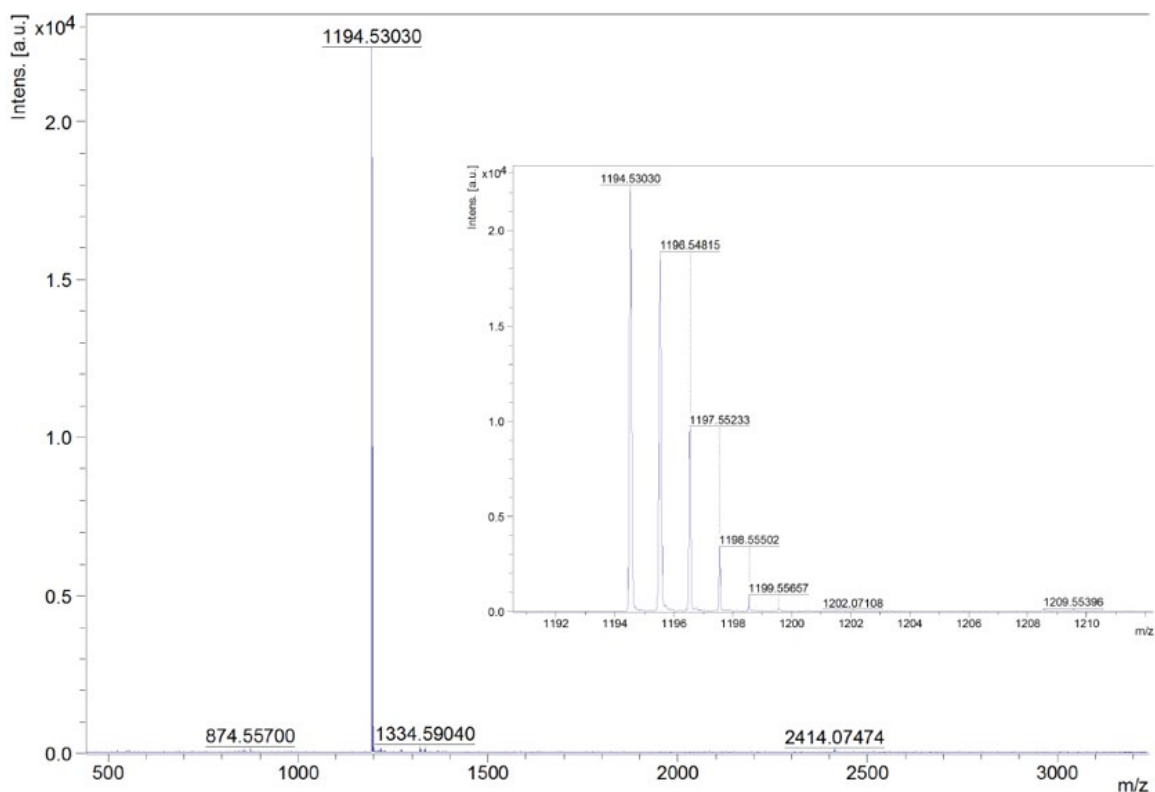


Figure A74. High-resolution mass spectrum (MALDI-TOF, neg. mode, matrix: DCTB 1:3 in chloroform) of *rac*-QBI-Me.

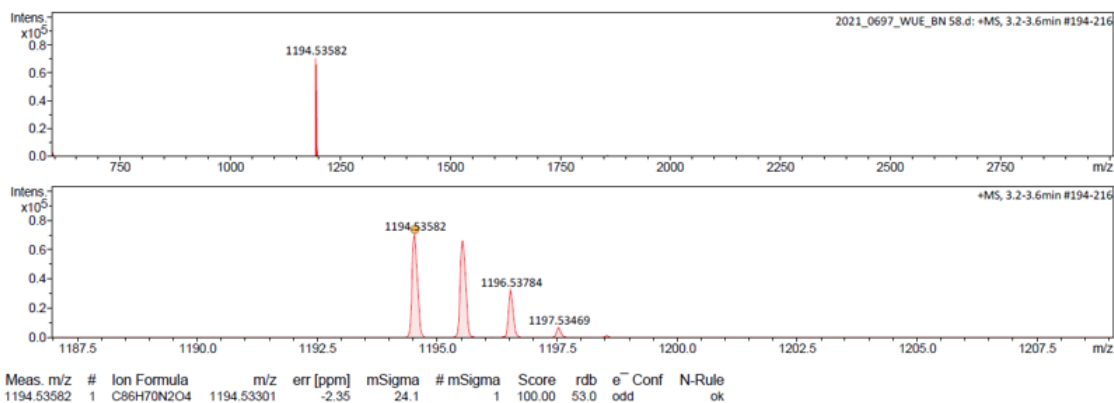


Figure A75. High-resolution mass spectrum (ESI-TOF, pos. mode, CHCl₃/MeCN) of *rac*-QBI-Me.

Bibliography

- [1] R. S. Cahn, C. Ingold, V. Prelog, *Angew. Chem., Int. Ed. Engl.* **1966**, *5*, 385-415.
- [2] S. Capozziello, A. Lattanzi, *Astrophys. Space Sci.* **2006**, *301*, 189-193.
- [3] N. H. Cho, A. Guerrero-Martínez, J. Ma, S. Bals, N. A. Kotov, L. M. Liz-Marzán, K. T. Nam, *Nat. Rev. Bioeng.* **2023**, *1*, 88-106.
- [4] F. Bertocchi, C. Sissa, A. Painelli, *Chirality* **2023**, *35*, 681-691.
- [5] S.-H. Yang, R. Naaman, Y. Paltiel, S. S. P. Parkin, *Nat. Rev. Phys.* **2021**, *3*, 328-343.
- [6] S. F. Ozturk, D. D. Sasselov, *Proc. Natl. Acad. Sci. U.S.A.* **2022**, *119*, e2204765119.
- [7] L. Francés-Soriano, E. Zaballos-García, J. Pérez-Prieto, *Adv. Opt. Mater.* **2023**, *11*, 2300337.
- [8] Y. Deng, M. Wang, Y. Zhuang, S. Liu, W. Huang, Q. Zhao, *Light Sci. Appl.* **2021**, *10*, 76.
- [9] J. Wade, J. N. Hilfiker, J. R. Brandt, L. Liirò-Peluso, L. Wan, X. Shi, F. Salerno, S. T. J. Ryan, S. Schöche, O. Arteaga, T. Jávorfí, G. Siligardi, C. Wang, D. B. Amabilino, P. H. Beton, A. J. Campbell, M. J. Fuchter, *Nat. Commun.* **2020**, *11*, 6137.
- [10] W. A. Baase, W. C. Johnson, Jr., *Nucleic Acids Res.* **1979**, *6*, 797-814.
- [11] N. J. Greenfield, *Circular Dichroism (CD) Analyses of Protein-Protein Interactions*, Springer New York, New York, **2015**.
- [12] Y. Tokunou, P. Chinotaikul, S. Hattori, T. A. Clarke, L. Shi, K. Hashimoto, K. Ishii, A. Okamoto, *Chem. Commun.* **2018**, *54*, 13933-13936.
- [13] M. Mukhina, *Light Sci. Appl.* **2022**, *11*, 157.
- [14] A. Lininger, G. Palermo, A. Guglielmelli, G. Nicoletta, M. Goel, M. Hinczewski, G. Strangi, *Adv. Mater.* **2023**, *35*, 2107325.
- [15] Z. Feng, T. Tang, T. Wu, X. Yu, Y. Zhang, M. Wang, J. Zheng, Y. Ying, S. Chen, J. Zhou, X. Fan, D. Zhang, S. Li, M. Zhang, J. Qian, *Light Sci. Appl.* **2021**, *10*, 197.
- [16] X. Li, Y. Xie, Z. Li, *Ad. Photonics Res.* **2021**, *2*, 2000136.
- [17] Y. Sang, J. Han, T. Zhao, P. Duan, M. Liu, *Adv. Mater.* **2020**, *32*, 1900110.
- [18] J. Wade, F. Salerno, R. C. Kilbride, D. K. Kim, J. A. Schmidt, J. A. Smith, L. M. LeBlanc, E. H. Wolpert, A. A. Adeleke, E. R. Johnson, J. Nelson, T. Mori, K. E. Jelfs, S. Heutz, M. J. Fuchter, *Nat. Chem.* **2022**.
- [19] F. Würthner, C. R. Saha-Möller, B. Fimmel, S. Ogi, P. Leowanawat, D. Schmidt, *Chem. Rev.* **2016**, *116*, 962-1052.
- [20] W. Qiu, S. Chen, X. Sun, Y. Liu, D. Zhu, *Org. Lett.* **2006**, *8*, 867-870.
- [21] Y. Cai, L. Huo, X. Sun, D. Wei, M. Tang, Y. Sun, *Adv. Mater.* **2015**, *5*, 1500032.
- [22] R. Renner, B. Mahlmeister, O. Anhalt, M. Stolte, F. Würthner, *Chem. Eur. J.* **2021**, *27*, 11997-12006.
- [23] N. Berova, P. L. Polavarapu, K. Nakanishi, R. W. Woody, *Comprehensive Chiroptical Spectroscopy, Vol. 1*, John Wiley & Sons, inc. Hoboken, New Jersey, **2012**.
- [24] R. B. Grossman, *J. Chem. Educ.* **1989**, *66*, 30.
- [25] L. Rosenfeld, *Zeitschrift für Physik* **1929**, *52*, 161-174.
- [26] J. A. Schellman, *Chem. Rev.* **1975**, *75*, 323-331.
- [27] T. Mori, *Chem. Rev.* **2021**, *121*, 2373-2412.
- [28] P. M. Bayley, *Prog. Biophys. Mol. Biol.* **1973**, *27*, 1-76.
- [29] E. U. Condon, *Rev. Mod. Phys.* **1937**, *9*, 432-457.

- [30] J. A. Schellman, *Acc. Chem. Res.* **1968**, *1*, 144-151.
- [31] L. L. Jones, H. Eyring, *Tetrahedron* **1961**, *13*, 235-240.
- [32] K. L. Bak, A. E. Hansen, K. Ruud, T. Helgaker, J. Olsen, P. Jørgensen, *Theor. Chim. Acta* **1995**, *90*, 441-458.
- [33] D. Aranda, N. J. Schuster, X. Xiao, F. J. Ávila Ferrer, F. Santoro, C. Nuckolls, *J. Phys. Chem. C* **2021**, *125*, 2554-2564.
- [34] J. L. Greenfield, J. Wade, J. R. Brandt, X. Shi, T. J. Penfold, M. J. Fuchter, *Chem. Sci.* **2021**, *12*, 8589-8602.
- [35] H. Kubo, T. Hirose, T. Nakashima, T. Kawai, J.-y. Hasegawa, K. Matsuda, *J. Phys. Chem. Lett.* **2021**, *12*, 686-695.
- [36] H. Tanaka, M. Ikenosako, Y. Kato, M. Fujiki, Y. Inoue, T. Mori, *Commun. Chem.* **2018**, *1*, 38.
- [37] S. Sato, A. Yoshii, S. Takahashi, S. Furumi, M. Takeuchi, H. Isobe, *Proc. Natl. Acad. Sci. U.S.A.* **2017**, *114*, 13097-13101.
- [38] F. S. Richardson, *Inorg. Chem.* **1980**, *19*, 2806-2812.
- [39] O. G. Willis, F. Zinna, L. Di Bari, *Angew. Chem. Int. Ed.* **2023**, *62*, e202302358.
- [40] J. G. Kirkwood, *Chem. Phys.* **1937**, *5*, 479-491.
- [41] W. Moffitt, *Chem. Phys.* **2004**, *25*, 467-478 (1956).
- [42] M. Kasha, H. R. Rawls, M. Ashraf El-Bayoumi, *Pure Appl. Chem.* **1965**, *11*, 371-392.
- [43] R. M. Hochstrasser, M. Kasha, *Photochem. Photobiol.* **1964**, *3*, 317-331.
- [44] A. S. Davydov, E. F. Sheka, *Phys. Status Solidi B* **1965**, *11*, 877-890.
- [45] N. Harada, K. Nakanishi, *Acc. Chem. Res.* **1972**, *5*, 257-263.
- [46] N. Harada, S.-M. L. Chen, K. Nakanishi, *J. Am. Chem. Soc.* **1975**, *97*, 5345-5352.
- [47] N. S. S. Nizar, M. Sujith, K. Swathi, C. Sissa, A. Painelli, K. G. Thomas, *Chem. Soc. Rev.* **2021**, *50*, 11208-11226.
- [48] K. Swathi, C. Sissa, A. Painelli, K. George Thomas, *Chem. Commun.* **2020**, *56*, 8281-8284.
- [49] I. Tinoco Jr, *Adv. Chem. Phys.* **1962**, 113-160.
- [50] T. Bruhn, G. Pescitelli, S. Jurinovich, A. Schaumlöffel, F. Witterauf, J. Ahrens, M. Bröring, G. Bringmann, *Angew. Chem. Int. Ed.* **2014**, *53*, 14592-14595.
- [51] G. Pescitelli, R. W. Woody, *J. Phys. Chem. B* **2012**, *116*, 6751-6763.
- [52] E. Freytag, M. Holzapfel, A. Swain, G. Bringmann, M. Stolte, F. Würthner, C. Lambert, *Chem. Sci.* **2022**, *13*, 12229-12238.
- [53] E. Freytag, L. Kreimendahl, M. Holzapfel, J. Petersen, H. Lackinger, M. Stolte, F. Würthner, R. Mitric, C. Lambert, *J. Org. Chem.* **2023**, *88*, 10777-10788.
- [54] M. Ōki, *Recent Advances in Atropisomerism, Topics in Stereochemistry, Vol. 14*, **1983**.
- [55] S. E. Penty, M. A. Zwijnenburg, G. R. F. Orton, P. Stachelek, R. Pal, Y. Xie, S. L. Griffin, T. A. Barendt, *J. Am. Chem. Soc.* **2022**, *144*, 12290-12298.
- [56] S. Hien, Ph.D. Thesis, University of Regensburg (Germany), **1995**.
- [57] F. Würthner, *Pure Appl. Chem.* **2006**, *78*, 2341-2349.
- [58] P. Osswald, D. Leusser, D. Stalke, F. Würthner, *Angew. Chem. Int. Ed.* **2005**, *44*, 250-253.
- [59] P. Osswald, M. Reichert, G. Bringmann, F. Würthner, *J. Org. Chem.* **2007**, *72*, 3403-3411.
- [60] P. Osswald, F. Würthner, *J. Am. Chem. Soc.* **2007**, *129*, 14319-14326.
- [61] M. M. Safont-Sempere, P. Osswald, M. Stolte, M. Grüne, M. Renz, M. Kaupp, K. Radacki, H. Braunschweig, F. Würthner, *J. Am. Chem. Soc.* **2011**, *133*, 9580-9591.
- [62] J. Li, P. Li, M. Fan, X. Zheng, J. Guan, M. Yin, *Angew. Chem. Int. Ed.* **2022**, *61*, e202202532.
- [63] Z. Xie, F. Würthner, *Org. Lett.* **2010**, *12*, 3204-3207.

- [64] L. Zhang, I. Song, J. Ahn, M. Han, M. Linares, M. Surin, H.-J. Zhang, J. H. Oh, J. Lin, *Nat. Commun.* **2021**, *12*, 142.
- [65] M. Queste, C. Cadiou, B. Pagoaga, L. Giraudet, N. Hoffmann, *New J. Chem.* **2010**, *34*, 2537-2545.
- [66] B. Pagoaga, L. Giraudet, N. Hoffmann, *Eur. J. Org. Chem.* **2014**, *2014*, 5178-5195.
- [67] Y. Cai, X. Guo, X. Sun, D. Wei, M. Yu, L. Huo, Y. Sun, *Sci. China Mater.* **2016**, *59*, 427-434.
- [68] W. Yang, G. Longhi, S. Abbate, A. Lucotti, M. Tommasini, C. Villani, V. J. Catalano, A. O. Lykhin, S. A. Varganov, W. A. Chalifoux, *J. Am. Chem. Soc.* **2017**, *139*, 13102-13109.
- [69] Y. Hu, G. M. Paternò, X.-Y. Wang, X.-C. Wang, M. Guizzardi, Q. Chen, D. Schollmeyer, X.-Y. Cao, G. Cerullo, F. Scotognella, K. Müllen, A. Narita, *J. Am. Chem. Soc.* **2019**, *141*, 12797-12803.
- [70] L. Zhang, S. Chen, J. Jiang, X. Dong, Y. Cai, H.-J. Zhang, J. Lin, Y.-B. Jiang, *Org. Lett.* **2022**, *24*, 3179-3183.
- [71] P. Leowanawat, A. Nowak-Król, F. Würthner, *Org. Chem. Front.* **2016**, *3*, 537-544.
- [72] A. Bedi, A. Manor Armon, Y. Diskin-Posner, B. Bogosalvsky, O. Gidron, *Nat. Commun.* **2022**, *13*, 451.
- [73] H. C. Friedman, E. D. Cosco, T. L. Atallah, S. Jia, E. M. Sletten, J. R. Caram, *Chem* **2021**, *7*, 3359-3376.
- [74] Y.-F. Wu, S.-W. Ying, L.-Y. Su, J.-J. Du, L. Zhang, B.-W. Chen, H.-R. Tian, H. Xu, M.-L. Zhang, X. Yan, Q. Zhang, S.-Y. Xie, L.-S. Zheng, *J. Am. Chem. Soc.* **2022**, *144*, 10736-10742.
- [75] M. Weh, J. Rühle, B. Herbert, A.-M. Krause, F. Würthner, *Angew. Chem. Int. Ed.* **2021**, *60*, 15323-15327.
- [76] M. Weh, K. Shoyama, F. Würthner, *Nat. Commun.* **2023**, *14*, 243.
- [77] M. Ball, B. Fowler, P. Li, L. A. Joyce, F. Li, T. Liu, D. Paley, Y. Zhong, H. Li, S. Xiao, F. Ng, M. L. Steigerwald, C. Nuckolls, *J. Am. Chem. Soc.* **2015**, *137*, 9982-9987.
- [78] M. Li, S. Nizar, S. Saha, A. Thomas, S. Azzini, T. W. Ebbesen, C. Genet, *Angew. Chem. Int. Ed.* **2023**, *62*, e202212724.
- [79] Z. Chen, U. Baumeister, C. Tschierske, F. Würthner, *Chem. Eur. J.* **2007**, *13*, 450-465.
- [80] B. E. Partridge, P. Leowanawat, E. Aqad, M. R. Imam, H.-J. Sun, M. Peterca, P. A. Heiney, R. Graf, H. W. Spiess, X. Zeng, G. Ungar, V. Percec, *J. Am. Chem. Soc.* **2015**, *137*, 5210-5224.
- [81] M. Hecht, P. Leowanawat, T. Gerlach, V. Stepanenko, M. Stolte, M. Lehmann, F. Würthner, *Angew. Chem. Int. Ed.* **2020**, *59*, 17084-17090.
- [82] M. Stolte, R. Hecht, Z. Xie, L. Liu, C. Kaufmann, A. Kudzus, D. Schmidt, F. Würthner, *Adv. Opt. Mater.* **2020**, *8*, 2000926.
- [83] T. E. Kaiser, V. Stepanenko, F. Würthner, *J. Am. Chem. Soc.* **2009**, *131*, 6719-6732.
- [84] Z. Xie, V. Stepanenko, K. Radacki, F. Würthner, *Chem. Eur. J.* **2012**, *18*, 7060-7070.
- [85] M. Hecht, F. Würthner, *Acc. Chem. Res.* **2021**, *54*, 642-653.
- [86] S. Herbst, B. Soberats, P. Leowanawat, M. Stolte, M. Lehmann, F. Würthner, *Nat. Commun.* **2018**, *9*, 2646.
- [87] M. Hecht, T. Schlossarek, S. Ghosh, Y. Tsutsui, A. Schmiedel, M. Holzapfel, M. Stolte, C. Lambert, S. Seki, M. Lehmann, F. Würthner, *ACS Appl. Nano Mater.* **2020**, *3*, 10234-10245.
- [88] K.-R. Wang, H.-W. An, Y.-Q. Wang, J.-C. Zhang, X.-L. Li, *Org. Biomol. Chem.* **2013**, *11*, 1007-1012.
- [89] K. Sun, C. Xiao, C. Liu, W. Fu, Z. Wang, Z. Li, *Langmuir* **2014**, *30*, 11040-11045.
- [90] K.-R. Wang, D. Han, G.-J. Cao, X.-L. Li, *Chem. Asian J.* **2015**, *10*, 1204-1214.

- [91] X. Liu, Z. Huang, Y. Huang, L. Zhu, J. Fu, *J. Phys. Chem. C* **2017**, *121*, 7558-7563.
- [92] C. Thalacker, F. Würthner, *Adv. Funct. Mater.* **2002**, *12*, 209-218.
- [93] A. P. H. J. Schenning, J. v. Herrikhuyzen, P. Jonkheijm, Z. Chen, F. Würthner, E. W. Meijer, *J. Am. Chem. Soc.* **2002**, *124*, 10252-10253.
- [94] F. Würthner, Z. Chen, F. J. M. Hoeben, P. Osswald, C.-C. You, P. Jonkheijm, J. v. Herrikhuyzen, A. P. H. J. Schenning, P. P. A. M. van der Schoot, E. W. Meijer, E. H. A. Beckers, S. C. J. Meskers, R. A. J. Janssen, *J. Am. Chem. Soc.* **2004**, *126*, 10611-10618.
- [95] X.-Q. Li, V. Stepanenko, Z. Chen, P. Prins, L. D. A. Siebbeles, F. Würthner, *Chem. Commun.* **2006**, 3871-3873.
- [96] M. Wehner, M. I. S. Röhr, M. Bühler, V. Stepanenko, W. Wagner, F. Würthner, *J. Am. Chem. Soc.* **2019**, *141*, 6092-6107.
- [97] S. Ghosh, X.-Q. Li, V. Stepanenko, F. Würthner, *Chem. Eur. J.* **2008**, *14*, 11343-11357.
- [98] F. Würthner, C. Bauer, V. Stepanenko, S. Yagai, *Adv. Mater.* **2008**, *20*, 1695-1698.
- [99] T. Ikeda, T. Masuda, T. Hirao, J. Yuasa, H. Tsumatori, T. Kawai, T. Haino, *Chem. Commun.* **2012**, *48*, 6025-6027.
- [100] Y. Huang, J. Hu, W. Kuang, Z. Wei, C. F. J. Faul, *Chem. Commun.* **2011**, *47*, 5554-5556.
- [101] C. D. Schmidt, C. Böttcher, A. Hirsch, *Eur. J. Org. Chem.* **2009**, *2009*, 5337-5349.
- [102] D. Franke, M. Vos, M. Antonietti, N. A. J. M. Sommerdijk, C. F. J. Faul, *Chem. Mater.* **2006**, *18*, 1839-1847.
- [103] L. Liang, X. Li, *J. Mol. Model.* **2018**, *24*, 51.
- [104] V. Dehm, Z. Chen, U. Baumeister, P. Prins, L. D. A. Siebbeles, F. Würthner, *Org. Lett.* **2007**, *9*, 1085-1088.
- [105] K.-R. Wang, H.-W. An, L. Wu, J.-C. Zhang, X.-L. Li, *Chem. Commun.* **2012**, *48*, 5644-5646.
- [106] S. Bai, S. Debnath, N. Javid, P. W. J. M. Frederix, S. Fleming, C. Pappas, R. V. Ulijn, *Langmuir* **2014**, *30*, 7576-7584.
- [107] D. Wei, Y. Yu, L. Ge, Z. Wang, C. Chen, R. Guo, *Langmuir* **2021**, *37*, 9232-9243.
- [108] S. Qiu, Z. Gao, X. Song, X. Hu, H. Yuan, W. Tian, *Chem. Commun.* **2022**, *58*, 4647-4650.
- [109] J. van Herrikhuyzen, A. Syamakumari, A. P. H. J. Schenning, E. W. Meijer, *J. Am. Chem. Soc.* **2004**, *126*, 10021-10027.
- [110] Y. Huang, Y. Yan, B. M. Smarsly, Z. Wei, C. F. J. Faul, *J. Mater. Chem.* **2009**, *19*, 2356-2362.
- [111] M. Kumar, M. D. Reddy, A. Mishra, S. J. George, *Org. Biomol. Chem.* **2015**, *13*, 9938-9942.
- [112] H. Zhao, S. Hussain, X. Liu, S. Li, F. Lv, L. Liu, S. Wang, *Chem. Eur. J.* **2019**, *25*, 9834-9839.
- [113] J. Gawroński, M. Brzostowska, K. Kacprzak, H. Kołbon, P. Skowronek, *Chirality* **2000**, *12*, 263-268.
- [114] P. Reine, A. M. Ortuño, I. F. A. Mariz, M. Ribagorda, J. M. Cuerva, A. G. Campaña, E. Maçôas, D. Miguel, *Front. Chem.* **2020**, *8*, 306.
- [115] T. Kawai, K. Kawamura, H. Tsumatori, M. Ishikawa, M. Naito, M. Fujiki, T. Nakashima, *ChemPhysChem* **2007**, *8*, 1465-1468.
- [116] J. Kumar, T. Nakashima, T. Kawai, *J. Phys. Chem. Lett.* **2015**, *6*, 3445-3452.
- [117] J. Kumar, H. Tsumatori, J. Yuasa, T. Kawai, T. Nakashima, *Angew. Chem. Int. Ed.* **2015**, *54*, 5943-5947.
- [118] J. Kumar, T. Nakashima, T. Kawai, *Langmuir* **2014**, *30*, 6030-6037.

- [119] C. Kaufmann, D. Bialas, M. Stolte, F. Würthner, *J. Am. Chem. Soc.* **2018**, *140*, 9986-9995.
- [120] J. Kumar, T. Nakashima, H. Tsumatori, T. Kawai, *J. Phys. Chem. Lett.* **2014**, *5*, 316-321.
- [121] S. Amiralaei, D. Uzun, H. Icil, *Photochem. Photobiol. Sci.* **2008**, *7*, 936-947.
- [122] S. Asir, A. S. Demir, H. Icil, *Dyes and Pigments* **2010**, *84*, 1-13.
- [123] A. Taniguchi, D. Kaji, N. Hara, R. Murata, S. Akiyama, T. Harada, A. Sudo, H. Nishikawa, Y. Imai, *RSC Adv.* **2019**, *9*, 1976-1981.
- [124] S.-K. Jung, J. H. Heo, B. M. Oh, J. B. Lee, S.-H. Park, W. Yoon, Y. Song, H. Yun, J. H. Kim, S. H. Im, O. P. Kwon, *Adv. Funct. Mater.* **2020**, *30*, 1905951.
- [125] X. Shang, I. Song, H. Ohtsu, Y. H. Lee, T. Zhao, T. Kojima, J. H. Jung, M. Kawano, J. H. Oh, *Adv. Mater.* **2017**, *29*, 1605828.
- [126] X. Shang, I. Song, J. H. Lee, W. Choi, J. Ahn, H. Ohtsu, J. C. Kim, J. Y. Koo, S. K. Kwak, J. H. Oh, *ACS Nano* **2020**, *14*, 14146-14156.
- [127] X. Shang, I. Song, H. Ohtsu, J. Tong, H. Zhang, J. H. Oh, *Sci. Rep.* **2017**, *7*, 5508.
- [128] V. Sharma, J. D. B. Koenig, G. C. Welch, *J. Mater. Chem. A* **2021**, *9*, 6775-6789.
- [129] Y.-J. Hwang, H. Li, B. A. E. Courtright, S. Subramanian, S. A. Jenekhe, *Adv. Mater.* **2016**, *28*, 124-131.
- [130] R. Xin, C. Zeng, D. Meng, Z. Ren, W. Jiang, Z. Wang, S. Yan, *ACS Omega* **2020**, *5*, 18449-18457.
- [131] W. Jiang, Z. Wang, *J. Am. Chem. Soc.* **2022**, *144*, 14976-14991.
- [132] F. Saal, F. Zhang, M. Holzappel, M. Stolte, E. Michail, M. Moos, A. Schmiedel, A.-M. Krause, C. Lambert, F. Würthner, P. Ravat, *J. Am. Chem. Soc.* **2020**, *142*, 21298-21303.
- [133] X. Tian, K. Shoyama, B. Mahlmeister, F. Brust, M. Stolte, F. Würthner, *J. Am. Chem. Soc.* **2023**, *145*, 9886-9894.
- [134] Y. Zhen, W. Yue, Y. Li, W. Jiang, S. Di Motta, E. Di Donato, F. Negri, S. Ye, Z. Wang, *Chem. Commun.* **2010**, *46*, 6078-6080.
- [135] W. Jiang, L. Ye, X. Li, C. Xiao, F. Tan, W. Zhao, J. Hou, Z. Wang, *Chem. Commun.* **2014**, *50*, 1024-1026.
- [136] Y. Liu, Z. Ma, Z. Wang, W. Jiang, *J. Am. Chem. Soc.* **2022**, *144*, 11397-11404.
- [137] Z. Ma, Q. Sun, J. Zhou, Y. Liu, Z. Shuai, Z. Wang, W. Jiang, *ACS Mater. Lett.* **2023**, 450-457.
- [138] Y. Zhong, B. Kumar, S. Oh, M. T. Trinh, Y. Wu, K. Elbert, P. Li, X. Zhu, S. Xiao, F. Ng, M. L. Steigerwald, C. Nuckolls, *J. Am. Chem. Soc.* **2014**, *136*, 8122-8130.
- [139] Y. Zhong, M. T. Trinh, R. Chen, W. Wang, P. P. Khlyabich, B. Kumar, Q. Xu, C.-Y. Nam, M. Y. Sfeir, C. Black, M. L. Steigerwald, Y.-L. Loo, S. Xiao, F. Ng, X. Y. Zhu, C. Nuckolls, *J. Am. Chem. Soc.* **2014**, *136*, 15215-15221.
- [140] M. Ball, Y. Zhong, Y. Wu, C. Schenck, F. Ng, M. Steigerwald, S. Xiao, C. Nuckolls, *Acc. Chem. Res.* **2015**, *48*, 267-276.
- [141] T. J. Sisto, Y. Zhong, B. Zhang, M. T. Trinh, K. Miyata, X. Zhong, X. Y. Zhu, M. L. Steigerwald, F. Ng, C. Nuckolls, *J. Am. Chem. Soc.* **2017**, *139*, 5648-5651.
- [142] Y.-C. Lin, N.-Z. She, C.-H. Chen, A. Yabushita, H. Lin, M.-H. Li, B. Chang, T.-F. Hsueh, B.-S. Tsai, P.-T. Chen, Y. Yang, K.-H. Wei, *ACS Appl. Mater. Interfaces* **2022**, *14*, 37990-38003.
- [143] Z. Jin, Q. Cheng, S. T. Bao, R. Zhang, A. M. Evans, F. Ng, Y. Xu, M. L. Steigerwald, A. E. McDermott, Y. Yang, C. Nuckolls, *J. Am. Chem. Soc.* **2022**, *144*, 13973-13980.
- [144] R. K. Dubey, M. Melle-Franco, A. Mateo-Alonso, *J. Am. Chem. Soc.* **2022**.
- [145] S. T. Bao, H. Jiang, C. Schaack, S. Louie, M. L. Steigerwald, C. Nuckolls, Z. Jin, *J. Am. Chem. Soc.* **2022**, *144*, 18772-18777.

- [146] X. Xiao, Q. Cheng, S. T. Bao, Z. Jin, S. Sun, H. Jiang, M. L. Steigerwald, C. Nuckolls, *J. Am. Chem. Soc.* **2022**, *144*, 20214-20220.
- [147] C. Weiss, D. I. Sharapa, A. Hirsch, *Chem. Eur. J.* **2020**, *26*, 14100-14108.
- [148] B. Liu, M. Böckmann, W. Jiang, N. L. Doltsinis, Z. Wang, *J. Am. Chem. Soc.* **2020**, *142*, 7092-7099.
- [149] T. Liu, Y. Ge, B. Sun, B. Fowler, H. Li, C. Nuckolls, S. Xiao, *J. Org. Chem.* **2019**, *84*, 2713-2720.
- [150] J. Tan, X. Xu, J. Liu, S. Vasylevskyi, Z. Lin, R. Kabe, Y. Zou, K. Müllen, A. Narita, Y. Hu, *Angew. Chem. Int. Ed.* **2023**, *63*, e202218494.
- [151] N. J. Schuster, D. W. Paley, S. Jockusch, F. Ng, M. L. Steigerwald, C. Nuckolls, *Angew. Chem. Int. Ed.* **2016**, *55*, 13519-13523.
- [152] S. Y. Han, R. K. Mow, A. K. Bartholomew, F. Ng, M. L. Steigerwald, X. Roy, C. Nuckolls, R. A. Wiscons, *J. Am. Chem. Soc.* **2022**, *144*, 5263-5267.
- [153] N. J. Schuster, R. Hernández Sánchez, D. Bukharina, N. A. Kotov, N. Berova, F. Ng, M. L. Steigerwald, C. Nuckolls, *J. Am. Chem. Soc.* **2018**, *140*, 6235-6239.
- [154] N. J. Schuster, L. A. Joyce, D. W. Paley, F. Ng, M. L. Steigerwald, C. Nuckolls, *J. Am. Chem. Soc.* **2020**, *142*, 7066-7074.
- [155] X. Xiao, S. K. Pedersen, D. Aranda, J. Yang, R. A. Wiscons, M. Pittelkow, M. L. Steigerwald, F. Santoro, N. J. Schuster, C. Nuckolls, *J. Am. Chem. Soc.* **2021**, *143*, 983-991.
- [156] G. Liu, T. Koch, Y. Li, N. L. Doltsinis, Z. Wang, *Angew. Chem. Int. Ed.* **2019**, *58*, 178-183.
- [157] D. Meng, G. Liu, C. Xiao, Y. Shi, L. Zhang, L. Jiang, K. K. Baldrige, Y. Li, J. S. Siegel, Z. Wang, *J. Am. Chem. Soc.* **2019**, *141*, 5402-5408.
- [158] S. Chen, D. Meng, J. Huang, N. Liang, Y. Li, F. Liu, H. Yan, Z. Wang, *CCS Chem.* **2021**, *3*, 78-84.
- [159] B. Mahlmeister, R. Renner, O. Anhalt, M. Stolte, F. Würthner, *J. Mater. Chem. C* **2022**, *10*, 2581-2591.
- [160] C. W. Tang, *Appl. Phys. Lett.* **1986**, *48*, 183-185.
- [161] A. Venkateswararao, K.-T. Wong, *Bull. Chem. Soc. Jpn.* **2020**, *94*, 812-838.
- [162] F. Würthner, *Chem. Commun.* **2004**, 1564-1579.
- [163] A. Nowak-Król, F. Würthner, *Org. Chem. Front.* **2019**, *6*, 1272-1318.
- [164] X. Wen, A. Nowak-Król, O. Nagler, F. Kraus, N. Zhu, N. Zheng, M. Müller, D. Schmidt, Z. Xie, F. Würthner, *Angew. Chem. Int. Ed.* **2019**, *58*, 13051-13055.
- [165] Z.-G. Zhang, B. Qi, Z. Jin, D. Chi, Z. Qi, Y. Li, J. Wang, *Energy Environ. Sci.* **2014**, *7*, 1966-1973.
- [166] Q. Shi, J. Wu, X. Wu, A. Peng, H. Huang, *Chem. Eur. J.* **2020**, *26*, 12510-12522.
- [167] Y. Lin, J. Wang, Z.-G. Zhang, H. Bai, Y. Li, D. Zhu, X. Zhan, *Adv. Mater.* **2015**, *27*, 1170-1174.
- [168] Y. Lin, F. Zhao, Q. He, L. Huo, Y. Wu, T. C. Parker, W. Ma, Y. Sun, C. Wang, D. Zhu, A. J. Heeger, S. R. Marder, X. Zhan, *J. Am. Chem. Soc.* **2016**, *138*, 4955-4961.
- [169] A. Armin, W. Li, O. J. Sandberg, Z. Xiao, L. Ding, J. Nelson, D. Neher, K. Vandewal, S. Shoaee, T. Wang, H. Ade, T. Heumüller, C. Brabec, P. Meredith, *Adv. Mater.* **2021**, *11*, 2003570.
- [170] A. Nowak-Król, K. Shoyama, M. Stolte, F. Würthner, *Chem. Commun.* **2018**, *54*, 13763-13772.
- [171] T. Huang, H. Chen, J. Feng, A. Zhang, W. Jiang, F. He, Z. Wang, *ACS Mater. Lett.* **2019**, *1*, 404-409.
- [172] Z. Ma, H. Fu, D. Meng, W. Jiang, Y. Sun, Z. Wang, *Chem. Asian J.* **2018**, *13*, 918-923.

- [173] Y. Lin, Y. Wang, J. Wang, J. Hou, Y. Li, D. Zhu, X. Zhan, *Adv. Mater.* **2014**, *26*, 5137-5142.
- [174] Y. Zhong, M. T. Trinh, R. Chen, G. E. Purdum, P. P. Khlyabich, M. Sezen, S. Oh, H. Zhu, B. Fowler, B. Zhang, W. Wang, C.-Y. Nam, M. Y. Sfeir, C. T. Black, M. L. Steigerwald, Y.-L. Loo, F. Ng, X. Y. Zhu, C. Nuckolls, *Nat. Commun.* **2015**, *6*, 8242.
- [175] T. Ye, R. Singh, H.-J. Butt, G. Floudas, P. E. Keivanidis, *ACS Appl. Mater. Interfaces* **2013**, *5*, 11844-11857.
- [176] R. Singh, J. Lee, M. Kim, P. E. Keivanidis, K. Cho, *J. Mater. Chem. A* **2017**, *5*, 210-220.
- [177] R. Schmidt, J. H. Oh, Y.-S. Sun, M. Deppisch, A.-M. Krause, K. Radacki, H. Braunschweig, M. Könemann, P. Erk, Z. Bao, F. Würthner, *J. Am. Chem. Soc.* **2009**, *131*, 6215-6228.
- [178] K. Fujimoto, M. Takahashi, S. Izawa, M. Hiramoto, *Materials* **2020**, *13*, 2148.
- [179] S.-H. Liao, H.-J. Jhuo, Y.-S. Cheng, S.-A. Chen, *Adv. Mater.* **2013**, *25*, 4766-4771.
- [180] T. Ikai, R. Kojima, S. Katori, T. Yamamoto, T. Kuwabara, K. Maeda, K. Takahashi, S. Kanoh, *Polymer* **2015**, *56*, 171-177.
- [181] M. Chen, X. Jiao, J. Li, W. Wu, H. Xin, C. R. McNeill, X. Gao, *Langmuir* **2019**, *35*, 6188-6195.
- [182] F. Zhang, Y. Hu, T. Schuettfort, C.-a. Di, X. Gao, C. R. McNeill, L. Thomsen, S. C. B. Mannsfeld, W. Yuan, H. Siringhaus, D. Zhu, *J. Am. Chem. Soc.* **2013**, *135*, 2338-2349.
- [183] R. B. Zerdan, N. T. Shewmon, Y. Zhu, J. P. Mudrick, K. J. Chesney, J. Xue, R. K. Castellano, *Adv. Funct. Mater.* **2014**, *24*, 5993-6004.
- [184] J. Liu, Y. Zhang, H. Phan, A. Sharenko, P. Moonsin, B. Walker, V. Promarak, T.-Q. Nguyen, *Adv. Mater.* **2013**, *25*, 3645-3650.
- [185] T. He, P. Leowanawat, C. Burschka, V. Stepanenko, M. Stolte, F. Würthner, *Adv. Mater.* **2018**, *30*, 1804032.
- [186] M. Chen, J. Li, X. Jiao, X. Yang, W. Wu, C. R. McNeill, X. Gao, *J. Mater. Chem. C* **2019**, *7*, 2659-2665.
- [187] K. Sugawara, N. Nakamura, Y. Yamane, S. Hayase, T. Nokami, T. Itoh, *Green Energy Environ.* **2016**, *1*, 149-155.
- [188] P. Josse, L. Favereau, C. Shen, S. Dabos-Seignon, P. Blanchard, C. Cabanetos, J. Crassous, *Chem. Eur. J.* **2017**, *23*, 6277-6281.
- [189] Y. Yang, B. Rice, X. Shi, J. R. Brandt, R. Correa da Costa, G. J. Hedley, D.-M. Smilgies, J. M. Frost, I. D. W. Samuel, A. Otero-de-la-Roza, E. R. Johnson, K. E. Jelfs, J. Nelson, A. J. Campbell, M. J. Fuchter, *ACS Nano* **2017**, *11*, 8329-8338.
- [190] I. Song, J. Ahn, X. Shang, J. H. Oh, *ACS Appl. Mater. Interfaces* **2020**, *12*, 49926-49934.
- [191] S. Ma, J. Gu, C. Lin, Z. Luo, Y. Zhu, J. Wang, *J. Am. Chem. Soc.* **2020**, *142*, 16887-16893.
- [192] G. Gao, X. Zhang, D. Meng, A. Zhang, Y. Liu, W. Jiang, Y. Sun, Z. Wang, *RSC Adv.* **2016**, *6*, 14027-14033.
- [193] B. Mahlmeister, Master Thesis, University of Würzburg (Germany), **2020**.
- [194] K. Ding, T. Shan, J. Xu, M. Li, Y. Wang, Y. Zhang, Z. Xie, Z. Ma, F. Liu, H. Zhong, *Chem. Commun.* **2020**, *56*, 11433-11436.
- [195] D. M. Stoltzfus, J. E. Donaghey, A. Armin, P. E. Shaw, P. L. Burn, P. Meredith, *Chem. Rev.* **2016**, *116*, 12920-12955.
- [196] J. C. Blakesley, F. A. Castro, W. Kylberg, G. F. A. Dibb, C. Arantes, R. Valaski, M. Cremona, J. S. Kim, J.-S. Kim, *Org. Electron.* **2014**, *15*, 1263-1272.
- [197] E. Sebastian, A. M. Philip, A. Benny, M. Hariharan, *Angew. Chem. Int. Ed.* **2018**, *57*, 15696-15701.

- [198] E. Castiglioni, S. Abbate, G. Longhi, R. Gangemi, *Chirality* **2007**, *19*, 491-496.
- [199] Y. Yang, R. C. da Costa, M. J. Fuchter, A. J. Campbell, *Nat. Photonics* **2013**, *7*, 634-638.
- [200] B. Mahlmeister, M. Mahl, H. Reichelt, K. Shoyama, M. Stolte, F. Würthner, *J. Am. Chem. Soc.* **2022**, *144*, 10507–10514.
- [201] M. Fujita, K. Wakabayashi, K. Nakada, K. Kusakabe, *J. Phys. Soc. Jpn.* **1996**, *65*, 1920-1923.
- [202] X. Li, X. Wang, L. Zhang, S. Lee, H. Dai, *Science* **2008**, *319*, 1229-1232.
- [203] A. Narita, X.-Y. Wang, X. Feng, K. Müllen, *Chem. Soc. Rev.* **2015**, *44*, 6616-6643.
- [204] J. Li, S. Sanz, N. Merino-Díez, M. Vilas-Varela, A. Garcia-Lekue, M. Corso, D. G. de Oteyza, T. Frederiksen, D. Peña, J. I. Pascual, *Nat. Commun.* **2021**, *12*, 5538.
- [205] O. V. Yazyev, *Acc. Chem. Res.* **2013**, *46*, 2319-2328.
- [206] A. Narita, X. Feng, K. Müllen, *Chem. Rec.* **2015**, *15*, 295-309.
- [207] A. Bedi, R. Carmieli, O. Gidron, *Chem. Commun.* **2019**, *55*, 6022-6025.
- [208] P. Malakar, V. Borin, A. Bedi, I. Schapiro, O. Gidron, S. Ruhman, *PCCP* **2022**, *24*, 2357-2362.
- [209] Y. Zhang, J. Qiao, S. Gao, F. Hu, D. He, B. Wu, Z. Yang, B. Xu, Y. Li, Y. Shi, W. Ji, P. Wang, X. Wang, M. Xiao, H. Xu, J.-B. Xu, X. Wang, *Phys. Rev. Lett.* **2016**, *116*, 016602.
- [210] E. Menard, V. Podzorov, S. H. Hur, A. Gaur, M. E. Gershenson, J. A. Rogers, *Adv. Mater.* **2004**, *16*, 2097-2101.
- [211] R. A. Pascal, *Chem. Rev.* **2006**, *106*, 4809-4819.
- [212] R. G. Clevenger, B. Kumar, E. M. Menuey, K. V. Kilway, *Chem. Eur. J.* **2018**, *24*, 3113-3116.
- [213] W. Chen, X. Li, G. Long, Y. Li, R. Ganguly, M. Zhang, N. Aratani, H. Yamada, M. Liu, Q. Zhang, *Angew. Chem. Int. Ed.* **2018**, *57*, 13555-13559.
- [214] W. Fan, T. Winands, N. L. Doltsinis, Y. Li, Z. Wang, *Angew. Chem. Int. Ed.* **2017**, *56*, 15373-15377.
- [215] R. K. Dubey, M. Melle-Franco, A. Mateo-Alonso, *J. Am. Chem. Soc.* **2021**, *143*, 6593-6600.
- [216] J. Liu, B.-W. Li, Y.-Z. Tan, A. Giannakopoulos, C. Sanchez-Sanchez, D. Beljonne, P. Ruffieux, R. Fasel, X. Feng, K. Müllen, *J. Am. Chem. Soc.* **2015**, *137*, 6097-6103.
- [217] K. Y. Cheung, C. K. Chan, Z. Liu, Q. Miao, *Angew. Chem. Int. Ed.* **2017**, *56*, 9003-9007.
- [218] M. Navakouski, H. Zhylitskaya, P. J. Chmielewski, T. Lis, J. Cybińska, M. Stępień, *Angew. Chem. Int. Ed.* **2019**, *58*, 4929-4933.
- [219] X.-Q. Sun, W.-S. Wong, Y. Li, D. Kuck, H.-F. Chow, *Org. Chem. Front.* **2021**, *8*, 5837-5846.
- [220] C. M. Cruz, I. R. Márquez, I. F. A. Mariz, V. Blanco, C. Sánchez-Sánchez, J. M. Sobrado, J. A. Martín-Gago, J. M. Cuerva, E. Maçôas, A. G. Campaña, *Chem. Sci.* **2018**, *9*, 3917-3924.
- [221] C. M. Cruz, S. Castro-Fernández, E. Maçôas, J. M. Cuerva, A. G. Campaña, *Angew. Chem. Int. Ed.* **2018**, *57*, 14782-14786.
- [222] S. Castro-Fernández, C. M. Cruz, I. F. A. Mariz, I. R. Márquez, V. G. Jiménez, L. Palomino-Ruiz, J. M. Cuerva, E. Maçôas, A. G. Campaña, *Angew. Chem. Int. Ed.* **2020**, *59*, 7139-7145.
- [223] P. Ravat, *Chem. Eur. J.* **2021**, *27*, 3957-3967.
- [224] P. J. Evans, J. Ouyang, L. Favereau, J. Crassous, I. Fernández, J. Perles, N. Martín, *Angew. Chem. Int. Ed.* **2018**, *57*, 6774-6779.

- [225] L. Hao, C. Xiao, J. Zhang, W. Jiang, W. Xu, Z. Wang, *J. Mater. Chem. C* **2013**, *1*, 7812-7818.
- [226] H. Quante, K. Müllen, *Angew. Chem., Int. Ed. Engl.* **1995**, *34*, 1323-1325.
- [227] Y. Geerts, H. Quante, H. Platz, R. Mahrt, M. Hopmeier, A. Böhm, K. Müllen, *J. Mater. Chem.* **1998**, *8*, 2357-2369.
- [228] J. H. Oh, W.-Y. Lee, T. Noe, W.-C. Chen, M. Könnemann, Z. Bao, *J. Am. Chem. Soc.* **2011**, *133*, 4204-4207.
- [229] P. Shao, M. Bai, *Chem. Commun.* **2012**, *48*, 9498-9500.
- [230] T. Miletić, A. Fermi, I. Papadakis, I. Orfanos, N. Karampitsos, A. Avramopoulos, N. Demitri, F. De Leo, S. J. A. Pope, M. G. Papadopoulos, S. Couris, D. Bonifazi, *Helv. Chim. Acta* **2017**, *100*, e1700192.
- [231] C. Former, S. Becker, A. C. Grimsdale, K. Müllen, *Macromolecules* **2002**, *35*, 1576-1582.
- [232] Y. Avlasevich, K. Müllen, *Chem. Commun.* **2006**, 4440-4442.
- [233] Y. Li, W. Xu, S. D. Motta, F. Negri, D. Zhu, Z. Wang, *Chem. Commun.* **2012**, *48*, 8204-8206.
- [234] M. Chen, N. E. Powers-Riggs, A. F. Coleman, R. M. Young, M. R. Wasielewski, *J. Phys. Chem. C* **2020**, *124*, 2791-2798.
- [235] M. Mahl, Ph.D. Thesis, University of Würzburg (Germany), **2021**.
- [236] K. Shoyama, M. Mahl, S. Seifert, F. Würthner, *J. Org. Chem.* **2018**, *83*, 5339-5346.
- [237] S. Seifert, K. Shoyama, D. Schmidt, F. Würthner, *Angew. Chem. Int. Ed.* **2016**, *55*, 6390-6395.
- [238] Z. Wang, C. Li, **2013**, CN 104418856 A.
- [239] Y. Zagranjarski, L. Chen, D. Jänsch, T. Gessner, C. Li, K. Müllen, *Org. Lett.* **2014**, *16*, 2814-2817.
- [240] M.-J. Lin, M. Schulze, K. Radacki, F. Würthner, *Chem. Commun.* **2013**, *49*, 9107-9109.
- [241] W. Yang, R. R. Kazemi, N. Karunathilake, V. J. Catalano, M. A. Alpuche-Aviles, W. A. Chalifoux, *Org. Chem. Front.* **2018**, *5*, 2288-2295.
- [242] R. L. Martin, *Chem. Phys.* **2003**, *118*, 4775-4777.
- [243] A. Alessi, M. Salvalaggio, G. Ruzzon, *J. Lumin.* **2013**, *134*, 385-389.
- [244] R. Englman, J. Jortner, *Mol. Phys.* **1970**, *18*, 145-164.
- [245] C.-A. Shen, M. Stolte, J. H. Kim, A. Rausch, F. Würthner, *J. Am. Chem. Soc.* **2021**, *143*, 11946-11950.
- [246] I. Lim, A. Vian, H. L. van de Wouw, R. A. Day, C. Gomez, Y. Liu, A. L. Rheingold, O. Campàs, E. M. Sletten, *J. Am. Chem. Soc.* **2020**, *142*, 16072-16081.
- [247] K. Rurack, M. Spieles, *Anal. Chem.* **2011**, *83*, 1232-1242.
- [248] E. D. Cosco, A. L. Spearman, S. Ramakrishnan, J. G. P. Lingg, M. Saccomano, M. Pengshung, B. A. Arús, K. C. Y. Wong, S. Glasl, V. Ntziachristos, M. Warmer, R. R. McLaughlin, O. T. Bruns, E. M. Sletten, *Nat. Chem.* **2020**, *12*, 1123-1130.
- [249] N. G. Pschirer, C. Kohl, F. Nolde, J. Qu, K. Müllen, *Angew. Chem. Int. Ed.* **2006**, *45*, 1401-1404.
- [250] M. D. Ward, J. Wade, X. Shi, J. Nelson, A. J. Campbell, M. J. Fuchter, *Adv. Opt. Mater.* **2022**, *10*, 2101044.
- [251] B. Mahlmeister, T. Schembri, V. Stepanenko, K. Shoyama, M. Stolte, F. Würthner, *J. Am. Chem. Soc.* **2023**, *145*, 13302-13311.
- [252] M. Schulz, F. Balzer, D. Scheunemann, O. Arteaga, A. Lützen, S. C. J. Meskers, M. Schiek, *Adv. Funct. Mater.* **2019**, *29*, 1900684.
- [253] I. Song, X. Shang, J. Ahn, J. H. Lee, W. Choi, H. Ohtsu, J. C. Kim, S. K. Kwak, J. H. Oh, *Chem. Mater.* **2022**, *34*, 8675-8683.
- [254] L. E. MacKenzie, R. Pal, *Nat. Rev. Chem.* **2021**, *5*, 109-124.

- [255] M. Schulz, J. Zablocki, O. S. Abdullaeva, S. Brück, F. Balzer, A. Lützen, O. Arteaga, M. Schiek, *Nat. Commun.* **2018**, *9*, 2413.
- [256] J. M. Fernández-García, P. Izquierdo-García, M. Buendía, S. Filippone, N. Martín, *Chem. Commun.* **2022**, *58*, 2634-2645.
- [257] M. Stępień, E. Gońka, M. Żyła, N. Sprutta, *Chem. Rev.* **2017**, *117*, 3479-3716.
- [258] Chaolumen, I. A. Stepek, K. E. Yamada, H. Ito, K. Itami, *Angew. Chem. Int. Ed.* **2021**, *60*, 23508-23532.
- [259] O. Smith, M. V. Popescu, M. J. Hindson, R. S. Paton, J. W. Burton, M. D. Smith, *Nature* **2023**, *615*, 430-435.
- [260] S. Hayakawa, A. Kawasaki, Y. Hong, D. Uruguchi, T. Ooi, D. Kim, T. Akutagawa, N. Fukui, H. Shinokubo, *J. Am. Chem. Soc.* **2019**, *141*, 19807-19816.
- [261] T. Liu, J. Yang, F. Geyer, F. S. Conrad-Burton, R. Hernández Sánchez, H. Li, X. Zhu, C. P. Nuckolls, M. L. Steigerwald, S. Xiao, *Angew. Chem. Int. Ed.* **2020**, *59*, 14303-14307.
- [262] N. Berova, L. D. Bari, G. Pescitelli, *Chem. Soc. Rev.* **2007**, *36*, 914-931.
- [263] F. Salerno, J. A. Berrocal, A. T. Haedler, F. Zinna, E. W. Meijer, L. Di Bari, *J. Mater. Chem. C* **2017**, *5*, 3609-3615.
- [264] A. Mukherjee, D. S. Pal, H. Kar, S. Ghosh, *Polym. Chem.* **2020**, *11*, 7481-7486.
- [265] M. Wehner, M. I. S. Röhr, V. Stepanenko, F. Würthner, *Nat. Commun.* **2020**, *11*, 5460.
- [266] R. S. Stoll, N. Severin, J. P. Rabe, S. Hecht, *Adv. Mater.* **2006**, *18*, 1271-1275.
- [267] L. I. Markova, V. L. Malinovskii, L. D. Patsenker, R. Häner, *Chem. Commun.* **2013**, *49*, 5298-5300.
- [268] A. Zampetti, A. Minotto, F. Cacialli, *Adv. Funct. Mater.* **2019**, *29*, 1807623.
- [269] D. Meng, R. Zheng, Y. Zhao, E. Zhang, L. Dou, Y. Yang, *Adv. Mater.* **2022**, *34*, 2107330.
- [270] K. Cai, J. Xie, D. Zhao, *J. Am. Chem. Soc.* **2014**, *136*, 28-31.
- [271] M. Murai, M. Abe, S. Ogi, S. Yamaguchi, *J. Am. Chem. Soc.* **2022**, *144*, 20385-20393.
- [272] Q. He, A. Basu, H. Cha, M. Daboczi, J. Panidi, L. Tan, X. Hu, C. C. Huang, B. Ding, A. J. P. White, J.-S. Kim, J. R. Durrant, T. D. Anthopoulos, M. Heeney, *Adv. Mater.* **2022**, *35*, 2209800.
- [273] A. Cravcenco, Y. Yu, F. Edhborg, J. F. Goebel, Z. Takacs, Y. Yang, B. Albinsson, K. Börjesson, *J. Am. Chem. Soc.* **2021**, *143*, 19232-19239.
- [274] A. P. Deshmukh, D. Koppel, C. Chuang, D. M. Cadena, J. Cao, J. R. Caram, *J. Phys. Chem. C* **2019**, *123*, 18702-18710.
- [275] G. Hong, A. L. Antaris, H. Dai, *Nat. Biomed. Eng.* **2017**, *1*, 0010.
- [276] M. M. J. Smulders, M. M. L. Nieuwenhuizen, T. F. A. de Greef, P. van der Schoot, A. P. H. J. Schenning, E. W. Meijer, *Chem. Eur. J.* **2010**, *16*, 362-367.
- [277] W. Wagner, M. Wehner, V. Stepanenko, F. Würthner, *J. Am. Chem. Soc.* **2019**, *141*, 12044-12054.
- [278] F. C. Spano, *J. Am. Chem. Soc.* **2009**, *131*, 4267-4278.
- [279] M. Casanova-Páez, L. Goerigk, *J. Chem. Theory Comput.* **2021**, *17*, 5165-5186.
- [280] B. Laidlaw, J. Eng, J. Wade, X. Shi, F. Salerno, M. J. Fuchter, T. J. Penfold, *Chem. Commun.* **2021**, *57*, 9914-9917.
- [281] M. Stolte, T. Schembri, J. Süß, D. Schmidt, A.-M. Krause, M. O. Vysotsky, F. Würthner, *Chem. Mater.* **2020**, *32*, 6222-6236.
- [282] F. Würthner, A. Sautter, J. Schilling, *J. Org. Chem.* **2002**, *67*, 3037-3044.
- [283] R. Sens, K. H. Drexhage, *J. Lumin.* **1981**, *24-25*, 709-712.
- [284] G. M. Sheldrick, *Acta Cryst.* **2008**, *A64*, 11.
- [285] Y. Sun, J. H. Seo, C. J. Takacs, J. Seifert, A. J. Heeger, *Adv. Mater.* **2011**, *23*, 1679-1683.

- [286] G. W. T. M. J. Frisch, H. B. Schlegel, G. E. Scuseria, M. A. Robb, J. R., G. S. Cheeseman, V. Barone, G. A. Petersson, H. Nakatsuji, X. Li, M., A. V. M. Caricato, J. Bloino, B. G. Janesko, R. Gomperts, B. Mennucci, J. V. O. H. P. Hratchian, A. F. Izmaylov, J. L. Sonnenberg, Williams, F. Ding,, F. E. F. Lipparini, J. Goings, B. Peng, A. Petrone, T. Henderson, D., V. G. Z. Ranasinghe, J. Gao, N. Rega, G. Zheng, W. Liang, M. Hada,, K. T. M. Ehara, R. Fukuda, J. Hasegawa, M. Ishida, T. Nakajima, Y., O. K. Honda, H. Nakai, T. Vreven, K. Throssell, J. A. Montgomery Jr., J. E., F. O. Peralta, M. J. Bearpark, J. J. Heyd, E. N. Brothers, K. N. Kudin, V., T. A. K. N. Staroverov, R. Kobayashi, J. Normand, K. Raghavachari, A. P., J. C. B. Rendell, S. S. Iyengar, J. Tomasi, M. Cossi, J. M. Millam, M. Klene,, R. C. C. Adamo, J. W. Ochterski, R. L. Martin, K. Morokuma, O. Farkas,, D. J. F. J. B. Foresman, *Wallingford, CT* **2016**.
- [287] G.-F. Zhang, H. Wang, M. P. Aldred, T. Chen, Z.-Q. Chen, X. Meng, M.-Q. Zhu, *Chem. Mater.* **2014**, *26*, 4433-4446.
- [288] S. S. Zaleskiy, V. P. Ananikov, *Organometallics* **2012**, *31*, 2302-2309.
- [289] G. M. Sheldrick, *Acta Cryst.* **2015**, *A71*, 3–8.
- [290] A. L. Spek, *Acta Cryst.* **2015**, *C71*, 9–18.
- [291] A. L. Spek, *J. Appl. Cryst.* **2003**, *36*, 7–13.
- [292] A. L. Spek, *Acta Cryst.* **2009**, *D65*, 148–155.
- [293] S. K. Lee, Y. Zu, A. Herrmann, Y. Geerts, K. Müllen, A. J. Bard, *J. Am. Chem. Soc.* **1999**, *121*, 3513-3520.
- [294] X. Zhao, Y. Xiong, J. Ma, Z. Yuan, *J. Phys. Chem. A* **2016**, *120*, 7554-7560.
- [295] J. Kim, J. Baek, E. Jeong, S. Han, Y. Kim, S. Hwang, **2019**.
- [296] W. Kabsch, *Acta Cryst.* **2010**, *D66*, 125–132.
- [297] Bruker, **2014**, pp. XPREP Version 2014/2012, Bruker AXS Inc., Madison.
- [298] G. M. Sheldrick, *Acta Cryst.* **2015**, *C71*, 3–8.
- [299] J.-D. Chai, M. Head-Gordon, *PCCP* **2008**, *10*, 6615-6620.
- [300] F. Weigend, R. Ahlrichs, *PCCP* **2005**, *7*, 3297-3305.
- [301] R. D. Gaussian 09, M. J. Frisch, G. W. Trucks, H. B. Schlegel, G. E. Scuseria, M. A. Robb, J. R. Cheeseman, G. Scalmani, V. Barone, B. Mennucci, G. A. Petersson, H. Nakatsuji, M. Caricato, X. Li, H. P. Hratchian, A. F. Izmaylov, J. Bloino, G. Zheng, J. L. Sonnenberg, M. Hada, M. Ehara, K. Toyota, R. Fukuda, J. Hasegawa, M. Ishida, T. Nakajima, Y. Honda, O. Kitao, H. Nakai, T. Vreven, J. A. Montgomery Jr., J. E. Peralta, F. Ogliaro, M. Bearpark, J. J. Heyd, E. Brothers, K. N. Kudin, V. N. Staroverov, T. Keith, R. Kobayashi, J. Normand, K. Raghavachari, A. Rendell, J. C. Burant, S. S. Iyengar, J. Tomasi, M. Cossi, N. Rega, J. M. Millam, M. Klene, J. E. Knox, J. B. Cross, V. Bakken, C. Adamo, J. Jaramillo, R. Gomperts, R. E. Stratmann, O. Yazyev, A. J. Austin, R. Cammi, C. Pomelli, J. W. Ochterski, R. L. Martin, K. Morokuma, V. G. Zakrzewski, G. A. Voth, P. Salvador, J. J. Dannenberg, S. Dapprich, A. D. Daniels, O. Farkas, J. B. Foresman, J. V. Ortiz, J. Cioslowski, D. J. Fox, **2013**, *Gaussian, Inc., Wallingford CT*.
- [302] T. Lu, F. Chen, *J. Comput. Chem.* **2012**, *33*, 580-592.
- [303] J. C. Chang, *Chem. Phys.* **1977**, *67*, 3901-3909.
- [304] H. Yamagata, C. M. Pochas, F. C. Spano, *J. Phys. Chem. B* **2012**, *116*, 14494-14503.
- [305] G. te Velde, F. M. Bickelhaupt, E. J. Baerends, C. Fonseca Guerra, S. J. A. van Gisbergen, J. G. Snijders, T. Ziegler, *J. Comput. Chem.* **2001**, *22*, 931-967.
- [306] *ADF 2013 SCM*.
- [307] J. P. Perdew, K. Burke, Y. Wang, *Phys. Rev. B* **1998**, *57*, 14999-14999.
- [308] P. L. Barbieri, P. A. Fantin, F. E. Jorge, *Mol. Phys.* **2006**, *104*, 2945-2954.
- [309] K. Senthilkumar, F. C. Grozema, F. M. Bickelhaupt, L. D. A. Siebbeles, *Chem. Phys.* **2003**, *119*, 9809-9817.

- [310] S.-H. Wen, A. Li, J. Song, W.-Q. Deng, K.-L. Han, W. A. Goddard, III, *J. Phys. Chem. B* **2009**, *113*, 8813-8819.
- [311] A. Austin, N. J. Hestand, I. G. McKendry, C. Zhong, X. Zhu, M. J. Zdilla, F. C. Spano, J. M. Szarko, *J. Phys. Chem. Lett.* **2017**, *8*, 1118-1123.

Individual Contributions

The co-authors of the manuscripts included in this cumulative thesis are informed and agree with the reprint and the respective individual contributions as stated below.

Axially chiral bay-tetraarylated perylene bisimide dyes as non-fullerene acceptors in organic solar cells

B. Mahlmeister, R. Renner, O. Anhalt, M. Stolte, F. Würthner, *J. Mater. Chem. C* **2022**, *10*, 2581–2591.

Autor	B.M.	R.R.	O.A.	M.S.	F.W.	Σ
Design of research				1%	3%	4%
Synthesis and purification	2%	14%				16%
Optical and structural characterization	12%	5%	8%	3%		28%
Device fabrication and characterization	30%					30%
Theoretical calculations	2%					2%
Publication writing	6%			1%		7%
Publication correction				3%	5%	8%
Publication coordination				1%	4%	5%
Summe	52%	19%	8%	9%	12%	100%

Helically Twisted Nanoribbons Based on Emissive Near-Infrared Responsive Quaterrylene Bisimides

B. Mahlmeister, M. Mahl, K. Shoyama, H. Reichelt, M. Stolte, F. Würthner, *J. Am. Chem. Soc.* **2022**, *144*, 10507–10515.

Autor	B.M.	M.M.	K.S.	H.R.	M.S.	F.W.	Σ
Design of research				2%		3%	5%
Synthesis	25%	25%					50%
Characterization	10%	7%	5%		3%		25%
Theoretical calculations	5%						5%
Publication writing	6%	1%			1%	2%	10%
Publication correction	3%				1%	1%	5%
Summe	49%	33%	5%	2%	5%	6%	100%

Enantiopure J-Aggregate of Quaterrylene Bisimides for Strong Chiroptical NIR-Response

B. Mahlmeister, T. Schembri, V. Stepanenko, K. Shoyama, M. Stolte, F. Würthner, *J. Am. Chem. Soc.* **2023**, *145*, 13302–13311.

Autor	B.M.	T.S.	V.S.	K.S.	M.S.	F.W.	Σ
Design of research	1%				1%	3%	5%
Synthesis	8%						8%
Characterization	20%		8%	9%	5%		42%
Theoretical calculations	20%	5%					25%
Publication writing	10%						10%
Publication correction	1%				2%	4%	7%
Publication coordination					1%	2%	3%
Summe	60%	5%	8%	9%	9%	9%	100%

Danksagung

Mein besonderer Dank gilt meinem Doktorvater **Prof. Dr. Frank Würthner** für die Möglichkeit zur Anfertigung dieser Arbeit auf einem sehr spannenden und vielfältigen Themengebiet unter hervorragenden Bedingungen. Vielen Dank für das mir entgegengebrachte Vertrauen und die damit verbundenen Freiheiten in der Bearbeitung der Themenstellungen, sowie die Wertschätzung der erbrachten Arbeit. Vielen Dank für die kritischen und konstruktiven wissenschaftlichen Diskussionen, die Hilfe beim Verfassen und Überarbeiten von Manuskripten, sowie die Bereitstellung der exzellenten Laborinfrastruktur, ohne die diese Arbeit nicht möglich gewesen wäre. Vielen Dank für Deine stets außerordentlich schnelle Rückmeldung und Hilfe bei allen wissenschaftlichen und organisatorischen Belangen. Ich möchte mich ebenfalls dafür bedanken, dass ich die Möglichkeit zum Besuch zweier großer internationaler Konferenzen erhalten habe.

Ein besonderer Dank gilt **Dr. Matthias Stolte**, der mich in allen Situationen, ob spektroskopischen oder materialwissenschaftlichen Fragestellungen, dem Konzipieren von Versuchen, beim Anfertigen von Vorträgen und Manuskripten, sowie vor allem menschlich stets begleitet und unterstützt hat. Danke für alles!

Ich möchte mich bei **Dr. Vladimir Stepanenko**, **Dr. Kazutaka Shoyama**, **Olga Anhalt** und **Tim Schembri** und bedanken, die mit ihrer speziellen Expertise in Kristallographie, Mikroskopie und theoretischen Berechnungen einen sehr wesentlichen Beitrag zum Gelingen dieser Arbeit geleistet haben.

Ich möchte mich bei den ehemaligen Doktoranden bedanken, die diese Arbeit mit auf den Weg gebracht haben: bei **Dr. Rebecca Renner** für die Synthesearbeit der tetraarylierten PBIs, bei **Dr. Magnus Mahl** für seine vorausgehenden Arbeiten an QBIs und bei **Dr. Kaan Menekse** für meine Einarbeitung in die Materialwissenschaften.

Ich bedanke mich bei allen technischen Angestellten des Arbeitskreises, insbesondere bei **Julius Albert**, **Hendrik Hebling**, **Astrid Kudzus** und **Olga Anhalt**. Vielen Dank an **Jennifer Begall**, **Sarah Bullheimer** und **Lisa Weidner** für Hilfe bei administrativen und organisatorischen Fragestellungen. Mein Dank gilt außerdem der Abteilung von **Dr. Juliane Adelman** für das Messen von Massenspektren.

Ich bedanke mich bei meinen Praktikanten **Franziska Schneider**, **Daniel Göbel**, **Yi-Chun Chen**, **Xincheng Miao** und **Jannick Windelberg**, sowie meiner Bachelorandin **Judith Jung** für ihre Arbeiten in Synthese, Spektroskopie und Programmierung.

Ich möchte mich bei **Dr. Joshua Selby**, **Emely Freytag** und **Alexander Schmiedel** für wissenschaftliche Diskussionen, sowie die sehr unkomplizierte Bereitstellung von Geräteteilen bedanken.

Tim Schembri und **Matthias Stolte** möchte ich für das Korrekturlesen von Teilen dieser Arbeit danken.

Ich möchte mich beim gesamten **Arbeitskreis Würthner** bedanken, insbesondere bei allen (ehemaligen) Mitarbeitern des CNC-Gebäudes, einschließlich dem **Arbeitskreis Nowak-Król**, der **Arbeitsgruppe Greenfield** und dem **Arbeitskreis Pöppler**. Die Gemeinschaft und das menschliche Miteinander hat mir immer sehr viel bedeutet, auch in etwas schwierigeren Situationen. Vielen Dank für die tolle Zeit der letzte Jahre!

Ich möchte mich auch bei allen **Freunden** bedanken, die diese Zeiten mit mir erlebt und mitgetragen haben.

Zuletzt möchte ich mich von ganzem Herzen bei meiner Familie bedanken: meinen **Eltern**, meinem **Bruder** und ganz besonders meiner **Freundin** und auch ihrer Familie. Vielen Dank für Eure bedingungslose Unterstützung während des gesamten Studiums und der Doktorarbeit!

List of Publications

Axially chiral bay-tetraarylated perylene bisimide dyes as non-fullerene acceptors in organic solar cells

B. Mahlmeister, R. Renner, O. Anhalt, M. Stolte, F. Würthner, *J. Mater. Chem. C* **2022**, *10*, 2581–2591.

Helically Twisted Nanoribbons Based on Emissive Near-Infrared Responsive Quaterrylene Bisimides

B. Mahlmeister, M. Mahl, H. Reichelt, K. Shoyama, M. Stolte, F. Würthner, *J. Am. Chem. Soc.* **2022**, *144*, 10507–10514.

Naphthalimide-Annulated [n]Helicenes: Red Circularly Polarized Light Emitters

X. Tian, K. Shoyama, B. Mahlmeister, F. Brust, M. Stolte, Frank Würthner, *J. Am. Chem. Soc.* **2023**, *145*, 9886–9894.

Enantiopure J-Aggregate of Quaterrylene Bisimides for Strong Chiroptical NIR-Response

B. Mahlmeister, T. Schembri, V. Stepanenko, K. Shoyama, M. Stolte, F. Würthner, *J. Am. Chem. Soc.* **2023**, *145*, 13302–13311